
Accretion and Ejection in Resistive GR-MHD

Qian Qian
Max-Planck-Institut für Astronomie

Heidelberg 2017

Accretion and Ejection in Resistive GR-MHD
submitted to the
Combined Faculties of the Natural Sciences and Mathematics
of the Ruperto-Carola-University of Heidelberg, Germany,
for the degree of
Doctor of Natural Sciences

Put forward by
Qian Qian
born in Shanghai, China

Oral examination: May 10th, 2017.

Accretion and Ejection in Resistive GR-MHD

**Referees: Priv. Doz. Dr. Christian Fendt
Prof. Dr. Cornelis P. Dullemond**

知人者智,自知者明。
胜人者有力,自胜者强。

Gottes Zeit, Gottes Zeit,
ist die allerbe...ste
ist die, allerbeste Zeit :-)¹

¹This is just a song for fun and no translation for the dedication in last page!

Abstract

In this thesis, the accretion and ejection processes from a black hole accretion system is investigated by means of resistive general relativistic magnetohydrodynamic simulations. As a supplement to the results from prior research with non-relativistic simulations, my results confirm that the winds and outflows originated from thin accretion disks can also be observed in general relativistic simulations. In the first part, the execution of the implementation of resistivity, namely magnetic diffusivity, into the existing non-resistive general relativistic magnetohydrodynamic code HARM is illustrated. The test simulations of the new code rHARM include the comparison with analytical solution of the diffusion equation and a classic shock tube test. rHARM shows reliable performances in these tests. In the second part, rHARM is applied to investigate the evolution of magnetized tori. The results show that the existence of resistivity leads to inefficient accretions of matter from tori onto black holes by weakening the magnetorotational instability inside the tori. An indication for a critical magnetic diffusivity in this simulation setup is found beyond which no magnetorotational instability develops in the linear regime. In the third part, as the main purpose of this PhD project, rHARM is used to perform simulations of magnetically diffusive thin accretion disks that are threaded by a large-scale poloidal magnetic field around non-rotating and rotating black holes. These long-term simulations last 3000 code time units, which are about 195 rotation periods at the disk inner boundary, correspondingly. Their computational domains extend from black hole horizon to 80 Schwarzschild radii. Outflows driven from the accretion disk are clearly seen. These outflows have the typical radial velocity of 0.1 speed of light. In my analyses, I argue that these outflows are driven by the magnetic pressure gradient from the toroidal magnetic field generated by the rotation of the disk. The small ratios of the poloidal field strengths to the toroidal field strengths suggest the interpretation of the outflows as “tower jet,” rather than centrifugally driven winds (Blandford-Payne effect). Furthermore, I find direct evidence of the growths of magnetorotational instabilities inside the accretion disks, which are suppressed by the increasing levels of magnetic diffusivity. This suppression leads to inefficient accretion and ejection processes of the accretion system. Finally, the influences of rotating black holes on the accretion systems are explored. The results show an suppression effect on the black hole spin on the accretion and ejection processes in the system. The tangled field lines within the ergosphere induced by the black hole rotation produce magnetic pressure that pushes against the accreting matter from the disk. In the simulations with large spin parameters, energy extraction from the black hole (Blandford-Znajek effect) is observed, which is, nevertheless, $\sim 10^2$ times smaller than the energy production from the disk outflow.

Zusammenfassung

In der vorliegenden Arbeit werden resistive allgemein-relativistische magnetohydrodynamische Simulationen benutzt, um die Akkretion, Winde und Jets von Akkretionsscheiben um ein schwarzes Loch zu untersuchen. Als Weiterführung bisheriger Arbeiten in der Literatur in nicht-relativistischer Näherung belegen meine Ergebnisse, dass von der Akkretionsscheibe erzeugte Winde und Ausflüsse auch in allgemein-relativistischen Simulationen zu beobachten sind. Im ersten Teil der Arbeit diskutiere ich die Implementierung der Resistivität, oder auch magnetischer Diffusivität, in dem bereits existierenden, nicht-resistiven allgemein-relativistischen magnetohydrodynamischen Code HARM. Testsimulationen meines neuen Codes rHARM werden mit der analytischen Lösung der Diffusionsgleichung und dem klassischen Problem einer zylinderförmigen Stoßfront (“Shock tube”) verglichen. Die Tests zeigen klar die Zuverlässigkeit von rHARM. Im zweiten Teil wird mit rHARM die Entwicklung von magnetisierten Tori untersucht. Die Ergebnisse zeigen, dass die Wirkung der Resistivität zu ineffizienter Massenakkretion der Tori auf schwarze Löcher führt. Hier kann ein Hinweis auf einen kritischen Wert der magnetischen Diffusivität gefunden werden, über dem keine Magnetorotationsinstabilität im linearen Bereich stattfindet. Im dritten Teil - dem Hauptteil dieses Promotionsprojekts - wird rHARM benutzt, um Simulationen von magnetisch diffusiven, dünnen Akkretionsscheiben um nicht-rotierende und rotierende schwarze Löcher durchzuführen. Insbesondere wird ein globales, offenes poloidales magnetisches Feld angenommen, das die Scheibe durchläuft. Diese Simulationen dünner Scheiben laufen 3000 Zeiteinheiten des Codes - was c.a. 195 Perioden von der innersten Scheibenlaufbahn entspricht. Das numerische Gitter erstreckt sich vom Horizont bis 80 Schwarzschildradien. Die von den Akkretionsscheiben generierten Ausflüsse sind eindeutig zu sehen. Die Ausflüsse haben eine radiale Geschwindigkeit von typischerweise 0,1 facher der Lichtgeschwindigkeit. In meiner Analyse argumentiere ich, dass diese Ausflüsse vom Gradienten des toroidalen magnetischen Feld getrieben werden, das von der Scheibenrotation induziert wird. Die kleinen Verhältnisse von poloidalen Feldstärke zu toroidalen Feldstärke in den Simulationen deuten an, die Ausflüsse als “Tower Jets” statt der zentrifugal getriebenen Winde (Blandford-Payne-Effekt) zu präsentieren. Darüber hinaus finde ich einen direkten Hinweis für das Wachstum der Magnetorotationsinstabilität innerhalb der Akkretionsscheiben. Diese Instabilität wird bei steigender magnetischer Diffusivität untergedrückt und führt dann zu ineffizienterer Akkretion und Winderzeugung. Schließlich wird der Einfluss der Lochrotation auf das Akkretionsystem erforscht. Die Ergebnisse zeigen, dass die Rotation des schwarzen Lochs die Akkretion und den Ausstoß von Winden im System unterdrückt. Das scheint daran zu liegen, dass der magnetische Druck der innerhalb der Ergosphäre induzierten und “aufgewickelten” Feldlinien die Massenakkretion der Scheibe bremst. In Simulationen schnell rotierender schwarzer Löcher wird die Energieentnahme aus dem Loch beobachtet (Blandford-Znajek-Effekt). Sie ist jedoch um einen Faktor 100 kleiner als die Energieerzeugung durch die Scheibenausflüsse.

Contents

1	Introduction	1
1.1	Astrophysical jets	1
1.2	Jets in active galactic nuclei	5
1.2.1	A brief AGN story	5
1.2.2	Observational features of AGN jets	9
1.2.3	Central engines of AGNs	11
1.3	Spacetime around the black hole	13
1.3.1	Spacetime and metric	14
1.3.2	Non-rotating/rotating black hole and the Boyer-Lindquist coordinates	16
1.3.3	The Kerr-Schild coordinates	18
1.3.4	Derivative in the curved spacetime	19
1.4	A brief introduction of magnetohydrodynamics	20
1.4.1	The MHD equations	20
1.4.2	The ideal MHD assumption	21
1.5	Jets in Numerical Simulation	22
1.5.1	The numerical approaches in jets simulation	23
1.5.2	The necessity of diffusivity in GR-MHD	23
1.5.3	Existing resistive codes	24
1.6	Convention and units in this thesis	25
1.7	Outline of the thesis	25
2	Physical process in accretion system	27

2.1	The Shakura and Sunyaev accretion disk model	27
2.1.1	The general picture of black hole accretion disk	27
2.1.2	The disk structure	29
2.2	Magnetorotational instability	31
2.2.1	The analysis of linear perturbation	31
2.2.2	Dependence of perturbation growth on field strength	33
2.3	Disk driven wind - the Blandford & Payne mechanism	36
2.3.1	The centrifugally driven outflow	36
2.3.2	Behavior of the disk wind in self-similar solution	37
2.4	Energy extraction from rotating black hole - the Blandford & Znajek mechanism	40
2.4.1	The force-free magnetosphere around a black hole	40
2.4.2	Dependence of the energy extraction efficiency on the black hole spin . .	42
3	Numerical Implementation of Resistive GR-MHD	43
3.1	Basics of rHARM	43
3.1.1	A brief introduction to the Godunov's scheme	43
3.1.2	The approximate flux on the cell board	45
3.1.3	Primitive variables and the inversion scheme	48
3.2	Implementation of magnetic resistivity	49
3.2.1	The general form of GR-MHD equations	49
3.2.2	Turbulent resistivity in rHARM	51
3.2.3	The inversion scheme	52
3.2.4	A preliminary test of the implementation	55
3.2.5	Time Evolution in HARM	55
3.3	Other common settings in rHARM	57
3.3.1	Units and normalization	57
3.3.2	Numerical grid	58

3.3.3	Boundary conditions and the initial condition for electric field	58
3.3.4	Scaling code units to reality	58
3.4	Diffusivity tests I – gas box test	60
3.4.1	Simulation region and boundary condition	60
3.4.2	Initial conditions	60
3.4.3	Test simulations of magnetic diffusivity	63
3.4.4	Diffusivity test near a black hole	65
3.5	Diffusivity tests II – shock tube test	66
3.5.1	Computational domain and initial conditions	66
3.5.2	Shock tube test simulations	66
3.6	The numerical diffusivity	69
3.7	Summary and conclusions	70
4	Simulations of resistive magnetized tori	75
4.1	Computational domain and initial conditions	75
4.2	Robustness of rHARM as seen from torus simulations	76
4.3	Comparing rHARM simulations to the HARM simulation <i>torT0</i>	79
4.4	MRI evolution in a resistive GR-MHD torus	81
4.5	Summary and conclusions	84
5	Resistive magnetized thin accretion disk and disk outflows	85
5.1	Simulation setup	85
5.1.1	Simulation region and boundary conditions	85
5.1.2	Initial disk density and the velocity profile	86
5.1.3	Initial condition for the magnetic field and diffusivity	88
5.1.4	About the choice of simulation parameters	89
5.2	Measuring the accretion rate and ejection rate	89

5.3	Very weakly magnetized accretion disk	92
5.3.1	Disk structure evolution	92
5.3.2	Accretion due to MRI	94
5.3.3	Matter collapsing towards the disk mid-plane	95
5.4	Outflows from accretion disk	95
5.4.1	Disk evolution	95
5.4.2	Disk wind evolution	97
5.4.3	Wind radial velocity	97
5.4.4	Inner boundary of the disk	100
5.5	Influence of diffusivity on accretion and ejection rates	100
5.5.1	Diffusivity and accretion	100
5.5.2	Efficiency of outflow launching	106
5.5.3	Simulations with different diffusivity profile	107
5.6	The driving force of outflow	107
5.6.1	Poloidal Alfvén Mach number	109
5.6.2	Magnetic field pressure	112
5.6.3	Thermal pressure	113
5.6.4	Tower jet	113
5.6.5	Collimation or not?	114
5.6.6	Comparison to non-relativistic simulations	114
5.7	Convergence issue in simulations <i>D8</i> and <i>D16</i>	115
5.8	The initial field structure dependence	115
5.9	The resolution dependence of the simulations	118
5.10	Summary and conclusions	121
6	Accretion system with rotating black hole	125
6.1	Influence of the black hole spin on accretion and ejection	125

<i>Contents</i>	xvii
6.2 Blandford-Znajek process in the simulation	129
6.3 Disk wind v.s. Blandford-Znajek effect	132
6.4 Summary and conclusions	133
7 Conclusions and Future Projects	135
Acknowledgments	141
A Appendixes	1
A.1 Superluminal motion	1
A.2 3+1 spacetime	2
A.2.1 Split spacetime into space and time	2
A.2.2 The projection tensors	4
A.3 Orbits shift of Keplerian rotating object	5
A.4 Different regimes in the radial direction of the Shakura & Sunyaev disk model . .	5
A.5 The electromagnetic component in the stress-energy tensor in resistive GR-MHD	7
A.6 Newton-Raphson Method	9

List of Figures

- 1.1 *left*: An image of HH47 jet taken by NASA Hubble Space Telescope in visible light. The center source of this roughly 0.5 lightyear-long jet is hidden inside a dust cloud at the lower left edge of the image. The jet has burrowed a cavity through the dense gas cloud and now travels at high speed into interstellar space. Shock waves form when the jet collides with interstellar gas, causing the jet to glow. Credit: J. Morse/STScI, and NASA. *right*: The false color image of HH212 jet taken by VLT in the infrared H_2 emission line (adapted from [Bally \(2007\)](#)). It shows a very young jet driven by an invisible protostar in the vicinity of the Horsehead nebula in Orion ([Zinnecker et al. 1998](#)). 2
- 1.2 A sequence of MERLIN observations of the X-ray binary GRS 1915+105 taken in 1997 October/November ([Fender et al. 1999](#)). This false color image shows the data observed using the MERLIN array at 4.994 GHz (radio wavelength) with a bandwidth of 16 MHz. The anti-parallel ejection of clouds in this plot were moving at relativistic velocities. Credit: MERLIN/VLBI National Facility. 3
- 1.3 *left*: An image taken by Hubble Space Telescope which shows the jet of matter ejected from M87 at nearly light speed, as it stretches 1.5 kpc from the galactic core. The appearance of the single jet component is due to the relativistic beaming effect (see Section 1.2.2). *right*: An image of radio galaxy 3C31 in ~ 100 kpc scale. Blue color shows the optical image from POSS II survey while the red color gives the radio image from the VLA at 21cm wavelength. It is clear to see the influence of the jets to its ambient in the galactic scale. Credit: NRAO/AUI. 4

- 1.4 *left*: A composite false color image of the spiral Seyfert galaxy NGC 4151. In the image, the X-rays (blue) from the Chandra X-ray Observatory are combined with optical data (yellow) showing positively charged hydrogen (“H II”) from observations with the 1-meter Jacobus Kapteyn Telescope on La Palma. The red around the bright core shows neutral hydrogen detected by radio observations with the NSF’s Very Large Array. *right*: An image from Hubble’s Wide Field and Planetary Camera 2 (WFPC2) of quasar 3C 273, which resides in a giant elliptical galaxy in the constellation of Virgo. Its light has taken some 2.5 billion years to reach us. Despite this great distance, it is still one of the closest quasars to Earth. 6
- 1.5 A schematic explanation of AGN unification model. The orientation of the AGN host galaxy (face on or edge on) plays an important role here. For the radio-loud AGNs, when observed at 90° from the jets (left), they appear as radio galaxies, when at an angle to the jet (middle), as quasars, and when directly down to the jet (right), as blazars. Since the fact that the galaxy’s disk can obscure certain ranges of AGN emission, the orientation-dependent model has also been applied to unify radio-quiet AGNs. For the radio-quiet, when the viewing angle is 90° (left), they appear as Seyfert 2 as galaxies, and when at an angle, as Seyfert 1 galaxies. Figure credit: Ron Kollgaard. 8
- 1.6 *left*: 3C31 as an example of FRI radio galaxy. Its relativistic electron jets detected in radio wavelengths extend for several kpc with the brightness of the jets decreasing outwards. *left*: FRII radio galaxy 3C219 detected in radio wavelengths. The filamentary lobes in the plot extend several hundred kpc with bright hot spots in both lobes. Figure credit: NRAO/AUI. 9
- 1.7 A VLBI high resolution radio interferometry image of M87 core in 10⁻²pc scale adapted from [Hada et al. \(2016\)](#). 10
- 1.8 *left*: An illustration plot of MRI. The originally straight magnetic field line was bent by a tiny random displacement between two parts in the disk. The magnetic tension then serves as restoring force and transports angular momentum between the two parts and results in accretion. Credit: Plasma Physics Group/Physics Department/University of Wisconsin–Madison. *right*: The centrifugally driven disk wind caused by the large scale magnetic field line that cross the accretion disk with an angle (see corresponding text). Plot adopted from [Sheikhnezami et al. \(2012\)](#). 12

- 1.9 A preliminary sketch of mass curved spacetime. In example a, mass is absent and spacetime is flat. In example b, spacetime is curved because of the attendance of the mass in the center. Imagine a tiny particle with ignorable mass moving along the trajectory of a grid line in example a, the orbit of this particle will be a straight line. However, putting this particle into example b and letting it again move along the same grid line, its orbit will become a curve although it actually follows the trajectory as in the flat space. Note that this sketch is a very rough illustration. The true spacetime is 4 dimensional and its curvature needs to be calculated according to the situation very carefully. Figure credit: Jacky Jerome. 15
- 1.10 A two dimensional illustration plot of the ergosphere of a rotating black hole. The axes in the plot are in units of GM/c^2 . And the parameter $a = 0.99M$. The inner horizon is the inner singularity and the outer horizon is the black hole event horizon. The grey area between event horizon the the ergosphere is called ergoregion where no object inside is able to hold still to an observer at infinity (see text). The ergosphere is not a strict spheroid since the BL coordinates are not strictly spherical. Credit: Yukterez (Simon Tyran, Vienna). 17
- 1.11 left: A closed curve C_1 embedded in and flow with the material. After time dt , the circle moves to C_2 . The surface closed by C_1 is f_1 , and f_1 by C_2 . right: Illustration figures of frozen filed lines in ideal MHD. v in the plot stands for velocity. In this case, no matter how the the magnetic field lines construct, fluid elements always follow the field lines to keep the magnetic flux unchanged inside the closed circle that moves from c to c' (see text). Credit: [Kippenhahn & Moellenhoff \(1975\)](#) 22
- 2.1 Two regime of matter flowing from a star in a binary system into the influence of the black hole: upper): a normal companion star that fills up its Roche volume and the matter flows mainly through the inner Lagrangian point. Lower): the size of the companion star is much smaller than the Roche volume. The matter will then lose part of its kinetic energy in the shock wave before being captured by the gravitational field of black hole. In both cases mentioned above, an accretion disk will form around the black hole. Figure credit: [Shakura & Sunyaev \(1973\)](#). 28
- 2.2 The mode amplitude from simulations with different magnetic field strength in the same numerical resolution, top: $\beta_z = 1000$, middle: $\beta_z = 4000$, lower: $\beta_z = 16000$. Below 2.2 orbital rotations, the perturbations are still in the linear regime. Some modes stay stable, while others start growing according to the corresponding critical wave numbers (see text). This figure is adopted from [Balbus & Hawley \(1991\)](#). 34

- 2.3 The poloidal field line structure in the simulation with $\beta_z = 1000$ at upper: $t=0$, lower: $t=3.3$ orbits. The dominant mode of unstable perturbation in this simulation is $\bar{k}_z = 1$ (see corresponding text). This figure is adopted from [Balbus & Hawley \(1991\)](#). 36
- 2.4 Equipotential surfaces for the fluid element A threaded on a magnetic field line that goes through the Keplerian accretion disk at point $(r_0, 0)$. The stable region has higher potential than the point $(r_0, 0)$, while the unstable regions have lower potential. An attempted movement for A from r_0 to the unstable region on the right hand side makes A leave the disk to the lower potential region. The dashed line at $r = \sqrt{3}r_0$ is the asymptote for the surface of marginal stability which reaches infinity in the z -direction. The angle between the right marginal stable surface and the disk is 60° . This figure is adopted from [Blandford & Payne \(1982\)](#). 38
- 2.5 The results of the “standard” solution for the cold ideal MHD flow in Keplerian accretion disk. left: The integrated field lines projected into the poloidal plane in self-similar coordinates (ξ, χ) . The dashed line presents the surface where the Alfvén Mach number $\sqrt{m} = 1$. The surfaces for certain pitch angles $\alpha = \tan^{-1} |B_\phi/B_p|$ are denoted by the dotted lines. right: The dynamics along a single outflow streamline. \sqrt{m} is the Alfvén Mach number, \sqrt{n} is the fast-mode magnetosonic Mach number, $\sqrt{U}f$ stands for the poloidal velocity and g represents the toroidal velocity. The ratio of the toroidal field strength to the poloidal field strength is also given in the plot. The parameter θ is the polar angle as measured from the origin of the coordinate system. Credit: [Blandford & Payne \(1982\)](#). 39
- 2.6 A sketch of the electrical flow on the equipotential surfaces of the magnetic field lines that penetrate the ergosphere of the black hole. The angular velocity of the magnetic field lines noted by Ω , is defined so that an observer orbiting with this angular velocity would not see any electric field. The black hole spins with angular velocity Ω_H . Ω_L is the angular velocity of an external load resistance. Here the mechanism of gamma-ray production can be treated as the external resistance (see corresponding text). This figure is adopted from [Blandford et al. \(1990\)](#), page 207. 41
- 3.1 The mesh grid sketch for the illustration of Godunov’s scheme (see text for the detail) adopted from the “Lecture Notes for the COMPSTAR School on Computational Astrophysics,” August 10, 2010 by Olindo Zanotti & Gian Mario Manca. 44

- 3.2 An example of the discontinuous distribution of the conserved variable U caused by the piece-wise constant method. This Figure is adopted from the “Lecture Notes for the COMPSTAR School on Computational Astrophysics,” August 10, 2010 by Olindo Zanotti & Gian Mario Manca. 46
- 3.3 *Left:* Control volume for the computation of the approximate HLL flux. *Right:* The average of U in different regions divided by the shock wave propagation in two directions. Both plots are adopted from the “Lecture Notes for the COMPSTAR School on Computational Astrophysics,” August 10, 2010 by Olindo Zanotti & Gian Mario Manca. 47
- 3.4 A flow chart for the basic structure of rHARM as a conservative scheme. Before the start of the next time evolution over conserved variables, primitive variables which determine the flux on the cell board mentioned in Section 3.1.2 need to be updated from the current conserved variables. Credit: [Mignone et al. \(2007\)](#). 48
- 3.5 The flow chart describing the numerical procedure of one time evolution in rHARM. Boxes with a grey background denotes one or a series of routines that achieve the function written inside those boxes. The flow chart on the left hand side presents the procedure of one time evolution while the large box on the right hand side is a detailed flow description for the process inside the box (3) on the left hand side. See the text for explanations of each step in the chart. . . . 56
- 3.6 Numerical tests of magnetic diffusivity. The radial profile of the magnetic field $B_\theta(r)$ is plotted along the equatorial plane. We show simulation *difT0* with $\eta = 10^{-10}$ (upper) and simulation *difT2* with $\eta = 10^{-2}$ (lower), both with a grid resolution 256x256. Different colors represent the corresponding simulation time steps t as labeled in the legend. The actual time \tilde{t} of these steps are $\tilde{t} = t_0 + t$, where t_0 depends on the initial condition. Solid lines are from simulation results, while dashed lines from analytic solutions. Note the difficulty in distinguishing dashed lines from solid lines, due to the perfect match between the analytical and numerical solutions. In simulation *difT0*, all 6 curves are plotted. Yet, they look like one curve, because with $\eta = 10^{-10}$, the magnetic field does not diffuse at all. 61

- 3.7 Numerical tests of magnetic diffusivity. The radial profile of the magnetic field $B_\theta(r)$ is plotted along the equatorial plane. We show simulation *difT1*, where $\eta = 10^{-3}$ (upper) is applied with a grid resolution 256x256 and simulation *difT3*, where $\eta = 10^{-3}$ is applied with a grid resolution 128x128 (lower). Different colors represent the corresponding simulation time steps t , as labeled in the legend. The actual time \tilde{t} of these steps are $\tilde{t} = t_0 + t$, where t_0 depends on the initial condition. Solid lines represent simulation results, while dashed lines represent analytic solutions. Note the difficulty in distinguishing dashed lines from solid lines, due to the perfect match between the analytical and numerical solutions. 62
- 3.8 Simulation *difT4* with $\eta = 10^{-3}$ in a box of $5 \times 5 r_H$ located at $r = 30 r_H$ and a grid resolution 256x256. The radial profile of the magnetic field $B_\theta(r)$ is plotted along the equatorial plane. The upper plot shows advection of magnetic flux by the infalling corona. The lower plot shows the same simulation results, but compensated for advection / infall with the magnetic profile maximum shifted back to the center of the simulation box (after the simulation). In the lower plot, solid lines represent the simulation result while dashed lines represent the analytic solution. 64
- 3.9 Shock tube simulation in ideal MHD regime. Density and vertical magnetic field at time $t = 0.55 t_g$. In this figure, we show results of simulations with grid resolution $N = 4500$, where the curves of the two simulations match perfectly to each other. Although the actual computational domain is larger, only the range $x = [300 r_g, 301 r_g]$ is plotted in order to easily compare to the two reference papers. 67
- 3.10 Shock tube simulations in diffuse MHD regime. Density and vertical magnetic field at time $t = 0.55 t_g$. In this figure, we show the results of simulations with $N = 600$. In addition, the magenta and cyan dashed lines in the lower plots represents the simulations with resolution $N = 120$. Although the actual computational domain is larger, only the range $x = [300 r_g, 301 r_g]$ is plotted in order to easily compare to the two reference papers. 68
- 3.11 Measure of numerical magnetic diffusivity. The simulations shown apply a numerical resolution of (128×128) and a physical magnetic diffusivity $\eta = 10^{-5}, 10^{-4}$ (see figure titles). Dashed curves show the analytic solution of the diffusion equation for the physical magnetic diffusivity (as in Section 3.4). Solid curves show the result of the numerical simulation for the same time steps. The decay of magnetic field lines in these plots are still dominated by physical magnetic diffusivity. 71

- 3.12 Measure of numerical diffusivity. The simulations shown apply a numerical resolution of (128×128) and a physical magnetic diffusivity $\eta = 10^{-7}, 10^{-6}$ (see figure titles). Dashed curves show the analytic solution of the diffusion equation for the physical magnetic diffusivity (as in Section 3.4). Solid curves show the result of the numerical simulation for the same time steps. The decay of magnetic field lines in these plots are dominated by numerical magnetic diffusivity, hence, the decreasing physical magnetic diffusivity value does not influence the decay of field lines. 72
- 4.1 The figure shows the comparison of simulations *torT0* and *torT1*. Simulation *torT0* applies ideal MHD HARM, while *torT1* applies rHARM with tiny magnetic diffusivity $\eta = 10^{-12}$. Mass accretion rates in simulations *torT0* (upper plot) and *torT1* (lower plot) are measured at $r = 2.2r_g$ close to the horizon. The average accretion rates given in the plot title are taken from $t = 240t_g$ to $t = 400t_g$ 77
- 4.2 Density ($\log(\rho)$) distribution of simulation *torT0* (upper plot) and *torT1* (lower plot) at $t = 400t_g$ (the computational domain covers only the right side of the plot, the left part is just mirrored). 78
- 4.3 Mass accretion rates of simulation *torT0* (upper plot) and *torT2* (lower plot) at $r = 2.2r_g$. The upper plot in Figure 4.1 is actually a part of the upper plot here. The average values shown in the plot titles were taken from $t = 300t_g$ to $t = 600t_g$. A continuous accretion appeared in *torT0* after about $t = 250t_g$, while no massive accretion observed in *torT2* until $t \sim 400t_g$. The presence of magnetic diffusivity delays the time point when disk accretion happens. 80
- 4.4 The figure presents $\log(\rho)$ of simulations *torT0* (upper plot) and *torT2* (lower plot) at time $600t_g$. In simulation *torT0*, MRI made the torus unstable and later the torus became turbulent with an accretion flow (Gammie et al. 2003). On the other hand, the torus structure of simulation *torT2* evolves in a less turbulent way, where MRI is damped by the magnetic diffusivity. 82

- 4.5 Mass flux as the indicator of MRI growth in simulations *mriT1-mriT6*. Two plots are shown in order to avoid confusion between the curves. In the upper plot, the mass accretion rates for $\eta = 10^{-6}$ (black), $\eta = 10^{-4}$ (cyan) and $\eta = 5 \times 10^{-4}$ (red) are shown, while in the lower plot, the accretion rates for $\eta = 1 \times 10^{-3}$ (blue), $\eta = 5 \times 10^{-3}$ (green) and $\eta = 10^{-2}$ (magenta) are given. The $\eta = 5 \times 10^{-4}$ (red dashed line) curve is plotted in the lower plot as a reference. As illustrated, the time when substantial accretion initiates is delayed with increasing η . The similar results for $\eta \leq 10^{-4}$ indicate a numerical diffusivity $\sim 10^{-5}$ (see Section 3.6). The delay in accretion can be explained by the magnetic diffusivity suppressing the MRI in the torus. For $\eta \leq 1 \times 10^{-3}$, only that part of the evolution is shown, afterwards these simulations experience numerical instabilities - similar to simulations *torT1* and *torT2*. Note that in these plots, the time point when massive accretion takes place differs from those in Qian et al. (2017) because of a slightly different setup in the code. 83
- 5.1 Shown is the logarithmic initial density of the disk simulation in code grids (see Section 3.3.2). With the grid resolution 128×128 , the radius inside the disk inner boundary $r = 6r_g$ is resolved by 38 grids. In the theta direction, the disk region from $\theta \approx 75.8^\circ$ - 104.2° is resolved by 48 grids. 86
- 5.2 The initial profiles of density (left plot) and diffusivity (right plot) at radius $r = 6r_g$ for simulation *D16*. Both profiles decrease steeply in the θ direction with increasing distance from the disk mid-plane. In the simulations, densities are normalized to the maximum density inside the disk. According to Equation (5.2), this value appears at the disk inner boundary. Thus the density profile in the plot here has a peak value 1. The magnetic diffusivities are normalized to η_0 (see Equation 5.6), which is 10^{-3} in simulation *D6*. Thus the diffusivity profile has the peak value of 10^{-3} 87
- 5.3 The density plot of simulation *D1* in logarithmic axes at time $t = 0t_g$. The maximum density is normalized to 1. The white solid lines in the plot show the structure of the large scale magnetic field lines. Note that the mosaic-like appearance in the disk comes from the external plotting-routine where the spherical code grids are converted into the cylindrical grids. The disk is well resolved in the simulation (see Section 5.1.2). 90
- 5.4 An illustration sketch of the surface where the accretion and ejection are measured. In our discussion below, we set a at $r = 6r_g$, b at $\theta = 75^\circ$ (disk initial upper surface) and c at $\theta = 105^\circ$ (disk initial lower surface). The radius of d is at $r = 60r_g$, when not redefined in the text. 91

- 5.5 Density snapshots in logarithm from simulation *D0* at $t = 0t_g$ (upper left), $t = 1000t_g$ (upper right), $t = 2000t_g$ (lower left) and $t = 3000t_g$ (lower right). Apart from for some turbulent structures on the surfaces, the accretion disk basically kept its disk-like shape during the time evolution and no outflow stream originates from the disk. The snapshots are presented in Kerr-Schild coordinates. As in the spherical plots in Section 4, the calculation domains only cover $\theta \in (0, 180)$ and the left hemispheres are just mirrored (same for all plots presented later). 93
- 5.6 *Left:* The disk angular velocity profile for simulation *D0* at time $t = 0t_g$ and $t = 3000t_g$. The red curve at $t = 0t_g$ also stands for the Paczyński-Witta profile with $R_{pw} = 1.0$. Through this plot, we know that the initial condition given in Equation (5.1) is very close to the angular velocity at $t = 3000t_g$, where the disk has evolved into a steady state. *Right:* A simple fit of R_{pw} in the initial angular velocity. It seems that a pure Paczyński-Witta profile is not able to fit the steady state. Yet, an initial profile with $R_{pw} \sim 1.7$ may reduce the discrepancy to the steady state. Note that the plot starts at $r = 6r_g$ since this is the disk inner radius. 94
- 5.7 Accretion and ejection rates and their average values for simulation *D0* from $t = 1000t_g$ to $t = 3000t_g$. The outer radius for accretion calibration is set at $r = 60r_g$. The most interesting plots are the most upper plot and the second lower plot, which show the accretion and negative ejection (matter moves towards disk plane instead of ejection). The total mass loss in the control volume is dominated the second upper plot, which reflex the radial density perturbation in side the disk (see above). 96
- 5.8 Magnetic field in the radial direction measured at $r = 12.6r_g$ at $t = 0t_g$ (left plot) and $t = 1000t_g$ (right plot). The different pointing directions of the radial magnetic field at $t = 0t_g$ is caused by the initial condition (see Figure 5.3), while the center-symmetric jagged curve within the disk range at $t = 1000t_g$ is released by MRI. Note that the curves in both plots are not magnetic field lines. 97
- 5.9 Density snapshots in logarithm from simulation *D6* at $t = 400t_g$ (top left), $t = 600t_g$ (top right), $t = 1000t_g$ (middle left), $t = 1600t_g$ (middle right), $t = 2200t_g$ (bottom left) and $t = 3000t_g$ (bottom right). During the time evolution, the process of outflow leaving the disk accretion is clearly observed. The snapshots are presented in Kerr-Schild coordinates. 98

- 5.10 Radial velocity profile for simulation *D6* at $t = 3000t_g$ with different contrast. In the left plot, the color bar resolves values from 0 to 0.1. We see that the disk wind has a moderate outward radial velocity $v_r \lesssim 0.1$ (the velocity is normalized by c). Also, to identify the accretion region, the color bar in the right plot resolves values from -0.005 to 0.005 . With the exception of minor turbulent patterns in the wind, negative radial velocities exist only in the accretion. The typical accretion velocity is $v_r \sim 10^{-3}$ 99
- 5.11 “Zoomed-in” density plots in logarithm from simulations *D1* (left plot) and *D6* (right plot) at $t = 3000t_g$. The massive accretion in simulation *D1* connects the disk and the BH while in *D6* the disk inner boundary still keeps its position at the $6r_g$ with a thin flow accreting onto the BH. Note that the circle shapes in both plots come from the initial condition described in Section 5.1. The circle is more obvious in the right plot as the stable inflow stream has not yet destroyed it unlike in the left plot. 99
- 5.12 The ejection rate and the inner accretion rate for simulations *D1* (upper plots) and *D6* (lower plots) from $t = 1000t_g$ to $t = 3000t_g$. The averages are taken in the time interval from $t = 2000t_g$ to $t = 3000t_g$. The accretion and ejection rates for simulations *D1* are much larger than simulation *D6*. Nevertheless, simulation *D6* has a better efficiency in the outflow production (see text). . . . 101
- 5.13 The ejection rate and the inner accretion rate for simulation *D17*. Since the simulation has not yet finished, we can only give the data from $t = 1000t_g$ to $t = 2400t_g$. The averages are taken in the time interval from $t = 2000t_g$ to $t = 2400t_g$. Due to the suppressed MRI process by the magnetic diffusivity, the accretion and ejection rates here are weaker than simulation *D6* and much weaker than simulation *D1*. 102
- 5.14 The time averaged accretion rate (left plot) and ejection rate (right plot) for simulations *D1*, *D2*, *D3*, *D4*, *D6*, *D17* with normalized diffusivity values $\eta_0 = 10^{-12}$, 10^{-6} , 10^{-5} , 10^{-4} , 10^{-3} and 10^{-2} , respectively. The averages are taken in the time interval from $t = 2000t_g$ to $t = 3000t_g$, except for simulation *D17*, which are taken in the time interval from $t = 2000t_g$ to $t = 2400t_g$ (see text). Note that the accretion rates in the left plot have been multiplied by -1 so that they could be plotted with a logarithm vertical axis. 102

- 5.15 The radial component of the magnetic field for simulations *D1* (upper left), *D6* (upper right) and *D17* (lower plot) measured by $r = 12.6r_g$ at $t = 2400t_g$. Note that the disk surfaces in our disk model are at $\theta = 75^\circ$ and $\theta = 105^\circ$ and the Keplerian rotation period at radius $r = 12.6r_g$ is $239.4t_g$. Through these plots, we can see an obvious suppression from the increasing diffusivity level on the MRI inside the disk. The MRI is still growing in simulations *D6* and *D17* (simulation *D17* much weaker than simulation *D6*), while the field in simulation *D1* has already become totally turbulent (see text). 103
- 5.16 Field line structures for simulation *D1* (left plot) and *D17* (right plot) at $t = 2000t_g$. In simulation *D1*, the field lines inside the accretion disk have become chaotic (especially within $r < 20r_g$) due to the turbulence caused by MRI. However, the field lines in simulation *D17* still keeps their original structure at $t = 2000t_g$; the reason for this is two-fold. First, the MRI inside the disk is suppressed by the magnetic diffusivity which makes disk less turbulent than in simulation *D1*. Second, with diffusivity, the matter flow is allowed to move across the field lines, which prevent the field lines from being disturbed by the accreting flow and the turbulence inside the disk. 104
- 5.17 The time averaged ejection rate and the inner accretion rate for simulations *D6* ($\chi = 0.8$), *D9* ($\chi = 1.0$), *D12* ($\chi = 1.2$), *D13* ($\chi = 1.4$) and *D14* ($\chi = 2.0$). The averages are taken in the time interval from $t = 2000t_g$ to $t = 3000t_g$. As illustrated in this plot, the accretion and ejection rates do not have significant difference in this set of simulations. 105
- 5.18 The magnetic field characters for simulation *D6* at $t = 3000t_g$ represented by the Alfvén Mach number (upper left), ratio of poloidal field strength divided by toroidal field strength (upper right), toroidal field strength in logarithm (lower left) and poloidal field strength in logarithm (lower right). According to the plots, the disk outflow becomes almost immediately super-Alfvénic after leaving the disk surface and the strength of the toroidal magnetic field is much larger than that of the poloidal field. To some extent, these facts refute the possibility that the disk wind is driven by centrifugal force, that is, the BP process. 108
- 5.19 *left*: The thermal pressure in logarithm for simulation *D6* at $t = 1000t_g$. The thermal pressure shown in this plot is comparable to the magnetic field strength inside the disk, however, it decays exponentially from the disk mid-plane and quickly becomes much smaller than the magnetic field strength. Therefore, the thermal pressure cannot be the dominant factor in the wind production/acceleration. *right*: The toroidal magnetic field strength for simulation *D6* at $t = 1000t_g$. According to this plot, the concentration behavior towards the axis in Figure 5.9 is not the “true collimation” caused by Lorentz force. 109

- 5.20 Field line structure for simulation *D6* at $t = 2000t_g$ (left plot) and $t = 3000t_g$ (right plot). Although the accretion and outflow become relative steady during this period, the state of the whole system, especially the structure of field lines, still evolves during the time forwarding, making it impossible to do a force analysis along the field lines. 110
- 5.21 Time evolution of the toroidal field strength in logarithm for simulation *D6* at $t = 100t_g$ (upper left), $t = 300t_g$ (upper right); $t = 1100t_g$ (lower left) and $t = 2000t_g$ (lower right), see also the lower left plot in Figure 5.18 for $t = 3000t_g$. It is evident that the propagation of the toroidal field in the direction vertical to the disk plane, which supports the outflow we see in simulation *D6*, is related to tower jets (see corresponding text). 111
- 5.22 Initial field line structure for simulations *D5* with parameter $m = 0.2$ (left plot) and *D8* with parameter $m = 0.6$ (right plot). The smaller the parameter m is, the more the field lines are inclined to the disk mid-plane. See also Figure 5.3 for the initial field line structure with parameter $m = 0.4$ 116
- 5.23 The ejection rate and the inner accretion rate for simulation *D5* from $t = 1000t_g$ to $t = 3000t_g$. The averages are taken in the time interval from $t = 2000t_g$ to $t = 3000t_g$. The accretion and ejection rates for simulations *D5* are both weaker than simulation *D6*. 117
- 5.24 The time averaged ejection rate and the inner accretion rate for simulations *D5*, *D6* and *D8* (see x axis ticks). The averages are taken in the time interval from $t = 500t_g$ to $t = 1200t_g$ where the outflow states from the simulations are not yet steady. According to this plot, the accretion is enhanced by the increasing parameter m . As well as the corresponding ejection rate. This implies a “more vertical” field is more efficient in the outflow production in our simulations. . . 117
- 5.25 The toroidal field strength in logarithm for simulation *D5* (left plot) and *D8* (right plot) at time $t = 1000t_g$. These plots imply that a “more vertical” field structure allows for a faster propagation of the toroidal field in the vertical direction. The wine glass shape in the right plot shows the boundary of the outflow from simulation *D8* at the aforementioned simulation time. 118
- 5.26 Density snapshots in logarithm from simulation *D7* at $t = 400t_g$ (top left), $t = 600t_g$ (top right), $t = 1000t_g$ (lower left) and $t = 1600t_g$ (lower right). The snapshots are presented in Kerr-Schild coordinates. The morphology of the disk wind evolution show differences when compared to simulation *D6* in Figure 5.9, which has the same initial condition but a lower resolution. 119

- 5.27 The radial component of the magnetic field vector for simulations *D6* (left) and *D7* (right) measured by $r = 12.6r_g$ at $t = 1000t_g$. Note that the disk surfaces in the disk model are at $\theta = 75^\circ$ and $\theta = 105^\circ$, the Keplerian rotation period at radius $r = 12.6r_g$ is $239.4t_g$. The resolution of simulation *D7* doubles that of simulation *D6* in both dimensions that provides the time evolution with less numerical diffusivity. 120
- 6.1 Density snapshots in logarithm from simulation *D9* at $t = 200t_g$ (top left), $t = 400t_g$ (top right), $t = 600t_g$ (lower left) and $t = 800t_g$ (lower right). The snapshots are presented in Kerr-Schild coordinates. The morphology of the disk wind evolution is very similar to simulation *D6* in Figure 5.9. 126
- 6.2 Density snapshots in logarithm from simulation *D16* at $t = 200t_g$ (top left), $t = 400t_g$ (top right), $t = 600t_g$ (lower left) and $t = 800t_g$ (lower right). The snapshots are presented in Kerr-Schild coordinates. The morphology of the disk wind evolution show differences being compared to simulation *D9* in Figure 6.1. 127
- 6.3 The time averaged accretion rate (left plot) and ejection rate (right plot) for simulations *D9*, *D10*, *D11*, *D15* and *D16* with the black hole spin parameter $a = 0, 0.1, 0.2, 0.5$ and 0.9375 , respectively. The averages are taken in the time interval from $t = 500t_g$ to $t = 800t_g$. Note that the accretion rates in the left plot have been multiplied by -1 so that they can be plot in a logarithmic vertical axis. 128
- 6.4 The toroidal magnetic field strength in logarithm for simulation *D9* (left plot) and *D16* (right plot) at time $t = 800t_g$. In the right plot, the field lines tangled by the black hole rotation create a large amount of toroidal magnetic field around the rotational axis. 128
- 6.5 *Left:* The time averaged profile of electromagnetic energy flux per solid angle ($F_E^{(EM)}$), defined by Equation 6.2) along θ for simulation *D16*. The values of $F_E^{(EM)}$ are calculated at $r = 2r_g$ and averaged from $t = 500t_g$ to $t = 800t_g$. *Right:* The same profile (but also hemisphere averaged) from an ideal GR-MHD simulation in McKinney & Gammie (2004). The simulation employed a gas torus surrounding a rotating black hole with spin parameter $a = 0.5$. This plot is adopted from McKinney & Gammie (2004). 130
- 6.6 The time averaged electromagnetic energy flux defined by Equation (6.1) measured at $r = 2r_g$ for simulations *D9*, *D10*, *D11*, *D15* and *D16*. The averages are taken in the time interval from $t = 500t_g$ to $t = 800t_g$. To eliminate the influence of accreting flow, I only integrate θ from 0° to 75° and 105° to 180° . The energy flux shows a clear enhancement with the increasing black hole spin. 130

- 6.7 The time averaged electromagnetic energy flux (left plot) defined by Equation (6.1) and the time averaged matter energy flux (right plot) defined by Equation (6.3) measured at different radius as indicated in the plots. The averages are taken in the time interval from $t = 500t_g$ to $t = 800t_g$. To eliminate the influence of accreting flow, I only integrate θ from 0° to 75° and 105° to 180° . The energy fluxes increase with the radius which implies that the disk wind has a positive influence on both the electromagnetic and matter energy fluxes. 131
- A.1 An illustration for the astronomical superluminal motion. Please see corresponding text for the derivation. Credit: Muhammad, Wikipedia 1
- A.2 A schematic explanation of the normal vector in 3+1 spacetime. Between the two slices of pure space, σ_t and σ_{t+dt} (see text), the red vector \mathbf{n} shows the heading of time in local Minkowski space, while the green vector \mathbf{t} shows the direction of coordinate time in curved spacetime, which actually has projections in spacial components. The shift in the space during the coordinate time t and $t + dt$ is given by the blue vector $\boldsymbol{\beta}$. Credit: Rezzolla & Zanotti (2013) . . . 3

List of Tables

- 3.1 Test simulations of magnetic diffusivity η in rHARM. Parameter choices in simulations *difT0*, *difT1*, *difT2*, *difT3*, *difT4*. The table shows the radial position of the domain in the equatorial plane and the domain size, both in units of r_g , as well as the grid resolution in the domain. The magnetic diffusivity η is constant in the domain. Simulations were done for $a = 0$ 63

- 4.1 Parameter choice in the torus simulations that use rHARM and ideal HARM. The table shows the value of diffusivities, innermost boundaries, and resolutions that are used in the torus simulations. With the exception of *torT0*, which was executed by ideal HARM, all other tests were done by rHARM. The Kerr parameter is $a = 0.9375$ in all simulations, thus $0.98r_H = 1.32r_g$ 76

- 5.1 Parameter choice in the thin disk simulations that use rHARM. The table shows the value of normalized magnetic diffusivities (defined in Section 5.1), plasma β , the scale of diffusivity profile (defined in Section 5.1), the large scale field line inclination parameter m , the black hole spin parameter a and grid resolutions that are used in the torus simulations. All simulations were done by rHARM. Please see Section 5.1 for other common setups. 123

Acronyms

AU	Astronomical unit
pc	Parsec
kpc	Kilo Parsec
Mpc	Mega Parsec
c	Speed of Light
AGN	Active Galactic Nucleus
BH	Black Hole
GRB	Gamma Ray Burst
ISM	Interstellar Medium
XRB	X-Ray Binary
YSO	Young Stellar Object
GR	General Relativity
GRMHD	General Relativistic Magnetohydrodynamics
MHD	Magnetohydrodynamics
BP (effect/process)	Blandford-Payne (effect/process)
BZ (effect/process)	Blandford-Znajek (effect/process)
BL (coordinates)	Boyer-Lindquist (coordinates)
KS (coordinates)	Kerr-Schild (coordinates)
MRI	Magnetorotational Instability
VLBI	Very-Long-Baseline Interferometry

*In thesis, I have intentionally reduced the usage of acronyms. Nevertheless, if they are used, their meaning can be found here.

Chapter 1

Introduction

Jets as collimated, supersonic flows are observed in various astrophysical contexts. The origin of these jets lies in the accretion processes in star formation or black hole accretion systems with strong magnetic fields. Launched from the center of an active galactic nucleus that contains a supermassive black hole, the beams of the collimated magnetized material jets, known for their relativistic speeds and the long ranges, can influence the surroundings on the galactic scale. Being mostly detected in synchrotron emission, the structure of these relativistic jet sources—the center engines in active galactic nuclei—remain unresolved by observations and numerical approaches are often used to investigate the generation of jets from active galactic nuclei.

1.1 Astrophysical jets

Basically, jets can be classified into three broad categories determined by the different types of their central sources – young stellar objects (YSOs), stellar mass black holes/neutron stars and super massive black holes in galactic centers.

The most common type of astrophysical jets are powered by YSOs. While stars with masses above about $10M_{\odot}$ sometimes generate wide-angle outflows, most low-mass stars produce highly collimated jets and outflows during their formation (Bally 2007). These jets have typical velocities of a few hundred km s^{-1} and drive outflows with sizes ranging from hundreds of AU to tens of parsecs (Reipurth et al. 1997; Hartigan et al. 2001; Gómez et al. 2005; Curiel et al. 2006). Shocks powered by YSO outflows excite many emission lines, e.g. the near-Infrared (IR) lines of H_2 and [FeII], visual-wavelength [OI], [SII] lines, hydrogen recombination lines, and forbidden lines depending on the medium and the velocity of jets (Bally 2007).

The first documented visual observation of an astrophysical jet was the outflow of the young star TTauri, recorded by Burnham (1890) as “variable nebula.” In the late 1950’s, the “Burnham’s nebula,” together with other peculiar nebulous objects observed at that time, were investigated and eventually recognized as the early stages of newly formed stars. Such objects are nowadays named as HH objects, after Herbig and Haro, who restarted the discussion of “Burnham’s nebula” sixty years after its first observation. In Figure 1.1, jets from two HH objects, HH47 and HH212,

are shown.

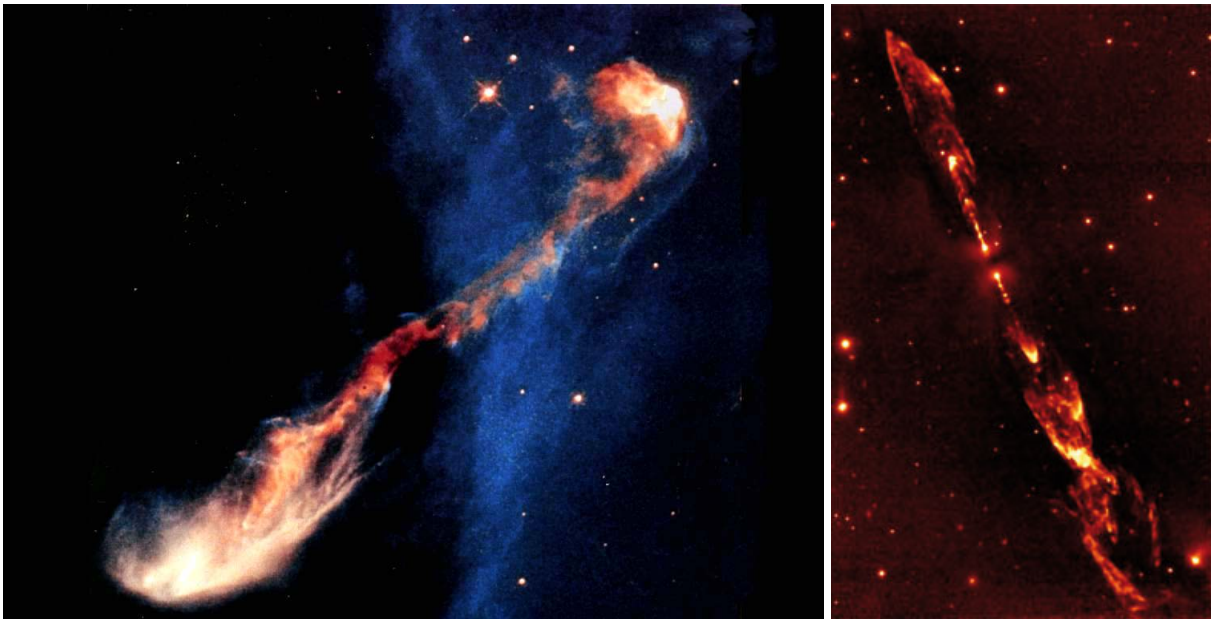


Figure 1.1: *left*: An image of HH47 jet taken by NASA Hubble Space Telescope in visible light. The center source of this roughly 0.5 lightyear-long jet is hidden inside a dust cloud at the lower left edge of the image. The jet has burrowed a cavity through the dense gas cloud and now travels at high speed into interstellar space. Shock waves form when the jet collides with interstellar gas, causing the jet to glow. Credit: J. Morse/STScI, and NASA. *right*: The false color image of HH212 jet taken by VLT in the infrared H_2 emission line (adapted from [Bally \(2007\)](#)). It shows a very young jet driven by an invisible protostar in the vicinity of the Horsehead nebula in Orion ([Zinnecker et al. 1998](#)).

In our galaxy, binary systems of stellar mass black holes and neutron stars can also produce jets that are even moving with relativistic speed ([Mirabel & Rodríguez 1999](#)). Due to the differing emission mechanism from YSO jets, these objects only give broad emission lines which makes it difficult to analyze the chemical ingredients of jets. Such binary systems are called X-ray binaries (XRBs) since they were mostly and originally discovered in either X-ray or hard X-ray bands ([Zhang et al. 1997](#)). On the other hand, according to the observations in the two extremes of the electromagnetic spectrum, namely, in the domain of the hard X-rays and radio wavelengths, the stellar-mass black holes mimic, on a smaller scale, many of the phenomena seen in quasars, they are hence known as microquasars ([Mirabel & Rodríguez 1998, 1999](#)).

The first superluminal jet within the Milky Way discovered by [Mirabel & Rodríguez \(1994\)](#) was a microquasar GRS 1915+105. This superluminal source is at a distance of about 11 kpc from Earth and has relativistic ejections with a stable jet axis at scales of 500-5000 AU ([Fender et al. 1999; Dhawan et al. 2000](#)). GRS 1915+105 has a black hole with mass $14 \pm 4M_{\odot}$ (M_{\odot} is the solar mass) in its center ([Greiner et al. 2001](#)). Due to the relativistic superluminal effect (see [Appendix A.1](#)), the apparent velocity of the ejecta moving towards the observer reached $1.25c$, but was actually moving with a speed of $0.92c$ at an angle $\theta = 70^{\circ}$ to the line of sight ([Mirabel &](#)

Rodríguez 1994). An observation of GRS 1915+105 in radio wavelength is shown Figure 1.2.

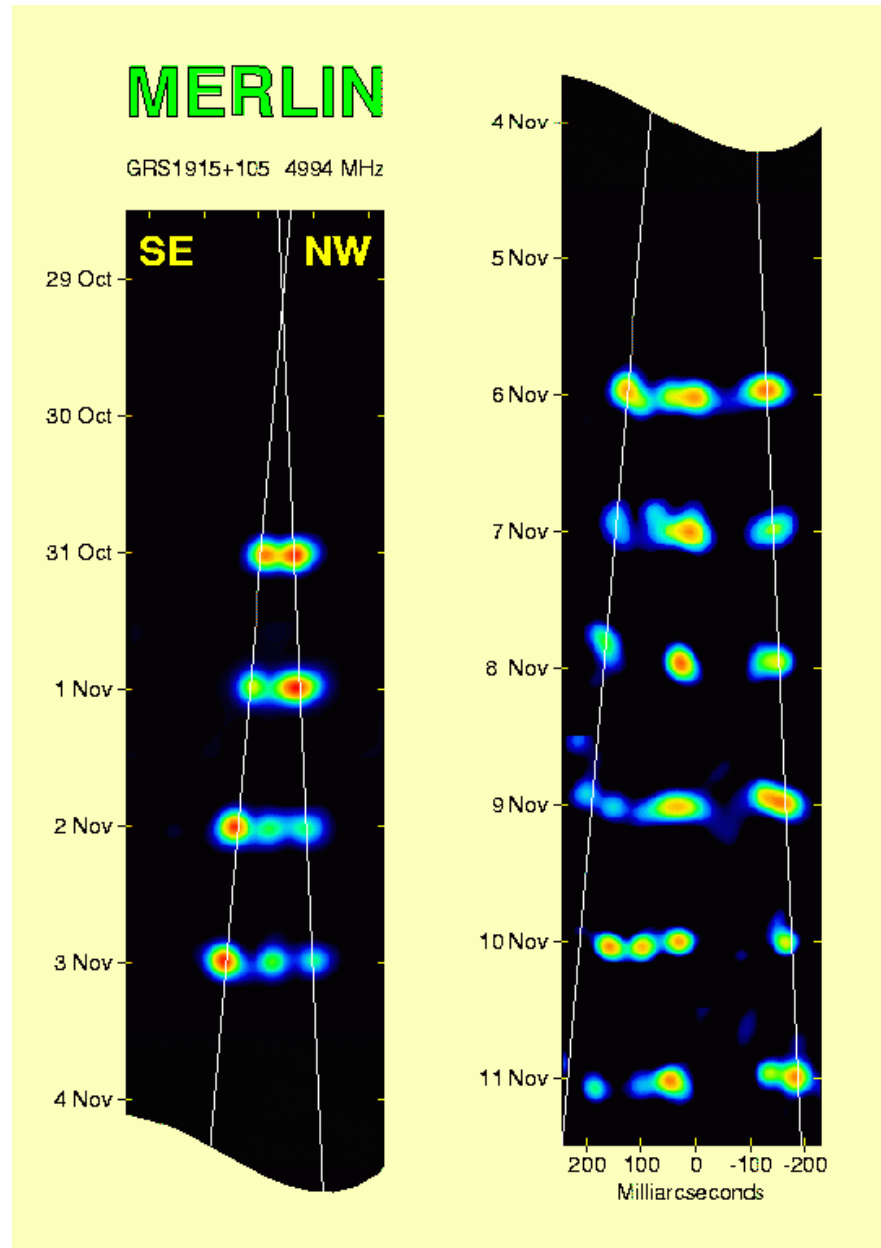


Figure 1.2: A sequence of MERLIN observations of the X-ray binary GRS 1915+105 taken in 1997 October/November (Fender et al. 1999). This false color image shows the data observed using the MERLIN array at 4.994 GHz (radio wavelength) with a bandwidth of 16 MHz. The anti-parallel ejection of clouds in this plot were moving at relativistic velocities. Credit: MERLIN/VLBI National Facility.

There are also other X-ray sources nearby like, e.g. XTE J1550-564 with a center black hole of mass $> 10M_{\odot}$ lies only about 5kpc from the earth (Orosz et al. 2002; Titarchuk & Shrader 2002). Although they are close to Earth (still in Milky Way), the highest angular resolution in terms of Schwarzschild radii (r_s) that can actually be achieved is in an extragalactic jet originating at the galaxy M87, whose the fastest superluminal feature reaches apparent velocity of six times the

speed of light (Biretta et al. 1999).

Although the galactic jets (microquasars) are much closer to us by distance, e.g. another nearby source XTE J1550-564 with a center black hole of mass $> 10M_{\odot}$ lies only about 5kpc from the earth (Orosz et al. 2002; Titarchuk & Shrader 2002), the highest angular resolution in terms of Schwarzschild radii (r_s) can actually be achieved in an extragalactic jet originating at the galaxy M87, the fastest superluminal feature of which reach apparent velocity of six times the speed of light (Biretta et al. 1999).

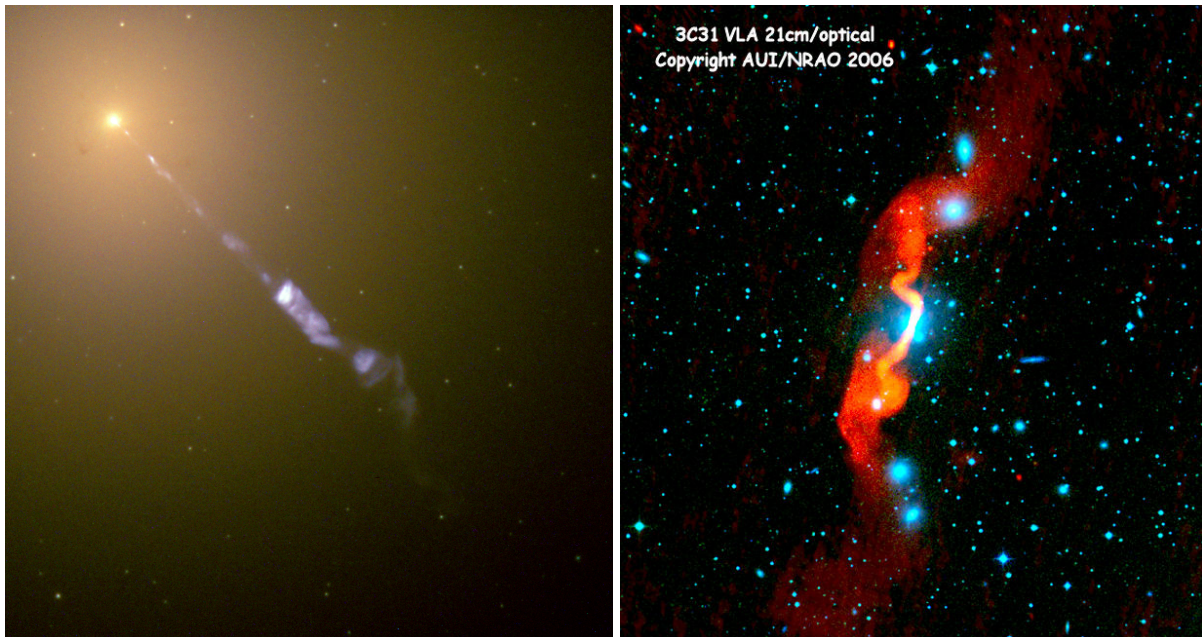


Figure 1.3: *left*: An image taken by Hubble Space Telescope which shows the jet of matter ejected from M87 at nearly light speed, as it stretches 1.5 kpc from the galactic core. The appearance of the single jet component is due to the relativistic beaming effect (see Section 1.2.2). *right*: An image of radio galaxy 3C31 in ~ 100 kpc scale. Blue color shows the optical image from POSS II survey while the red color gives the radio image from the VLA at 21cm wavelength. It is clear to see the influence of the jets to its ambient in the galactic scale. Credit: NRAO/AUI.

M87 (or NGC 4486) is a supergiant elliptical galaxy in the constellation Virgo located at a distance of 16.7 ± 0.6 Mpc which contains a supermassive black hole of $(6.2 \pm 0.4) \times 10^9 M_{\odot}$ in its center (Doeleman et al. 2012). The observations by very-long-baseline interferometry (VLBI) have reached angular resolutions less than $10r_s$ (Doeleman et al. 2012; Hada et al. 2013, 2016; Kim et al. 2016). Observations showed that the relativistic jet of energetic plasma that originates at the core and extends outward at least 1.5 kpc (Doeleman et al. 2012) with the radio lobes extended further out to a distance of 77 kpc (Figure 1.3 left plot; Klein 1999). The engine of the extragalactic jets from M87 is an active galactic nucleus (AGN) powered by accretion of matter onto the supermassive black hole in its galactic center. The galaxies that host active galactic nuclei are called active galaxies. Approximately 10% of active galactic nuclei exhibit relativistic jets. In the right plot of Figure 1.3, another observed active galactic nucleus 3C31 that produces

relativistic jets is shown. I will discuss the formation of these extragalactic jets in Chapter 1.2.

Jets often play a key role in various astrophysical processes. The YSO jets feedback has an effect on the local environment of a star and further afield in interstellar medium on galactic scale. The relativistic jets from XRBs and AGNs are the key to explaining gamma-ray bursts (GRBs),¹ which are believed to be produced when the kinetic energy of an ultra-relativistic flow is dissipated via internal shock (Piran 2004). The feedbacks of the AGN jets, although not fully understood, have been observed in numerical simulations, where the onset of the jets lead to an increase in the star formation rate by a factor of 2 and even more in the star forming gaseous disk of 10kpc scale (Antonuccio-Delogu & Silk 2010; Gaibler et al. 2012).

Unlike YSOs jets, relativistic jets are mostly detected in synchrotron emission. For this reason, while jets from YSOs can be rather well resolved and typical features such as mass fluxes, velocities, or even rotation can be observed (Bacciotti et al. 2002; Coffey et al. 2004), the structure of the relativistic jet sources remains unresolved. What the relativistic jets are made of or how they are produced, is still a mystery of astrophysics.

1.2 Jets in active galactic nuclei

An active galactic nucleus (hereafter AGN) is a compact region at the center of a galaxy that produces an excess of electromagnetic radiation. The host galaxy of an AGN is called an active galaxy. Figure 1.4 shows images of different types of AGNs. While all the stars from a normal (non-active) galaxy together yield a typical luminosity of 10^{44} ergs⁻¹, AGNs can, in the most extreme manifestations, exceed this value by a thousand times. Approximately 10% of AGNs exhibit relativistic jets (Doeleman et al. 2012). Observations suggest that the majority of AGN jets have velocities lower than Lorentz factor $\Gamma = 10$, while some others, can reach $\Gamma = 50$ (Jorstad et al. 2005; Lister et al. 2009). The radiation and the relativistic jets originated from AGN are believed to be the result of accretion of matter onto the black hole in the center of the host galaxy. However, the mechanism detail of this process is still a mystery.

1.2.1 A brief AGN story

Unlike any other astronomical object, the electromagnetic radiation from an AGN can be extremely broad-band. Due to the different observational conditions (e.g. environment around AGN, viewing angle of the host galaxy to the line of sight, etc.), it is possible that only a part of the AGN spectrum is visible in an observation. Thus, before the unification theory, which classifies AGNs into two basic types—radio quiet and radio louds (see below), different types of

¹GRB is the γ -ray flash in the sky for a duration from 10^{-3} s to 10^3 s which releases energy of the order 10^{51} - 10^{54} ergs per second.

AGNs were often thought to be various astrophysical objects.

The first detected AGN was documented by [Fath \(1909\)](#). In this observation, NGC 1068 was described as a “spiral nebula” with “a diffuse nucleus” which had unusual bright emission lines in optical/infrared wavelength. In the seminal paper of Carl K. Seyfert, NGC 1068 was discussed with NGC 4151 and other galaxies as objects with “an exceedingly luminous stellar or semistellar nucleus which contains a relatively large percentage of the total light of the system” ([Seyfert 1943](#)). These objects later defined the term “Seyfert galaxy.” By the end of the 1950s, more important characteristics of Seyfert galaxies were discovered, including that their nuclei are extremely compact ($< 100\text{pc}$) and have mass $\sim 10^{9\pm 1}M_{\odot}$ ([Woltjer 1959](#)).

Seyfert galaxies are now known as one of the two largest groups of active galaxies, which depending on the subclass (type 1 or 2), show optical range nuclear continuum emission, narrow (Seyfert 2) and broad (Seyfert 1) emission lines, and occasionally strong nuclear X-ray emission (Seyfert 1). Seyfert galaxies are usually spiral or irregular galaxies. In [Figure 1.4](#) left plot, an image of NGC 4151, a type I Seyfert galaxy, is shown.

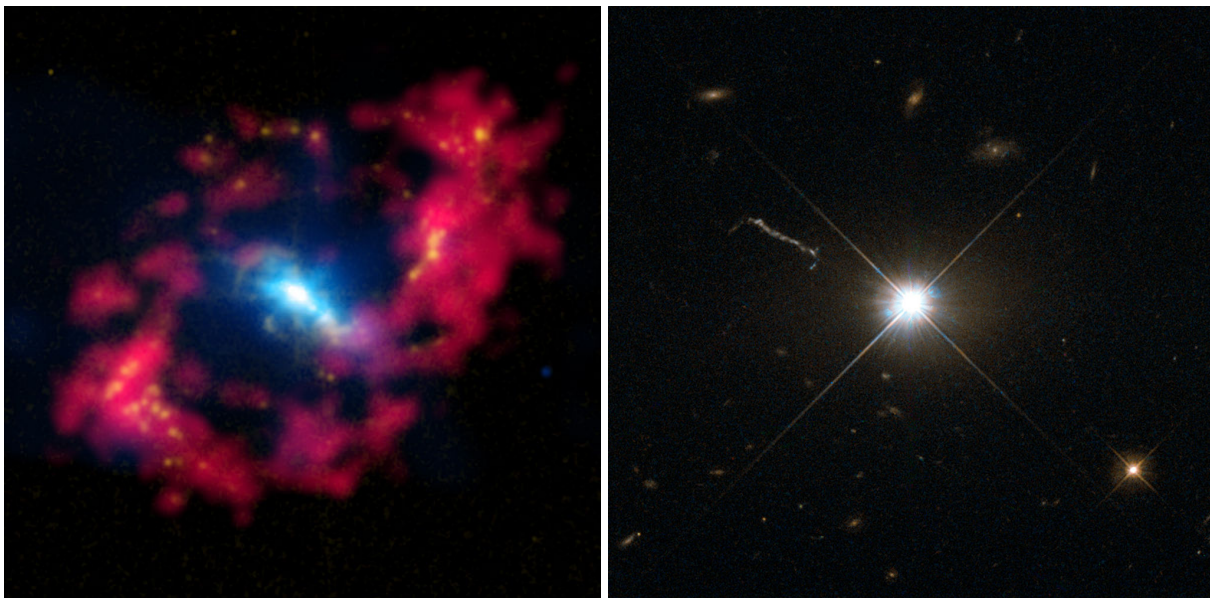


Figure 1.4: *left*: A composite false color image of the spiral Seyfert galaxy NGC 4151. In the image, the X-rays (blue) from the Chandra X-ray Observatory are combined with optical data (yellow) showing positively charged hydrogen (“H II”) from observations with the 1-meter Jacobus Kapteyn Telescope on La Palma. The red around the bright core shows neutral hydrogen detected by radio observations with the NSF’s Very Large Array. *right*: An image from Hubble’s Wide Field and Planetary Camera 2 (WFPC2) of quasar 3C 273, which resides in a giant elliptical galaxy in the constellation of Virgo. Its light has taken some 2.5 billion years to reach us. Despite this great distance, it is still one of the closest quasars to Earth.

Quasars (quasi-stellar radio sources) represent the other large group of AGNs. As revealed by its name, quasars were originally observed in radio wavelength ([Matthews & Sandage 1962](#); [Bolton et al. 1963](#); [Greenstein & Schmidt 1964](#); [Bolton et al. 1965](#)). While the host galaxies of Seyferts

are clearly detectable, quasars appeared usually as point sources, indistinguishable from stars, except for their peculiar spectra. They emit, almost uniformly, from X-rays to the far-infrared with a peak in the ultraviolet-optical bands; some quasars are strong sources of radio emission and of gamma-rays.

Although quasars appear faint when viewed from Earth, they are among the most luminous and energetic objects known in the universe. The quasar that appears brightest in the sky is 3C 273 (see Figure 1.4 right plot) discovered in the early 1960s (Schmidt 1963; Greenstein & Schmidt 1964). It has an apparent magnitude of 12.8, but its absolute magnitude reaches -26.7, which represents a luminosity about 100 times that of the Milky Way (Greenstein & Schmidt 1964).

To see the emission contribution of jets in AGNs, it is convenient to divide AGN into two classes, conventionally called radio-quiet and radio-loud. Radio-quiet AGNs, including Seyfert galaxies and the majority of quasars, do not show manifestation of jets. Radio-loud AGNs, on the other hand, have emission contributions from the jets (see Section 1.2.2) that dominate the luminosity of the AGN at radio wavelengths. Radio-loud quasars, blazars and radio galaxies belong to this class.

Radio-loud quasars, e.g. 3C 273, behave exactly like radio-quiet quasars except for the additional jet emission, while blazars are distinguished by rapidly variable, polarized optical, radio and X-ray emission. Radio galaxies, in addition to the similar radio emission character of the two relative groups, usually display large-scale structure jets (see Section 1.2.2). Despite different observational appearances of radio-loud AGNs, the similar emission and dynamic properties brought them to the same intrinsic structure within the unification model.

In the late 1970s, superluminal phenomenon with one-sided jets morphology on the milliarcsec scale were found in quasars (Cohen et al. 1977; Readhead et al. 1978, 1979). This morphology was explained to be a relativistic jet viewed at a small angle to the line of sight (Rees 1966; Blandford & Königl 1979). The explanation later became the base of the unification theory of the radio-loud AGNs, which claims, in simple words, that the blazars and quasars were normal radio galaxies observed at some angles to the line of sight (Antonucci & Ulvestad 1985; Barthel 1989; Urry & Padovani 1995). The unification model explains the facts that many superluminal sources have blazar properties, one-sided core-jet radio morphology, and usually small broad emission line widths (Readhead et al. 1978; Wills & Browne 1986; Impey 1987; Barthel 1989).

A similar orientation model has been applied to the unification of radio-quiet Seyfert galaxies, where the Seyfert 2 galaxies are simply the edge on version of Seyfert 1 galaxies (Antonucci 1993). A schematic explanation of AGN unification model can be found in Figure 1.5 (see also Antonucci (1993) for more detail). Although the unification model shows a quite straightforward way to unify AGNs, it is not yet clear and still cannot explain all the observed differences among different AGN classifications.

It has been argued that an AGN must be powered by accretion of mass onto massive black holes. During this process, kinetic energy and gravitational potential energy of the material falling onto the black hole are converted to radiation. Several models of the accretion process, in other words

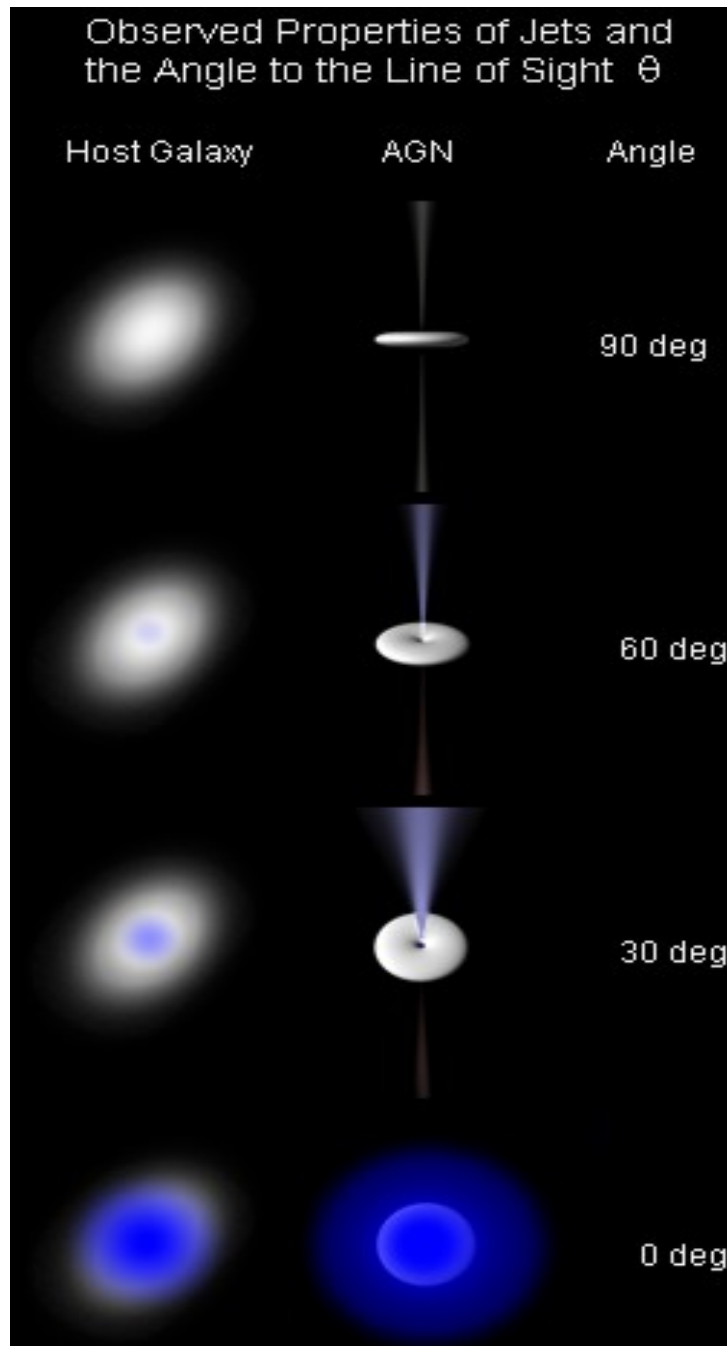


Figure 1.5: A schematic explanation of AGN unification model. The orientation of the AGN host galaxy (face on or edge on) plays an important role here. For the radio-loud AGNs, when observed at 90° from the jets (left), they appear as radio galaxies, when at an angle to the jet (middle), as quasars, and when directly down to the jet (right), as blazars. Since the fact that the galaxy's disk can obscure certain ranges of AGN emission, the orientation-dependent model has also been applied to unify radio-quiet AGNs. For the radio-quiet AGNs, when the viewing angle is 90° (left), they appear as Seyfert 2 galaxies, and when at an angle, as Seyfert 1 galaxies. Figure credit: Ron Kollgaard.

– the central engines, have been proposed to this point. As the main subject of this doctoral thesis, they will be introduced in Section 1.2.3 and described in detail in Chapter 2. The corresponding results will be discussed in Chapter 5.

1.2.2 Observational features of AGN jets

The first observed AGN jet was reported by Curtis (1918) as “A curious straight ray which lies in a gap in the nebulosity..., apparently connected with the nucleus by a thin line of matter” in M87 (NGC4486). After a century of research, it is known that the extragalactic jets are usually ejected from radio-loud AGNs and are supposed to be bipolar (“two-sided twin jets”). It has already been confirmed that they have relativistic motions. In some observations, the common values of Lorentz factor of jets can reach $\Gamma \sim 10 - 20$ (which corresponds to a velocity of $0.995c - 0.999c$) (Jorstad et al. 2005; Lister et al. 2009; Homan 2012). Under certain observational conditions together with this level of speed, the relativistic velocities of AGN jets can result in two important relativistic effects – beaming and superluminal motion.

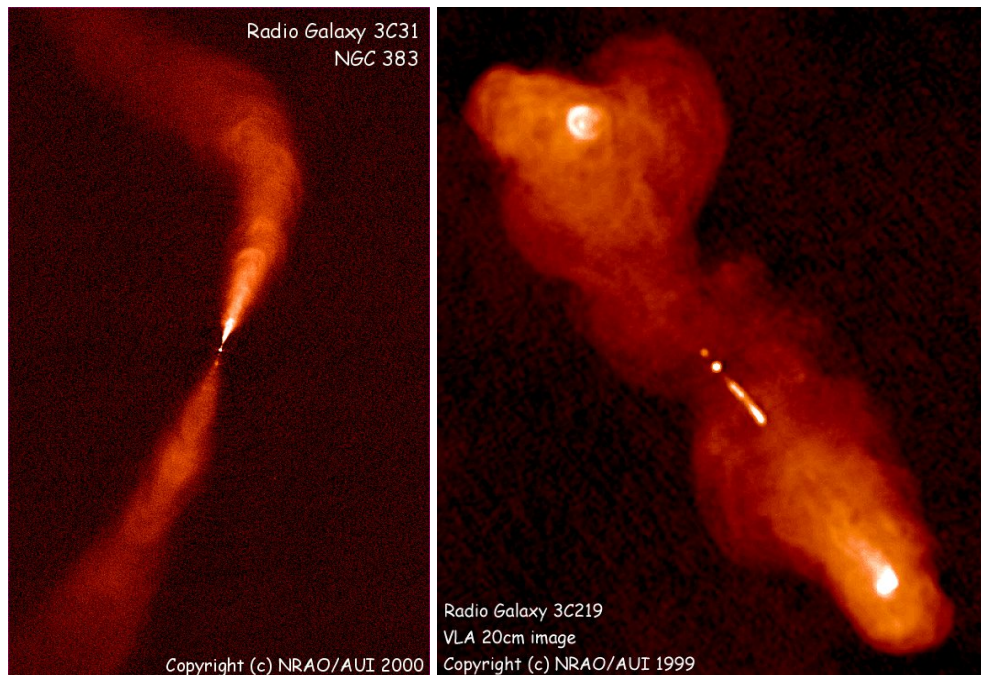


Figure 1.6: *left*: 3C31 as an example of FRI radio galaxy. Its relativistic electron jets detected in radio wavelengths extend for several kpc with the brightness of the jets decreasing outwards. *left*: FR II radio galaxy 3C219 detected in radio wavelengths. The filamentary lobes in the plot extend several hundred kpc with bright hot spots in both lobes. Figure credit: NRAO/AUI.

The relativistic beaming effect is the process by which relativistic effects modify the apparent luminosity of emitting matter that is moving at speeds close to the speed of light, and originally comes from the idea first presented by Rees (1966). According to the beaming theory, it is possible to boost the observed flux at certain frequency from a moving source to over 10^3 times larger for a large range of β ($\beta = v/c$) when the source moves towards the observer with a

small angle to the line of sight while the observed flux from the same source can be diminished significantly by moving away from the observer (Blandford & Königl 1979; Vermeulen & Cohen 1994).

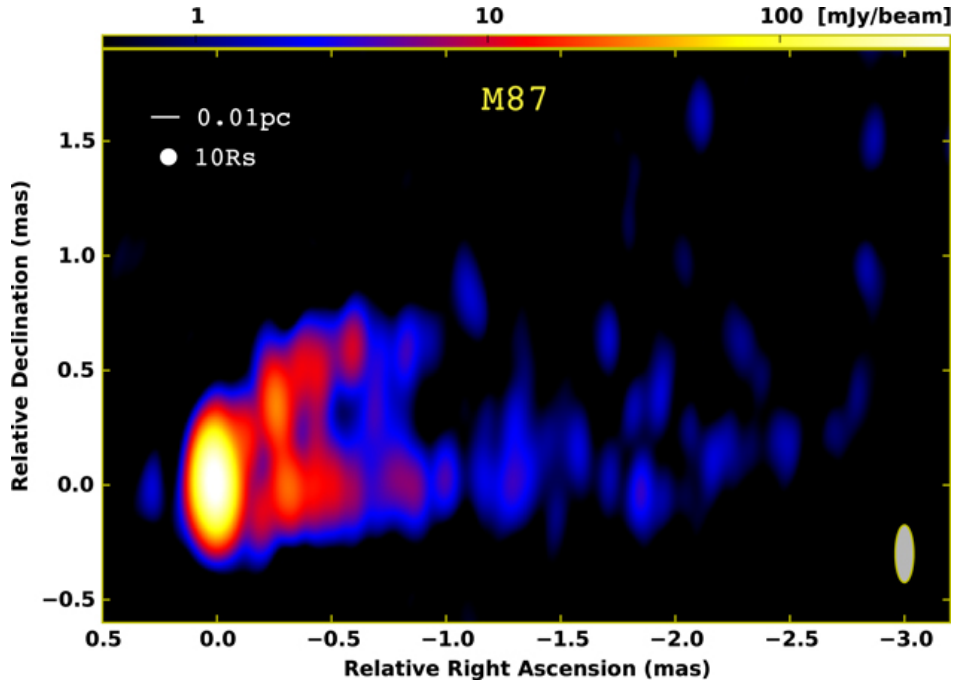


Figure 1.7: A VLBI high resolution radio interferometry image of M87 core in 10^{-2} pc scale adapted from Hada et al. (2016).

In Figure 1.3 left plot, the twin jets in M87 show how beaming affects their appearance in observations. On the one hand, the one jet of M87 moves almost directly towards Earth, hence, is clearly visible to telescopes and is many times brighter due to beaming. On the other hand, the other jet is moving away from us and is so much fainter due to the Doppler shift (redshift) that it is rendered invisible. In Figure 1.3 right plot, the bipolar jets from radio galaxy 3C 31 move perpendicular to the line of sight, thus showing comparable brightnesses although their observed fluxes were affected by the beaming effect as well.

Superluminal motion was first discovered in the late 1960s during the discovery of quasars. It is caused by jets travelling very close to the speed of light within a certain range of angles towards the observer. Due to the angle to the line of sight, later emitted light passes a shorter distance than the earlier emitted light, thus “catches up” in the time, which makes the velocity of the motion sometimes greater than c from appearance. Theoretically, the superluminal effect cannot be triggered if the velocity of the jet is less than $0.7c$ (see Appendix A.1 for the detailed model).

The radio emission from radio-loud AGN jets is synchrotron emission that has very smooth, broad-band nature and strong polarization. This implies that the radio-emitting plasma contains electrons with relativistic speeds and magnetic fields. Sometimes, the particles (electrons) in the jets can be accelerated to high enough energies to produce synchrotron radiation in infrared, optical, ultraviolet or even X-ray. The interaction between the relativistic electrons and the ambient photons, can also trigger the inverse-Compton process, in which the photons are scattered to high

energies. This process turns out to be particularly important in the X-rays emission (Croston et al. 2005).

Since the synchrotron radiation from radio loud AGN jets are mostly in radio wavelength, the observations of these jets take great advantage of the unmatched resolution by interferometry. Radio interferometric imaging of jets (as example from radio galaxies) often shows extended structure on the kpc (kilo parsec) to Mpc (mega parsec) scale called lobes. The lobes are double, often fairly symmetrical, roughly ellipsoidal structures placed on either side of the AGNs. In 1974, the extended jets morphology was quantified by Fanaroff and Riley into two classes (FRI AND FR II) according to the luminosity and the relative distance of high brightness region and low brightness region from the host galaxy (Fanaroff & Riley 1974). As shown in Figure 1.6, FRI sources were brightest towards the centre (left plot), while FR II sources were brightest at the edges (right plot). FRI jets are inefficient in the sense that they radiate a significant amount of their energy away as they travel. In comparison, FR IIs appear to be able to transport energy efficiently to the ends of the lobes.

Although the large scale of AGN jets can be observed with good resolution, their “cores” from which the jets are launched and ejected stay unresolved. Today’s best resolution level of AGN center sources comes from VLBI observations. As shown in Figure 1.7, a resolution of $\sim 10r_s$ (r_s is Schwarzschild radius) is not enough to reveal the inner structure of the region where jets from M87 are originally produced. For this reason, numerical simulations are often used as the tools to resolved the jet generation processes (see later).

1.2.3 Central engines of AGNs

Several theoretical models have been established to describe the “AGN engine”, namely to explained different processes during mass accretion and ejection that are happening in the yet unresolved origin of jets. In this section, I will briefly introduce the models proposed by previous seminal works to explain the jet ejection that are involved in the research of this thesis. The detailed illustrations with equations are in Chapter 2.

The core question here is: what kind of energy source powers AGN jets? For decades, it has been argued that AGNs are powered by the black hole accretion systems. A black hole by itself is not able to generate energy. However, a black hole coupled with a magnetized accretion disk is possibly the most efficient way to produce large amounts of energy in the universe by converting kinetic energy and gravitational potential energy of the disk material falling onto the black hole to radiation. The accretion disk is usually made of plasma gas that rotates differentially in circular orbits around a supermassive black hole in the center of the AGN host galaxy. Due to conservation of angular momentum, gas particles in the accretion disk circulating the black hole need to lose their angular momentum when moving from a larger orbit to a smaller orbit (see Appendix A.3). In the seminal paper, Shakura & Sunyaev (1973) suggested that the tangential stresses between adjacent layers provided by the magnetic field, together with the turbulence in the disk, contribute to the mechanism of angular momentum transport. The efficiency of angular

momentum transport can be characterized by an α parameter, which is a function of turbulent velocity, sound speed, density and the magnetic field strength (see Section 2.1.1). It was also predicted in this work that “the field is most likely to be chaotic and of small scale” within the disk. Nevertheless, in the absence of the complete theory of turbulence and the observational check at that time, they just assumed its presence.

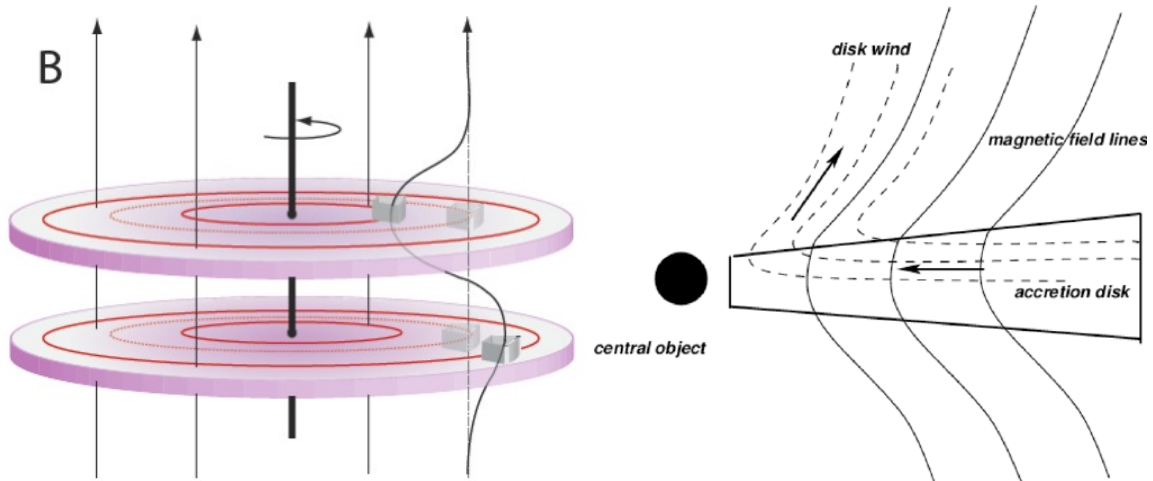


Figure 1.8: *left*: An illustration plot of MRI. The originally straight magnetic field line was bent by a tiny random displacement between two parts in the disk. The magnetic tension then serves as restoring force and transports angular momentum between the two parts and results in accretion. Credit: Plasma Physics Group/Physics Department/University of Wisconsin–Madison. *right*: The centrifugally driven disk wind caused by the large scale magnetic field line that cross the accretion disk with an angle (see corresponding text). Plot adopted from [Sheikhnezami et al. \(2012\)](#).

The generation and evolution process of the “turbulence viscosity” was investigated in [Balbus & Hawley \(1991\)](#) analytically and numerically as the local shear instability in the weak magnetized disk. In this work, they used a model where the Keplerian differentially rotating accretion disk was penetrated everywhere by weak magnetic field lines which are originally parallel to the disk rotating axis. Since in ideal magneto-hydrodynamics (MHD), matter (plasma) can only move along the field lines (see Section 1.4.2), a displacement randomly generated between the two parts from the same radius and different height of the disk will bend the same field that penetrates them as shown in the Figure 1.8 left plot. The magnetic tension will then serve as the restoring force just like a stretched elastic band. This tension will break one part and accelerate the other part. As a result, both parts are not able to stay at their original orbits. The accelerated part will move outwards while the decelerated part moves inward (see Section 2.2.1). Consequently, the magnetic field in the disk becomes turbulent together with the disk itself. The instability caused by this process is named magnetorotational instability (MRI). The numerical study in [Balbus & Hawley \(1991\)](#) show that within the linear regime in time MRI only takes place in a certain spatial scale range (wave number), while it takes place in all spatial scales after stepping into the non-linear regime (see Section 2.2.2).

While MRI reveals a way to transport the angular momentum locally using magnetic field, [Bland-](#)

ford & Payne (1982) examined the possibility to remove energy and angular momentum magnetically from accretion discs by field lines that penetrate the disc surface and extend to large distances. Under the assumptions of ideal MHD (infinite conductivity), axial symmetry, self-similarity etc., they solved the equations of MHD and showed it is possible that matter flow from a Keplerian accretion disc can be driven centrifugally from the disc, if the poloidal component of the magnetic field makes an angle of less than 60° with the disc surface (see Section 2.3.1). As shown in Figure 1.8 right plot, once the matter is loaded onto the field lines and reaches the surface of the disk, they can be spun centrifugally and leave the disk, where the angular momentum gained by outflowing matter comes from the rotating disk. The Blandford-Payne (BP) process has been later introduced to the accretion systems of YSOs as the mechanism for protostellar jets (Pudritz & Norman 1986).

Besides the rotating accretion disk around black hole as a power source, Blandford & Znajek (1977) demonstrated that when the black hole is rotating, energy can also be extracted from the black hole itself (Blandford-Znajek process). They showed that if the magnetic field and angular momentum are large enough, a force-free magnetosphere will be created, surrounding the black hole by a cascading production of electron-positron pairs in the unstable vacuum. By solving the energy and momentum conservation equations under general relativity, it has been proven that under such circumstance, the energy flux at the event horizon can be positive, thus implying energy extraction from black hole (see Section 2.4). A physical observer rotating at constant radius close to the horizon will see a Poynting flux of energy entering the hole, but he will also see a sufficiently strong flux of angular momentum leaving the hole to ensure the positive energy flux at horizon (Blandford & Znajek 1977). Thus, the black hole spin is slowed down during this process. The produced energy will then be carried by the outflowing electrons while the positrons flow into the black hole.

Blandford-Payne and Blandford-Znajek processes are considered to be the two most important theoretical models that describe the mechanism of energy sources in AGNs. Nevertheless, the Blandford-Payne process takes place within tens of $10r_s$, while the Blandford-Znajek process occurs in the ergosphere of a rotating black hole. This makes current observational tools incapable of resolving either of them. The efforts to investigate the contribution of the two processes can thus only be done by the numerical simulations (see Section 1.5).

In addition to the two processes, Lynden-Bell (1996) introduced an interpretation of jets from accretion systems as tower jets which “are primarily growing towers of twisted magnetic field together with the currents that they carry”. The tower jets are also observed in the later simulation results in this thesis (see Section 5.6.4).

1.3 Spacetime around the black hole

In general, the exact expressions of equations describing physical events depend on the geometry (metric) of the spacetime where the events happen. Additionally, different coordinate systems are

used under differing circumstances. In this section, the spacetime and the coordinate systems that are employed to investigate black holes are introduced. It is also discussed how they influenced the main physical equations used in this thesis work. Since it is not the concern of this thesis to derive general relativity, most of the equations will be given directly. The equations in this section follow the common convention in Section 1.6.

1.3.1 Spacetime and metric

Once an observer builds up her/his coordinate system, she/he is able to denote an event (e.g. the appearance of a tiny particle) by recording the time and the position when/where the event takes place with a number set (one number stores the time information and three numbers store the position information). This number set can be put into an infinite four-dimensional space called spacetime. Whether the particle is moving or not, its existence shows a trajectory in the spacetime. On the other hand, when the trajectory for a particle in spacetime is given in the first place, its position at anytime including the future can be determined from the trajectory. Physical laws were therefore built to calculate the trajectory of objects in spacetime under certain conditions. The Lagrange equation and the Euler equations are well-known examples of these physical laws.

The theory of general relativity (Einstein 1916) proposed that objects with masses are able to curve spacetime (see Figure 1.9) and the natural phenomenon that all things with mass are brought toward one another is resulted by the curved spacetime. In general relativity, Newtonian gravity is considered as a limitation case for the “low mass densities” (e.g. mass density of the sun) and “low velocities” (e.g. the orbital motion of the earth around the sun). The spacetime that is not influenced (curved) by any mass is called a flat spacetime or Minkowski spacetime.

Now consider an observation of a tiny particle in Minkowski spacetime. The mass of the particle is ignorable, hence its mass will not disturb the flat spacetime around it. Our four-dimensional coordinate system x is denoted by

$$x = (x^0, x^1, x^2, x^3), \quad (1.1)$$

where x^0 is the time component and x^1, x^2, x^3 are the three Cartesian spatial components. If the particle makes an infinitesimal movement in the spacetime from point x to neighbouring point x'' , the displacement of this movement will be denoted by

$$x'' - x = dx = (dx^0, dx^1, dx^2, dx^3), \quad (1.2)$$

where dx here is a vector. As known from special relativity, the observer-frame-invariant “distance” in the four-dimensional spacetime is given by

$$ds^2 = -(dx^0)^2 + (dx^1)^2 + (dx^2)^2 + (dx^3)^2. \quad (1.3)$$

Equation (1.3) is a special case for flat spacetime. To introduce the curved spacetime in general

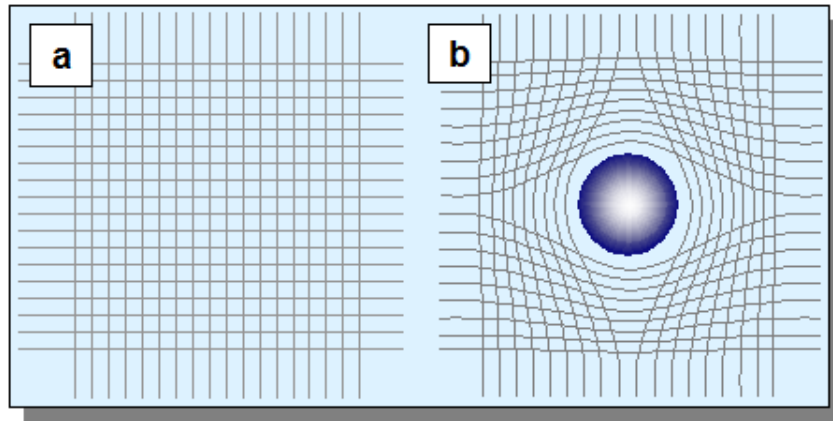


Figure 1.9: A preliminary sketch of mass curved spacetime. In example a, mass is absent and spacetime is flat. In example b, spacetime is curved because of the attendance of the mass in the center. Imagine a tiny particle with ignorable mass moving along the trajectory of a grid line in example a, the orbit of this particle will be a straight line. However, putting this particle into example b and letting it again move along the same grid line, its orbit will become a curve although it actually follows the trajectory as in the flat space. Note that this sketch is a very rough illustration. The true spacetime is 4 dimensional and its curvature needs to be calculated according to the situation very carefully. Figure credit: Jacky Jerome.

relativity, we need to rewrite it using the form of vector inner product

$$ds^2 = g_{\mu\nu} dx^\mu dx^\nu, \quad (1.4)$$

where μ and ν run from 0 to 3 (see Section 1.6). Tensor $g_{\mu\nu}$ is the metric tensor. The metric captures all the geometric and causal structure of spacetime, and is used to define notions such as time, distance, volume, curvature, and angle. In other words, the metric tensor tells us whether and how the spacetime is curved (see also Section 1.3.4). The metric tensor of a flat spacetime has the following form

$$g_{\mu\nu} = \eta_{\mu\nu} = \begin{bmatrix} -1 & 0 & 0 & 0 \\ 0 & 1 & 0 & 0 \\ 0 & 0 & 1 & 0 \\ 0 & 0 & 0 & 1 \end{bmatrix},$$

where $\eta_{\mu\nu}$ is called the Minkowski metric. Equation (1.3) can be retrieved by applying the Minkowski metric to Equation (1.4). The metric of Minkowski spacetime can also be written in other coordinate system, e.g. for the spherical coordinates $(x^0, x^1, x^2, x^3) = (t, r, \theta, \phi)$

$$g_{\mu\nu} = \begin{bmatrix} -1 & 0 & 0 & 0 \\ 0 & 1 & 0 & 0 \\ 0 & 0 & r^2 & 0 \\ 0 & 0 & 0 & r^2 \sin^2 \theta \end{bmatrix},$$

or

$$ds^2 = -dt^2 + dr^2 + r^2 d\theta^2 + r^2 \sin^2 \theta d\phi^2. \quad (1.5)$$

(Hereafter the metric will be presented always in the form of a line element.) This metric still represents the flat spacetime although it contains components other than -1 and 1 .

If one wants to learn physical laws in a curved spacetime it is necessary to get the metric of that spacetime first. As mentioned above, it is mass that curved the spacetime. Thus, the relation that connects the mass and spacetime geometry is the key to solve for the metric. The solution was given by Albert Einstein first published in [Einstein \(1915\)](#) (see also [Einstein 1917](#)), where the spacetime geometry and the energy-momentum tensor were put into one relation known as the Einstein field equation

$$G_{\mu\nu} - \Lambda g_{\mu\nu} = \frac{8\pi G}{c^4} T_{\mu\nu}. \quad (1.6)$$

In this equation, $G_{\mu\nu}$ is the Einstein tensor which is a function of metric g (see Section 1.3.4) and $T_{\mu\nu}$ is the energy-momentum tensor. The factor Λ is the cosmological constant responsible for the accelerating universe expansion which will not be further considered here ($\Lambda = 0$), since we only care about the local universe of a black hole. With Equation (1.6), we are able to solve for the spacetime around the black hole as will be seen in the next subsection.

1.3.2 Non-rotating/rotating black hole and the Boyer-Lindquist coordinates

Non-rotating black holes are also called ‘‘Schwarzschild black holes,’’ the solution for their spacetime was first given in ([Schwarzschild 1916](#)). The Schwarzschild solution is a time independent spherically symmetric solution of Einstein’s field equations for vacuum spacetime. It is originally supposed to describe the spacetime around a non-rotating homogeneous spherical ‘‘mass piece.’’ However, when the mass piece is compact enough, it becomes a black hole (see below).

In spherical coordinates (t, r, θ, ϕ) , to fulfill the static and spherically symmetric condition, the metric must have the form

$$ds^2 = -e^{2a(r)} dt^2 + e^{2b(r)} dr^2 + r^2(d\theta^2 + \sin^2 \theta d\phi^2). \quad (1.7)$$

Functions $a(r)$ and $b(r)$ in the equation must vanish for $r \rightarrow \infty$ since the spacetime at infinity from the black hole is flat. Additionally, the assumption for vacuum means a zero energy-momentum tensor which makes the Einstein tensor in Equation (1.6) vanish. Writing the Einstein tensor using the metric tensor in Equation (1.7) (see Section 1.3.4) and solving for $G_{\mu\nu} = 0$, it gives the condition

$$e^{2a} = e^{-2b} = 1 - \frac{2M}{r}, \quad (1.8)$$

where M is the mass of the center ‘‘mass piece.’’ (see [Schutz 2009](#), page 258-263 for derivation). The Schwarzschild solution can then be presented by

$$ds^2 = -\left(1 - \frac{2M}{r}\right) dt^2 + \left(1 - \frac{2M}{r}\right)^{-1} dr^2 + r^2(d\theta^2 + \sin^2 \theta d\phi^2). \quad (1.9)$$

On the one hand, this solution (the spacetime) refers back to Minkowski spacetime when no matter exists, namely $M = 0$. On the other hand, a singularity due to the choice of coordinates

has arisen at $r_H = 2M$. When the mass piece plunges itself into this radius (e.g., stellar collapse), a black hole will form (Schutz 2009, page 281). r_H is then the radius of the black hole horizon. For an external observer, events inside the horizon of a black hole can never influence the exterior. The singularity at $r = 2M$ can only be removed by a special choice of coordinate system (see Section 1.3.3).

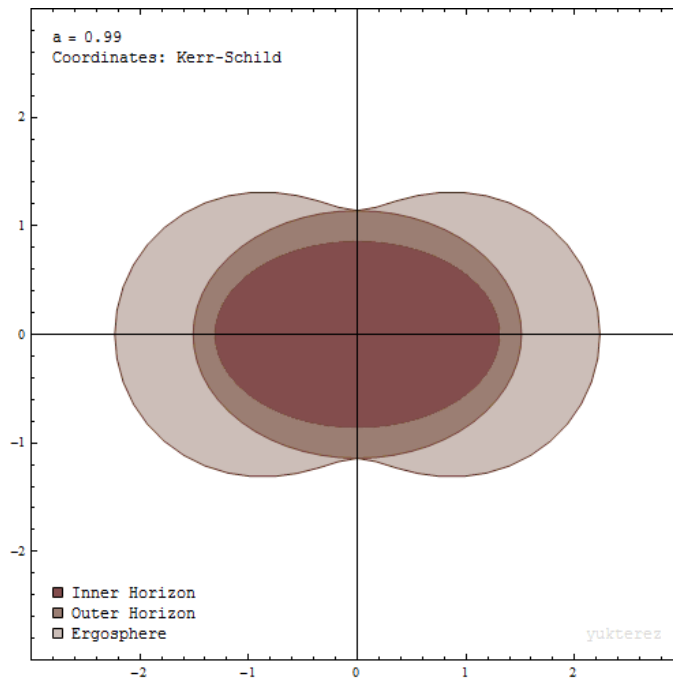


Figure 1.10: A two dimensional illustration plot of the ergosphere of a rotating black hole. The axes in the plot are in units of GM/c^2 . And the parameter $a = 0.99M$. The inner horizon is the inner singularity and the outer horizon is the black hole event horizon. The grey area between event horizon the the ergosphere is called ergoregion where no object inside is able to hold still to an observer at infinity (see text). The ergosphere is not a strict spheroid since the BL coordinates are not strictly spherical. Credit: Yukterez (Simon Tyran, Vienna).

The spacetime looks different when the center mass is rotating. The solution of the metric around a rotating black hole/mass piece was first published by Roy Kerr in 1967 (see Kerr & Schild 2009 for the republication version). For this reason, the family of rotating black holes are also called Kerr black holes. Boyer & Lindquist (1967) rewrite Kerr’s solution in a form similar to the Schwarzschild solution in Equation (1.9) by using the “Boyer-Lindquist”(BL) coordinates $(t_{bl}, r_{bl}, \theta_{bl}, \phi_{bl})$ whose spatial components have the following relation to the usual Cartesian coordinates

$$\begin{aligned} x &= \sqrt{r^2 + a^2} \sin \theta \cos \phi, \\ y &= \sqrt{r^2 + a^2} \sin \theta \sin \phi, \\ z &= r \cos \theta. \end{aligned} \tag{1.10}$$

If we define a as the angular momentum \mathcal{J} per unit mass ($a \in [-M, M]$, M is the mass of the black

hole), the Kerr solution in BL coordinates is

$$ds^2 = \left(-1 + \frac{2Mr}{\rho^2}\right)dt^2 - 2 \cdot \frac{2Mra \sin^2 \theta}{\rho^2} dt d\phi + \frac{\rho^2}{\Delta} dr^2 + \rho^2 d\theta^2 + \frac{\Sigma^2 \sin^2 \theta}{\rho^2} d\phi^2, \quad (1.11)$$

where

$$\begin{aligned} \rho^2 &= r^2 + a^2 \cos^2 \theta, \\ \Delta &= r^2 - 2Mr + a^2, \\ \Sigma^2 &= (r^2 + a^2)^2 - \Delta a^2 \sin^2 \theta. \end{aligned} \quad (1.12)$$

Equation (1.11) reduces to Schwarzschild metric in Equation (1.9) when the center object is not rotating ($a = 0$). The Kerr solution in BL coordinates has two singularities at $r = M \pm \sqrt{M - a^2}$ ($\Delta = 0$). The horizon of the Kerr black hole is the outer singularity, namely $r_H = M + \sqrt{M - a^2}$.

The rotation of mass drags the spacetime with it which is known as “frame dragging”. Due to the frame dragging, a test particle falling freely towards the center object will have a non-zero angular velocity

$$\Omega = -\frac{g_{t\phi}}{g_{\phi\phi}} \quad (1.13)$$

with respect to an observer at infinity. In the case of black hole, it can be concluded by Equation (1.11) (Schutz 2009, page 311-312), that there exists a spheroid like surface (see Figure 1.10) called an ergosphere outside the horizon at $r = M + \sqrt{M^2 - a^2 \cos^2 \theta}$, inside which objects cannot stay stationary to an observer at infinity, unless they were to move faster than the speed of light (an impossibility) with respect to the local spacetime.

1.3.3 The Kerr-Schild coordinates

As mentioned in Section 1.3.2, the BL coordinates have singularities at $\Delta = 0$ when expressing the metric around a rotating black hole. These singularities are resulted by the special choice of coordinates, thus can be removed by changing the coordinate system. In the case of the Kerr metric, it can be done by writing the metric in Kerr-Schild (KS) coordinates $(t_{ks}, r_{ks}, \theta_{ks}, \phi_{ks})$. The relation between BL and KS coordinates is

$$\begin{aligned} dt_{ks} &= dt_{bl} + \frac{2Mr_{bl}}{\Delta} dr_{bl}, \\ dr_{ks} &= dr_{bl}, \\ d\theta_{ks} &= r d\theta_{bl}, \\ d\phi_{ks} &= d\phi_{bl} - \frac{a}{\Delta} dr_{bl}. \end{aligned} \quad (1.14)$$

In KS coordinates, the Kerr metric is

$$\begin{aligned} ds^2 &= dr^2 + 2a \sin^2 \theta dr d\phi + (r^2 + a^2) \sin^2 \theta d\phi^2 + \rho^2 d\theta^2 - dt^2 \\ &\quad + \frac{2Mr}{\rho^2} \left(dr + a \sin^2 \theta d\phi + dt \right)^2 \end{aligned} \quad (1.15)$$

(Boyer & Lindquist 1982). Note that the coordinates r and θ do not change during the transformation, thus Δ and ρ^2 can be a function of either r_{ks} or r_{bl} . In KS coordinates, the components of the KS metric pass through the horizon $r = M + \sqrt{M - a^2}$ smoothly. The only possible singularity in the metric is at $r = 0$ which is a physical singularity (cannot be removed by any coordinate transformation). In numerical simulations, one can extend the computation area inside the black hole horizon by choosing KS coordinates. The simulation code rHARM employed by this thesis, is namely executed in a modified KS coordinate system (see Section 3.3.2).

1.3.4 Derivative in the curved spacetime

Physical laws are often expressed in the form of differential equations. In the flat spacetime, differential equations consist of partial derivatives with respect to the coordinates. As an example, the conservation law of the stress-energy tensor $T^{\mu\nu}$ in Cartesian coordinates is

$$\partial_\nu T^{\mu\nu} = 0. \quad (1.16)$$

Under the context of general relativity, the partial derivatives in Equation (1.16) must be adjusted to fit the curved spacetime. Thus, the partial derivatives will be replaced by the covariant derivatives ∇ – the “derivative” in the curved space time. (see Chapter 5 and Chapter 6 in Schutz 2009 for detailed derivation of the following equations) The notation of the operator ∇ is used in the way

$$\nabla_\nu y, \quad (1.17)$$

where ν is a vector and y can be a scalar function, a vector or a tensor. The operation in Equation (1.17) tells how the components in y change if y is moved in the spacetime by a displacement ν . If we define ∂_i as the local direction of a infinitesimal change in the i th component of the coordinate system and $_{,i} = \frac{\partial}{\partial x_i}$ as the partial derivative with respect to the i th coordinate component, the components of the covariant derivatives are related to the spacetime geometry by

$$\nabla_{\partial_i} \partial_j \equiv \Gamma_{ij}^l \partial_l, \quad (1.18)$$

where Γ_{ij}^l are called the Christoffel symbols and are defined by

$$\Gamma_{ij}^l = \frac{1}{2} g^{lk} (g_{ik,j} + g_{jk,i} - g_{ij,k}). \quad (1.19)$$

Using Equation (1.19), the Ricci tensor $R_{\mu\nu}$ is calculated by

$$R_{\mu\nu} = \Gamma_{\nu\mu,\delta}^\delta - \Gamma_{\delta\mu,\nu}^\delta + \Gamma_{\nu\mu}^\lambda \Gamma_{\delta\lambda}^\delta - \Gamma_{\delta\mu}^\lambda \Gamma_{\nu\lambda}^\delta. \quad (1.20)$$

The Einstein tensor in Equation (1.6) can be then defined by

$$G_{\mu\nu} \equiv R_{\mu\nu} - \frac{R}{2} g_{\mu\nu}, \quad (1.21)$$

where $R = R_{\mu\nu}g^{\mu\nu}$ is the Ricci scalar. Clearly, if we apply Equation (1.19) and (1.20) to Equation (1.21), the Einstein tensor $G_{\mu\nu}$ becomes only a function of the metric g .

With the notation $\nabla_i = \nabla_{\partial_i}$, the general form of the energy-momentum conservation in Equation (1.16) is defined in any coordinate system and any spacetime by

$$\nabla_\nu T^{\mu\nu} = 0. \quad (1.22)$$

One can further derive Equation (1.19) and get

$$\Gamma_{\mu l}^l = (\sqrt{-g})_{,\mu} / \sqrt{-g}, \quad (1.23)$$

where g is the determinant of the spacetime metric. This allows us to rewrite Equation (1.22) as

$$\frac{1}{\sqrt{-g}} (\sqrt{-g} T^{\mu\nu})_{,\nu} = 0. \quad (1.24)$$

The conservation equations in Chapter 3 employ the form of Equation (1.24).

1.4 A brief introduction of magnetohydrodynamics

Magnetohydrodynamics (MHD) is the study of the magnetic properties of electrically conducting fluids. The fundamental concept behind MHD is that magnetic fields can induce currents in a moving conductive fluid, which in turn polarizes the fluid and changes the magnetic field itself. The resistive GR-MHD equations in Section 3.2.1 based namely on the MHD equations, which is showed in this section.

1.4.1 The MHD equations

The equations that describe the physics in MHD system are based on the following assumptions. First, the velocity \mathbf{v} of the observed fluid satisfies

$$\mathbf{v} \ll c. \quad (1.25)$$

Second the characteristic length L and the characteristic time scale τ of the fluid system satisfies,

$$\frac{L}{\tau} \ll c. \quad (1.26)$$

The MHD system can then be described by the mass continuity equation

$$\frac{\partial \rho}{\partial t} + \nabla \cdot (\rho \mathbf{v}) = 0, \quad (1.27)$$

the momentum equation

$$\rho \left(\frac{\partial}{\partial t} + \mathbf{v} \cdot \nabla \right) \mathbf{v} = \mathbf{J} \times \mathbf{B} - \nabla p, \quad (1.28)$$

the energy equation

$$\frac{d}{dt} \left(\frac{p}{\rho^\gamma} \right), \quad (1.29)$$

and the equations for the electric magnetic field

$$\begin{aligned} \nabla \times \mathbf{B} &= \mathbf{J}, \\ \frac{\partial \mathbf{B}}{\partial t} &= -\nabla \times \mathbf{E}, \\ \nabla \cdot \mathbf{B} &= 0, \\ \mathbf{J} &= \lambda(\mathbf{E} + \mathbf{v} \times \mathbf{B}). \end{aligned} \quad (1.30)$$

Here, ρ is the fluid density, p is the pressure, \mathbf{v} is the velocity vector, \mathbf{B} is the magnetic field vector, \mathbf{E} is the electric field vector, \mathbf{J} is the current density and λ is the conductivity. These differential equations must be solved simultaneously, either analytically or numerically (as done in an usual MHD numerical simulation).

1.4.2 The ideal MHD assumption

The ideal MHD assumption describes the behavior of the magnetic field in moving plasma. Plasma is a state of matter which is considered as a gaseous mixture of negatively charged electrons and highly charged positive ions, created by heating a gas or by subjecting gas to a strong electromagnetic field. The derivation of the ideal MHD assumption can be found in , [Kippenhahn & Moellenhoff \(1975\)](#) (page 60-62). Here only the results are given.

Consider a closed curve C in plasma, it encloses a surface \mathbf{f} (see Figure 1.11, left plot). The curve line is embedded in the plasma, which means the curve always follows the plasma and becomes bigger when the material enclosed in the surface expands, and smaller when the material contracts during the proceeding time. The curve C_1 flows with the plasma and becomes C_2 after time dt . The surface enclosed by C_2 is \mathbf{f}_2 . The magnetic flux through the two surfaces is calculated by

$$\phi_i = \int_{\mathbf{f}_i} \mathbf{B} \cdot d\mathbf{f}_i, \quad (1.31)$$

with $i = 1, 2$. The expression $(\phi_2 - \phi_1)/dt = d\phi/dt$ shows how the magnetic flux through the closed curve changes moving with the plasma. If any magnetic field line passes through the side surface M during this process, $d\phi/dt$ will not be zero. Further derivation shows

$$\frac{d\phi}{dt} = - \int_{C_1} \eta \mathbf{J} \cdot d\mathbf{l}_1, \quad (1.32)$$

where $\eta \equiv 1/\lambda$ is the magnetic resistivity. In ideal MHD, $\eta = 0$ (or $\mathbf{E} = -\mathbf{v} \times \mathbf{B}$, see Equation 1.30), hence

$$\frac{d\phi}{dt} = 0. \quad (1.33)$$

This result implies that under the ideal MHD condition, fluid elements will be coupled with magnetic field lines. Or in other words, a fluid element threaded by one magnetic field line is not allowed to leave this field line when it moves. This conclusion leads to two important regimes. In the case where fluid/gas pressure is predominant, the magnetic field will be strictly enclosed to (“frozen in”) the matter flow. On the other hand, if the magnetic pressure is stronger than the matter pressure, the fluid elements can then only move along the field lines (no perpendicular movement) as shown in Figure 1.11 right plot. The coupling of the fluid elements and the magnetic field is namely the ideal MHD assumption, which turns out to affect the disk structure and the accretion process (see Chapter 4 and 5).

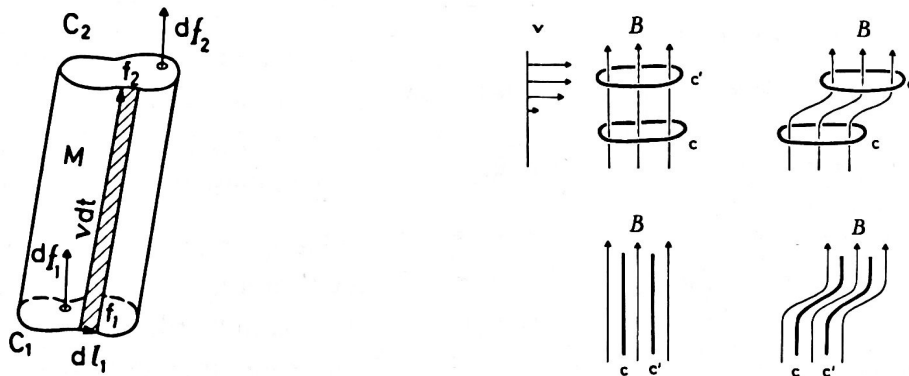


Figure 1.11: left: A closed curve C_1 embedded in and flow with the material. After time dt , the circle moves to C_2 . The surface closed by C_1 is f_1 , and f_1 by C_2 . right: Illustration figures of frozen field lines in ideal MHD. v in the plot stands for velocity. In this case, no matter how the the magnetic field lines construct, fluid elements always follow the field lines to keep the magnetic flux unchanged inside the closed circle that moves from c to c' (see text). Credit: [Kippenhahn & Moellenhoff \(1975\)](#)

1.5 Jets in Numerical Simulation

BP and BZ effects are both feasible mechanisms in the vicinity where AGN jets are originally produced (see Section 1.2.3). Nevertheless, while jets from young stars can be rather well resolved and typical features such as mass fluxes, velocities, or even rotation can be observed ([Bacciotti et al. 2002](#); [Coffey et al. 2004](#)), the structure of the AGN jet sources stays unresolved, and the dynamical jet parameters are uncertain as these jets are mostly detected in synchrotron emission. On the other hand, the physical equations governing such systems are non-linear, time-dependent, and intrinsically multidimensional, so their solution is difficult. Therefore, this subject has often been investigated by means of numerical methods.

1.5.1 The numerical approaches in jets simulation

The accretion disk consists of gas plasma with an electromagnetic field embedded in it. Because the inner boundary of the disk is very close to the black hole², the spacetime curvature cannot be neglected. Under such environment, the numerical simulations need to employ general relativistic magnetohydrodynamics (GR-MHD) to solve for the process of relativistic jet formation.

In the past, a few numerical schemes have been developed to evolve the GR-MHD equations. The first GR-MHD simulation was already presented by Wilson and Ruffini (Ruffini & Wilson 1975; Wilson 1977). However, it took another two decades before research returned to this topic. The GR-MHD schemes have also been supported by the substantial advancement of CPU power.

A few stages have been experienced before the modern GR-MHD schemes were realized, including the construction of non-relativistic MHD schemes (see e.g. Stone & Norman 1992), special relativistic hydrodynamics codes (Del Zanna & Bucciantini 2002), special relativistic MHD (Komissarov 1999; Del Zanna et al. 2003), general relativistic hydrodynamics (Hawley et al. 1984; De Villiers & Hawley 2002), and also MHD with pseudo-Newtonian potential (Hawley & Balbus 2002).

Today, upon the milestones established by these schemes, quite a few GR-MHD codes have been accomplished (Koide et al. 1999; De Villiers & Hawley 2003; Gammie et al. 2003; Del Zanna et al. 2007), being mainly used to simulate the evolution of black hole accretion systems (see e.g. Koide et al. 1999; De Villiers & Hawley 2003; McKinney & Gammie 2004; McKinney 2006). All of the codes cited above work in the ideal GR-MHD regime (thus neglecting resistivity or magnetic diffusivity).

1.5.2 The necessity of diffusivity in GR-MHD

In order to disentangle the powering mechanism for relativistic jets, one needs to investigate the two important processes for jet formation, that is (1) the Blandford-Znajek effect and (2) the Blandford-Payne effect (see Section 1.2.3). Energy extraction from a black hole by the Blandford-Znajek effect has been observed in ideal GR-MHD simulations (McKinney & Gammie 2004; McKinney 2006; McKinney et al. 2012). On the other hand, the jet formation from an accretion disk due to the Blandford-Payne effect has been observed and investigated in non-relativistic simulations (Ouyed & Pudritz 1997; Fendt & Čemeljić 2002) and also special relativistic simulations (Porth & Fendt 2010; Porth et al. 2011; Porth 2013). However, the *launching* problem, the transition from accretion to ejection that requires the presence of a substantial amount of magnetic diffusivity in order to allow for persistent disk outflows has not been treated in GR-MHD. Thus a jet formed from an accretion disk by the Blandford-Payne effect has yet to be observed in GR-MHD simulations.

²Due to the general relativity effect, the innermost stable circular orbit for a rotating particle is at $3r_H$ where r_H is the radius of horizon. Thus the inner boundary of a stable accretion disk never “touches” the black hole horizon.

The launching question is essential because it allows us to compare the mass fluxes of the disk and jet consistently, as demonstrated by non-relativistic simulations of several groups (Casse & Keppens 2002; Zanni et al. 2007; Sheikhnezami et al. 2012; Fendt & Sheikhnezami 2013; Stepanovs & Fendt 2014, 2016). As the MAJOR MOTIVATION of this thesis, we believe that it is the absence of disk magnetic diffusivity in recent GR-MHD simulations that does not allow the formation of long-lasting powerful disk winds which may turn into jets. With magnetic diffusivity, a magnetized disk wind is launched and the angular momentum of the orbiting disk material can be efficiently removed, allowing for efficient accretion.

In the ideal GR-MHD regime, the matter cannot “cross” the magnetic field lines (see Section 1.4.2). Such field lines that vertically thread the accretion disk are expected from advection of the magnetic flux from outer disk areas. Thus, any mass that is ejected from the disk into the jet cannot be replenished by accretion from outer disk areas, and jet formation will decay. In this case, the accretion flow will push the magnetic field lines inwards, which will accumulate out of the horizon of the black hole and a magnetically arrested disk (MAD) will form, allowing for further accretion only via the magnetic interchange instability (Igumenshchev et al. 2003; Narayan et al. 2003; McKinney et al. 2012).

In order to allow for a relative motion between plasma and magnetic field, we are going to apply resistive MHD, thus magnetically diffusive MHD (see also Ferreira 1997; Casse & Keppens 2002). Furthermore, being able to handle the re-distribution of mass flux that is needed for the launching mechanism of disk outflows, a resistive code can also treat physical magnetic reconnection (Fendt 2009; Del Zanna et al. 2016) which may be able to explain the observed X-ray emission (Machida & Matsumoto 2003).

1.5.3 Existing resistive codes

A few of resistive relativistic MHD codes have been developed (although none of them dealt with accretion disk simulation), starting from Watanabe & Yokoyama (2006) who investigated relativistic magnetic reconnection. Pioneering work by Komissarov (2007) presented a multi-dimensional upwind scheme with resistivity in special relativity. In Palenzuela et al. (2009) an implicit-explicit (IMEX) Runge-Kutta method was used to solve the stiff relaxation terms arising from resistivity. That work has been further extended to three dimensions and the general relativistic regime by Dionysopoulou et al. (2013). In Takamoto & Inoue (2011), a one-dimensional resistive approach was undertaken in special relativistic regime using a method of characteristics. More recently, Mizuno (2013) investigated the role of the equation of state in resistive GR-MHD.

In this thesis, I implement resistivity, namely magnetic diffusivity, into the existing ideal GR-MHD code HARM (Noble et al. 2006). The new code³ follows the prescription of Bucciantini & Del Zanna (2013) who extended the 3+1 GR-MHD code ECHO (Del Zanna et al. 2007) by implementing a mean-field dynamo closure and resistivity.

³The new code is denoted as rHARM which takes meaning from “resistive HARM”.

1.6 Convention and units in this thesis

The equations and derivations in this thesis follow the conventional notation of [Misner et al. \(1973\)](#). In particular, the sign convention for the metric is $(-, +, +, +)$. When the upper index and the lower index share the same letter, their final product follow Einstein notation. The Greek alphabet is used for space and time components, where indices take on values 0, 1, 2, 3. The Latin alphabet is used for spatial components only, where indices take on values 1, 2, 3. Bold letters denote vectors while the corresponding thin letters with indices represent vector components. For example,

$$\begin{aligned}\partial_\nu T^{\mu\nu} &= \partial_0 T^{\mu 0} + \partial_1 T^{\mu 1} + \partial_2 T^{\mu 2} + \partial_3 T^{\mu 3}, \\ v_i \mathcal{B}^i &= v_1 \mathcal{B}^1 + v_2 \mathcal{B}^2 + v_3 \mathcal{B}^3, \\ \mathcal{B} &= (\mathcal{B}^0, \mathcal{B}^1, \mathcal{B}^2, \mathcal{B}^3).\end{aligned}\tag{1.34}$$

The Levi-Civita symbol is defined by

$$\begin{aligned}\epsilon_{\alpha\beta\gamma\delta} &= \sqrt{-g}[\alpha\beta\gamma\delta], \\ \epsilon^{\alpha\beta\gamma\delta} &= -\frac{1}{\sqrt{-g}}[\alpha\beta\gamma\delta],\end{aligned}\tag{1.35}$$

where $[\alpha\beta\gamma\delta]$ is the conventional permutation of the numbers that are included. Without additional mention, $G = c = \mu_0 = 1$ is applied where G is the gravitational constant, c is the speed of light, and μ_0 stands for permeability of the vacuum. In rHARM, mass of the black hole is set to $M = 1$, while the spherical coordinates in the code denote the Kerr-Schild coordinates. The units of basic quantities are given in Section 3.3.1. In Chapter 4 and 5, the accretion rate, the ejection rate and the energy flux are all presented in code units.

1.7 Outline of the thesis

In this thesis, the accretion and ejection processes in the black hole accretion system is investigated using resistive GR-MHD simulations.

Chapter 2

Reviews the prevailing theories including the α parameter accretion disk model, the theory of magnetorotational instability, the Blandford-Payne mechanism and the Blandford-Znajek mechanism, which describe the accretion and ejection processes of the black hole accretion system.

Chapter 3

Illustrates the implementation of magnetic diffusivity into the existing ideal GR-MHD code HARM (Noble et al. 2006) and provides test simulations. The equations of the time evolution for the variables, the numerical structure and features in the new code rHARM are presented in detail. This chapter follows from my publication Qian et al. (2017) with my supervisor Christian Fendt.

Chapter 4

Shows the results of simulations by rHARM applied to a more astrophysical context, namely, investigating the development of the magneto-rotational instability (MRI) in tori that are magnetically diffusive. This chapter follows from my publication Qian et al. (2017) with my supervisor Christian Fendt.

Chapter 5

Presents the results of the preliminary survey study of rHARM simulating the launching of disk winds from a thin accretion disk threaded by inclined open poloidal field lines. The importance of the magnetic field strength, field structure and magnetic resistivity to disk wind evolution are discussed. The driving forces of the disk wind are analyzed.

Chapter 6

Shows, as a further study of Chapter 5, the influence of the black hole spin on the accretion and ejection processes.

Chapter 7

Summarizes the main conclusions of this thesis and gives an outlook on the future projects extending this work.

Chapter 2

Physical process in accretion system

Black hole accretion systems are considered the energy source for AGN jets. In Section 1.2.3, I briefly mentioned the prevailing theories that describe the main physical processes in the black hole accretion system. In this chapter, I will illustrate these theories, namely the seminal works from [Shakura & Sunyaev \(1973\)](#), [Blandford & Znajek \(1977\)](#), [Blandford & Payne \(1982\)](#) and [Balbus & Hawley \(1991\)](#) in detail with mathematical expressions.

2.1 The Shakura and Sunyaev accretion disk model

The background of accretion disk models started with the investigation of the gas streams in close binary systems. In the 1960s and 1970s, it was intensively argued that the most probable model of a binary system containing a collapsar (black hole, neutron star etc.) is accretion with formation of a disk around the collapsar ([Gorbatskii 1965](#); [Prendergast & Burbidge 1968](#); [Pringle & Rees 1972](#); [Shakura 1973](#); [Shakura & Sunyaev 1973](#)). This section is written based on the seminal work of [Shakura & Sunyaev \(1973\)](#), which gave a detailed picture of an accretion disk which can be applied to the black hole accretion system. In [Shakura & Sunyaev \(1973\)](#), the angular momentum transport and the corresponding energy release is characterized by the parameter α (see Section 2.1.1). The accretion disk is then divided into three distinct parameter regimes and the physical quantities in each regime can be expressed in terms of explicit algebraic formulae (see Section 2.1.2 and A.4). The discussion of the spectrum features of the disk will not be highlighted as it is not the concern of this project.

2.1.1 The general picture of black hole accretion disk

In a binary system that consists of a black hole and a normal star, if matter flows strongly outward from the star, some fraction of the matter flow will fall under influence of the gravitational field of the black hole. In the case that the matter falls radially towards the the black hole, it will just flow into the horizon without any energy release. Nevertheless, in a binary system, the matter outflow from a star onto the black hole has considerable angular momentum. For this reason, at some distance, the centrifugal forces of the falling matter will be comparable to the gravitational

forces and matter will begin to rotate in circular orbits. Consequently, an accretion disk is formed around the black hole (see Figure 2.1).

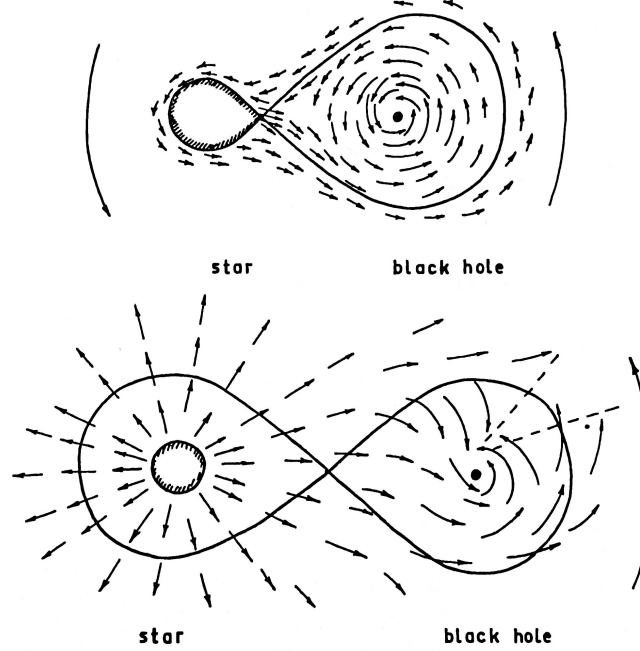


Figure 2.1: Two regime of matter flowing from a star in a binary system into the influence of the black hole: upper): a normal companion star that fills up its Roche volume and the matter flows mainly through the inner Lagrangian point. Lower): the size of the companion star is much smaller than the Roche volume. The matter will then lose part of its kinetic energy in the shock wave before being captured by the gravitational field of black hole. In both cases mentioned above, an accretion disk will form around the black hole. Figure credit: [Shakura & Sunyaev \(1973\)](#).

In such an accretion disk, the role of molecular viscosity is negligibly small and cannot lead to disk accretion. On the other hand, angular momentum cannot be transported by means of radiation which itself originates from accretion. Thus, the matter in the disk is stable against further accretion due to the rule of angular momentum conservation (see Appendix A.3 for an example in Keplerian circular orbits). However, if there is a mechanism to transfer angular momentum outwards in the the disk, then it is possible to have accretion further from the disk. [Shakura & Sunyaev \(1973\)](#) suggested that the tangential stresses between adjacent layers, provided by the magnetic field together with the turbulence in the disk, contribute to the mechanism of angular momentum transport. In their model, the magnetic stresses, w_m , can be written:

$$w_m \sim -\frac{H^2}{4\pi}, \quad (2.1)$$

where H is the magnetic field strength. The stresses caused by turbulence is

$$w_t = -\rho v_t l \frac{d\omega}{dR} \sim -\rho v_t l \frac{v_\phi}{R}, \quad (2.2)$$

where v_t is the turbulent velocity, l the maximal turbulent cell scale, ω and v_ϕ are the angular velocity and the Keplerian orbit velocity at radius R . The turbulent l is on the order of the disk thickness, thus

$$l \sim R \frac{v_s}{v_\phi}, \quad (2.3)$$

where v_s denotes the sound speed. Insert Equation (2.3) into Equation (2.2) and the turbulent stresses can be expressed by

$$w_t \sim -\rho v_s v_t. \quad (2.4)$$

The total stress is then

$$-w \sim -(w_m + w_t) = \rho v_s^2 \left(\frac{v_t}{v_s} + \frac{H^2}{4\pi\rho v_s^2} \right) = \alpha \rho v_s^2. \quad (2.5)$$

Since the efficiency of angular momentum transport is related directly to the stresses (see Equation 2.11), it can then be characterized by only the parameter α :

$$\alpha = \frac{v_t}{v_s} + \frac{H^2}{4\pi\rho v_s^2}. \quad (2.6)$$

The choice of a negative sign before w in Equation (2.5) gives the parameter α positive value. The parameter α is a function of radius. For a wide choices of disk conditions, $\alpha \ll 1$. It has been argued that in the range $10^{-15}(\dot{M}/\dot{M}_{\text{cr}}) < \alpha < 1$ (\dot{M}_{cr} is the accretion rate at Eddington luminosity), the disk structure is not significantly changed, thus, the external appearance of the disk can be computed without deciding which mechanism (w_m or w_t) dominates the angular momentum transfer.

In the case of an AGN accretion system, the cold material in the vicinity of the galactic center, that falls into the potential well of the supermassive black hole, also carries a large amount of angular momentum, which at a certain time will prevent its further infall. An accretion disk around the supermassive black hole is then also expected. Such an accretion disk includes a strong magnetic field, the origin of which is still poorly understood. Thus the accretion theory in [Shakura & Sunyaev \(1973\)](#) is thoroughly applicable under the context of this thesis project since the principle physical processes in the accretion disk do not vary due to the black hole mass.

2.1.2 The disk structure

With the α parameter, the approximation of the disk structure can be given upon the assumption of a Keplerian disk. The rotational velocity and angular velocity are then

$$\begin{aligned} v_\phi &= \sqrt{\frac{GM}{R}}, \\ \Omega &= \sqrt{\frac{GM}{R^3}}. \end{aligned} \quad (2.7)$$

In the vertical direction of the disk, the vertical component of the black hole gravitational force is balanced by the turbulent, gas pressure gradient, magnetic pressures and radiation pressures. According to the hydrostatic equilibrium equation, the half-thickness of such disk is

$$z_0 = \frac{v_s}{v_\phi} R. \quad (2.8)$$

We can further define the surface density

$$u_0 = 2 \int_0^{z_0} \rho dz, \quad (2.9)$$

and the stress between adjacent layers

$$W = 2 \int_0^{z_0} w dz = -\alpha u_0 v_s^2. \quad (2.10)$$

The angular momentum efficiency is then related to the stress by

$$u_0 \frac{d\Omega}{dt} R^2 = -u_0 v_r \frac{d\Omega}{dR} R^2 = \frac{1}{R} \frac{dW}{dR} R^2, \quad (2.11)$$

where $v_r = dR/dt$ is the radial velocity of the accreting flow caused by the friction between the adjacent layers. In the stationary case, $v_r < 0$ and the mass accretion rate $\dot{M} = 2\pi u_0 v_r R$ is time independent. After integrating Equation (2.11), we obtain

$$\dot{M} \Omega R^2 = -2\pi W R^2 + C. \quad (2.12)$$

The integration constant C is determined by the condition, that $W \simeq 0$ at the innermost stable circular orbit R_0 , where $R_0 = 3r_H$ in the Schwarzschild black hole case (see Section 1.3.2 for the definition of horizon r_H). Thus, $C = \dot{M} \Omega(R_0) R_0^2$. Replacing $\Omega(R_0)$ by Equation (2.7) and inserting the result into Equation (2.12), we have

$$\dot{M} \Omega \left[1 - \left(\frac{R_0}{R} \right)^{1/2} \right] = 2\pi \alpha u_0 v_s^2. \quad (2.13)$$

The energy flux radiated from the disk surface unit per unit time is given by

$$\begin{aligned} Q &= \frac{1}{2} W R \frac{d\Omega}{dR} \\ &= \frac{1}{4\pi R} \frac{d}{dR} \left[\dot{M} \left(\frac{v_\phi^2}{2} - \frac{GM}{R} \right) - 2\pi R^2 W \Omega \right] \\ &= \frac{3}{8\pi} \dot{M} \frac{GM}{R^3} \left[1 - \left(\frac{R_0}{R} \right)^{1/2} \right]. \end{aligned} \quad (2.14)$$

At a given flux Q , the energy density of radiation at the surface density u_0 is determined by

$$\varepsilon = \frac{3}{4} \frac{Q}{c} \sigma u_0 = \frac{9}{32} \dot{M} \frac{GM}{R^3} \frac{\sigma u_0}{c} \left[1 - \left(\frac{R_0}{R} \right)^{1/2} \right], \quad (2.15)$$

where σ is the opacity of the matter. According to the Stefan-Boltzmann law, the effective temperature of the disk can then be expressed by

$$T = \left(\frac{\varepsilon}{b} \right)^{1/4}, \quad (2.16)$$

where b is the Stefan–Boltzmann constant. The physical quantities of the accretion disk in Equation (2.8) and Equations (2.13) - (2.16) only depend on α when the sound speed v_s is given. In [Shakura & Sunyaev \(1973\)](#), the disk is considered to be composed of the combination of three distinct regimes:

- a) the radiation pressure is dominant and $v_s^2 = \varepsilon/3\rho$. The opacity $\sigma = \sigma_{ff}$, which is the free-free absorption opacity.
- b) the gas pressure is dominant and $v_s^2 = kT/m_p$ where k is Boltzmann constant and m_p is the proton mass. The opacity $\sigma = \sigma_T$ which is the cross section of Thomson scattering on free electrons.
- c) the sound speed is given by $v_s^2 = kT/m_p$ and the opacity $\sigma = \sigma_{ff}$.

The two c) regions are the outermost and the very narrow, closest to the black hole where the radiation is dominant. The two b) regions are intermediate between a) and c). Thus the structure of disk truncation looking from the disk side is, in the language of regime a), b) and c): “BH–c–b–a–b–c”. If these the conditions are applied to the equations above, then the physical quantities from different disk regions can be expressed in explicit algebraic formulae (see Appendix A.4).

2.2 Magnetorotational instability

[Shakura & Sunyaev \(1973\)](#) predicted that a chaotic magnetic field in the accretion disk can lead to the angular momentum transfer between adjacent disk layers. Nevertheless, due to the absence of the complete theory, they just assumed the existence of magnetic turbulence and argued that nonlinear perturbations would be required to disrupt the laminar flow. After about two decades, John F. Hawley and Steven A. Balbus investigated the local shear instability in magnetized disk in detail. They showed with both an analytical solution and numerical simulations that the disturbance to the regular rotation of a Keplerian disk by the weak magnetic field is local and extremely powerful, and can also take place in the linear perturbation regime. The content in this section is based on [Balbus & Hawley \(1991\)](#).

2.2.1 The analysis of linear perturbation

The theoretical analysis of magnetorotational instability (MRI) requires the assumption of ideal MHD. To get a general picture of MRI in mind, let us consider a differentially rotating disk which

is threaded by a vertical magnetic field. If a fluid element in the disk is displaced outwardly, the field line that threads the element will move outward so that the element can keep being penetrated by the same magnetic field line (see Section 1.4.2). The field line will, on one hand, try to return the element back to its original position by resisting stretching, and on the other hand, enforce the rigid rotation by resisting shearing. While the first situation is stabilizing, the latter adds to the instability in the disk. The fluid element is then forced by the magnetic field to rotate faster than the angular velocity of its new orbit and hence, is driven farther outward until the return force is finally conquered by the destabilization.

The analytical model set up in [Balbus & Hawley \(1991\)](#) employs a standard cylindrical coordinate system (R, ϕ, z) . The equilibrium angular velocity of the disk $\Omega(R)$ is assumed to be constant on cylinders. The basic dynamical equations for the physical quantities are

$$\begin{aligned} \frac{d \ln \rho}{dt} + \nabla \cdot \mathbf{v} &= 0, \\ \frac{d\mathbf{v}}{dt} + \frac{1}{\rho} \nabla \left(P + \frac{\mathbf{B}^2}{8\pi} \right) - \frac{1}{4\pi\rho} (\mathbf{B} \cdot \nabla) \mathbf{B} + \nabla \Phi &= 0, \\ \frac{\partial \mathbf{B}}{\partial t} - \nabla \times (\mathbf{v} \times \mathbf{B}) &= 0. \end{aligned} \quad (2.17)$$

The symbols in the equations have their usual meanings unless the notation Φ is the external gravitational potential and d/dt denotes the Lagrangian derivative. The perturbations with space-time dependence is considered as $e^{i(k_R R + k_z z - \omega t)}$, where k_R and k_z refer to the wave vector in the corresponding direction.

In the following, I review the condition for the stability of the perturbation. Let us denote the Fourier amplitudes of perturbed flow attributes of variable x as δx . If we apply the perturbation and Fourier transformation to Equation (2.17) and only keep the linear order, the components can be written out as

$$\begin{aligned} k_R \delta v_R + k_z \delta v_z &= 0, \\ -i\omega \delta v_R + \frac{ik_R}{\rho} \delta P - 2\Omega \delta v_\phi - \frac{\delta \rho}{\rho^2} \frac{\partial P}{\partial R} + \frac{ik_R}{4\pi\rho} (B_\phi \delta B_\phi + B_z \delta B_z) - \frac{ik_z}{4\pi\rho} B_z \delta B_R &= 0, \\ -\omega \delta v_z + \frac{ik_z \delta P}{\rho} - \frac{\delta \rho}{\rho^2} \frac{\partial P}{\partial z} + \frac{ik_z}{4\pi\rho} B_\phi \delta B_\phi &= 0, \\ -i\omega \delta v_\phi + \delta v_R \frac{\kappa^2}{2\Omega} - ik_z B_z \frac{\delta B_\phi}{4\pi\rho} &= 0, \\ -i\omega \delta B_R - ik_z B_z \delta v_R &= 0, \\ -i\omega \delta B_z - ik_z B_z \delta v_z &= 0, \\ -i\omega \delta B_\phi - \frac{d\Omega}{d \ln R} \delta B_R - ik_z B_z \delta v_\phi &= 0, \end{aligned} \quad (2.18)$$

where

$$\kappa^2 \equiv \frac{2\Omega}{R} \frac{d(R^2\Omega)}{dR}, \quad (2.19)$$

is the square of the epicyclic frequency. Combining these equations with the requirement that the entropy for adiabatic perturbations is in the Boussinesq approximation, we get, after rearranging and simplification (see [Balbus & Hawley 1991](#)), a dispersion relation:

$$\frac{k_z^2 + k_R^2}{k_z^2} \tilde{\omega}^4 - \left[\kappa^2 + \left(\frac{k_R}{k_z} N_z - N_R \right)^2 \right] \tilde{\omega}^2 - 4\Omega^2 k_z^2 v_{Az}^2 = 0. \quad (2.20)$$

The variable $v_{Az} = B_z^2/(4\pi\rho)$ is the z component of the Alfvén velocity and $\tilde{\omega}^2 \equiv \omega^2 - k_z^2 v_{Az}^2$. N_R and N_z are defined by

$$\begin{aligned} N_z^2 &\equiv -\frac{3}{5\rho} \frac{\partial P}{\partial z} \frac{\partial \ln P \rho^{-5/3}}{\partial z}, \\ N_R^2 &\equiv -\frac{3}{5\rho} \frac{\partial P}{\partial R} \frac{\partial \ln P \rho^{-5/3}}{\partial R}. \end{aligned} \quad (2.21)$$

Since ω is always real, $\tilde{\omega}$ must be real and a continuous function of its parameters in Equation (2.20). We may then investigate the stability of the disk by considering the condition of $\Omega^2 = 0$. Equation (2.20) then becomes

$$k_R^2 (k_z^2 v_{Az}^2 + N_z^2) - 2k_R k_z N_R N_z + k_z^2 \left(\frac{d\Omega^2}{d\ln R} + N_R^2 + k_z^2 v_{Az}^2 \right) = 0. \quad (2.22)$$

Now we treat the Equation (2.22) as a quadratic equation for k_R . To assure the stability of the perturbation, real solutions for k_R are not allowed. Consequently, the discriminant of the quadratic equation should be negative

$$k_z^4 v_{Az}^4 + k_z^2 v_{Az}^2 \left[(N_z^2 + N_R^2) + \frac{d\Omega^2}{d\ln R} \right] + N_z^2 \frac{d\Omega^2}{d\ln R} > 0. \quad (2.23)$$

Note that if $d\Omega/dR \geq 0$ is fulfilled, then the stability criterion always holds. But a normal gravitationally bound accretion disk does not satisfy this condition. Solving Equation (2.23), we finally find a critical value for k_z^2 :

$$(k_z^2)_{crit}^2 = \frac{1}{2v_{Az}^2} \left\{ \left[\left(N_z^2 + \frac{d\Omega^2}{d\ln R} \right)^2 - 4N_z^2 \frac{d\Omega^2}{d\ln R} \right]^{1/2} - \left[N_z^2 + \frac{d\Omega^2}{d\ln R} \right] \right\}. \quad (2.24)$$

Perturbations with wave number $k_z^2 > (k_z^2)_{crit}$ are still able to keep their stability in the linear regime. In other words, perturbations that have the wave number $k_z^2 \leq (k_z^2)_{crit}$, will become unstable and grow exponentially!

2.2.2 Dependence of perturbation growth on field strength

In Section 2.2.1, we saw that a linear perturbation in a weak magnetized accretion disk is unstable. The dynamical instability leads to the exponential growth of magnetic fields and rapid angular momentum transfer. These effects can be seen clearly by the numerical simulation results in [Balbus & Hawley \(1991\)](#). In these simulations, a 2D gas box taken from the truncation

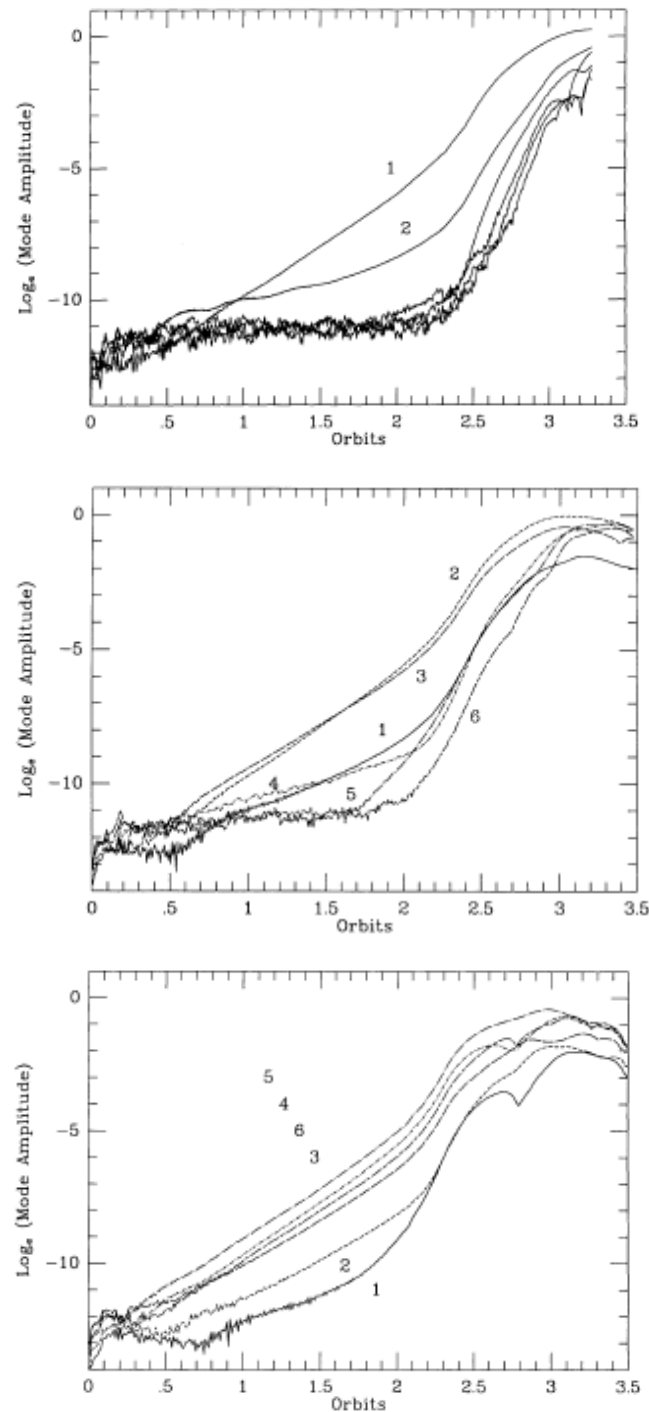


Figure 2.2: The mode amplitude from simulations with different magnetic field strength in the same numerical resolution, top: $\beta_z = 1000$, middle: $\beta_z = 4000$, lower: $\beta_z = 16000$. Below 2.2 orbital rotations, the perturbations are still in the linear regime. Some modes stay stable, while others start growing according to the corresponding critical wave numbers (see text). This figure is adopted from [Balbus & Hawley \(1991\)](#).

of Keplerian disk is investigated. The box is penetrated by a pure vertical magnetic field (only $B_z \neq 0$) and the plasma gas has infinite conductivity (ideal MHD assumption). The strength of

the initial vertical field is controlled by the plasma-*beta*

$$\beta_z = \frac{P}{(B_z^2/8\pi)}, \quad (2.25)$$

where P is the pressure of the plasma gas. The growth of the perturbation will shift the gas element from their original orbit either inwards or outwards and draw the field lines with them. A radial component of the magnetic field will then be induced, which is initially zero. Thus the diagnostics of the power of the perturbation instability with the wave number k_z can be represented by

$$\frac{1}{R_{\text{out}} - R_{\text{in}}} \int_{R_{\text{out}}}^{R_{\text{in}}} \ln |f| dr, \quad (2.26)$$

where

$$f(R) = \int_0^a B_R(R, z) e^{ik_z z/a} dz \quad (2.27)$$

is the average radial component of the magnetic field in the vertical direction. Here, $a = 1$ is the size of the simulation box.

The factor $1/2v_{Az}^2$ in the critical wave number equation (Equation 2.24) is related to the vertical Alfvén velocity

$$v_{Az} = \frac{B_z}{\mu_0 \rho}. \quad (2.28)$$

This implies, if a certain B_z allows the instability for wave number $k \leq \mathcal{K}$, then a weaker field strength, e.g. $B_z/2$, will allow the instability for $k \leq 2\mathcal{K}$ in the linear regime.

The results of the simulations in Balbus & Hawley (1991) is shown in Figure 2.2, the top plot is the perturbation evolution with $\beta_z = 1000$. In this plot, the modes $\bar{k}_z \equiv k_z/2\pi = 1, 2$ have exponential growth, while all other modes with higher wave numbers are stable in the linear regime. The corresponding critical wavelength is $\lambda_{\text{min}} = 0.513$. After about 2.2 orbital rotations, all perturbation modes step out of the linear regime and start growing rapidly. In the middle plot, $\beta_z = 4000$ indicates a magnetic field with only half strength compared to the top simulation. The wave numbers 1 through 4 are now unstable with the minimal wavelength $\lambda_{\text{min}} = 0.25$. The modes $\bar{k}_z = 5, 6$ are still not growing in the linear regime. In the lower plot, β_z is 16000, hence $k_{z,\text{crit}}$ should be doubled again. As expected, all wave modes from 1 to 6 are unstable and start growing in the linear regime.

In Figure 2.3, the poloidal field structures at the beginning and end of the simulation with $\beta_z = 1000$ are shown. The top plot presents the initial magnetic field which is purely vertical. As analyzed above, the growth of the perturbation (with $\bar{k}_z = 1, 2$) leads to angular momentum transfer among the gas elements, the radial movements of which also draws the magnetic field inwards and outwards. The evolution of the field configuration depends on the unstable perturbation mode that is dominating. In this simulation, $\bar{k}_z = 1$ (one wave per unit disk thick length) is predominant, thus the field line structure at 3.3 orbits looks like that in the lower plot of Figure 2.3.

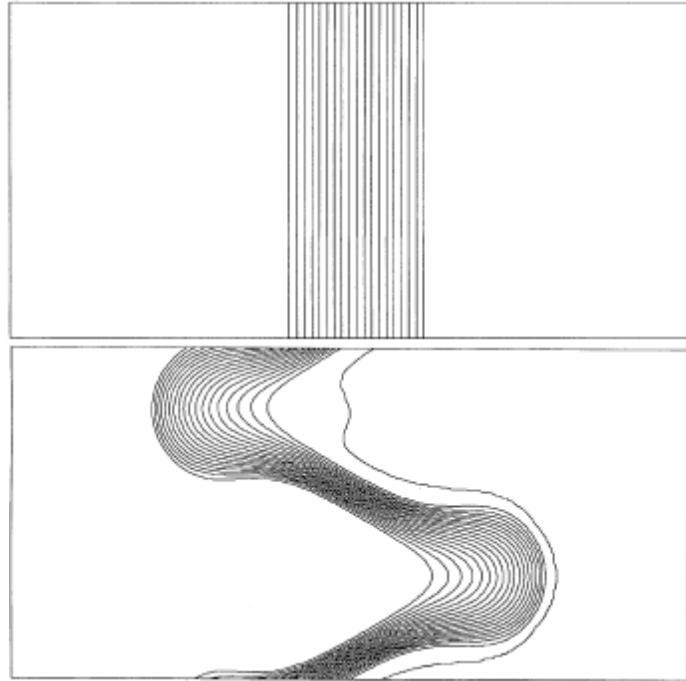


Figure 2.3: The poloidal field line structure in the simulation with $\beta_z = 1000$ at upper: $t=0$, lower: $t=3.3$ orbits. The dominant mode of unstable perturbation in this simulation is $\bar{k}_z = 1$ (see corresponding text). This figure is adopted from [Balbus & Hawley \(1991\)](#).

2.3 Disk driven wind - the Blandford & Payne mechanism

While [Balbus & Hawley \(1991\)](#) focused on the local angular momentum transfer mechanism inside the weak magnetized accretion disk, [Blandford & Payne \(1982\)](#) have investigated the wind/jet that is driven centrifugally by the strong, large-scale magnetic field that penetrates the accretion disk and given a self-similar solution of the cold MHD flow from the disk. In this section, I will introduce the fundamental idea of centrifugally disk-driven wind and the behavior of the wind according to the self-similar solution based on the work of [Blandford & Payne \(1982\)](#).

2.3.1 The centrifugally driven outflow

As mentioned in Section 1.4.2, in an ideal MHD flow, the fluid elements and the magnetic field lines are coupled. In the case of a strong magnetic field ($P_{\text{mag}} \gg P_{\text{fluid}}$), the motion of fluid elements follows the magnetic field lines. With this background, let us consider a rotating accretion disk, the surfaces of which are penetrated by field lines that extend to large distances (see Figure 1.8 right plot as an example). At the disk surfaces, magnetic pressure is dominant. Fluid elements loaded on a field line can be treated as beads threaded by a rigid wire. This wire (the field line) is rotating with the disk rigidly and all the beads on this wire are forced to rotate with the same angular velocity, which is decided by the position where the wire is anchored on the disk surface. The centrifugal force for the circular motion required by the beads at larger radii

will then exceed that of the gravitational force. These beads will then fly outwards.

To see this process in mathematical language, let us consider a 2-D truncation in the radial direction of Keplerian disk. The simulation employs cylindrical coordinates (r, z) , where the black hole is set at point $(0, 0)$, and the gravitational potential can be expressed by

$$\Phi_{\mathcal{G}}(r, z) = -\frac{GM}{(r^2 + z^2)^{1/2}}. \quad (2.29)$$

On the other hand, the centrifugal force of an arbitrary element in the disk is only a function of r

$$C(r) = \Omega^2 r = \frac{GM}{r^3} r. \quad (2.30)$$

For a fluid element A at (r, z) , bound to a strong magnetic field line that penetrates the accretion disk through $(r_0, 0)$, rotates with the same angular velocity as at r_0 . Thus, we apply $r = r_0$ in the angular velocity in Equation (2.30) and integrate it to get the potential of centrifugal force

$$\Phi_{\mathcal{C}}^A(r) = \frac{1}{2} \frac{GM r^2}{r_0^3}. \quad (2.31)$$

Now we combine Equation (2.29) and (2.31) to get a total potential for element A

$$\Phi(r, z) = \Phi_{\mathcal{G}} - \Phi_{\mathcal{C}}^A = -\frac{GM}{r_0} \left[\frac{1}{2} \left(\frac{r}{r_0} \right)^2 + \frac{r_0}{(r^2 + z^2)^{1/2}} \right]. \quad (2.32)$$

The equipotential surfaces of Φ is shown in Figure 2.4, where lower surface has lower value of Φ .

We now release the fluid element A from rest at r_0 . The total force in the direction perpendicular to the field line always vanishes since the field line is assumed to be rigid. Along the field line, the total force that acts on A is $\mathcal{F} = -\partial\Phi/\partial\mathbf{v}$, where \mathbf{v} is the unit vector along the field line starting from r_0 . It is clear that if \mathbf{v} points to the stable region in Figure 2.4, that is, the element A makes an attempt to leave the rotating disk to the stable region, then \mathcal{F} will be negative and the higher potential will push A back to the disk. Nevertheless, if \mathbf{v} points to the unstable region on the right hand side, then the centrifugal force becomes dominant and A will keep moving farther from the disk to the lower potential. The unstable region on the left hand side is gravity dominant (accretion onto the black hole) and is not our concern. Note that the angle between the right marginal stable surface and the disk is 60° . Thus we can conclude that if the magnetic field lines which penetrate the accretion disk make an angle less than 60° to the disk mid-plane, then the fluid elements loaded on the field lines become unstable against the rotation and the outflow is created.

2.3.2 Behavior of the disk wind in self-similar solution

As shown in Section 2.3.1, it is possible to drive outflow centrifugally from an accretion disk through magnetic field lines. The behavior of the disk outflow after leaving the disk surface is

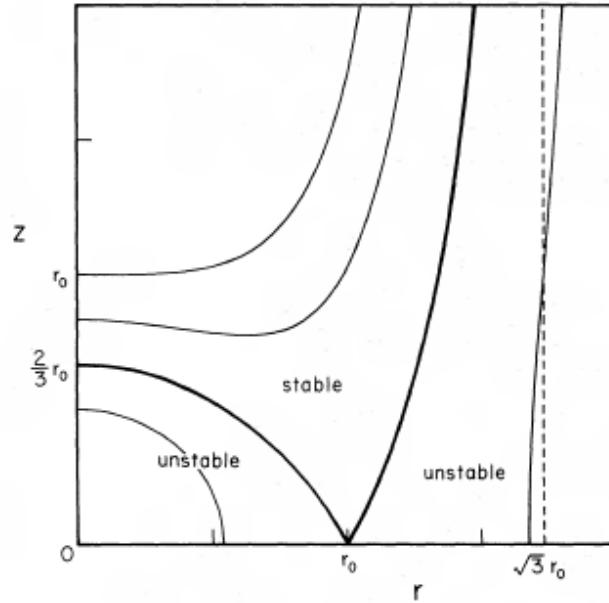


Figure 2.4: Equipotential surfaces for the fluid element A threaded on a magnetic field line that goes through the Keplerian accretion disk at point $(r_0, 0)$. The stable region has higher potential than the point $(r_0, 0)$, while the unstable regions have lower potential. An attempted movement for A from r_0 to the unstable region on the right hand side makes A leave the disk to the lower potential region. The dashed line at $r = \sqrt{3}r_0$ is the asymptote for the surface of marginal stability which reaches infinity in the z -direction. The angle between the right marginal stable surface and the disk is 60° . This figure is adopted from [Blandford & Payne \(1982\)](#).

important as well. In [Blandford & Payne \(1982\)](#), this problem is investigated by solving the time independent ideal MHD equations under cold MHD flow conditions (ignoring the thermal term) in axisymmetric cylindrical coordinates $(r, \phi, z) \rightarrow (r, z)$. The accretion disk around a black hole with mass M has Keplerian differential rotation with the field strength $B(r, 0) \propto r^{-5/4}$. In the solution, the coordinates in r and z are rescaled by ξ and χ

$$\mathbf{r} = [r_0 \xi(\chi), \phi, r_0 \chi], \quad (2.33)$$

so that all quantities will scale with spherical radius along a given direction. After the rescaling, the magnetic field looks self-similar in the new coordinates (ξ, χ) . The rescale function $\xi(\chi)$ depends on the construction of the magnetic field lines. In reverse, the choice of $\xi(\chi)$ decides what kind of magnetic field a specific solution is dealing with. Parameters that define the final solution are the specific energy, the specific angular momentum, the magnetic field configuration and the ratio of the constant mass flux to the constant magnetic flux.

The derivation of the solutions is rather abstract and lengthy, so I will give the solution with the “standard set” of parameters in [Blandford & Payne \(1982\)](#) directly. The integrated flow streamlines (magnetic field lines) projected into the poloidal plane for the “standard” solution is shown in Figure 2.5 left plot. With these parameters, the opening angle of the jet is $\theta = 6^\circ$ and the flow becomes super-Alfvénic at the points where the dashed line intersects the field lines in the plot. The positions for certain pitch angles $\alpha = \tan^{-1} |B_\phi/B_p|$ (B_p represents the poloidal

field strength) of the magnetic field are denoted by the dotted lines. As is presented in the plot, all outflow streams are bent after leaving the disk and possess toroidal motion. This implies that the rigid field line assumption used in Section 2.3.1 cannot hold above a certain distance from the disk depending on the radius where the stream flows out, i.e., where the field line is anchored in the disk. When the stream comes from a smaller radius with faster rotation, the bending of the stream takes place earlier.

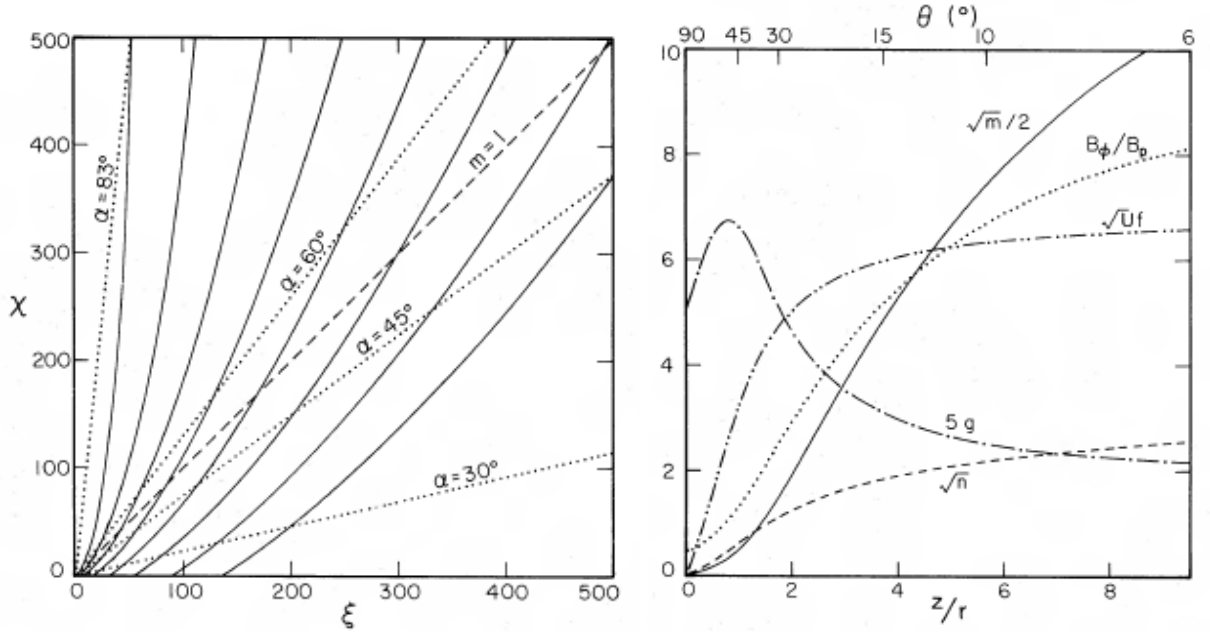


Figure 2.5: The results of the “standard” solution for the cold ideal MHD flow in Keplerian accretion disk. left: The integrated field lines projected into the poloidal plane in self-similar coordinates (ξ, χ) . The dashed line presents the surface where the Alfvén Mach number $\sqrt{m} = 1$. The surfaces for certain pitch angles $\alpha = \tan^{-1} |B_\phi/B_p|$ are denoted by the dotted lines. right: The dynamics along a single outflow streamline. \sqrt{m} is the Alfvén Mach number, \sqrt{n} is the fast-mode magnetosonic Mach number, $\sqrt{U}f$ stands for the poloidal velocity and g represents the toroidal velocity. The ratio of the toroidal field strength to the poloidal field strength is also given in the plot. The parameter θ is the polar angle as measured from the origin of the coordinate system. Credit: [Blandford & Payne \(1982\)](#).

The mechanics of the outflow stream along a single field line is shown in Figure 2.5 right plot. In this plot, the toroidal velocity increases until the Alfvén critical point ($v = v_A$) is almost reached, as the matter is accelerated along the field line by the magnetic stresses. During this process, the toroidal flow always attempts to rotate slower to keep the angular momentum when moving to the larger radius; this is also the reason for field line bending mentioned previously. Beyond the Alfvén critical point, the matter starts dominating the azimuthal and causes the decrease of toroidal velocity. Furthermore, the poloidal velocity in the plot increases until the Mach number of the fast-mode magnetosonic wave is unity. Far before this point, the toroidal velocity had already started decreasing, thus weakening the centrifugal force. The acceleration of the poloidal field here implies that the matter flow is also accelerated by the magnetic pressure gradient. It

has also been discussed in [Blandford & Payne \(1982\)](#) that there exists a value n_t for the square of the fast-mode magnetosonic Mach number n , above which the radial velocity becomes negative and the flow converges towards the z -axis, which corresponds to the collimation phase of a jet.

The solution in [Blandford & Payne \(1982\)](#) has been extended to a more general solution in [Pelletier & Pudritz \(1992\)](#). The maximal opening angle between the magnetic field lines and the disk surface, which allows the operation of the centrifugally driven outflow, is as much as $\approx 70^\circ$ when a finite gas pressure is considered.

2.4 Energy extraction from rotating black hole - the Blandford & Znajek mechanism

In Section [2.3.1](#), a mechanism was shown where the outflow/jet is powered by the rotational energy of an accretion disk around the BH. During this process the accretion disk will be slowed down due to the loss of angular momentum energy. Through a quite different mechanism - the Blandford & Znajek process, which was inspired by the radiation mechanism of pulsars ([Ruderman & Sutherland 1975](#)), [Blandford & Znajek \(1977\)](#) presented a way to extract rotational energy from the rotating black hole. This process requires the presence of magnetic field at the vicinity of black hole horizon. When the field is large enough, a cascade production of electron-positron pairs is produced, creating a force-free magnetosphere. Under this circumstance, it is possible to have positive radial energy flux at the horizon of the black hole. In the following, the Blandford & Znajek process will be illustrated based on the work [Blandford & Znajek \(1977\)](#).

2.4.1 The force-free magnetosphere around a black hole

Assuming that the accretion disk around the black hole (if not totally, at least almost) satisfies the ideal MHD condition in the disk¹, the magnetic flux frozen into the material flow will accrete with the flow, so the field strength close to the horizon can become quite large. Because the black hole is rotating, the field lines that penetrate the ergosphere of the black hole rotates with spacetime (see Section [1.3.2](#)). Similar to a homopolar generator experiment, the adjacent layers of magnetic equipotential surfaces will then have different electric potential $\Delta V \propto \Omega_H \Phi$, where Ω_H is the black hole angular velocity and Φ denotes the magnetic flux included by an equipotential surface. Any stray charged particles flowing between the adjacent magnetic surfaces will then be accelerated (see Figure [2.6](#)). For each Ω_H there exists a magnetic field strength above which electrons can reach an energy high enough to radiate gamma-ray photons by the curvature process. These high energy photons cause the instability of the vacuum and, consequently, create electron-positron pairs which in turn are accelerated, leading to a cascade. The freely produced charges will then make the electromagnetic field approximately force-free in the vicinity of the

¹This condition is actually not really satisfied in the simulations in Section [6](#)

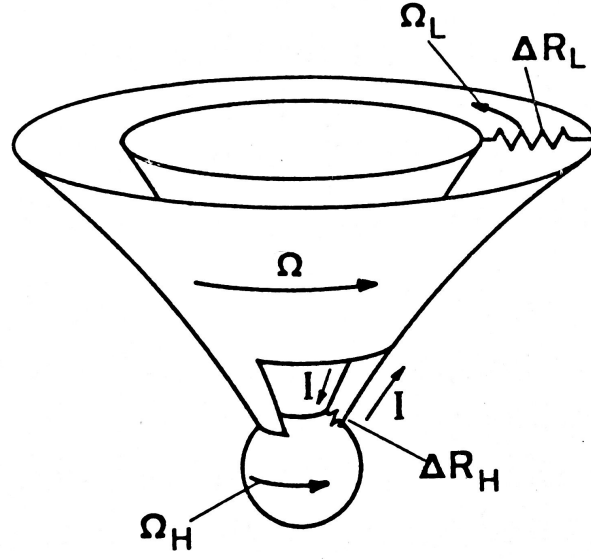


Figure 2.6: A sketch of the electrical flow on the equipotential surfaces of the magnetic field lines that penetrate the ergosphere of the black hole. The angular velocity of the magnetic field lines noted by Ω , is defined so that an observer orbiting with this angular velocity would not see any electric field. The black hole spins with angular velocity Ω_H . Ω_L is the angular velocity of an external load resistance. Here the mechanism of gamma-ray production can be treated as the external resistance (see corresponding text). This figure is adopted from [Blandford et al. \(1990\)](#), page 207.

horizon.

In a force-free magnetosphere, the electromagnetic field tensor $F^{\mu\nu}$ satisfies

$$F_{\mu\nu}J^\nu = 0, \quad (2.34)$$

where J^ν is the current 4-vector. $F_{\mu\nu}$ can be defined by a vector potential A_μ so that

$$F_{\mu\nu} = A_{\nu,\mu} - A_{\mu,\nu}. \quad (2.35)$$

The expression $X_{,y}$ denotes the derivative of quantity X to y (since we are in GR, the derivative here is the covariant derivative). If we apply Equation (2.35) to Equation (2.34) in the Boyer-Lindquist coordinates and define the toroidal magnetic field strength as $B_T = -g^{rr} \sin \theta B_\phi$, under the certain boundary conditions, the toroidal field on the surface of the black hole horizon can be expressed by

$$B_T[A_\phi(r_H, \theta)] = \frac{\sin \theta [\Omega(r_H^2 + a^2) - a]}{r_H^2 + a^2 \cos^2 \theta} A_{\phi,\theta}(r_H, \theta), \quad (2.36)$$

where $a \in [-1, 1]$ stands for the black hole spin parameter (see Section 1.3.2) and $\Omega = -A_{0,\theta}/A_{\phi,\theta}$ is the electromagnetic angular velocity which is not necessarily equal to any material angular

velocity (see also Figure 2.6). The radial energy flux and angular momentum flux can be denoted by

$$\begin{aligned}\mathcal{E}^r &= -\frac{\Omega\epsilon_0 A_{\phi,\theta} B_T}{\sin\theta(r_H^2 + a^2 \cos^2)}, \\ \mathcal{L}^r &= \frac{\mathcal{E}^r}{\Omega},\end{aligned}\quad (2.37)$$

where ϵ_0 is the vacuum permittivity. The total rate of energy extraction from the black hole measured at infinity is then (see Blandford & Znajek (1977) for the detailed derivation)

$$\int_0^{2\pi} d\phi \int_0^\pi d\theta \mathcal{E}^r \sin\theta (r_H^2 + a^2 \cos^2) = -4\pi\epsilon_0 \int_{A_\phi(\theta=0)}^{A_\phi(\theta=\pi/2)} dA_\phi B_T \Omega. \quad (2.38)$$

Similarly, the angular momentum extraction rate is given by

$$\int_0^{2\pi} d\phi \int_0^\pi d\theta \mathcal{L}^r \sin\theta (r_H^2 + a^2 \cos^2) = -4\pi\epsilon_0 \int_{A_\phi(\theta=0)}^{A_\phi(\theta=\pi/2)} dA_\phi B_T. \quad (2.39)$$

Since \mathcal{E}^r and \mathcal{L}^r are only dependent on the potential A_ϕ and the spin parameter a , and once A_ϕ is known, we will have a relation between the energy and momentum extraction rate from the black hole and the spin parameter.

2.4.2 Dependence of the energy extraction efficiency on the black hole spin

Nevertheless, the exact solution of A_ϕ is not trivial. In Blandford & Znajek (1977), a perturbation method is introduced to find a solution which is valid for a slowly rotating black hole $|a| \ll 1$. It has been concluded that the power P radiated from the horizon satisfies $P \propto a^2$. After being confirmed by numerical simulations (Komissarov 2005; McKinney & Gammie 2004), the Blandford-Znajek effect has frequently been investigated through numerical approaches. In Tchekhovskoy et al. (2010), a survey over a wide range of black hole spin parameter a has been executed by GR-MHD simulations under the force-free condition. From the data fitting, a solution that accurately describes the scaling of the jet power is given by

$$P \approx k\Phi_{tot} \left[\left(\frac{a}{r_H} \right)^2 + \alpha \left(\frac{a}{r_H} \right)^4 + \beta \left(\frac{a}{r_H} \right)^6 \right]. \quad (2.40)$$

In this equation, Φ_{tot} is the total poloidal magnetic flux in the jet and k is a constant which depends on the geometry choices in the simulation. The parameter $\alpha \sim 1.38$ and $\beta \sim -9.2$. Clearly, Equation (2.40) reduces to $P \propto a^2$ for tiny a .

Chapter 3

Numerical Implementation of Resistive GR-MHD

As mentioned in Section 1.5, the dynamical structure of the AGN jet sources are unresolved by observations since jets are mostly detected in synchrotron emission. Neither is any analytical solution available because of the complexity of the MHD equations that govern the accretion system. For these reasons, AGN jet production has often been investigated by means of numerical simulations. In this thesis project, we decide to implement magnetic resistivity into the existing ideal GR-MHD code HARM (Gammie et al. 2003) and run simulations with this updated code in order to get stable outflows from the accretion disk. The new code is named rHARM where the letter “r” stands for “resistive.” In this chapter, I will introduce the structure and features of rHARM in detail. As the code is newly developed, two verification tests of the code will also be shown. The derivation of equations and tests of the new code in this chapter can also be found in the published paper Qian et al. (2017) by my supervisor Christian Fendt and I.

3.1 Basics of rHARM

The resistive GR-MHD code rHARM is developed on the basis of the 2D non-resistive GR-MHD code HARM (Gammie et al. 2003), which is a Godunov’s (conservative shock-capturing) scheme for evolving the GR-MHD equations. In this section, the basic equations of the Godunov’s scheme, the approximate flux Riemann solver and the basic structure of rHARM, which is in common with HARM, will be presented.

3.1.1 A brief introduction to the Godunov’s scheme

Godunov’s scheme is a conservative numerical scheme, created by Sergei K. Godunov for solving partial differential equations. The application of a conservative form of the equations in the Godunov’s scheme is important, especially when dealing with problems admitting shocks or other discontinuities in the solution. Since the GR-MHD equations can all be written in the conservative form, Godunov’s scheme is widely used in performing the time evolution of GR-MHD.

For the illustration, we can take the $\mu = 0$ component of Equation (1.24) in the one dimensional

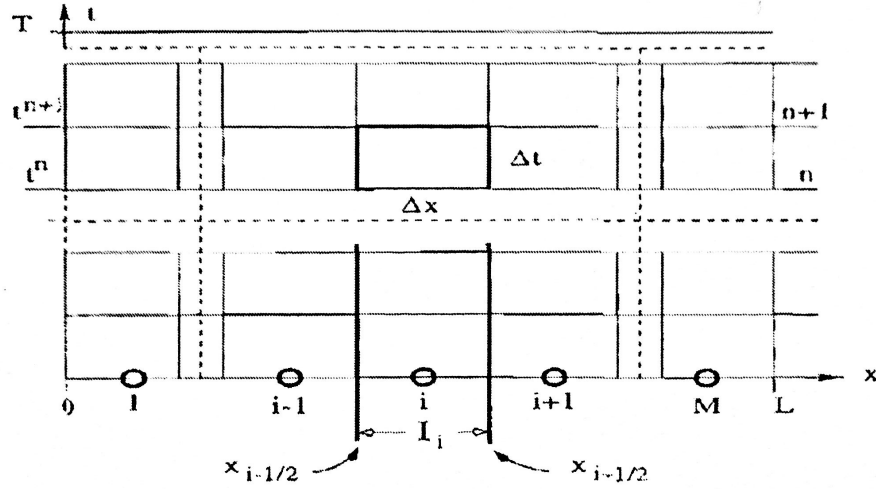


Figure 3.1: The mesh grid sketch for the illustration of Godunov's scheme (see text for the detail) adopted from the "Lecture Notes for the COMPSTAR School on Computational Astrophysics," August 10, 2010 by Olindo Zanotti & Gian Mario Manca.

case with the 0th component denoting time and the 1st component denoting position,

$$\partial_t(\sqrt{-g}T^{00}) + \partial_x(\sqrt{-g}T^{01}) = 0. \quad (3.1)$$

This is a partial differential equation made of the conserved variable $\sqrt{-g}T^{00}$, hereafter U , and its flux $\sqrt{-g}T^{01}$, hereafter F . Equation (3.1) can then be written as

$$\partial_t U + \partial_x F = 0. \quad (3.2)$$

The variables $U(x, t)$ and $F(x, t)$ are position dependent and time dependent. Now we discretize the spatial domain into N computing cells $I_i = [x_{i-1/2}, x_{i+1/2}]$, so each cell has the size $\Delta x = x_{i+1/2} - x_{i-1/2}$ with $i = 1, \dots, N$. A time forwarding step $\Delta t > 0$ is defined by $\Delta t = t^{n+1} - t^n$. We now focus on the physical equation in the "control volume" $V \equiv I_i \times [t^n, t^{n+1}]$ as shown in Figure 3.1. If we integrate Equation (3.2) first over I_i

$$\frac{d}{dt} \int_{x_{i-1/2}}^{x_{i+1/2}} U(x, t) dx = F(x_{i-1/2}, t) - F(x_{i+1/2}, t), \quad (3.3)$$

and then over the time interval Δt

$$\int_{x_{i-1/2}}^{x_{i+1/2}} U(x, t^{n+1}) dx = \int_{x_{i-1/2}}^{x_{i+1/2}} U(x, t^n) dx + \int_{t^n}^{t^{n+1}} F(x_{i-1/2}, t) dt - \int_{t^n}^{t^{n+1}} F(x_{i+1/2}, t) dt, \quad (3.4)$$

we then obtain the integral form of Equation (3.2). To execute the integral over time via numerical simulation, we need to write Equation (3.4) in discrete form. By defining the average of U in the cell

$$U_i^n = \frac{1}{\Delta x} \int_{x_{i-1/2}}^{x_{i+1/2}} U(x, t^n) dt \quad (3.5)$$

and the average of F in the time interval Δt

$$F_{i\pm 1/2} = \frac{1}{\Delta t} \int_{t^n}^{t^{n+1}} F(x_{i\pm 1/2}, t) dt, \quad (3.6)$$

we can finally rewrite Equation (3.2) as

$$U_i^{n+1} = U_i^n + \frac{\Delta t}{\Delta x} (F_{i-1/2} - F_{i+1/2}). \quad (3.7)$$

The average conserved variable U at time t^{n+1} can then be calculated by Equation (3.7). The average of the conserved variable defined by Equation (3.5) is called “piece-wise constant” (see also Martí & Müller 1999, Komissarov 1999 and the lecture notes for the COMPSTAR school on computational astrophysics¹). Readers might have already found that Equation (3.7) itself is an exact mathematical expression with no approximation. Nevertheless, $F(x, t)$ is usually a function of the primitive variables (non-conserved variables like density, velocity, etc., see later) that can be obtained by conserved variables like $U(x, t)$ in practice. Thus, we do not possess the knowledge of $F(x, t)$ in $t \in [t^n, t^{n+1}]$ since it depends on the knowledge of $U(x, t)$ in $t \in [t^n, t^{n+1}]$, which again requires the integral of $F(x, t)$ towards the future. Together with the fact that U becomes discontinuous on the cell board because of the piece-wise method, $F_{x_{i\pm 1/2}}$ values are usually approximated (see Section 3.1.2). When the integrals of flux $F(x, t)$ over time in Equation (3.6) are approximated by certain methods, Equation (3.7) becomes indeed a numerical scheme – “Godunov scheme,” which is the basic equation of the time numerical evolution in rHARM.

As an important remark for the Godunov scheme, the time interval Δt that is allowed must satisfy

$$\Delta t \leq \frac{\Delta x}{|v_{max}^n|} \quad (3.8)$$

to keep the causality for a step forward time evolution, where v_{max}^n , composed by the sum of flow speed and sound speed, presents the maximum wave velocity through the computational domain at time t^n . In rHARM, the time step constraint is controlled by both Equation (3.8) and the resistive time scale Equation (3.34).

3.1.2 The approximate flux on the cell board

As has been mentioned in Section 3.1.1, the flux terms $F_{i\pm 1/2}$ in Equation (3.7) need to be approximated by certain methods. The time integral in Equation (3.6) can be easily approximated by $F_{i\pm 1/2} = F(x_{i\pm 1/2}, 0)$ which holds well when Δt is small. $F(x_{i\pm 1/2}, 0)$ depends on the conserved variable U on cell boards. But because of the piece-wise method applied in Equation (3.5), we only have the information of the average U of each cell which forms a discontinuous distribution as shown in Figure 3.2. The flux on the board can then be solved by approximate Riemann

¹Lecture Notes for the COMPSTAR School on Computational Astrophysics, August 10, 2010 by Olindo Zanotti & Gian Mario Manca

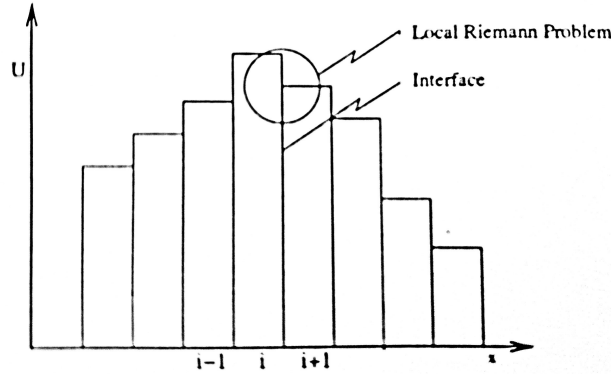


Figure 3.2: An example of the discontinuous distribution of the conserved variable U caused by the piece-wise constant method. This Figure is adopted from the “Lecture Notes for the COMPSTAR School on Computational Astrophysics,” August 10, 2010 by Olindo Zanotti & Gian Mario Manca.

solvers. Typical approximate Riemann solvers can be divided into two types: approximate state Riemann solvers, where $U(x_{i\pm 1/2}, t)$ is first solved to evaluate $F(x_{i\pm 1/2}, t)$, and approximate flux Riemann solvers, where an approximation is given to the flux directly without computing the state $U(x_{i\pm 1/2}, t)$. In rHARM, the solver of the latter type is employed.

To illustrate the solver, let us focus on the board between cell $i-1$ and i in Figure 3.1 and redefine the coordinates $x_{i-1} = x_L$, $x_i = x_R$ and $x_{i-1/2} = 0$, as shown in Figure 3.3 left plot. We ignore the occurrence of rarefaction waves and assume that both nonlinear waves are shock waves. The solid lines originate from $(0, 0)$ point in the plot representing the propagation path of the sound waves in the left and right directions with velocities $S_L = v_L - a_L$ and $S_R = v_R + a_R$, respectively. Here, v is the flow velocity and a presents the sound speed. The time t^n is set to 0 and $t^{n+1} = T$. Thus, the control volume is now $V \equiv [x_{i-1}, x_i] \times [0, T]$. The state in this volume can be divided like in Figure 3.3 right plot. The two regions that are untouched by the shock waves have their original states from cell $i-1$ and i denoted by U_L and U_R . The state of the region in the middle influenced by the shock is denoted by U_{HLL} (HLL stands for Harten, Lax and van Leer, who were the contributors of this solver). The fluxes from left to right are then F_L , F_{HLL} and F_R .

Applying Equation (3.3) to the region $[x_L, 0]$, yields

$$\frac{d}{dt} \int_{x_L}^{x_0} U(x, t) dx = F(x_L, t) - F(0, t). \quad (3.9)$$

According to the discontinuity in Figure 3.3, the right hand side of this equation can be split as

$$\frac{d}{dt} \int_{x_L}^{x_0} U(x, t) dx = \frac{d}{dt} \int_{x_L}^{TS_L} U(x, t) dx + \frac{d}{dt} \int_{TS_L}^0 U(x, t) dx. \quad (3.10)$$

Applying the formula

$$\frac{d}{dt} \int_{x_1(t)}^{x_2(t)} f(x, t) dx = \int_{x_1(t)}^{x_2(t)} \frac{\partial f(x, t)}{\partial t} dx + f(x_2(t), t) \frac{dx_2(t)}{dt} - f(x_1(t), t) \frac{dx_1(t)}{dt}. \quad (3.11)$$

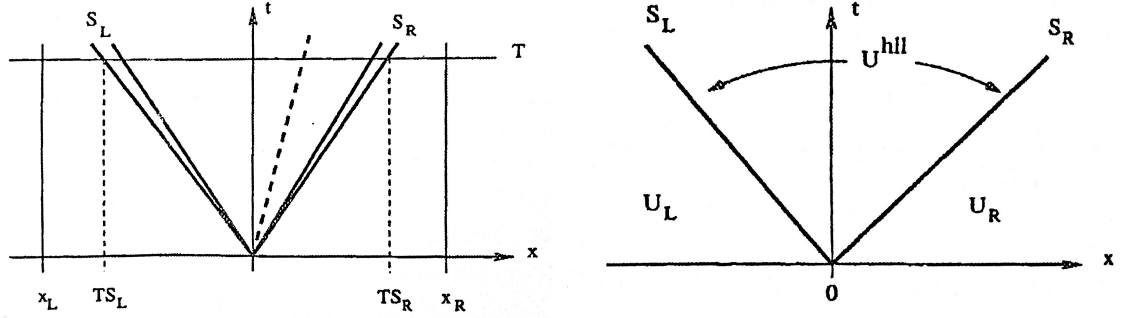


Figure 3.3: *Left:* Control volume for the computation of the approximate HLL flux. *Right:* The average of U in different regions divided by the shock wave propagation in two directions. Both plots are adopted from the “Lecture Notes for the COMPSTAR School on Computational Astrophysics,” August 10, 2010 by Olindo Zanotti & Gian Mario Manca.

to Equation (3.10), yields

$$\begin{aligned} \frac{d}{dt} \int_{x_L}^{TS_L} U(x, t) dx &= \int_{x_L}^{TS_L} \frac{\partial U(x, t)}{\partial t} dx + U(TS_L^-, t) S_L^-, \\ \frac{d}{dt} \int_{TS_L}^0 U(x, t) dx &= \int_{TS_L}^0 \frac{\partial U(x, t)}{\partial t} dx - U(TS_L^+, t) S_L^+, \end{aligned} \quad (3.12)$$

where S_L^- and S_L^+ stands for the left and right limit for the sound velocity S_L at $x = TS_L$. With the result in Equation (3.12), Equation (3.9) can be written as

$$\begin{aligned} F(x_L, t) - F(0, t) &= U(TS_L^-, t) S_L^- - U(TS_L^+, t) S_L^+ \\ &+ \int_{x_L}^{TS_L} \frac{\partial U(x, t)}{\partial t} dx + \int_{TS_L}^0 \frac{\partial U(x, t)}{\partial t} dx. \end{aligned} \quad (3.13)$$

The points (x_L, t) and (TS_L^-, t) are always in the left region uninfluenced by the shock wave, so $F(x_L, t) = F_L$ and $U(TS_L^-, t) = U_L$. The points $(0, t)$ and (TS_L^+, t) are always inside the shock region, thus $F(0, t) = F_{\text{HLL}}$ and $U(TS_L^+, t) = U_{\text{HLL}}$. If the time interval T is small enough, the partial integrals in Equation (3.13) vanish. Assuming $S_L^- \simeq S_L^+ = S_L$ and meanwhile keeping the difference between U_L and U_{HLL} , Equation (3.13) becomes

$$F_{\text{HLL}} = F_L + S_L(U_{\text{HLL}} - U_L). \quad (3.14)$$

Equation (3.14) is a variation of the Rankine-Hugoniot condition which connects states and fluxes across a discontinuity (in this case at $x = x_L$). The same procedure from Equation (3.9) to (3.14) can also be applied to the right propagation wave S_R to get

$$F_{\text{HLL}} = F_R + S_R(U_{\text{HLL}} - U_R). \quad (3.15)$$

Finally, if we combine Equations (3.14) and (3.15) to eliminate U_{HLL} , which we want to avoid from the beginning, we obtain the HLL flux

$$F_{\text{HLL}} = \frac{S_R F_L - S_L F_R + S_L S_R (U_R - U_L)}{S_R - S_L} \quad (3.16)$$

(see also the lecture notes for the COMPSTAR school on computational astrophysics ²). Do not forget that F_{HLL} in Equation (3.16) is $F_{i-1/2}$ in Equation (3.7). The Godunov scheme described in Section 3.1.1 can work for cell i once the $F_{i+1/2}$ is found by the same method described in this Section. In this thesis, we have applied a variation of F_{HLL} , which is called Lax-Friedrichs flux, to rHARM, in order to improve the efficiency of the simulations. By assuming $S_L = -S_R = S$, the Lax-Friedrichs flux is expressed by

$$F_{\text{LAXF}} = \frac{1}{2} [F_L + F_R - S (U_R - U_L)]. \quad (3.17)$$

3.1.3 Primitive variables and the inversion scheme

In case of rHARM, primitive variables are those variables like density, velocity, internal energy, etc. (see Section 3.2.3), which compose the expressions of the conserved variables (see Section 3.2.1). They are not evolved by Equation (3.7), with the exception of some variables which are both conservative and primitive, as we will see in Section 3.2.1. Furthermore, primitive variables are needed for the calculation of the fluxes in Equation (3.7) (see Section 3.2.1). Thus, after a time evolution of conserved variables or in other words, before the beginning of the next time evolution of conserved variables, we need to calibrate primitive variables as described by flow chart in Figure 3.4. The expressions of conserved variables as functions of primitive variables are explicit. Nevertheless, primitive variables can seldom be expressed by conserved variables explicitly. For this reason, a whole scheme is usually used in a conservative code to inverse conserved variables to primitive variables. The inversion scheme in rHARM is the core of the code, which I will illustrate in detail in Section 3.2.3.

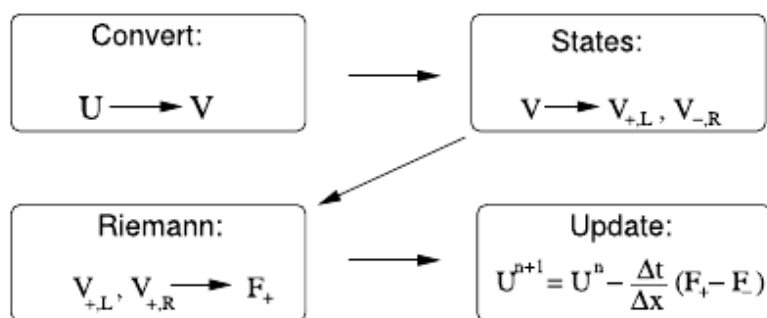


Figure 3.4: A flow chart for the basic structure of rHARM as a conservative scheme. Before the start of the next time evolution over conserved variables, primitive variables which determine the flux on the cell board mentioned in Section 3.1.2 need to be updated from the current conserved variables. Credit: Mignone et al. (2007).

²Lecture Notes for the COMPSTAR School on Computational Astrophysics, August 10, 2010 by Olindo Zanotti & Gian Mario Manca

3.2 Implementation of magnetic resistivity

In the following section, I will derive the equations of resistive MHD in general relativity that are implemented in the existing ideal GR-MHD code HARM (Gammie et al. 2003; Noble et al. 2006). As the core of rHARM, the inversion scheme that is used in the code will also be illustrated in detail. The derivations follow Bucciantini & Del Zanna (2013), who have also implemented resistivity in their code ECHO. Significant changes to HARM had to be made, such as implementing new variables to describe the electric field and the magnetic diffusivity. The metric g that will be used in the derivations refers to the definition of the Kerr metric in Section 1.3.3. The notation in this section follows the convention mentioned in Section 1.6. In order to avoid confusion, it needs to be specified that the sign convention in the definition of the Levi-Civita tensors (see Equation 1.35) in these section follows Misner et al. (1973), which differs from the convention used in Bucciantini & Del Zanna (2013) (see Section 3.2.1).

3.2.1 The general form of GR-MHD equations

Like in HARM, rHARM applies the two observer frames that are defined by the co-moving observer, u^μ , and the normal observer, n^μ . The spacetime of the normal observer is split into the so called “3+1” form (see Appendix A.2). The electric and the magnetic four vectors that are measured in the two frames are denoted by e^μ , b^μ and \mathcal{E}^μ , \mathcal{B}^μ , respectively. For the normal observer frame we follow Noble et al. (2006) with the normal observer four velocity $n_\mu = (-\alpha, 0, 0, 0)$ and the lapse time $\alpha = 1/\sqrt{-g^{tt}}$.

As a conservative scheme, the time evolution in rHARM follows the description in Section 3.1.1 and 3.1.2, except that it evolves eleven conserved variables simultaneously, instead of only one as in the example. The time evolution of these eleven variables is then governed by eleven equations. Correspondingly, these equations consider the conservation of mass, energy, momentum and the evolution of the electric and the magnetic field. Among these eleven equations only the equation for mass conservation can be taken from HARM,

$$\frac{1}{\sqrt{-g}}\partial_\mu(\sqrt{-g}\rho u^\mu) = 0, \quad (3.18)$$

with $g \equiv \det(g_{\mu\nu})$ and the mass density ρ . The equations considering the conservation of energy-momentum keep their general form,

$$\partial_t(\sqrt{-g}T^t_\mu) + \partial_i(\sqrt{-g}T^i_\mu) = \sqrt{-g}T^\kappa_\lambda \Gamma^\lambda_{\mu\kappa}, \quad (3.19)$$

where $\Gamma^\lambda_{\mu\kappa}$ is the metric connection defined by Equation (1.19) and T^μ_ν is the stress-energy tensor consisting of a fluid part and an electromagnetic (EM) part,

$$T^{\mu\nu} = T^{\mu\nu}_{\text{fluid}} + T^{\mu\nu}_{\text{EM}}. \quad (3.20)$$

Here, a difference to the ideal GR-MHD equations arises. The general definition for $T^{\mu\nu}_{\text{EM}}$ is

$$T^{\mu\nu}_{\text{EM}} = F^{\mu\alpha}F^\nu_\alpha - \frac{1}{4}g^{\mu\nu}F_{\alpha\beta}F^{\alpha\beta}. \quad (3.21)$$

For the ideal GR-MHD version of $T_{EM}^{\mu\nu}$ I refer to [Gammie et al. \(2003\)](#). For the resistive case, the $T_{EM}^{\mu\nu}$ needs to consider the electric field, thus, to implement the anti-symmetric Faraday tensor,

$$\begin{aligned} F^{\mu\nu} &= u^\mu e^\nu - e^\mu u^\nu + \epsilon^{\mu\nu\lambda\kappa} u_\lambda b_\kappa \\ F_{\mu\nu} &= u_\mu e_\nu - e_\mu u_\nu + \epsilon_{\mu\nu\lambda\kappa} u^\lambda b^\kappa \end{aligned} \quad (3.22)$$

in $T_{EM}^{\mu\nu}$. The $\epsilon_{\mu\nu\lambda\kappa}$ in the equations are the Levi-Civita tensors defined in Section 1.6. For u^μ , we may use the four velocity of an arbitrary observer, while e^μ and b^μ , respectively, are the electric and the magnetic field measured in this observer's frame. Similar equations hold for the dual Faraday tensor $*F^{\mu\nu}$. After some lengthy algebra (for derivation, please see Appendix A.5), we have for the electromagnetic energy-momentum tensor

$$T_{EM}^{\mu\nu} = (b^2 + e^2) \left(u^\mu u^\nu + \frac{1}{2} g^{\mu\nu} \right) - b^\mu b^\nu - e^\mu e^\nu - u_\lambda e_\beta b_\kappa \left(u^\mu \epsilon^{\nu\lambda\beta\kappa} + u^\nu \epsilon^{\mu\lambda\beta\kappa} \right), \quad (3.23)$$

which is in agreement with [McKinney \(2006\)](#). In order to avoid confusion, it needs to be specified that the sign convention in the definition of the Levi-Civita tensors in the equations here follow [Misner et al. \(1973\)](#), which differs from the convention used in [Bucciantini & Del Zanna \(2013\)](#). Eventually, the stress-energy tensor that I apply in rHARM becomes

$$\begin{aligned} T^{\mu\nu} &= (\rho + u + p + b^2 + e^2) u^\mu u^\nu + \left(p + \frac{1}{2} (b^2 + e^2) \right) g^{\mu\nu} \\ &\quad - b^\mu b^\nu - e^\mu e^\nu - u_\lambda e_\beta b_\kappa \left(u^\mu \epsilon^{\nu\lambda\beta\kappa} + u^\nu \epsilon^{\mu\lambda\beta\kappa} \right). \end{aligned} \quad (3.24)$$

Here, u is the internal energy, p denotes the gas pressure and $b^2 = b^\mu b_\mu$, $e^2 = e^\mu e_\mu$.

In rHARM, both the electric and the magnetic field are evolved in the normal observer frame. The evolution of the magnetic field four vector follows from the Maxwell equation,

$$\partial_i (\sqrt{-g} *F^{it}) = -\partial_i (\sqrt{-g} *F^{ij}), \quad (3.25)$$

and the constraint

$$\partial_i (\sqrt{-g} *F^{it}) = 0. \quad (3.26)$$

Similar to the modification of the stress-energy tensor, the complete form of the dual Faraday tensor,

$$*F^{\mu\nu} = -u^\mu b^\nu + b^\mu u^\nu + \epsilon^{\mu\nu\lambda\kappa} u_\lambda e_\kappa, \quad (3.27)$$

is required for the EM field evolution here.

With the definition $\mathcal{B}^i \equiv n_\nu *F^{\nu i} = \alpha *F^{it}$ and $\mathcal{B}^0 \equiv n_\nu *F^{\nu t} = 0$, a direct relation follows between the $*F^{it}$ and the magnetic field four vector \mathcal{B}^μ , which is the magnetic field in the normal observer's frame. Similarly, the electric field four vector is defined by $\mathcal{E}^i \equiv n_\nu F^{i\nu} = -\alpha F^{it}$, while $\mathcal{E}^0 = 0$. In order to present the equations more comprehensively, we will use \mathcal{B}^μ , \mathcal{E}^μ for the theoretical derivation instead of $*F^{it}$, $-F^{it}$, which are actually used in rHARM. The time evolution of the electric field four vector \mathcal{E}^μ follows from

$$\gamma^{-1/2} \partial_t (\gamma^{1/2} \mathcal{E}) - \nabla \times (\alpha \mathcal{B} - \boldsymbol{\beta} \times \mathcal{E}) + (\alpha \mathbf{v} - \boldsymbol{\beta}) = -\alpha \Gamma [\mathcal{E} + \mathbf{v} \times \mathcal{B} - (\mathcal{E} \cdot \mathbf{v}) \mathbf{v}] / \eta, \quad (3.28)$$

(Bucciantini & Del Zanna 2013), where $\boldsymbol{\beta} = \{\beta^i\}$ is the spatial shift vector in the 3+1 formalism, Γ denotes the Lorentz factor and $\gamma = \sqrt{-g}/\alpha$ is the determinant of its spatial 3-metric. The \mathbf{v} denotes the three velocity in the normal observer frame (see Section 3.2.3). Here a new variable enters the system of equations, specifically the resistivity or magnetic diffusivity η (see Section 3.2.2). Note that Equation (3.28) is the combination of the two Maxwell equations for the electric field

$$\begin{aligned}\gamma^{-1/2}\partial_t(\gamma^{1/2}\boldsymbol{\mathcal{E}}) - \nabla \times (\alpha\boldsymbol{\mathcal{B}} - \boldsymbol{\beta} \times \boldsymbol{\mathcal{E}}) &= -(\alpha\boldsymbol{\mathcal{J}} - q\boldsymbol{\beta}), \\ \nabla \cdot \boldsymbol{\mathcal{E}} &= q\end{aligned}\quad (3.29)$$

and the resistive condition $e^\mu = \eta j^\mu$ (see also Section 3.2.2), where q is the electric charge density, $\boldsymbol{\mathcal{J}}$ is the electric current for the normal observer and j^μ denotes the components of the electric current in the co-moving observer frame (see Bucciantini & Del Zanna 2013 for a detailed derivation).

3.2.2 Turbulent resistivity in rHARM

Essentially, two new physical quantities enter the system of equations in rHARM. These are the electric field variable (as the electric field was replaced by $\boldsymbol{E} = -\mathbf{v} \times \boldsymbol{B}$ in the ideal HARM) and the resistivity (or magnetic diffusivity) $\eta = \eta(r, \theta)$. We understand the resistivity is due to turbulence, thus is closely related to the alpha-viscosity in turbulent accretion disks (Shakura 1973; Shakura & Sunyaev 1973). In the following I will briefly motivate the use of a turbulent resistivity, mainly quoting from derivations presented by Khanna & Camenzind (1996) and Bucciantini & Del Zanna (2013).

Starting from classical Ohm's law $\boldsymbol{E} + \mathbf{v} \times \boldsymbol{B} = \eta_0 \boldsymbol{J}$ with the (microscopic) resistivity η_0 and assuming turbulent fluctuations in the velocity \mathbf{v}' , the electric field \boldsymbol{E}' , and the magnetic field \boldsymbol{B}' , mean-field averaging will lead to a revised mean electric current

$$\overline{\boldsymbol{E}} + \overline{\mathbf{v}} \times \overline{\boldsymbol{B}} = -\overline{\mathbf{v}' \times \boldsymbol{B}'} + \eta_0 \overline{\boldsymbol{J}}, \quad (3.30)$$

with the mean-field velocity and fields $\overline{\mathbf{v}}, \overline{\boldsymbol{B}}, \overline{\boldsymbol{E}}$, respectively. The term $\overline{\mathbf{v}' \times \boldsymbol{B}'}$ does not vanish, since the fluctuating quantities inside are presumably correlated. A key assumption is that this term can usually be written as a linear combination of both the mean magnetic field and its curl, namely

$$\overline{\mathbf{v}' \times \boldsymbol{B}'} = -\alpha_D \overline{\boldsymbol{B}} - \eta_t \nabla \times \overline{\boldsymbol{B}}, \quad (3.31)$$

where the two scalars α_D and η_t are isotropic coefficients and are both proportional to the local turbulent correlation time. With this assumption and dropping the bars from now on, we can rewrite Ohm's law as

$$\boldsymbol{E} + \mathbf{v} \times \boldsymbol{B} = \alpha_D \boldsymbol{B} + (\eta_t + \eta_0) \boldsymbol{J}. \quad (3.32)$$

The α_D -term may introduce exponentially growing modes and is usually known as the mean-field dynamo, while the η_t -term acts as a resistivity – a turbulent resistivity. In this thesis, I will not

consider the dynamo term (see [Bugli et al. 2014](#) for an application) further. I will mostly focus on the diffuse effect of resistivity, and also refer to it as magnetic diffusivity. In astrophysical plasma, usually $\eta_t \gg \eta_o$ so I will apply $\eta \equiv \eta_t \simeq \eta_t + \eta_o$ and write Ohm's law as $\mathbf{E} + \mathbf{v} \times \mathbf{B} = \eta \mathbf{J}$, or, in a covariant form of the equation in the co-moving frame, where $v = 0$,

$$e^\mu = \eta j^\mu. \quad (3.33)$$

The scalar η in Equation (3.33) is exactly the input diffusivity in the present version of rHARM. The ideal GR-MHD regime can be retrieved by setting $\eta = 0$, namely $e^\mu = 0$. Applying magnetic diffusivity, the numerical time stepping Δt requires consideration of the diffusive time scale on the grid scale, thus

$$\Delta t_\eta < \Delta x^2 / \eta, \quad (3.34)$$

where Δx is the smallest cell size. This turned out to be critical, especially when running the code with at relative large η , where the dynamic time scale becomes larger than the diffusive time scale.

3.2.3 The inversion scheme

Precisely, rHARM uses the following set of conserved variables

$$\mathbf{U} \equiv \sqrt{-g}(D, T^t, T^t_i, {}^*F^{it}, -F^{it}), \quad (3.35)$$

where $D \equiv \rho u^t$. $T^{\mu\nu}$ and T^t_ν are related by $T^t_\nu = g_{\nu\alpha} T^{\mu\alpha}$.

The time evolution of \mathbf{U} is performed by using the equations derived in the previous section. These equations are written in the so-called conserved form, for which the time derivative of the variable depends on the position derivative of its ‘‘flux’’. To model these fluxes \mathbf{F} for \mathbf{U} across the surfaces of the simulation cells, an additional set of so-called ‘‘primitive’’ variables is needed. Similar to the ideal HARM, the ‘‘primitive’’ variables in rHARM are

$$\mathbf{P} = (\rho, u, v^i, {}^*F^{it}, -F^{it}) \quad (3.36)$$

where ρ stands for density, u for internal energy, and v^i for the spatial 3-velocity for the normal observer. The ${}^*F^{it}$ and $-F^{it}$ are related to the magnetic and the electric four vectors for the normal observer by a factor of α (see Section 3.2.1) and they are both conserved as well as primitive variables.

As discussed in [Gammie et al. \(2003\)](#), the variables $\mathbf{U}(\mathbf{P})$ and $\mathbf{F}(\mathbf{P})$ can be expressed as analytic functions of primitive variables, but the inverse operations do not have a closed-form. Therefore, the numerical inversion scheme to extract \mathbf{P} from \mathbf{U} at each time step after the evolution of \mathbf{U} is the core of a conservative GR-MHD code.

The resistive term in Equation (3.28) could become *stiff* ([Bucciantini & Del Zanna 2013](#)), as we usually deal with a small resistivity $\eta \lesssim 10^{-2}$. Unfortunately, the stiff term also contains \mathcal{E} , which

makes \mathcal{E} impossible to evolve in time simultaneously with other conserved variables. Therefore, its solution has to be found by some *implicit* scheme, e.g. together with primitive variables, and the inversion scheme used in ideal GR-MHD HARM must be emended in rHARM under the resistive context.

Following [Noble et al. \(2006\)](#), it is convenient to project the energy-momentum density into normal observer frame

$$Q^\mu \equiv -n_\nu T^{\mu\nu}, \quad (3.37)$$

together with the projection tensors $j_{\mu\nu} = g_{\mu\nu} + n_\mu n_\nu$, and the energy-momentum flux perpendicular to the normal observer can be described by $\tilde{Q}^\mu = j^\mu_\nu Q^\nu$. \tilde{Q}^μ is a four vector with its zeroth component always being zero, and we note it as \tilde{Q}^i . Also, we define $U \equiv -Q_\mu n^\mu = \alpha^2 T^{00}$. Obviously, \tilde{Q}^i and U inherit the information from conserved variables T^t_μ .

With the Lorentz factor Γ , W is defined by $W \equiv (\rho + p + u)\Gamma^2$. The flow velocity relative to the normal observer is denoted by $\tilde{v}^i = j^i_\mu u^\mu$ and $v_i = \tilde{v}^i/\Gamma$, $v^2 \equiv v_i v^i$. Γ is a function of v^2 where $\Gamma^2 = 1/(1 - v^2)$. The gas pressure p is a function of v^2 and W depending on the equation of state, which is $u = p/(\gamma_{\text{gas}} - 1)$ in rHARM.

The variables to be solved by the inversion scheme are ρ , v^i and \mathcal{E}^i . The relation between the conserved variables and ρ , v^i is given (with help of the above definitions) by

$$\begin{aligned} D &= \rho\Gamma \\ \tilde{\mathcal{Q}} &= W\mathbf{v} + \mathcal{E} \times \mathcal{B} \\ U &= W - p + (\mathcal{E}^2 + \mathcal{B}^2)/2 \end{aligned} \quad (3.38)$$

([Noble et al. 2006](#); [Del Zanna et al. 2007](#)). The ideal GR-MHD regime is retrieved by replacing the vector \mathcal{E} with $-v \times \mathcal{B}$. However, in the resistive case, \mathcal{E} needs to be solved separately. Rewriting Equation (3.28) into the numerical form, the relation between \mathcal{E}^i and other variables is ([Bucciantini & Del Zanna 2013](#))

$$\mathcal{E}^i = \{\epsilon^{ijk} \tilde{v}_j \mathcal{B}_k + \tilde{\eta}[N^i + (N^k \tilde{v}_k \tilde{v}^i)/(1 + \tilde{\eta}\Gamma)]\}/(\Gamma + \tilde{\eta}), \quad (3.39)$$

where

$$N^i = \mathcal{E}^{i(0)} + \Delta t[-(\alpha v^i - \beta^i)\gamma^{-1/2}\partial_k(\gamma^{1/2}\mathcal{E}^{k(0)}) - \epsilon^{ijk}\partial_j(\alpha\mathcal{B}_k - \epsilon_{klm}\beta^l\mathcal{E}^m)]. \quad (3.40)$$

The expression $\tilde{\eta}$ is defined by $1/\tilde{\eta} = \Delta\alpha/\eta$. The N^i comes from the *none-stiff* term, which does not include η , and hence can be solved explicitly. The $\mathcal{E}^{i(0)}$ and $\mathcal{E}^{k(0)}$ denote the electric field four vector from the last time step. The sign flip preceding ϵ^{ijk} , in comparison to [Bucciantini & Del Zanna \(2013\)](#), is due to the different definitions of Levi-Civita tensor as mentioned above.

[Noble et al. \(2006\)](#) have suggested a way to combine Equation (3.38) (under the condition $\mathcal{E} = -v \times \mathcal{B}$) into an equation system with two equations of only conserved variables, W and v^2 . This equation system can eventually be solved by a 2-dimensional Newton-Raphson (NR) method

(see Appendix A.6). We keep this feature in our inversion scheme and combined Equation (3.38) by calculating $\tilde{Q}^2 = \tilde{Q}^i \tilde{Q}_i$

$$\begin{aligned}\tilde{Q}^2 &= (W\mathbf{v} + \mathcal{E} \times \mathcal{B})^2 \\ &= W^2 v^2 + (\mathcal{E} \times \mathcal{B})^2 - 2W\mathcal{E} \cdot (\mathbf{v} \times \mathcal{B}).\end{aligned}\quad (3.41)$$

To eliminate \mathbf{v} , it is useful to calculate

$$\tilde{Q} \times \mathcal{B} = W\mathbf{v} \times \mathcal{B} + (\mathcal{E} \times \mathcal{B}) \times \mathcal{B}, \quad (3.42)$$

which gives the relation

$$\mathbf{v} \times \mathcal{B} = W^{-1}[\tilde{Q} \times \mathcal{B} - (\mathcal{E} \times \mathcal{B}) \times \mathcal{B}]. \quad (3.43)$$

Inserting this into Equation (3.41), and using some simple algebra we obtain

$$\tilde{Q}^2 = v^2 W^2 - (\mathcal{E} \times \mathcal{B})^2 - 2\mathcal{E} \cdot (\tilde{Q} \times \mathcal{B}). \quad (3.44)$$

Since p is a function of v^2 and W , the last equation in Equation (3.38) already satisfies the requirement and together with Equation (3.44), they give an equation system that only consists of conserved variables, v^2 and W

$$\begin{aligned}\tilde{Q}^2 - v^2 W^2 + (\mathcal{E} \times \mathcal{B})^2 + 2\mathcal{E} \cdot (\tilde{Q} \times \mathcal{B}) &= 0, \\ U - W + p(v^2, W) - \frac{1}{2}(\mathcal{E}^2 + \mathcal{B}^2) &= 0.\end{aligned}\quad (3.45)$$

For a given \mathcal{E} , Equation 3.45 can be solved by a 2D NR-method. Once v^2 and W are solved, ρ , u and v^i can be retrieved by

$$\begin{aligned}\rho &= D(1 - v^2)^{1/2} \\ v^i &= W^{-1}[\tilde{Q}^i - \mathcal{E} \times \mathcal{B}^i], \\ u &= p/(\gamma_{\text{gas}} - 1).\end{aligned}\quad (3.46)$$

Nevertheless, \mathcal{E} does not evolve with other conserved variables and cannot be considered as *given* at the beginning of the inversion scheme. We solve this problem by considering an extra loop, which specifically makes \mathcal{E} converge. In sum, the inversion scheme to extract the primitive variables from the conserved variables in rHARM follows the steps below.

1. Take the conserved variables after a new time evolution, except the \mathcal{E} that is taken from the former time step (or initial time step).
2. Apply them to the two equations in Equation (3.45) and solve for the primitive variables u , v^i with the 2D NR scheme.
3. Renew \mathcal{E} with the solution obtained in step 2 using Equation (3.39).
4. Repeat step 2 and step 3 until W , v^2 and \mathcal{E} converge.

5. Calculate the primitive variables using Equation (3.46).

Since this inversion scheme uses a 2D Newton-Raphson method with an additional extra loop over \mathcal{E} , we find it convenient to denote it by the term *2D+1 scheme*. Note that in ideal HARM, a series of inversion schemes had been included (see Noble et al. 2006), from which we only revised the 2D scheme, no other inversion scheme works in rHARM for now. A schematic flow chart with a description of the numerical procedures for the time evolution in rHARM is shown in Section 3.2.5.

3.2.4 A preliminary test of the implementation

The implementation of the electric field can be tested by running rHARM with $\eta \rightarrow 0$ (I used $\eta = 10^{-12}$), comparing the evolution of the conservative variables and the fluxes from all grid cells generated by the primitive variables for a few time steps. I find that they coincide within errors of 10^{-10} . I then compared the primitive variables obtained by the inversion scheme of the first time step with those obtained by the ideal HARM, finding similar accuracy. We may thus confirm the correct implementation of the new stress-energy tensor and the new inversion scheme which now also considers the electric field. Further tests of rHARM considering $\eta > 0$ will be discussed in Section 3.4 and Section 3.5.

3.2.5 Time Evolution in HARM

The ‘‘building blocks’’ for rHARM are now complete. The numerical procedures of one step in time evolution in rHARM can be then expressed by a flow chart (see Figure 3.5) with the following explanations to each step shown in the chart:

- (1) Take the primitive variables $\mathbf{P}(t_n)$ from the previous step t_n and convert them to the conserved variables $\mathbf{U}(t_n)$ (see Section 3.2.3 for the definitions of \mathbf{P} and \mathbf{U}). D can be calculated by $D \equiv \rho u^t$ as defined by Equation (3.35). The T^t_μ can be obtained with the help of Equation (3.24). The magnetic and electric fields $\alpha^* F^{it}$, $-\alpha F^{it}$ (hereafter \mathcal{B} , \mathcal{E} , see Section 3.2.1) are already provided, since they are both conserved and primitive variables.
- (2) Evolve the conserved variables from $\mathbf{U}(t_n)$ to $\mathbf{U}(t_{n+1})$ (except \mathcal{E}). To do so, we first need to calculate the flux of $\mathbf{U}(t_n)$. Knowing \mathbf{P} , the flux of $D \equiv \rho u^t$ is ρu^i and the fluxes of T^t_μ are T^i_μ , which can be obtained from Equation (3.24). The flux of \mathcal{B}^i is $*F^{ij}$, defined by Equation (3.27). The D , T^t_μ , $*F^{it}$ are then evolved through Equations (3.18), (3.19) and (3.25) advancing dt_n in time. The evolution of the electric field \mathcal{E} is implicit, and hence cannot be evolved with other conserved variables. Still the ‘‘non-stiff part’’ (N^i in Equation 3.40) is a function of only $\mathbf{P}(t_n)$, and is therefore calculated using the primitive variables from the time step t_n .

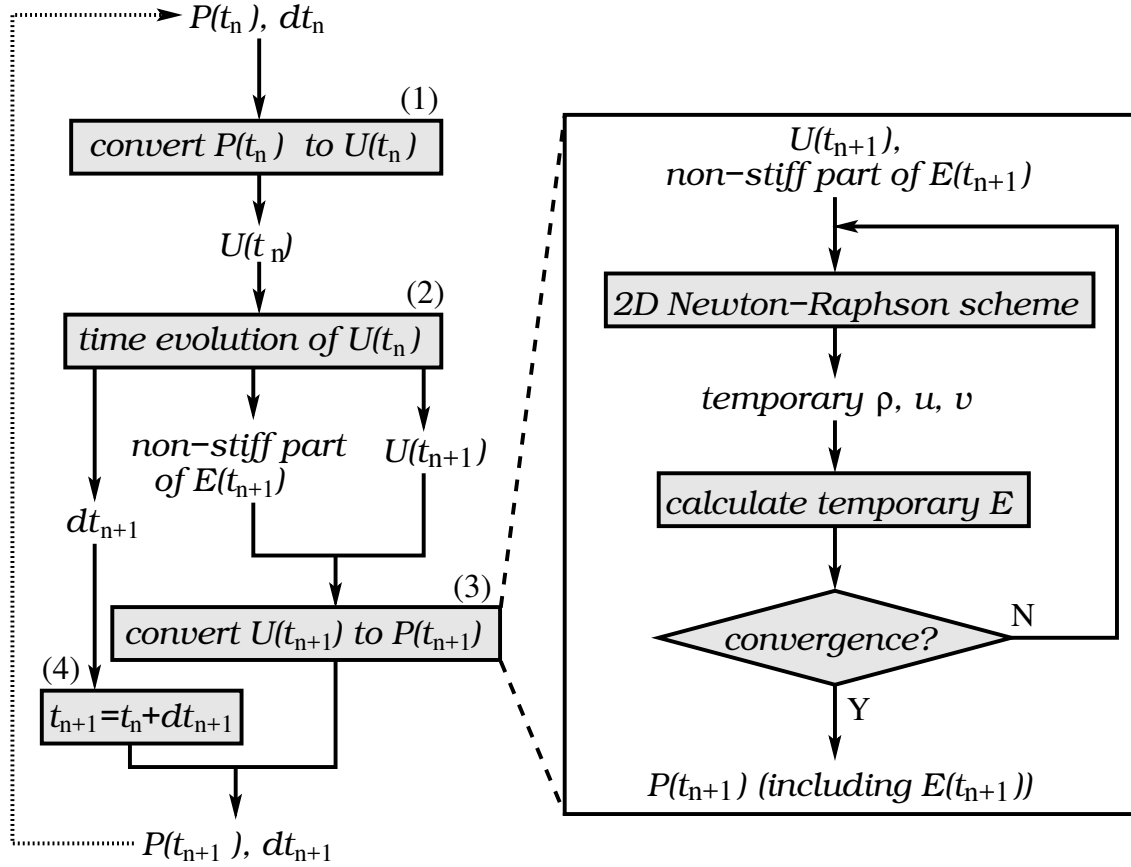


Figure 3.5: The flow chart describing the numerical procedure of one time evolution in rHARM. Boxes with a grey background denotes one or a series of routines that achieve the function written inside those boxes. The flow chart on the left hand side presents the procedure of one time evolution while the large box on the right hand side is a detailed flow description for the process inside the box (3) on the left hand side. See the text for explanations of each step in the chart.

- (3) Apply $U(t_{n+1})$ and the non-stiff part of $\mathcal{E}(t_{n+1})$ to the inversion scheme in order to extract $\mathbf{P}(t_{n+1})$ and the complete $\mathcal{E}(t_{n+1})$. As discussed above (see Section 3.2.3), we first use $U(t_{n+1})$, except the electric field that is taken from the previous time step, namely, $\mathcal{E}(t_n)$. We use the two equations in Equation (3.45) and solve for the temporary primitive variables u, v^i by applying the 2D Newton-Raphson scheme. We update \mathcal{E} using Equation (3.39) with the temporary primitive variables just obtained. We return the temporary \mathcal{E} and the temporary primitive variables back to the 2D Newton-Raphson scheme, and repeat this process until the primitive variables and \mathcal{E} converge. The converged primitive variables and \mathcal{E} are now $\mathbf{P}(t_{n+1})$ and $\mathcal{E}(t_{n+1})$.
- (4) The new time interval dt is calculated considering also the diffusion time scale (see Section 3.2.2), together with $\mathbf{P}(t_{n+1})$ (including $\mathcal{E}(t_{n+1})$ as primitive variables). We finally arrive at the evolutionary time step ($t_n \rightarrow t_{n+1}$).

To make the flow chart in Figure 3.5 look methodical, I simplify the time evolving loop that is executed in rHARM. However no structural changes are made at this point. The actual time

evolution in rHARM keeps the simple first-second scheme built in ideal HARM, where the flux for the time forwarding Δt is calculated by the primitive variables from $\Delta t/2$. In general, the time evolution of the conserved variables can be written in the form

$$\begin{aligned}\partial t \mathbf{U} &= K(\mathbf{U}, \mathcal{E}), \\ \partial t \mathcal{E} &= G(\mathbf{U}, \mathcal{E}) + \frac{1}{\eta} R(\mathbf{U}, \mathcal{E}).\end{aligned}\quad (3.47)$$

In the case of rHARM, the first equation is responsible for the evolution of conserved variables except for electric field variables, and the second equation only for the evolution of electric field variables. The structure of function K depends on corresponding relations in Equations (3.18), (3.19) and (3.25), while the structures of functions G and R depend on the relation in Equation (3.28). According to the definition of conserved variables in Section 3.2.1, K , G and R are functions of primitive variables in Equation (3.36). But we know that the primitive variables are calibrated through the knowledge of conserved variables (see Section 3.2.3), thus we can write K , G and R as functions of \mathbf{U} and \mathcal{E} . If we denote the indices at the initial state (outcomes from the last time evolution), the half time step and the complete time step as n , $n + 1/2$ and $n + 1$, respectively, and take Δt as the time interval of the time evolution, then the simple first-second scheme used in the time evolution in rHARM can be described by going through the procedure

$$\begin{aligned}\mathbf{U}^{n+1/2} &= \mathbf{U}^n + \frac{\Delta t}{2} K(\mathbf{U}^n, \mathcal{E}^n), \\ \mathcal{E}^{n+1/2} &= \mathcal{E}^n + \frac{\Delta t}{2} G(\mathbf{U}^n, \mathcal{E}^n) + \frac{\Delta t}{2\eta} R(\mathbf{U}^{n+1/2}, \mathcal{E}^{n+1/2}), \\ \mathbf{U}^{n+1} &= \mathbf{U}^n + \frac{\Delta t}{2} K(\mathbf{U}^{n+1/2}, \mathcal{E}^{n+1/2}), \\ \mathcal{E}^{n+1} &= \mathcal{E}^n + \frac{\Delta t}{2} G(\mathbf{U}^{n+1/2}, \mathcal{E}^{n+1/2}) + \frac{\Delta t}{2\eta} R(\mathbf{U}^{n+1}, \mathcal{E}^{n+1}).\end{aligned}\quad (3.48)$$

In the context of the flow chart above, steps (1) to (3) in Figure 3.5 are actually executed two times with time interval $\Delta t/2$ and Δt for one time forwarding referring to the first two equations and the last two equations in Equation (3.48).

3.3 Other common settings in rHARM

In this section I will briefly mention the common setup for rHARM, which is used for the numerical simulations and results presentation in this thesis. I basically follow the setup in ideal HARM (Gammie et al. 2003; Noble et al. 2006) with minor additions in the boundary conditions for the electric field.

3.3.1 Units and normalization

The length unit in rHARM is set by $r_g \equiv GM/c^2$ with the condition $GM = c = 1$. The time unit is then $t_g \equiv GM/c^3$. The dimensionless Kerr parameter $a = J/M$ where $-1 \leq a \leq 1$ is defined by

the black hole angular momentum $J = jGM^2/c$. I use the notation $r_H = 1 + \sqrt{1 - a^2}$ to denote the event horizon, which varies with the black hole spin parameter a . The densities, mass fluxes and energy fluxes presented in this thesis are in the code unit.

3.3.2 Numerical grid

The numerical integrations in rHARM are carried out on a uniform grid with so-called modified Kerr-Schild coordinates: x_0, x_1, x_2, x_3 , where $x_0 = t, x_3 = \phi$ are the same as in Kerr-Schild coordinates (see Section 1.3.3), while the radial and θ coordinates are calculated by the relation:

$$\begin{aligned} r &= R_0 + e^{x_1}, \\ \theta &= \pi x_2 + \frac{1}{2}(1 - h) \sin(2\pi x_2). \end{aligned} \quad (3.49)$$

Different R_0 and $h \in [0, 1]$ will return different concentrations of grid resolution in radial and θ directions. A smaller h value indicates a better concentration in θ around equatorial plane. Except for the 1D shock tube test presented in Section 3.5, which employs a flat spacetime with uniform Cartesian coordinates, we used the modified Kerr-Schild coordinates with $R_0 = 0$ as the executing coordinates in the code for all simulations in this thesis. Without special announcement, the data results will be presented in normal Kerr-Schild coordinates. Note that for scalars, the r and θ vector components are invariant against the transfer to Boyer-Lindquist coordinates, only the time component and ϕ -component transform differently.

3.3.3 Boundary conditions and the initial condition for electric field

The outflow condition is applied at inner and outer boundaries, for which all the primitive variables are projected into the ghost zones, while inflow is forbidden at inner and outer boundaries. Both axial boundaries have a reflection condition, where the primitive variables are projected into the ghost zone with a mirror effect. Boundary conditions for the electric field have been added for rHARM, similar to those for the magnetic field³. The initial electric field is chosen to be equal to the ideal MHD value, $\mathcal{E} = -\mathbf{v} \times \mathcal{B}$. It turned out that this choice worked very well in the non-ideal GR-MHD simulations.

3.3.4 Scaling code units to reality

The code units of rHARM is determined by a factor “ κ ” in gas pressure and the “plasma β ” which is the ratio of gas pressure to the magnetic pressure. The scaling of the code units works through these two parameters as following. The motion of an arbitrary particle inside the accretion disk

³Note that for our test simulations of rHARM, a variety of geometrical setups and boundary conditions were used (see Section 3.4 and Section 3.6 for detail).

is determined together by the gravitational acceleration a_g , gas pressure gradient acceleration a_p and the acceleration by the electromagnetic force a_{em} . a_g is independent of disk density while a_p is a function of disk density. The initial magnetic field is normalized to gas pressure through plasma β , thus a_{em} is a function of density as well. In general, if we reduce κ in the simulation, the gas pressure and the magnetic field will decrease correspondingly while the gravity keeps the same. The ratios between a_g and a_p , a_{em} will then change so that the accretion system in the simulation is equivalent to a system with the same black hole mass but a lighter disk compared to the simulation with the larger κ .

As an example, assume that the relation between disk density and gas pressure satisfies

$$p = \kappa \rho^{\gamma_G}, \quad (3.50)$$

where $\gamma_G = 4/3$ is the polytropic exponent. The magnetic field strength is defined by

$$B = \sqrt{\frac{8\pi p}{\beta}} = \sqrt{\frac{8\pi(\kappa\rho^{\gamma_G})}{\beta}}. \quad (3.51)$$

If $\kappa = \kappa_1 = 1$, then

$$\begin{aligned} p_1 &= \kappa_1 \rho_1^{\gamma_G} = \rho_1^{\gamma_G}, \\ B_1 &= \sqrt{\frac{8\pi(\kappa_1 \rho_1^{\gamma_G})}{\beta}} = \sqrt{\frac{8\pi(\rho_1^{\gamma_G})}{\beta}}. \end{aligned} \quad (3.52)$$

Now we change κ to $\kappa_2 \neq 1$, the gas pressure and the magnetic pressure become

$$\begin{aligned} p_2 &= \kappa_2 \rho_1^{\gamma_G} = (f\rho_1)^{\gamma_G}, \\ B_2 &= \sqrt{\frac{8\pi(\kappa_2 \rho_1^{\gamma_G})}{\beta}} = \sqrt{\frac{8\pi[(f\rho_1)^{\gamma_G}]}{\beta}}, \end{aligned} \quad (3.53)$$

where

$$f = \frac{1}{\sqrt[\gamma_G]{\kappa_2}}. \quad (3.54)$$

On the one hand, the acceleration through gas pressure gradient $a_p \propto p$ and the acceleration by Lorentz force $a_{em} \propto B$. On the other hand, the gravitational acceleration a_g does not change from Equation 3.52 to Equation 3.53. Thus, changing κ from 1 to κ_2 is equivalent to choosing a disk density which is f times of the density when $\kappa = 1$. The simulations in Chapters 5 and 6 have $\kappa = 10^{-3}$. Apply this value to Equation 3.54, we get $f \approx 5.6 \times 10^{-3}$, hence the density in the code is 177.8 times smaller than the density with $\kappa = 1$.

Nevertheless, the meaning of ρ must be normalized to the disk mass in relation to the black hole mass, which is yet unknown. For this reason, the physical quantities like density, accretion rate and ejection rate, etc., can only be expressed in code units in the thesis.

3.4 Diffusivity tests I – gas box test

In this section, a test for the implementation of magnetic diffusivity by comparison with an analytic solution of the diffusion equation is presented. The test follows the procedure suggested by Fendt & Čemeljić (2002). A similar approach was presented by Bucciantini & Del Zanna (2013): the evolution of a self-similar current sheet. The test simulations are performed in a small, almost rectangular box of hydrostatic gas at varying distance from the black hole. The gas in the box is “heavy” and is penetrated by a “weak” magnetic field, such that dynamical effects due to Lorentz forces are negligible and the magnetic field distribution changes only by diffusion. Different levels of diffusivity (set constant in the domain) have been applied. The results are compared to the known analytic solution and a perfect match was found between the numerical and the analytical results.

3.4.1 Simulation region and boundary condition

The simulation area is chosen as a small sub-sector of the axisymmetric spherical uniform grid along the equatorial plane; it is small enough that the shape of the area is rectangular to a high degree. The size of this area extends ΔR in radius and $\Delta\theta$ in latitude, and is located at a radius r_0 . The concentration parameter is set to $h = 1$, which means the spacing in the θ direction is uniform. For $\Delta r \ll r_0$, the sector can indeed be treated as a rectangular box with $r \in [r_0 - \Delta r/2, r_0 + \Delta r/2]$, $\theta \in [\pi/2 - \Delta\theta/2, \pi/2 + \Delta\theta/2]$ and $\Delta r = r_0\Delta\theta = R$.

In the test simulations the Kerr parameter, $a = 0$ and the event horizon, in this case, is the Schwarzschild radius, $r_H = 2$. A continuous outflow boundary condition is set for all four boundaries of the box. Our simulations are denoted by *difT0*, *difT1*, *difT2*, *difT3*, and *difT4* (see Table 3.1).

3.4.2 Initial conditions

We apply a relativistic gas with polytropic index $\gamma_G = 4/3$. Initially, the gas in the box is in hydrostatic equilibrium. Both the density profile and the magnetic field profile are set to be uniform in the θ direction. In the radial direction, the density profile was set such that the pressure gradient cancels the gravity,

$$\nabla_r p(r) = -\rho(r)r^{-2}. \quad (3.55)$$

For simplicity, we have used a Newtonian potential in Equation (3.55). This choice works well for large distances from the black hole. Close to the black hole, our choice is inconsistent with GR. Specifically, a hydrostatic state no longer exists (see below). Nevertheless, these inconsistencies were small and did not significantly influence our main conclusion regarding the test of magnetic diffusivity. From Equation (3.55) we apply the following radial profiles for density and

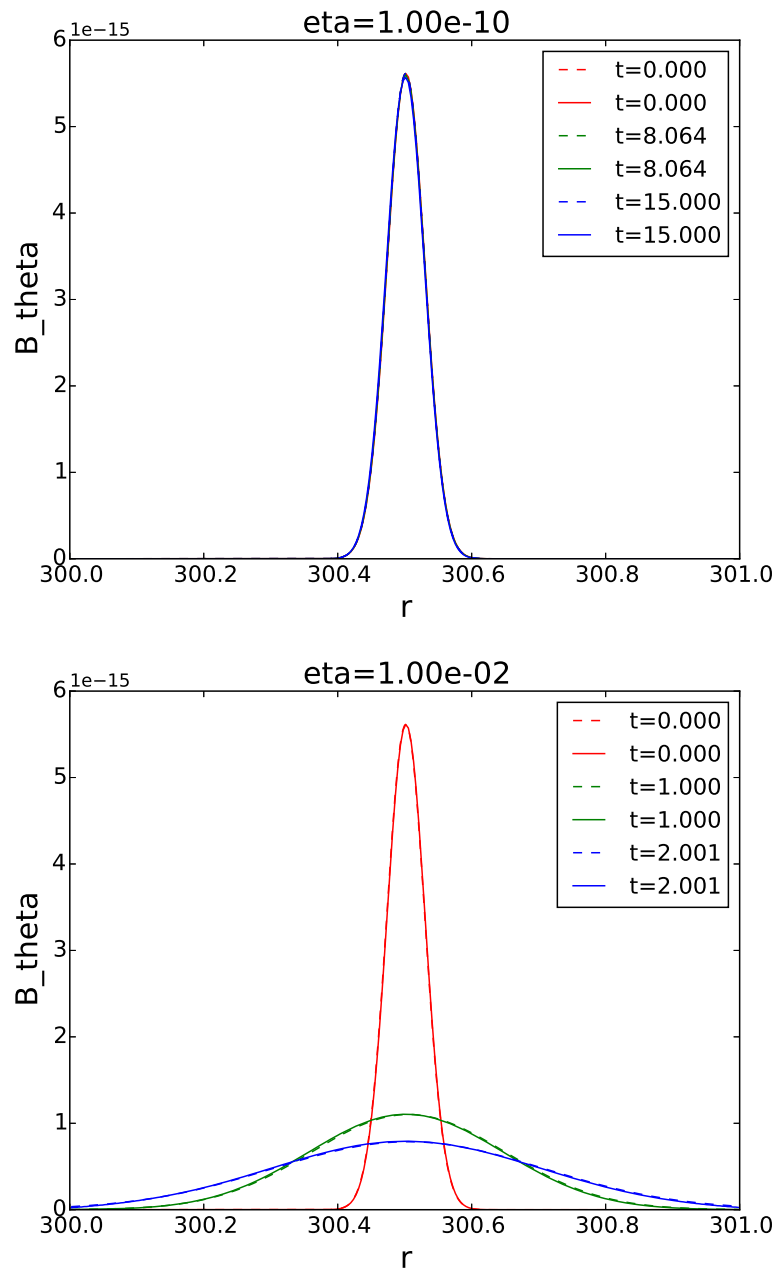


Figure 3.6: Numerical tests of magnetic diffusivity. The radial profile of the magnetic field $B_\theta(r)$ is plotted along the equatorial plane. We show simulation *difT0* with $\eta = 10^{-10}$ (upper) and simulation *difT2* with $\eta = 10^{-2}$ (lower), both with a grid resolution 256×256 . Different colors represent the corresponding simulation time steps t as labeled in the legend. The actual time \tilde{t} of these steps are $\tilde{t} = t_0 + t$, where t_0 depends on the initial condition. Solid lines are from simulation results, while dashed lines from analytic solutions. Note the difficulty in distinguishing dashed lines from solid lines, due to the perfect match between the analytical and numerical solutions. In simulation *difT0*, all 6 curves are plotted. Yet, they look like one curve, because with $\eta = 10^{-10}$, the magnetic field does not diffuse at all.

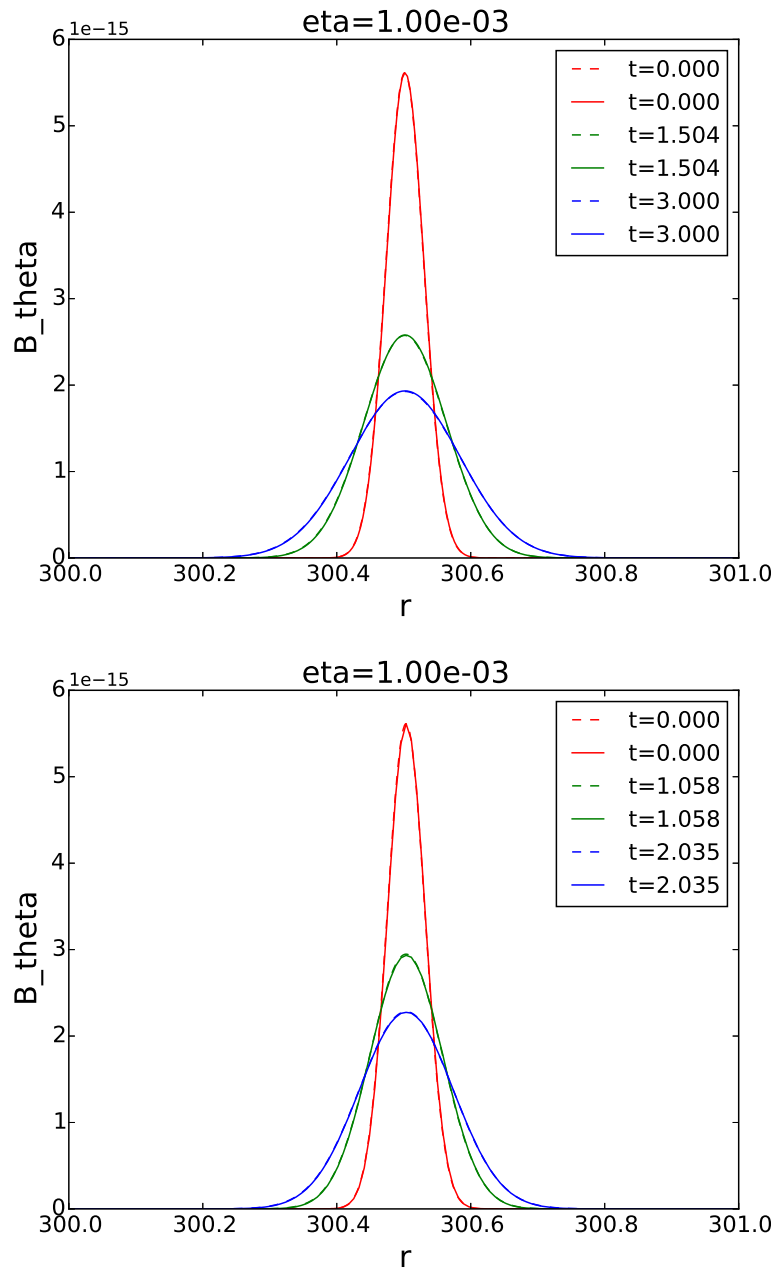


Figure 3.7: Numerical tests of magnetic diffusivity. The radial profile of the magnetic field $B_\theta(r)$ is plotted along the equatorial plane. We show simulation *difT1*, where $\eta = 10^{-3}$ (upper) is applied with a grid resolution 256×256 and simulation *difT3*, where $\eta = 10^{-3}$ is applied with a grid resolution 128×128 (lower). Different colors represent the corresponding simulation time steps t , as labeled in the legend. The actual time \tilde{t} of these steps are $\tilde{t} = t_0 + t$, where t_0 depends on the initial condition. Solid lines represent simulation results, while dashed lines represent analytic solutions. Note the difficulty in distinguishing dashed lines from solid lines, due to the perfect match between the analytical and numerical solutions.

Table 3.1: Test simulations of magnetic diffusivity η in rHARM. Parameter choices in simulations *difT0*, *difT1*, *difT2*, *difT3*, *difT4*. The table shows the radial position of the domain in the equatorial plane and the domain size, both in units of r_g , as well as the grid resolution in the domain. The magnetic diffusivity η is constant in the domain. Simulations were done for $a = 0$.

run	η	distance from origin	domain size	grid size
<i>difT0</i>	10^{-10}	$300r_g$	$1 \times 1 r_g^2$	256x256
<i>difT1</i>	10^{-3}	$300r_g$	$1 \times 1 r_g^2$	256x256
<i>difT2</i>	10^{-2}	$300r_g$	$1 \times 1 r_g^2$	256x256
<i>difT3</i>	10^{-3}	$300r_g$	$1 \times 1 r_g^2$	128x128
<i>difT4</i>	10^{-3}	$30r_g$	$5 \times 5 r_g^2$	256x256

pressure in the box,

$$\begin{aligned}\rho(r) &= C \cdot r^\alpha, \\ p(r) &= \beta \cdot \rho^{\gamma_G},\end{aligned}\tag{3.56}$$

where $\alpha = 1/(1 - \gamma_G)$, $\beta = 1/(1 - \alpha)$ and C denotes a proper normalization constant.

For the magnetic field, we only consider the θ component. The initial field strength B_θ is chosen from the solution of the one dimensional diffusion equation for infinite space, resembling a Gaussian profile with time evolution

$$B_\theta(r, \tilde{t}) = \frac{1}{\sqrt{\tilde{t}}} \exp\left(-\frac{(r - r_0)^2}{4\eta\tilde{t}}\right).\tag{3.57}$$

Here, $\tilde{t} = t_0 + t$ and in our context t is the actual code running time. The parameter t_0 is then defined by the choice of the peak value of the initial Gaussian profile. The initial B_θ is thus defined by $t = 0$. The solution (Equation 3.57) will later be compared to our simulation results. We choose a very weak magnetic field with a plasma beta $\beta \equiv p_{\text{gas}}/p_{\text{mag}} = 10^8$. The diffusivity η is set to be uniform throughout the simulation region.

3.4.3 Test simulations of magnetic diffusivity

In this subsection, we show the results of test simulations *difT0* to *difT3* with a box of size of $1 \times 1 r_g$ placed at $r_0 = 300$. At this distance, GR effects can be neglected and the box can safely be considered ‘‘rectangular.’’ In general, the grid resolution is 256x256, with the exception of simulation *difT3*, which has a grid size of 128x128 in the interest of exploring resolution effects.

In order to compare the simulation results to the analytic solutions, we show the magnetic field

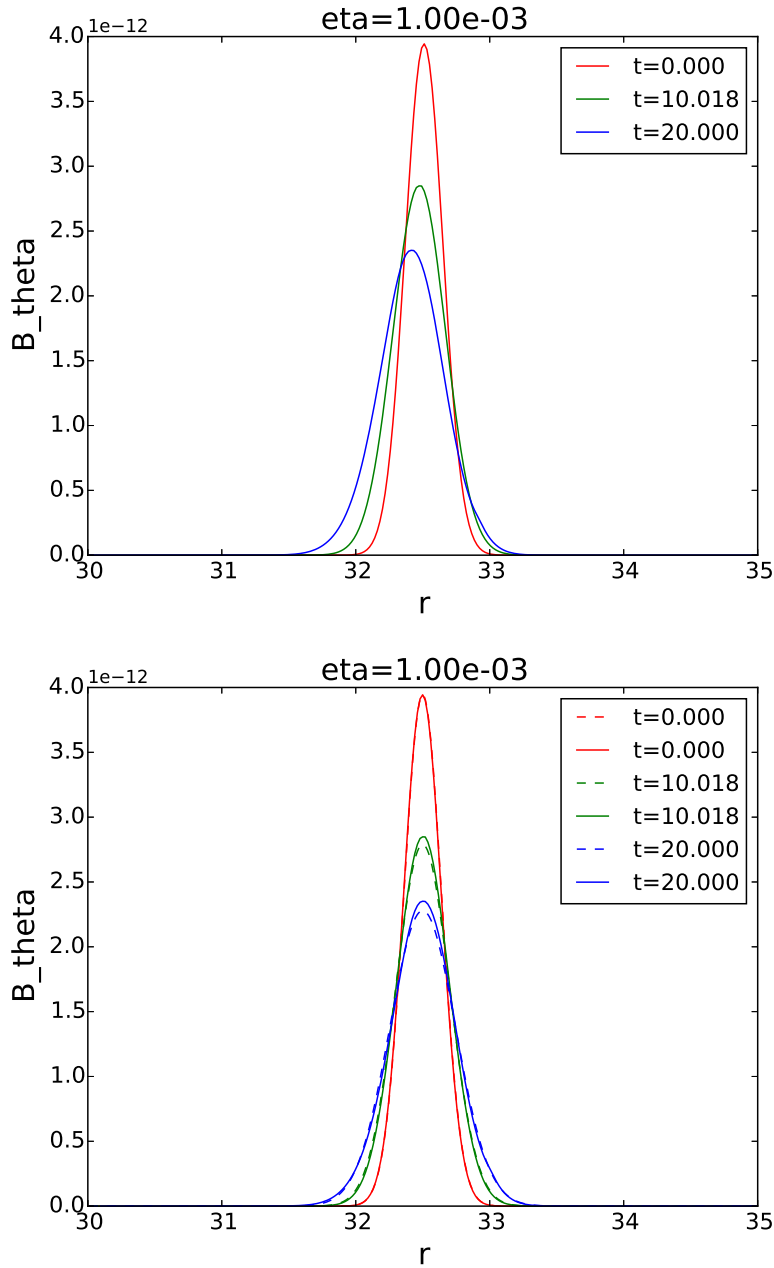


Figure 3.8: Simulation *difT4* with $\eta = 10^{-3}$ in a box of $5 \times 5 r_H$ located at $r = 30 r_H$ and a grid resolution 256×256 . The radial profile of the magnetic field $B_\theta(r)$ is plotted along the equatorial plane. The upper plot shows advection of magnetic flux by the infalling corona. The lower plot shows the same simulation results, but compensated for advection / infall with the magnetic profile maximum shifted back to the center of the simulation box (after the simulation). In the lower plot, solid lines represent the simulation result while dashed lines represent the analytic solution.

$B_\theta(r)$ along the equatorial plane $\theta = \pi/2$ at different time steps (see Figures 3.6 and 3.7). Numerical results are plotted in solid lines, while the analytic solution is shown in dashed lines.

In the first test, we ran simulation *difT0* considering a tiny resistivity $\eta = 10^{-10}$ (the upper plot in Figure 3.6). As a result, we retrieve the behavior of the ideal MHD gas, such that the magnetic field did not diffuse at all. Simulations *difT1* and *difT2* apply a high diffusivity with $\eta = 10^{-3}$ and $\eta = 10^{-2}$, respectively (upper plot in Figure 3.7 and lower plot in Figure 3.6). In both cases, the initial Gaussian profiles decay nicely, following the analytic solution exactly. Simulation *difT3* with two times lower resolution (lower plot in Figure 3.7) performed similarly well, except that the peak of the Gaussian is not as well resolved as before.

3.4.4 Diffusivity test near a black hole

It is essential to test the implementation of magnetic diffusivity in rHARM for regions closer to the black hole also. In order to test the code performance in this regime, we have set up simulation run *difT4*, for which we chose a “box” size of 5×5 and a box location located at $r_0 = 30r_g$. We show the results in Figure 3.8.

The left plot shows that in addition to the diffusive decay of the magnetic field, the magnetic flux is also advected inwards. The velocity of this motion is about $v_r \simeq -10^{-3}$ at time $t = 3t_g$. This effect can also be observed in the simulations discussed previously, only that the radial velocities are much lower (about 10^{-5} at $t = 3t_g$), and thus negligible. In the simulation runs discussed in Appendix 3.6, the run time is comparatively much longer, so that the acceleration towards the black hole can be seen more clearly. We attribute this effect to our choice of an initially hydrostatic corona, derived using a Newtonian potential (Thus, this setup becomes more inconsistent with GR for small radii). The gas in the computational domain will start to fall towards the black hole, and will thereby advect magnetic flux. We can, however, easily disentangle this effect and compare the magnetic diffusion in the simulation with the analytic solution. In order to do so, we have shifted the profile of the magnetic field distribution resulting from the simulations outwards to the center of the simulation area, compensating for the advection of magnetic flux. We can see (lower plot) that the shifted curves and the analytic solution are in very good agreement, again verifying our implementation of magnetic diffusivity.

We note that the numerical curves are slightly higher compared to the analytic solutions in this case. This can be explained by the infall of gas that comes along, in addition with a compression of the gas and magnetic field. Close to the black hole, the simulation area is rather a sector of a ring than a rectangular box (note that $r_0 \Delta\theta = 5r_g \sim r_0$).

3.5 Diffusivity tests II – shock tube test

In this section, I will present the results of test simulations of the magnetic diffusivity implementation applying a classical shock tube setup (Dumbser & Zanotti 2009; Bucciantini & Del Zanna 2013). The test simulations for the shock tube test were executed in 1D tube in Minkowski spacetime. We have applied different levels of (constant) magnetic diffusivity and compared the results to those in the above mentioned papers.

3.5.1 Computational domain and initial conditions

The shock tube simulation applies Minkowski spacetime and Cartesian coordinates with an equally spaced grid. The dimensional computational domain extends from x_0 to $x_0 + 1.5r_g$. In principal, x_0 can be set arbitrarily; here we chose $x_0 = 299.75r_g$ and a computational domain $x = [299.75r_g, 301.25r_g]$. The initial conditions of primitive variables follow the setup in Dumbser & Zanotti (2009) and Bucciantini & Del Zanna (2013), which are

$$(\rho, p, v^x, v^y, v^z, B^x, B^y, B^z) = (1.08, 0.95, 0.4, 0.3, 0.2, 2.0, 0.3, 0.3) \quad (3.58)$$

for $x < 300.5$ and

$$(\rho, p, v^x, v^y, v^z, B^x, B^y, B^z) = (1.0, 1.0, -0.45, -0.2, 0.2, 2.0, -0.7, 0.5) \quad (3.59)$$

for $x > 300.5$. The initial electric field is set to the ideal MHD value $E^i = -\epsilon^{ijk} B_j v_k$. We apply Dirichlet boundary condition, where the primitive variables of both boundaries are fixed to the initial condition. The adiabatic index here is $\gamma = 5/3$, following the test solutions from the literature.

3.5.2 Shock tube test simulations

In shock tube test simulations, three different resolutions with $N = 4500, 600, 120$ equidistant cells have been applied for different types of tests. First, a high resolution test was done with $N = 4500$ and $\eta = 10^{-12}$ in rHARM and then compared to a similar simulation applying the ideal HARM code. Both simulations match perfectly as shown in Figure 3.9. The curves also recover all features seen in Dumbser & Zanotti (2009).

We then compare simulations ran with $\eta = 10^{-12}, 10^{-4}, 10^{-3}$ and 10^{-2} by rHARM in order to see the impact of diffusivity on the shock structure. Since the time stepping of the code becomes dominated by the diffusive time step for high diffusivity, a resolution $N = 4500$ cannot be reached. Thus, for this set of tests we chose $N = 600$ grid cells for the resolution. The results are shown in Figure 3.10 by solid lines. Due to the lower resolution, thus the larger numerical diffusivity, the discontinuities at the shock wave front for the $\eta = 10^{-12}$ curve are broader than those for the high resolution plots. Moreover, the $\eta = 10^{-4}$ curve does not differ much from

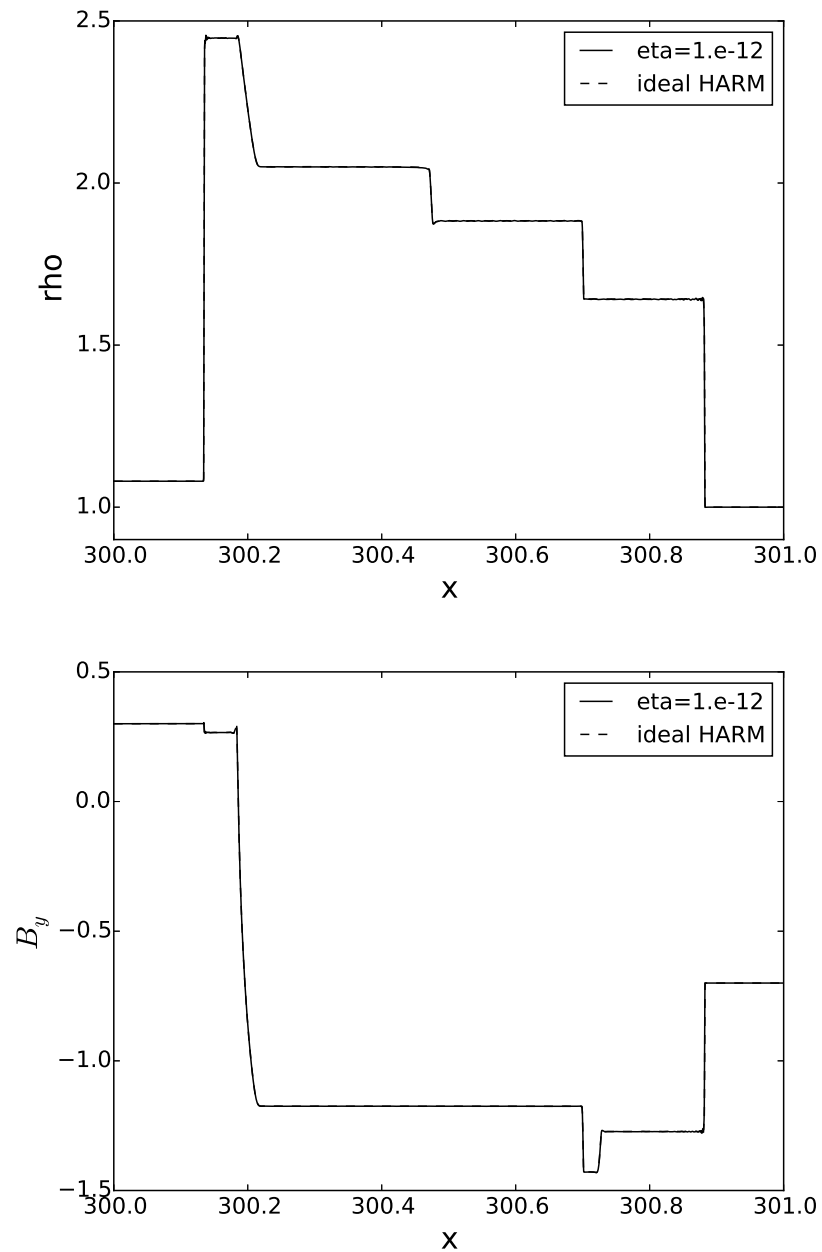


Figure 3.9: Shock tube simulation in ideal MHD regime. Density and vertical magnetic field at time $t = 0.55t_g$. In this figure, we show results of simulations with grid resolution $N = 4500$, where the curves of the two simulations match perfectly to each other. Although the actual computational domain is larger, only the range $x = [300r_g, 301r_g]$ is plotted in order to easily compare to the two reference papers.

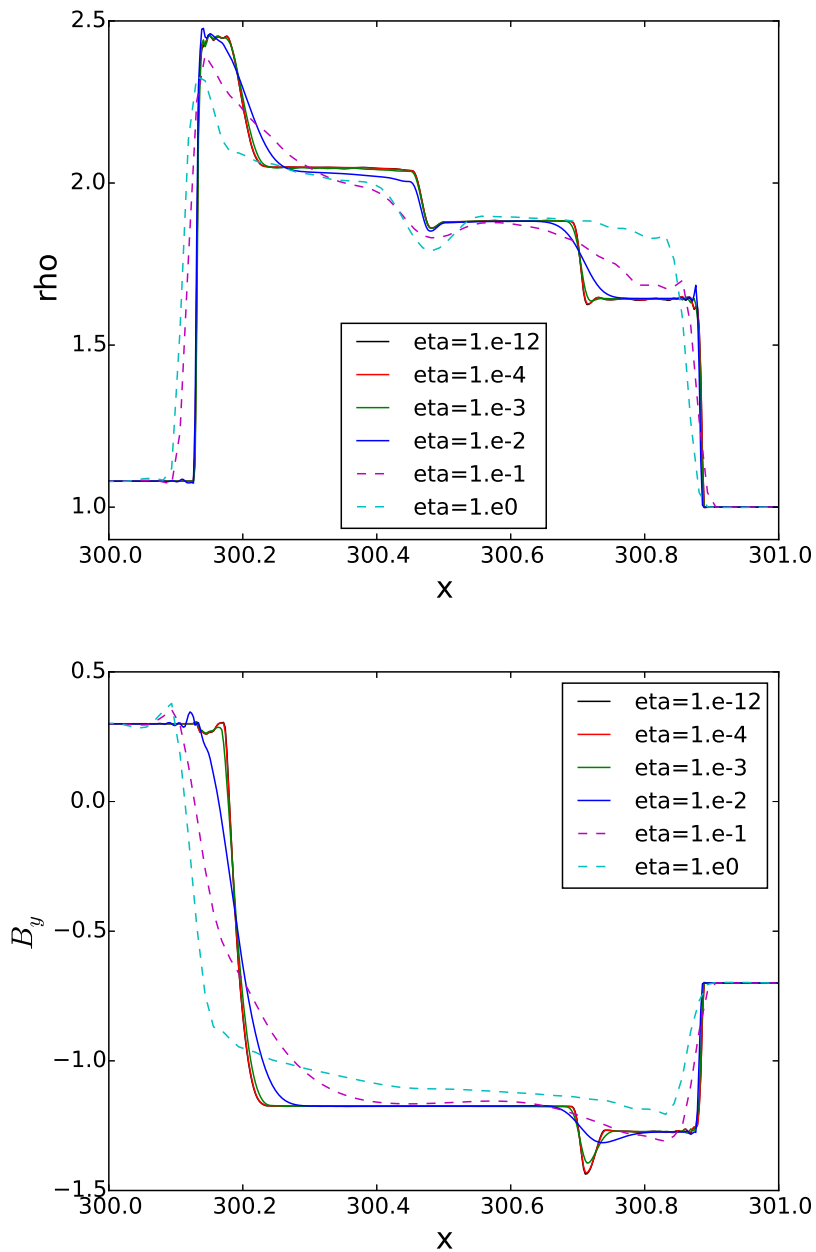


Figure 3.10: Shock tube simulations in diffuse MHD regime. Density and vertical magnetic field at time $t = 0.55t_g$. In this figure, we show the results of simulations with $N = 600$. In addition, the magenta and cyan dashed lines in the lower plots represents the simulations with resolution $N = 120$. Although the actual computational domain is larger, only the range $x = [300r_g, 301r_g]$ is plotted in order to easily compare to the two reference papers.

the $\eta = 10^{-12}$ simulation, essentially indicating a numerical diffusivity of similar order in this setup. Nevertheless, the two curves representing $\eta = 10^{-3}$ and $\eta = 10^{-2}$ nicely agree with those in [Dumbser & Zanotti \(2009\)](#) and [Bucciantini & Del Zanna \(2013\)](#).

For simulations with $\eta > 10^{-2}$, we chose a resolution with $N = 120$ cells for two reasons. On one hand, we recognized that some cell-scale oscillations that appear on the edge of the shock propagation (visible in Figure 3.10 for $\eta > 10^{-2}$) grow stronger and finally disturb the evolution of the shock propagation. A lower resolution can dissipate these oscillations (see below for a discussion). On the other hand, the time costs of such diffusivity level require a lower resolution. However, note that the numerical diffusivity for this lower resolution is still below the physical diffusivity. Our results for high diffusivity are shown by the dashed lines in Figure 3.10. The shape of these curves implies that the evolutions are still dominated by the physical diffusivity. However, the discrepancy between these two simulations and those from the literature ([Dumbser & Zanotti 2009](#); [Bucciantini & Del Zanna 2013](#)) is obvious.

We believe that instability appearing at the shock front mentioned above results from the shock capturing abilities we use in rHARM. We find that this instability strongly depends on how the derivatives are calculated in the non-stiff term in Equation (3.40). We have tried various limiters, such as monotonized central, van Leer and minmod slope limiters. Different slope limiters always return slightly different results, but the problem could not be fixed by simply changing the slope limiter. Note also, that rHARM uses a simple first-second scheme for time evolution instead of the IMEX scheme applied in [Palenzuela et al. \(2009\)](#), which was also employed in [Bucciantini & Del Zanna \(2013\)](#). This might add to the inaccuracy of the code in the high- η regime as well. However, since the magnetic diffusivity values we apply in our accretion-ejection setup will always be below $\eta = 10^{-2}$, we decided not to go deeper into this problem, at this point in time.

3.6 The numerical diffusivity

With a physical magnetic diffusivity in the code, it is now possible to measure the numerical diffusivity of rHARM. This can be achieved using the model setup in Section 3.4 by simply decreasing the physical diffusivity within an extended parameter range and meanwhile watching the behavior of the decay magnetic strength curve; When the physical diffusivity is below the numerical diffusivity, the decaying curve should be no more sensitive to the change of physical diffusivity, in which way the numerical diffusivity can be found.

As in Section 3.4, the simulations were executed in a box size of $(\Delta r \times r\Delta\theta) = (1.0 \times 1.0)$, located at $r = 300$, with numerical grids of (16×16) , (32×32) , (64×64) , (128×128) , and (256×256) applied. Depending on the resolution, the range of physical magnetic diffusivities that were applied are between $\eta = 10^{-8}$ and 10^{-3} .

As a typical example, the simulations with resolution (128×128) are shown in Figure 3.11 and

3.12. The physical magnetic diffusivities applied for these simulations were $\eta = 10^{-7}, 10^{-6}, 10^{-5}, 10^{-4}$. The dashed curves show the analytic solution of the diffusion equation for the physical magnetic diffusivity, while the solid curves show the result of the numerical simulation for the same time steps. Note that we did not correct for the mass infall (see discussion in Section 3.4). This results in the slight acceleration of the material towards the black hole, and an average infall velocity of $v_{\text{fall}} \equiv \Delta r \Delta t \simeq 0.2/150 = 1.3 \times 10^{-3}$ (in code units).

For $\eta = 10^{-4}$ (upper plot Figure 3.11), the numerical simulation follows the analytic solution, indicating that the decay of the magnetic field was dominated by the physical magnetic diffusivity. This simulation has been executed only until $t = 50$, which is about the decay time scale for $\eta = 10^{-4}$ in the analytic solution. For $\eta = 10^{-5}$ (lower plot Figure 3.11), numerical diffusivity seems to contribute to the decaying curve which can be seen more clearly as the time went on. For $\eta = 10^{-6}$ (upper plot Figure 3.12), numerical diffusivity becomes predominant, as the analytic solution would only slightly decay within the time frame applied, while the actual decaying curve fell quickly. This can be confirmed by the simulation with $\eta = 10^{-7}$ (lower plot Figure 3.12), where the numerical evolution of the magnetic field is practically identical to the simulation results from $\eta = 10^{-6}$, implying that the systems now evolve only under numerical diffusivity. In this case, the physical diffusivity prescribed is too small compared to the numerical diffusivity to contribute to the evolution of the magnetic curve and so, numerical diffusivity is the only one that matters. With the results above, we can conclude that for the given setup with resolution (128×128) , the numerical diffusivity is of the order of $\eta_{\text{num}} \sim 10^{-5}$. Furthermore, a similar study with resolution (256×256) showed that with this resolution, the numerical diffusivity is of the order $\eta_{\text{num}} \sim 10^{-6}$, while for (64×64) the numerical diffusivity is $\eta_{\text{num}} \sim 10^{-4}$.

As an alternate study, a range of different grid resolutions have been applied for a fixed (physical) magnetic diffusivity of $\eta = 10^{-5}$ and $\eta = 10^{-4}$. In agreement with the previous study, we find that the numerical magnetic diffusivity equalize the physical magnetic diffusivity for a certain resolution and dominates the physical diffusivity for lower resolution.

Clearly, the exact values of numerical diffusivities depend on the numerical setup, but in order to evolve physical diffusion processes in rHARM with a physical diffusivity of $\eta = 10^{-4} \dots 10^{-2}$, a grid resolution of $\Delta r \leq 10^{-2}$ is needed. Also, for a physical magnetic diffusivity varying in space (for example, a disk magnetic diffusivity) the numerical diffusivity serves as a “floor” value - a value depending on resolution.

3.7 Summary and conclusions

In this chapter, I have illustrated the implementation of resistivity and magnetic diffusivity into the ideal GR-MHD code HARM (Noble et al. 2006) and provided test simulations. The implementation of resistivity applies the general definition of the Faraday tensor - the general form of the stress energy tensor, including the electric field - to the new code rHARM. We followed the equations in Bucciantini & Del Zanna (2013) to calculate the electric field. The inversion

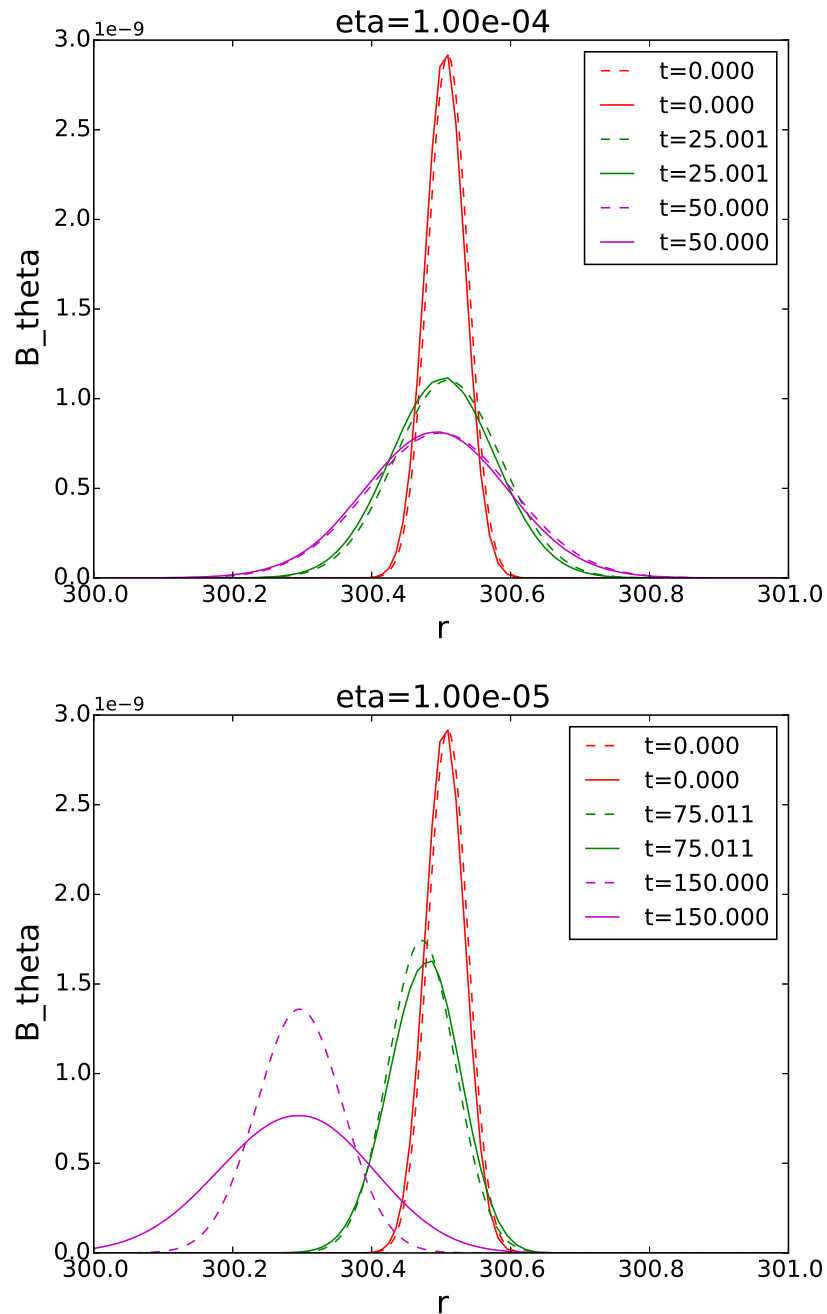


Figure 3.11: Measure of numerical magnetic diffusivity. The simulations shown apply a numerical resolution of (128×128) and a physical magnetic diffusivity $\eta = 10^{-5}, 10^{-4}$ (see figure titles). Dashed curves show the analytic solution of the diffusion equation for the physical magnetic diffusivity (as in Section 3.4). Solid curves show the result of the numerical simulation for the same time steps. The decay of magnetic field lines in these plots are still dominated by physical magnetic diffusivity.

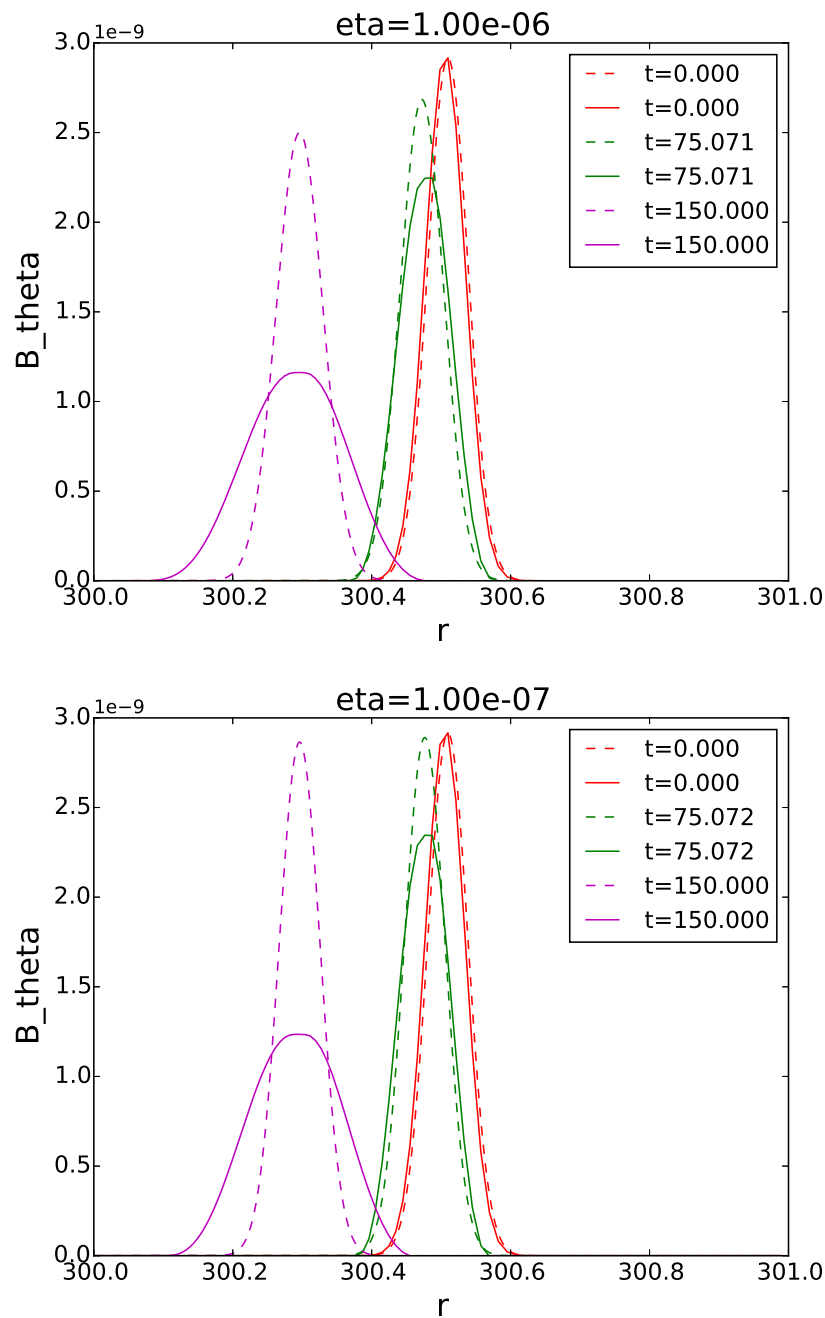


Figure 3.12: Measure of numerical diffusivity. The simulations shown apply a numerical resolution of (128×128) and a physical magnetic diffusivity $\eta = 10^{-7}, 10^{-6}$ (see figure titles). Dashed curves show the analytic solution of the diffusion equation for the physical magnetic diffusivity (as in Section 3.4). Solid curves show the result of the numerical simulation for the same time steps. The decay of magnetic field lines in these plots are dominated by numerical magnetic diffusivity, hence, the decreasing physical magnetic diffusivity value does not influence the decay of field lines.

scheme in rHARM that is based on the 2D inversion scheme in [Noble et al. \(2006\)](#), which uses an extra loop to make the electric field variables converge.

The implementation of resistivity in rHARM is verified by comparing the diffusion of an initial magnetic field distribution to the analytic time evolution of the profile as given by the diffusion equation. These simulations were performed in rectangular boxes of weakly magnetized gas, excluding any dynamical effect by Lorentz forces. Boxes at different distances from the black hole were investigated. The magnetic diffusion evolving in rHARM are identical to the known analytic solution for different magnetic diffusivities from $\eta = 10^{-10}$ to $\eta = 10^{-2}$.

We have further tested rHARM by a classical shock tube problem, finding very good agreement for magnetic diffusivities $\eta < 0.1$. For larger diffusivity, rHARM does not capture the shock front perfectly anymore, but such large diffusivities are beyond the scope of our aims of treating the disk accretion-ejection structure.

Having implemented physical magnetic diffusivity in the code, we are able to measure the numerical diffusivity. The magnetic diffusivity clearly depends on the setup and resolution. For a cell size of $\Delta x \simeq 0.01$, the numerical diffusivity is $\eta_{\text{num}} \sim 10^{-5}$.

Chapter 4

Simulations of resistive magnetized tori

In this chapter, the resistive GR-MHD code rHARM is applied to a problem that is more astrophysically relevant - the evolution of a magnetized torus around a rotating black hole. The simulations follow the general setup in [Gammie et al. \(2003\)](#) prescribing an axisymmetric torus of rotating gas with a magnetic field distribution that is confined in the torus. The simulations will be presented with two choices of grid resolution and also different values for a magnetic diffusivity that is constant in space and time. For comparison, another simulation is executed using the original ideal HARM code ([Noble et al. 2006](#)). The parameters of the simulation runs are listed in [Table 4.1](#). Simulations denoted by *torT0...2* apply a grid resolution of 256x256 and are intended to further test the implementation of magnetic diffusivity in rHARM by comparing *torT1* and *torT2* to the ideal MHD HARM simulation *torT0*. Simulations denoted by *mriT1...6* apply a grid resolution of 128x128 and intend to survey how magnetic diffusivity affects the evolution of the magneto-rotational instability (MRI) in the torus. The simulations and discussions presented in this section are also to be found in the published paper [Qian et al. \(2017\)](#) my supervisor Christian Fendt and I.

4.1 Computational domain and initial conditions

The computational domain used here is an axisymmetric half sphere with the radius ranging from $r_{\text{in}} = 0.98r_{\text{H}}$ to $r_{\text{out}} = 40r_{\text{g}}$. For all the simulations, the angle θ ranges from 0 to π and the grid concentration parameter is set to $h = 0.3$. As we apply a Kerr black hole with $a/M = 0.9375$, the event horizon $r_{\text{H}} \approx 1.35t_{\text{g}}$ (see [Section 3.3](#)).

The simulations in this section evolve an equilibrium gas torus surrounding a black hole, which is a particular solution of the class of equilibria found by [Fishbone & Moncrief \(1976\)](#) and [Abramowicz et al. \(1978\)](#). The torus is embedded in a vacuum (of a certain floor density). Centrifugal forces and gas pressure in the torus balance gravity (see also [Gammie et al. 2003](#)). The torus inner edge is set at $(r, \theta) = (6, \pi/2)$ and the pressure maximum is located at $r_{\text{max}} = 12r_{\text{g}}$. The orbital period of the torus at the radius of pressure maximum is about $267t_{\text{g}}$, measured by an observer at infinity. A polytropic equation of state $p = (\gamma_{\text{G}} - 1)u$ is applied with $\gamma_{\text{G}} = 4/3$. The purely poloidal initial magnetic field consists of concentric field lines superposed on the

Table 4.1: Parameter choice in the torus simulations that use rHARM and ideal HARM. The table shows the value of diffusivities, innermost boundaries, and resolutions that are used in the torus simulations. With the exception of *torT0*, which was executed by ideal HARM, all other tests were done by rHARM. The Kerr parameter is $a = 0.9375$ in all simulations, thus $0.98r_H = 1.32r_g$.

	η	grid size	code
<i>torT0</i>	-	256x256	HARM
<i>torT1</i>	10^{-12}	256x256	rHARM
<i>torT2</i>	10^{-3}	256x256	rHARM
<i>mriT1</i>	10^{-6}	128x128	rHARM
<i>mriT2</i>	10^{-4}	128x128	rHARM
<i>mriT3</i>	5×10^{-4}	128x128	rHARM
<i>mriT4</i>	10^{-3}	128x128	rHARM
<i>mriT5</i>	5×10^{-3}	128x128	rHARM
<i>mriT6</i>	10^{-2}	128x128	rHARM

density contours of the equilibrium torus, applying a vector potential $A_\phi \propto \max(\rho/\rho_{\max} - 0.2, 0)$ (Gammie et al. 2003). The field is normalized such that the minimum value of the plasma beta is $\beta = p_{\text{gas}}/p_{\text{mag}} = 10^2$ (Gammie et al. 2003).

The diffusivity in the torus simulations is constant in space and time. According to our previous test results of rHARM, a diffusivity $\eta = 10^{-12}$ in simulation *torT1* will retrieve the ideal MHD regime of HARM, while with $\eta = 10^{-3}$, diffusive MHD effects should appear in simulation *torT2*. For the MRI simulations, we choose a range of diffusivity, between $\eta = 10^{-12}$ and $\eta = 10^{-3}$, in order to scan the impact of diffusivity on the evolution of the MRI.

4.2 Robustness of rHARM as seen from torus simulations

For most of the simulations presented in this Chapter, the inversion scheme converged to high accuracy for almost all grid cells. However, under certain conditions - such as very low magnetic diffusivity or a very strong magnetic field - convergence might fail. While the strong-field limit is a typical problem of MHD codes in general, the case of low resistivity is usually not applied with a resistive code (we applied this only for testing the implementation of resistivity). Still, advancing the inversion scheme for applications of the code in these regimes will be one of the next steps in further developing our code.

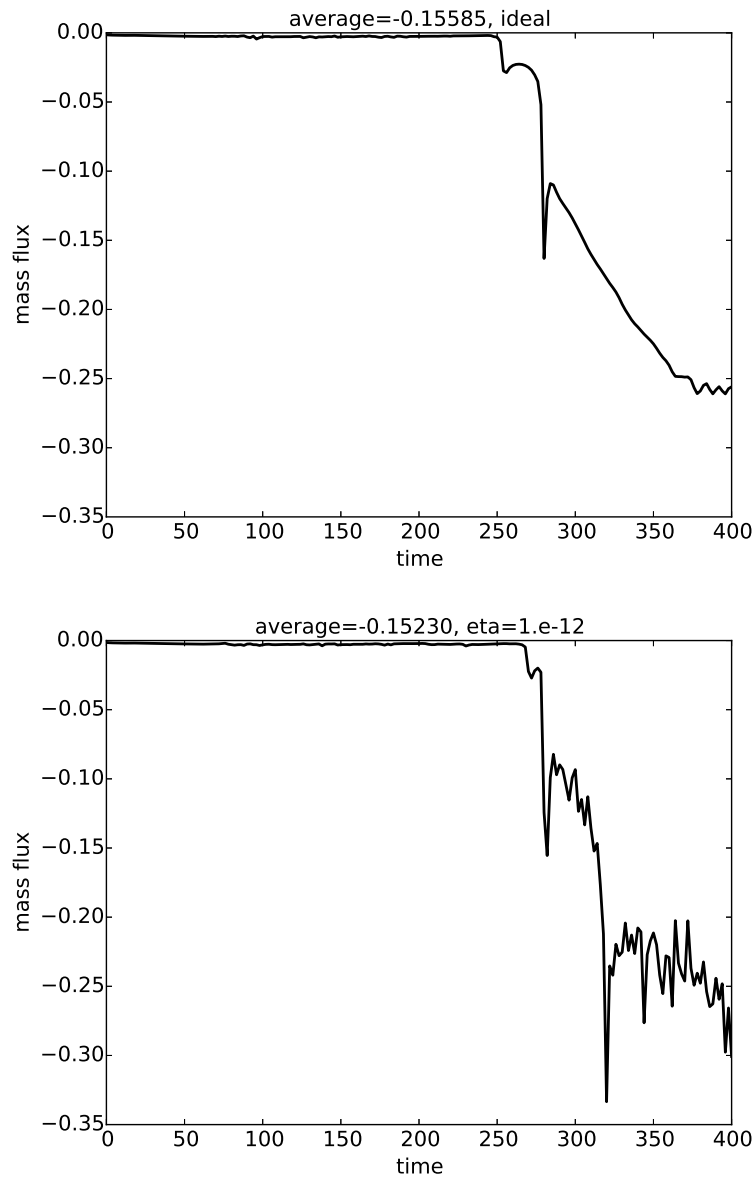


Figure 4.1: The figure shows the comparison of simulations *torT0* and *torT1*. Simulation *torT0* applies ideal MHD HARM, while *torT1* applies rHARM with tiny magnetic diffusivity $\eta = 10^{-12}$. Mass accretion rates in simulations *torT0* (upper plot) and *torT1* (lower plot) are measured at $r = 2.2r_g$ close to the horizon. The average accretion rates given in the plot title are taken from $t = 240t_g$ to $t = 400t_g$.

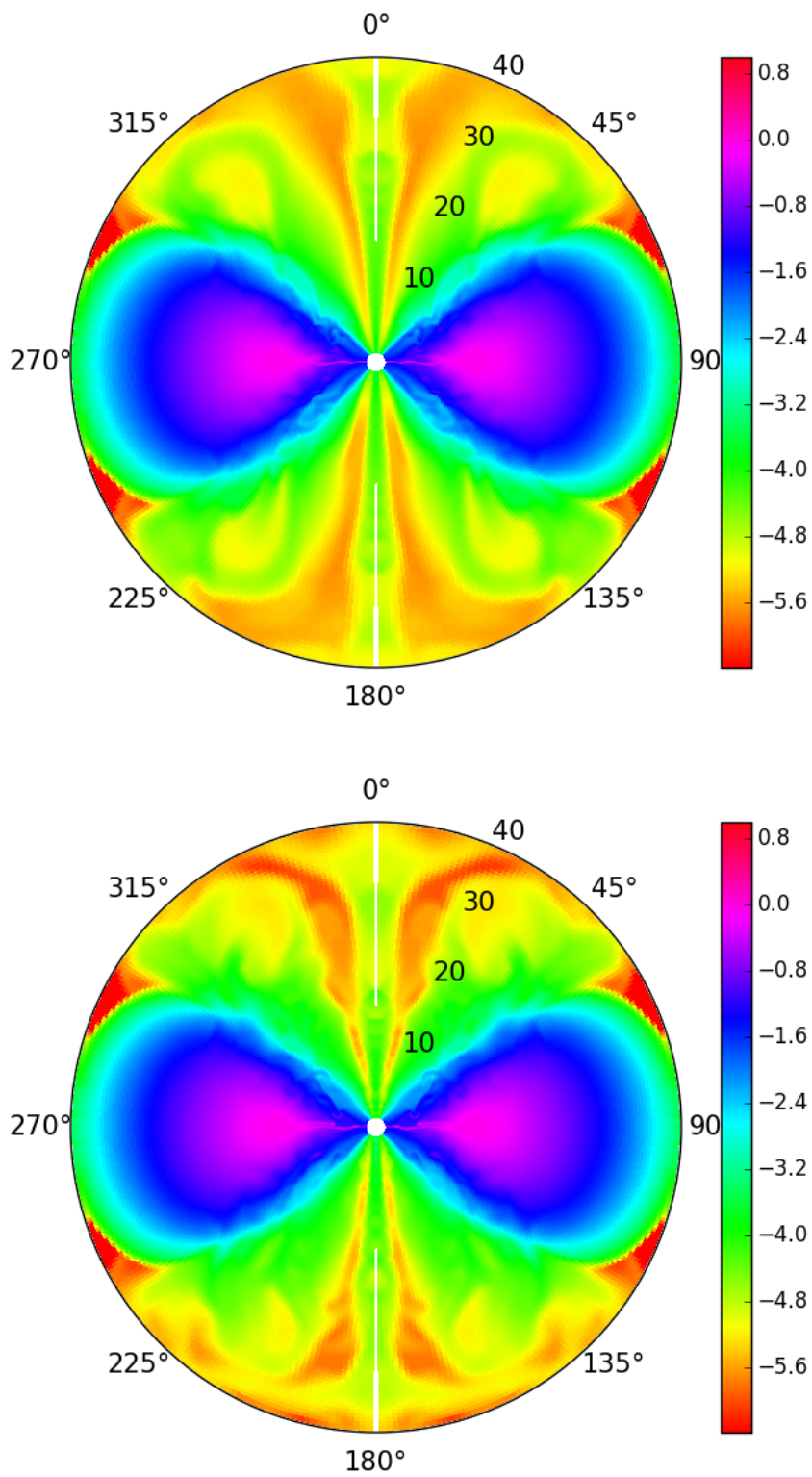


Figure 4.2: Density ($\log(\rho)$) distribution of simulation *torT0* (upper plot) and *torT1* (lower plot) at $t = 400t_g$ (the computational domain covers only the right side of the plot, the left part is just mirrored).

Due to the problems mentioned above, it is not possible to compare the diffusive simulations *torT1* and *torT2* over the same period of time as the ideal MHD simulation *torT0* was running. For example, simulation *torT1* is supposed to retrieve the evolution of *torT0* for which massive accretion of matter sets in as soon as the MRI is established. However, even in the ideal HARM simulation, we observe that the inversion scheme is “overburdened” at cells close to the horizon when a density discontinuity develops after massive accretion starts. The scheme returns primitive variables with less accuracy and even fails to converge on singular grid cells after time $t = 250t_g$, which is about the time of first accretion impact (see Figure 4.1). This problem is augmented in rHARM for the sake of the extra loop to make electric field variables converge in the 2D+1 scheme. In the end, this somewhat diminishes the robustness of the inversion scheme in the present version of rHARM.

Note that also the simulation *torT2* runs longer than simulation *torT1* since the accretion rate in *torT2* is much lower (and hence produces a milder density jump) and occurs much later. Nevertheless, we can still compare simulation *torT0* to the data from simulations *torT1* and *torT2* for a limited period of evolution. In the following, we compare results of these simulations.

4.3 Comparing rHARM simulations to the HARM simulation *torT0*

We first compare the results from simulations *torT0* and *torT1*. As mentioned above, these two simulations are supposed to be consistent with each other. We calculate their mass accretion rates at $r = 2.2r_g$, from $t = 0$ to $t = 400t_g$, and plot them in Figure 4.1. The accretion rates (\dot{M}) are calculated using

$$\dot{M}(r) = \int_0^\pi 2\pi\rho(r, \theta)u^r(r, \theta)\sqrt{-g}d\theta. \quad (4.1)$$

As can be seen from the plots for the accretion rate, the torus in both simulations keep their equilibrium state until the angular momentum transport supported by MRI (Balbus & Hawley 1991; Gammie et al. 2003) finally allows for accretion after about $t = 220t_g$. The features of accretion beginning in simulation *torT0* are retrieved quite well in simulation *torT1*. Figure 4.2 shows the density plots of the two simulations at $t = 400t_g$ where the accretion has already started and began to disturb the surface of the gas torus. In sum, the \dot{M} calculation and the density plot from simulation *torT1* nicely match those of simulation *torT0*.

Having verified the validity of rHARM in the ideal GR-MHD regime, we compare the results from simulations *torT0* and *torT2* to see how magnetic diffusivity influences the torus evolution. Since simulation *torT2* lasted longer than simulation *torT1*, we plot the accretion rate from $t = 0$ to $t = 600t_g$ and compare it to simulation *torT0*. Both plots are shown in Figure 4.3. In simulation *torT0* (upper plot), the equilibrium of the torus breaks slowly and at about $t = 220t_g$ the accretion starts. The perturbation of the inflow (choked accretion) tended to be steady after $t = 300t_g$. The average value of the mass accretion rate in simulation *torT0*, from $t = 300t_g$ to $t = 600t_g$, is about

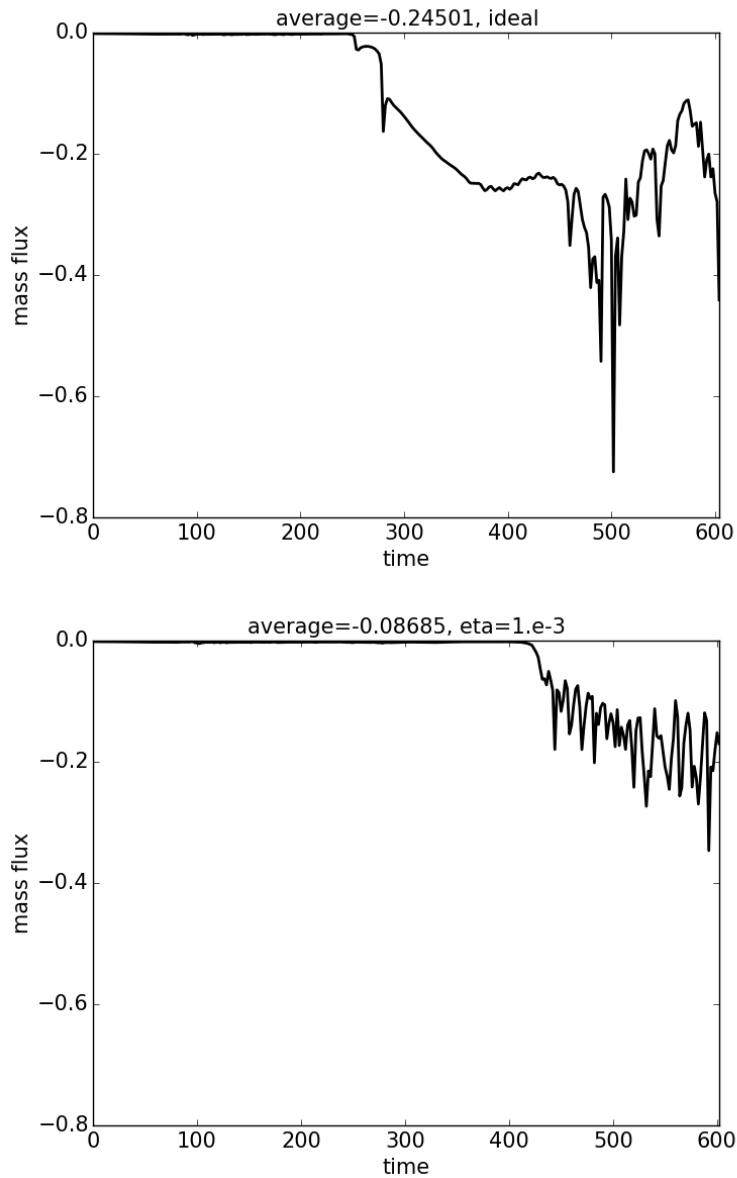


Figure 4.3: Mass accretion rates of simulation *torT0* (upper plot) and *torT2* (lower plot) at $r = 2.2r_g$. The upper plot in Figure 4.1 is actually a part of the upper plot here. The average values shown in the plot titles were taken from $t = 300t_g$ to $t = 600t_g$. A continuous accretion appeared in *torT0* after about $t = 250t_g$, while no massive accretion observed in *torT2* until $t \sim 400t_g$. The presence of magnetic diffusivity delays the time point when disk accretion happens.

-0.25 . However, in simulation *torT2* with $\eta = 10^{-3}$ (lower plot), there was no sign of massive accretion before $t \sim 400t_g$ and the average value of the mass accretion rate in simulation *torT2*, from $t = 300t_g$ to $t = 600t_g$, is only -0.087 . The presence of magnetic diffusivity suppresses MRI and thus the angular momentum transport by allowing for relative motion between matter and magnetic field (see Section 4.4 for a detailed discussion). The lack of coupling prevents the decay of the torus equilibrium state and hence only allows for inefficient accretion within the chosen time interval. This can be seen even more clearly in Figure 4.4, where we plot the density from simulations *torT0* and *torT2* at time $600t_g$. The evolution of the torus in simulation *torT2* is much smoother (less turbulent) than in simulation *torT0*.

4.4 MRI evolution in a resistive GR-MHD torus

We have shown that the evolution of the MRI can be suppressed by magnetic diffusivity, and therefore influences the mass accretion rate from the torus to the black hole. In order to quantify the gradual influence of diffusivity, we have performed simulations considering various strengths of diffusivity η (denoted by *mriT*-simulations). Here we present the results for η ranging from 10^{-12} to 10^{-3} .

It has been mentioned in Fleming et al. (2000) that for a given diffusivity η , the magnetic diffusion rate will be of order $k^2\eta$, where k stands for wave number. According to Balbus & Hawley (1991), the MRI may grow only in a certain range of wave numbers $k \in [0, k_{\max}]$, in the linear MRI regime. Furthermore, there exists a wave number k_{MRI} for which the MRI growth rate reaches a maximum (see Hawley & Balbus 1992 for the case of a Keplerian disk). A certain number of MRI modes can therefore be damped out when $k_{\text{MRI}}^2\eta$ is comparable to the maximum growth rate of the MRI. Moreover, for a large enough η , it is even possible to damp out most of the MRI modes in the linear evolution of the MRI.

In the following, we apply the time evolution of the mass accretion rate as the indicator of the MRI growth in the torus. The mass accretion rate is attributed to the turbulent angular momentum exchange, triggered by the MRI. For this reason, when magnetic diffusivity damps the growth of MRI, the point in time when massive accretion will set in is delayed. Also, the MRI evolution in Balbus & Hawley (1991) started to be non-linear after about 2 rotations. In our simulations, the rotation period of the torus at pressure maximum is $267t_g$ and about $98t_g$ at the inner edge of torus. Thus, we assume that the growth of MRI becomes non-linear after $t = 530t_g$.

The results of our simulations treating a magnetically diffusive torus are shown in Figure 4.5. We see that for this setup the accretion rate for the magnetic diffusivity $\eta = 10^{-4}$ is indistinguishable from that for $\eta = 10^{-6}$. In both cases, massive accretion takes place at about the same time compared the ideal GR-MHD simulation *torT1*. Thus, a small $\eta \leq 10^{-4}$ does not affect the growth of the MRI significantly. Note that this is the range of η , for which simulations are probably dominated by numerical diffusivity (see Section 3.6 for a discussion on numerical diffusivity).

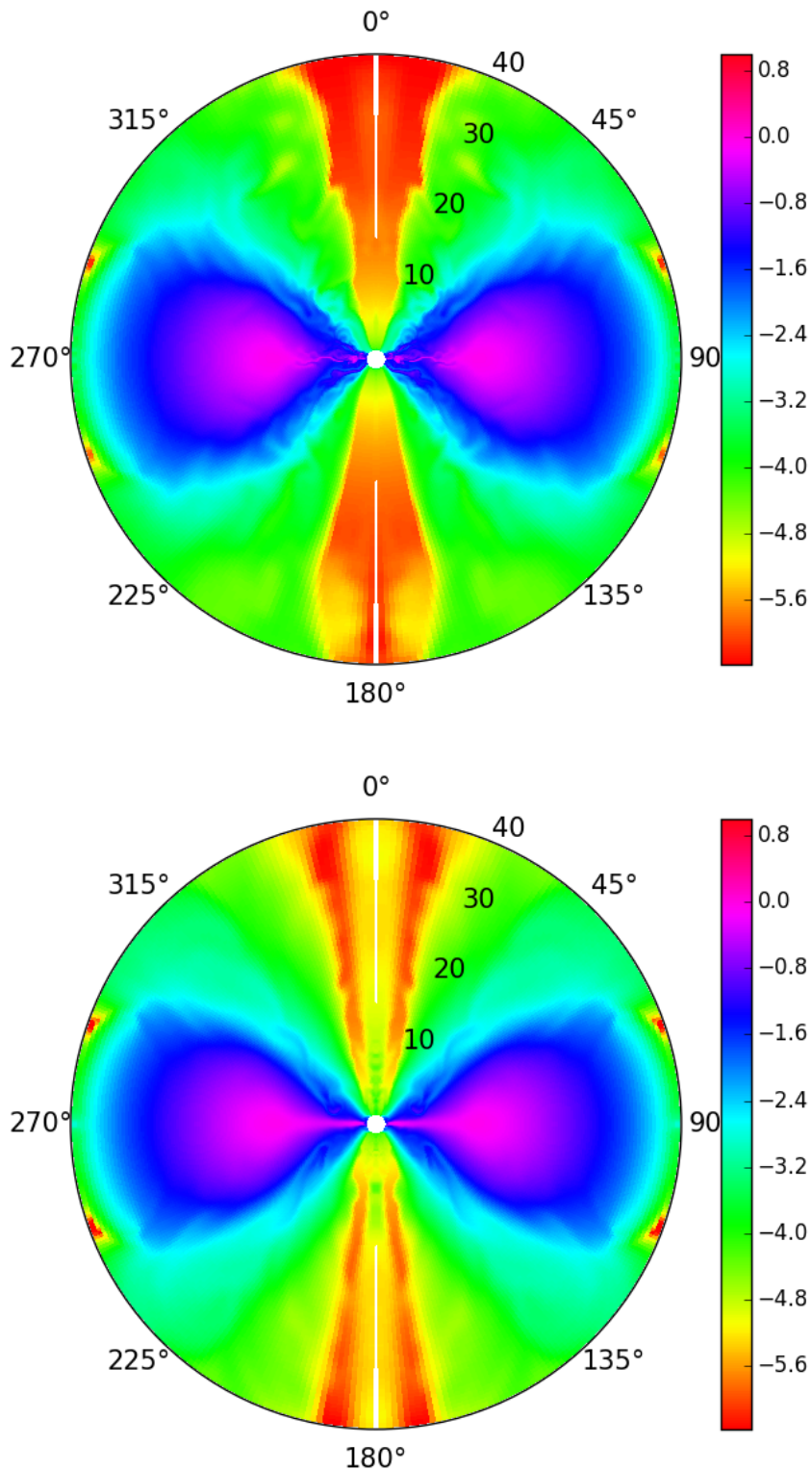


Figure 4.4: The figure presents $\log(\rho)$ of simulations *torT0* (upper plot) and *torT2* (lower plot) at time $600t_g$. In simulation *torT0*, MRI made the torus unstable and later the torus became turbulent with an accretion flow (Gammie et al. 2003). On the other hand, the torus structure of simulation *torT2* evolves in a less turbulent way, where MRI is damped by the magnetic diffusivity.

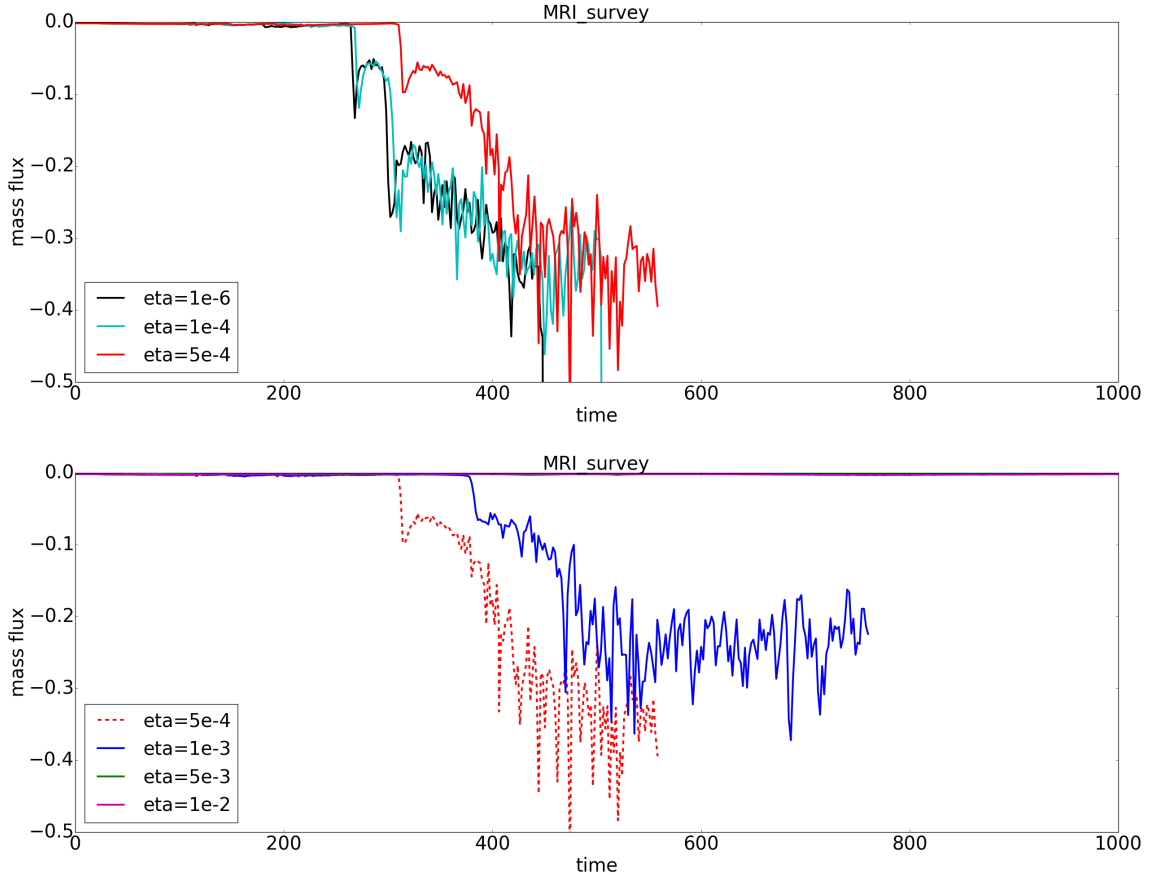


Figure 4.5: Mass flux as the indicator of MRI growth in simulations *mriT1-mriT6*. Two plots are shown in order to avoid confusion between the curves. In the upper plot, the mass accretion rates for $\eta = 10^{-6}$ (black), $\eta = 10^{-4}$ (cyan) and $\eta = 5 \times 10^{-4}$ (red) are shown, while in the lower plot, the accretion rates for $\eta = 1 \times 10^{-3}$ (blue), $\eta = 5 \times 10^{-3}$ (green) and $\eta = 10^{-2}$ (magenta) are given. The $\eta = 5 \times 10^{-4}$ (red dashed line) curve is plotted in the lower plot as a reference. As illustrated, the time when substantial accretion initiates is delayed with increasing η . The similar results for $\eta \leq 10^{-4}$ indicate a numerical diffusivity $\sim 10^{-5}$ (see Section 3.6). The delay in accretion can be explained by the magnetic diffusivity suppressing the MRI in the torus. For $\eta \leq 1 \times 10^{-3}$, only that part of the evolution is shown, afterwards these simulations experience numerical instabilities - similar to simulations *torT1* and *torT2*. Note that in these plots, the time point when massive accretion takes place differs from those in Qian et al. (2017) because of a slightly different setup in the code.

On the other hand, for the simulations with $\eta \geq 10^{-4}$, the onset of massive accretion is delayed. We find indication for a critical value of $10^{-3} \simeq \eta_{\text{crit}} \simeq 5 \times 10^{-3}$ for the magnetic diffusivity concerning MRI growth and mass accretion. This value, of course, holds for the choice of our simulation setup, grid resolution and magnetic field strength. While for $\eta \gtrsim 5 \times 10^{-4}$ there is an obvious delay for massive accretion; for $\eta > 5 \times 10^{-3}$, the MRI seems to be completely suppressed during the linear regime and for this parameter regime. This result is consistent with [Longaretti & Lesur \(2010\)](#), who demonstrated that the growth rate of the MRI substantially decreases with $1/\eta$ as soon as critical diffusivity is exceeded.

4.5 Summary and conclusions

In this chapter, rHARM has been applied to a more astrophysical context, namely, investigating the development of the magneto-rotational instability (MRI) in tori that are magnetically diffusive. For the MRI simulation survey, we followed the initial setup in [Gammie et al. 2003](#); [Noble et al. 2006](#) which is an initially stable gas torus carrying a poloidal magnetic field that follows the density contours. As further verification of the new code rHARM, we ran a simulation with a very small magnetic diffusivity $\eta = 10^{-12}$ (clearly below the numerical diffusivity of the code). This simulation recovers the time evolution of the accretion rate that has been found previously by using the ideal GR-MHD code HARM. In contrast, in the simulation with a high diffusivity $\eta = 10^{-3}$, the mass accretion onto the black hole decreases significantly due to the suppression of MRI. In order to investigate further the influence of magnetic diffusivity on relativistic MRI tori, we have performed a parameter survey ranging from $\eta = 10^{-12}$ to $\eta = 10^{-3}$. we find indication for a critical magnetic diffusivity value of $\eta \gtrsim 5 \times 10^{-4}$ (in this specific simulation model), above which the MRI inside the torus does not grow in the linear regime.

Chapter 5

Resistive magnetized thin accretion disk and disk outflows

Numerical investigations of the launching of disk winds, thus the simulations of the accretion-ejection transition have mostly been done for non-relativistic systems (see e.g. Casse & Keppens 2002; Zanni et al. 2007; Tzeferacos et al. 2009; Sheikhnezami et al. 2012; Stepanovs & Fendt 2014; Sheikhnezami & Fendt 2015). Here I extend this treatment to disks in GR-MHD for the first time. In this chapter and Chapter 6, I apply rHARM to the astrophysical context where a thin accretion disk is threaded by inclined open poloidal field lines. The parameters of my simulation runs are listed in Table 5.1. These simulations include several surveys that investigate the influences of the magnetic field strength, magnetic diffusivity (and its profile), magnetic field structure and the black hole spin (see Chapter 6) on the accretion and ejection processes in black hole accretion systems. The instruction of the surveys is shown in Section 5.1.4. Due to the time limitation of my PhD project (the current version of the code is not parallel and the disk simulations are very time consuming), the discussions in this chapter regarding the disk simulation results are mostly preliminary.

5.1 Simulation setup

In this section, the model setup for the disk simulations is presented. The different initial conditions for the simulations are listed in Table 5.1. (*Note that Table 5.1 is located at the end of this chapter.)

5.1.1 Simulation region and boundary conditions

For all disk simulations, the computational domain is an axisymmetric half sphere similar to the one used in the torus simulations. In the radial direction, the computational domain ranges from $r_{in} = r_H$ to $r_{out} = 80r_g$ (r_g is defined in Section 3.3.1), where the black hole horizon $r_H \equiv 1 + \sqrt{1 - a^2}$ in code units. The angle θ ranges from 0 to π and the grid concentration is set to $h = 0.3$ (see Section 3.3.2). The boundary condition for the inner radius and outer

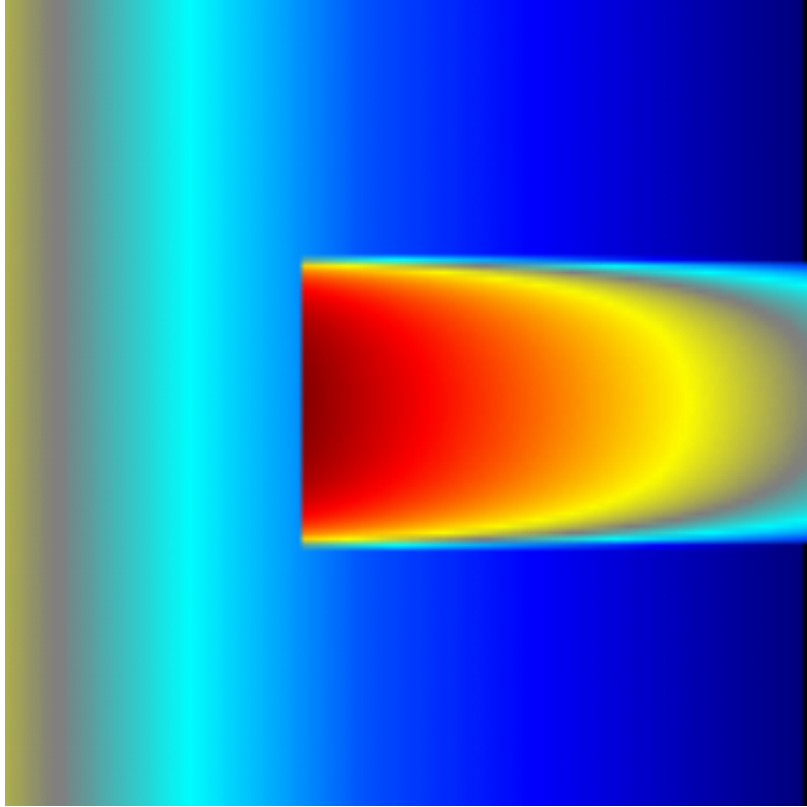


Figure 5.1: Shown is the logarithmic initial density of the disk simulation in code grids (see Section 3.3.2). With the grid resolution 128×128 , the radius inside the disk inner boundary $r = 6r_g$ is resolved by 38 grids. In the theta direction, the disk region from $\theta \approx 75.8^\circ$ - 104.2° is resolved by 48 grids.

radius forbids the mass inflow from outside into the simulation domain. Thus the matter flows either into the black hole or out of the computational region. With the exception of the magnetic field variables and electric field variables (see Section 3.3), the two polar (axial) boundaries have continuous condition, where the physical values in the ghost zone are simply copied from the simulation boundary.

5.1.2 Initial disk density and the velocity profile

I apply a pure Keplerian rotation with Paczyński-Witta approximation as the disk velocity profile (Paczyński & Wiita 1980), where the angular velocity is

$$\Omega = r^{-3/2} \left(\frac{r}{r - R_{\text{pw}}} \right). \quad (5.1)$$

The smoothing length scale $R_{\text{pw}} = 1.0$ (see also Equation 5.2) for all simulations. The reason for choosing the Paczyński-Witta rotation profile is mainly a matter of simplicity, since the system will evolve anyway into a new dynamical equilibrium, thus with a new distribution of physical quantities. The disk and the black hole (if $a \neq 0$) share the common rotation axis. Additionally,

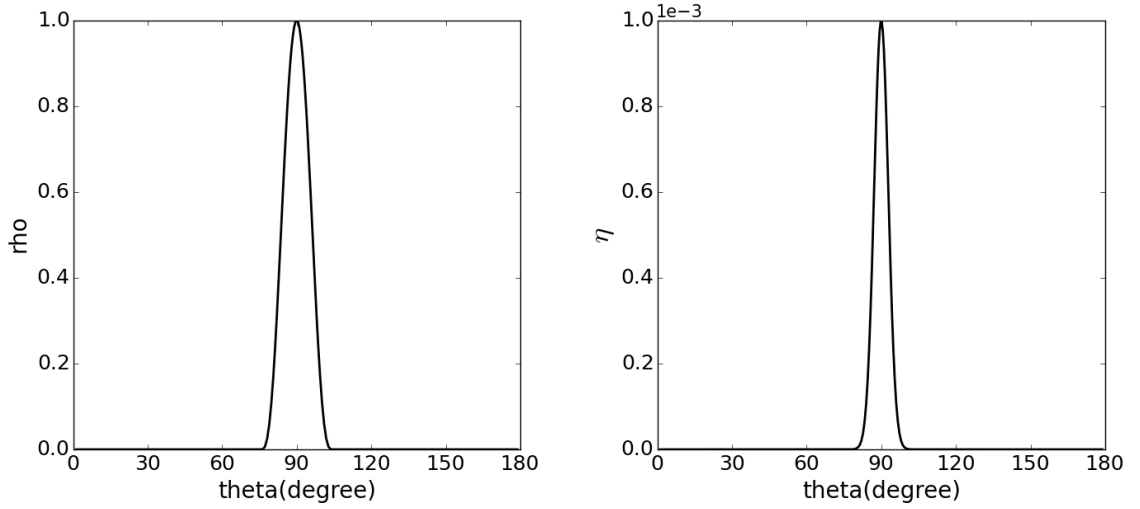


Figure 5.2: The initial profiles of density (left plot) and diffusivity (right plot) at radius $r = 6r_g$ for simulation *D16*. Both profiles decrease steeply in the θ direction with increasing distance from the disk mid-plane. In the simulations, densities are normalized to the maximum density inside the disk. According to Equation (5.2), this value appears at the disk inner boundary. Thus the density profile in the plot here has a peak value 1. The magnetic diffusivities are normalized to η_0 (see Equation 5.6), which is 10^{-3} in simulation *D6*. Thus the diffusivity profile has the peak value of 10^{-3} .

with this kinematically stable profile (not sub-Keplerian nor super-Keplerian), we are also able to see the importance of the magnetic field presence in the disk for the disk wind generation (see the discussion for simulation *D0* below).

For the disk density and pressure distribution, I apply the solution from the non-relativistic simulations (Casse & Keppens 2002), where

$$\rho(r, \theta) = \frac{R_{\text{ck}}^3}{(R_{\text{ck}}^2 + r^2)^{3/2}} \left(1 - (\gamma_G - 1) \frac{\cos^2 \theta}{2\epsilon_D^2} \right)^{1/(\gamma_G - 1)}. \quad (5.2)$$

R_{ck} and R_{pw} are theoretically unrelated, so I choose $R_{\text{ck}} = R_{\text{pw}}$ for simplicity (see Section 5.3 for the disk evolution consequence by this choice). γ_G in Equation (5.2) is the polytropic exponent. The parameter ϵ_D is the classical disk aspect ratio defined by the local disk height divided by the radius. In the simulations, I apply $\epsilon_D = 0.1$ and set the upper and lower surfaces of the disk at θ_{min} and θ_{max} , where

$$\begin{aligned} \theta_{\text{min}} &= \arccos \left(\sqrt{\frac{2\epsilon_D^2}{\gamma_G - 1}} \right), \\ \theta_{\text{max}} &= \arccos \left(-\sqrt{\frac{2\epsilon_D^2}{\gamma_G - 1}} \right), \end{aligned} \quad (5.3)$$

respectively. In difference to the simulations in the Newtonian limit (see e.g. Ouyed & Pudritz 1997; Casse & Keppens 2002; Zanni et al. 2007), I adopt the polytropic exponent $\gamma_G = 4/3$

for the relativistic case. The normalized polytropic constant κ is set to 10^{-3} (see Section 3.3.4). Applying $\epsilon_D = 0.1$ and $\gamma_G = 4/3$ to Equation (5.3), the disk has the angle range $\theta \approx 75.8^\circ$ - 104.2° . The inner boundary of the disk is at $r = 6r_g$, which is the innermost stable circular orbit for a non-rotating black hole. The rotation period at the inner boundary is $15.4t_g$. Inside the disk (the region that satisfies $r > 6r_g$ and $75.8 < \theta < 104.2$), the density in Equation (5.2) is defined and the gas pressure follows the polytropic equation of state

$$p(r, \theta) = p = \kappa \rho^{\gamma_G}. \quad (5.4)$$

The density profile defined by Equation (5.2), hence also the pressure, decreases steeply in the θ direction with increasing distance from the disk mid-plane (see Figure 5.2 left plot). Outside the disk (the regions that satisfy $r < 6r_g$, or $\theta < 75.8$, or $\theta > 104.2$), I apply a corona in hydrostatic equilibrium as described in Section 3.4.2 to intentionally prevent the expansion of the disk in the θ direction. The density and pressure setup are kept unchanged in all simulations in this section.

As aforementioned, the grid setup follows the description in Section 3.3.2. Figure 5.1 shows the image of the initial density in code grids. In the case of grid resolution 128×128 (which is applied to all disk simulations except simulation *D7*), the region within the disk inner boundary $r = 6r_g$ is resolved by 46 grids in radius. Inside the disk, the disk height is resolved by 48 grids. Thus the choice of grid resolution here should be sufficient to resolve the dynamics within the disk inner boundary and inside the disk.

5.1.3 Initial condition for the magnetic field and diffusivity

The initial magnetic field is set to be pure poloidal and follows the setup in Zanni et al. (2007) and Sheikhnezami et al. (2012), where the field lines are solved by the vector potential

$$A(r, \theta) = \frac{5}{2} B_{p,0} (r \sin \theta)^{3/4} \frac{m^{5/4}}{(m^2 + \tan^{-2} \theta)^{5/8}}. \quad (5.5)$$

The parameter $B_{p,0}$ determines the strength of the initial magnetic field and is determined by the choice of the plasma $\beta \equiv p_{\text{gas}}/p_{\text{mag}} = 8\pi p_{\text{gas}}/B^2$. The parameter m defines the inclination angle of the magnetic field lines to the disk surface. The smaller m is, the more oblique the field lines are towards the disk mid-plane.

In disk simulations, the magnetic diffusivity is not constant in the computational domain as in Section 4. Instead, the profile of the diffusivity is θ dependent and symmetric to the disk mid-plane while decreasing exponentially with distance from the disk mid-plane (see Figure 5.2 right plot),

$$\eta(r, \theta) = \eta_0 \exp \left[-2 \left(\frac{\alpha}{\alpha_\eta} \right)^2 \right]. \quad (5.6)$$

Here, $\alpha \equiv \pi/2 - \theta$ is the angle towards the disk mid-plane, and $\alpha_\eta \equiv \arctan(\chi \cdot \epsilon_D)$ is the angle defining the scale height of the diffusivity profile. χ is a scale parameter (see below). Equation (5.6) is a Gaussian profile over θ , whose maximum value is determined by parameter η_0 (see

also the model setup in [Sheikhnezami et al. 2012](#)). Thus, the choice of η_0 decides the peak of the Gaussian and can be treated as the indication of the diffusivity level, while the choice of χ controls the width of the Gaussian. A χ value that is greater than 1 indicates a diffusivity profile, that is broader than the disk density profile while $\chi < 1$ implies a profile narrower than it.

The choice of magnetic field and magnetic diffusivity are very important in accretion and ejection processes. Thus, η_0 , χ , plasma β and inclination parameter m are all the parameters that are controlled in the simulations as shown in [Table 5.1](#). To have an intuitive understanding of the initial disk morphology (see [Figure 5.3](#), which shows the initial density and magnetic field structure profile of simulation *D1*).

In the simulations, the density profile is normalized to the maximum density value inside the disk which appears at the disk inner boundary (see [Figure 5.2](#) left plot). The pressure is then calculated from [Equation \(5.4\)](#). Furthermore, the magnetic field strength is normalized according to the value of plasma β . The interpretation of this normalization in reality is discussed in [Section 3.3.4](#). The simulations are set to stop at $t = 3000t_g$.

5.1.4 About the choice of simulation parameters

The simulations which I am going to discuss are shown in [Table 5.1](#). The purpose of these simulations is to investigate the influence of different initial conditions on the accretion and ejection process in the black hole accretion system. Specifically, simulations *D1*, *D2*, *D3*, *D4*, *D6* and *D17* consist of a survey where different levels of magnetic diffusivity is investigated (see [Section 5.5](#)), while the survey with simulations *D6*, *D9*, *D12*, *D13* and *D14* investigate the influence of different magnetic diffusivity profiles (see [Section 5.5.3](#)). Simulations *D5*, *D6* and *D8* belong to the survey where different inclinations of the initial magnetic field to the accretion disk mid-plane is the control variable (see [Section 5.8](#)). The survey with simulations *D9*, *D10*, *D11*, *D15* and *D16* is meant to investigate the influence of different black hole rotations (see [Section 6](#)). Finally, the comparison between simulations *D6* and *D7* shows the influence of the grid resolution, namely numerical diffusivity (see [Section 5.9](#)).

Simulation *D0* is a control simulation to examine the choice of initial density and angular velocity, where the behavior of a very weakly magnetized thin disk is investigated. As readers shall see in [Section 5.2](#), simulation *D0* is the only case in the presented simulations where no disk outflow is observed.

5.2 Measuring the accretion rate and ejection rate

I use the mass accretion rate and ejection rate as one of the tools to investigate the simulation results. Specifically, I calculate the accretion and ejection rate with the help of a control volume

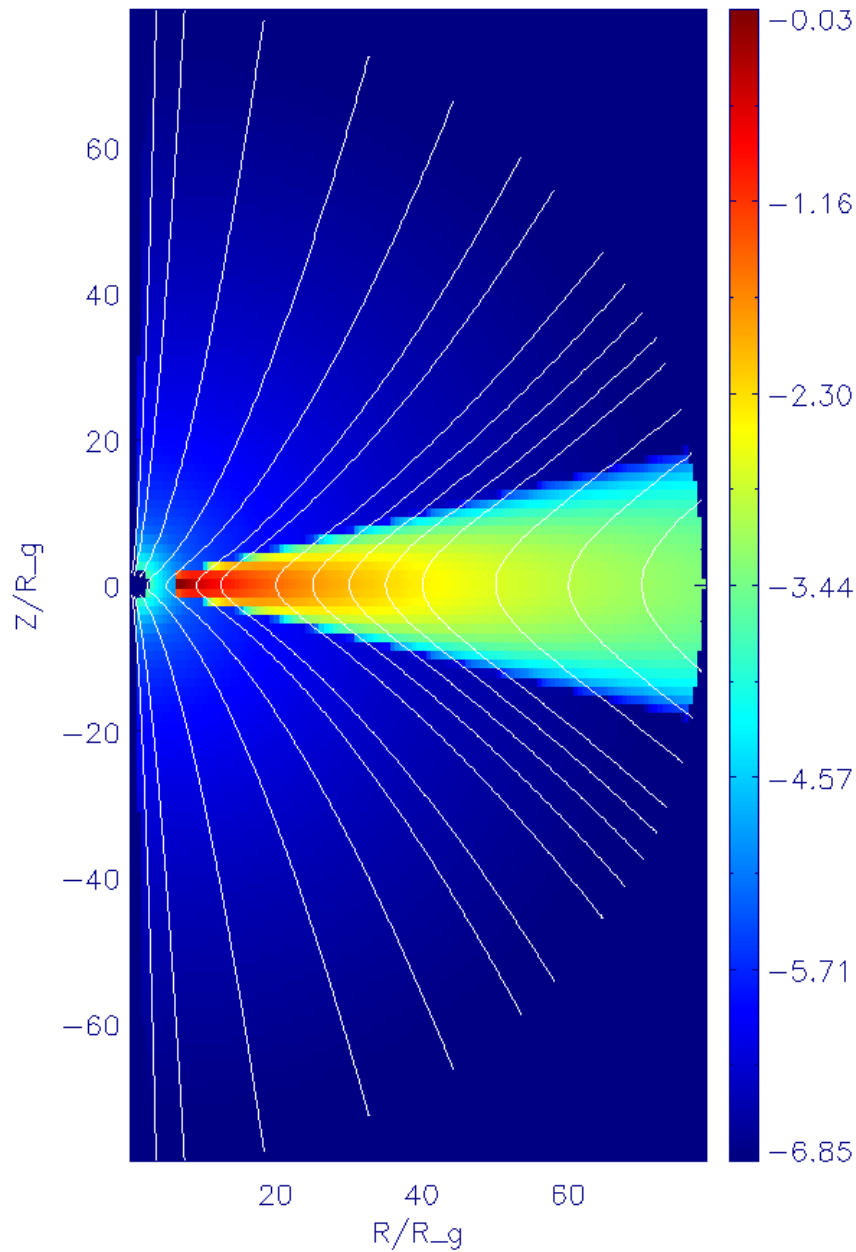


Figure 5.3: The density plot of simulation *D1* in logarithmic axes at time $t = 0t_g$. The maximum density is normalized to 1. The white solid lines in the plot show the structure of the large scale magnetic field lines. Note that the mosaic-like appearance in the disk comes from the external plotting-routine where the spherical code grids are converted into the cylindrical grids. The disk is well resolved in the simulation (see Section 5.1.2).

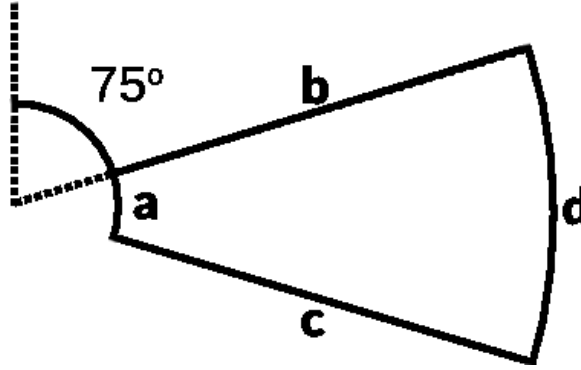


Figure 5.4: An illustration sketch of the surface where the accretion and ejection are measured. In our discussion below, we set a at $r = 6r_g$, b at $\theta = 75^\circ$ (disk initial upper surface) and c at $\theta = 105^\circ$ (disk initial lower surface). The radius of d is at $r = 60r_g$, when not redefined in the text.

as shown in Figure 5.4. The accretion rate is the same as in Section 4.3, namely

$$\dot{M}_{\text{acc}}(r) = \int_{\theta_1}^{\theta_2} 2\pi\rho(r, \theta)u^r(r, \theta)\sqrt{-g}d\theta. \quad (5.7)$$

The ejection rate is defined by

$$\dot{M}_{\text{eject}}(\theta) = \mp \int_{r_1}^{r_2} 2\pi\rho(r, \theta)u^\theta(r, \theta)\sqrt{-g}dr, \quad (5.8)$$

which is the poloidal flow that passes the surface at a certain angle vertically. The minus sign is valid for surface b , while the plus sign for surface d (see below). I calibrate the radial accretion at surface a and d using Equation (5.7), while at surface b and c , the poloidal ejection will be measured by Equation (5.8). According to the initial condition of the disk inner radius and the disk thickness, I set a at $r = 6r_g$ (disk inner boundary), while d is set to $r = 60r_g$ (note that the choice of the positions of a and d also decides the length of surfaces b and c). The surface b is set at $\theta_1 = 75^\circ$ (disk initial upper surface), c at $\theta_2 = 105^\circ$ (disk initial lower surface). The ejection processes in the simulations are basically symmetric to the disk mid-plane, thus the ejection rates presented in the data analysis are the sum of \dot{M}_{eject} at surfaces b and c .

For the discussion below, I specify that a negative accretion rate at radius a and d means radial accretion towards the black hole, while a positive value indicates outwards radial motion. For the ejection, a positive ejection rate at surfaces b and c indicates disk wind outflow, while a negative value refers to mass concentration towards disk mid-plane. Furthermore, I define the negative total mass loss as the matter gain inside the control volume. As the readers will see, the outer accretion rate at $r = 60r_g$ does not return much useful information. Thus I will use both terms “accretion rate” and “inner accretion rate,” to indicate the accretion rate at the disk inner boundary $r = 6r_g$.

5.3 Very weakly magnetized accretion disk

To eliminate the influence of the magnetic field in the disk wind production, I have run simulation *D0*, where the thin disk is very weakly magnetized. The plasma β in simulation *D0* is 10^8 , like in the diffusive tests in Section 3.4. Under such circumstance, the magnetic field is meant to be negligible. Thus, the choice of parameters χ and m are unimportant here. Since strong magnetic field is always required in the theories for disk-driven wind (see Section 1.2.3 and 2.3.1), the disk evolution in simulation *D0* is not expected to produce disk wind.

5.3.1 Disk structure evolution

In Figure 5.5, the density for simulation *D0* at $t = 0t_g$ (upper left), $t = 1000t_g$ (upper right), $t = 2000t_g$ (lower left) and $t = 3000t_g$ (lower right) is presented. During the simulation time, some discontinuous structures along the radial direction at the disk surface and also inside the disk can be observed. The magnetorotational instability may be responsible for turbulence inside the disk, but it cannot cause such appearance as described in Section 2.2. Nor is the Blandford-Payne-effect able to influence the disk evolution due to the weak magnetic field. Therefore, I consider the time evolution of the density and radial velocity profile along the disk mid-plane ($\theta = \pi/2$). I find that this choked structure began with a density perturbation at the beginning of the simulation. In the data from the first saved time step ($t = 10t_g$), this perturbation showed up at the inner disk boundary, while the remaining density distribution kept the initial profile. The perturbation propagated outwards in the radial direction with the evolving time and later spread to the whole disk.

I attribute this disk density evolution to the initial condition. I argue that the non-relativistic density profile (Equation 5.2) does not fit the relativistic Paczyński-Witta velocity profile (Equation 5.1) well in the vicinity close to the black hole (the density profile determines the pressure profile inside the accretion disk, thus is also important in force balancing). In Figure 5.6, the angular velocity along the disk mid-plane is shown. In the left plot, the initial angular velocity and the angular velocity at $t = 3000t_g$ are presented. It is worth mentioning that the angular velocity along the disk mid-plane rarely evolves after $t \sim 2000t_g$. Thus, it is possible to treat the angular velocity profile at $t = 3000t_g$ as a steady state and compare it to the profile at $t = 0t_g$. In general, the initial profile has a good match to the profile at $t = 3000t_g$. Nevertheless, there is discrepancy near the black hole, especially within $r < 10r_g$. This discrepancy, namely the sub-steady rotation, will then cause a radial velocity which triggers the density perturbation and, consequently, the discontinuous structures. In Figure 5.6 right plot, I compare the angular velocity profile with different choices of R_{pw} in Equation (5.1) to the profile from simulation *D0* at $t = 3000t_g$. It turns out that no matter which R_{pw} I choose, there is always slight differences in the profile near the disk inner boundary. But a value of $R_{pw} \sim 1.7$ fits best to the long-term evolution, and thus may reduce the impact of the discrepancy. Apart from the perturbation patterns, the accretion disk basically keeps its disk-like shape as expected.

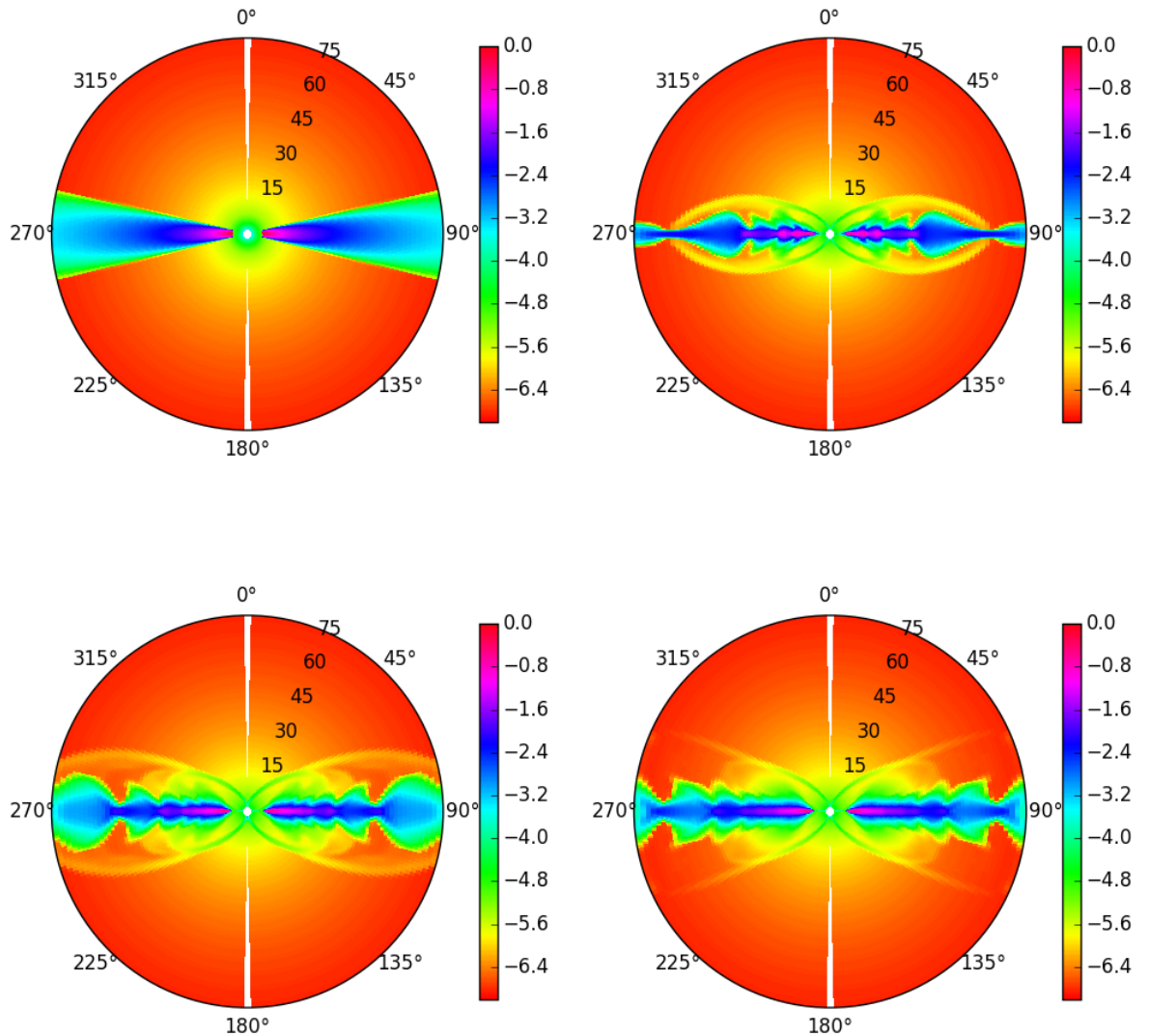


Figure 5.5: Density snapshots in logarithm from simulation $D0$ at $t = 0t_g$ (upper left), $t = 1000t_g$ (upper right), $t = 2000t_g$ (lower left) and $t = 3000t_g$ (lower right). Apart from for some turbulent structures on the surfaces, the accretion disk basically kept its disk-like shape during the time evolution and no outflow stream originates from the disk. The snapshots are presented in Kerr-Schild coordinates. As in the spherical plots in Section 4, the calculation domains only cover $\theta \in (0, 180)$ and the left hemispheres are just mirrored (same for all plots presented later).

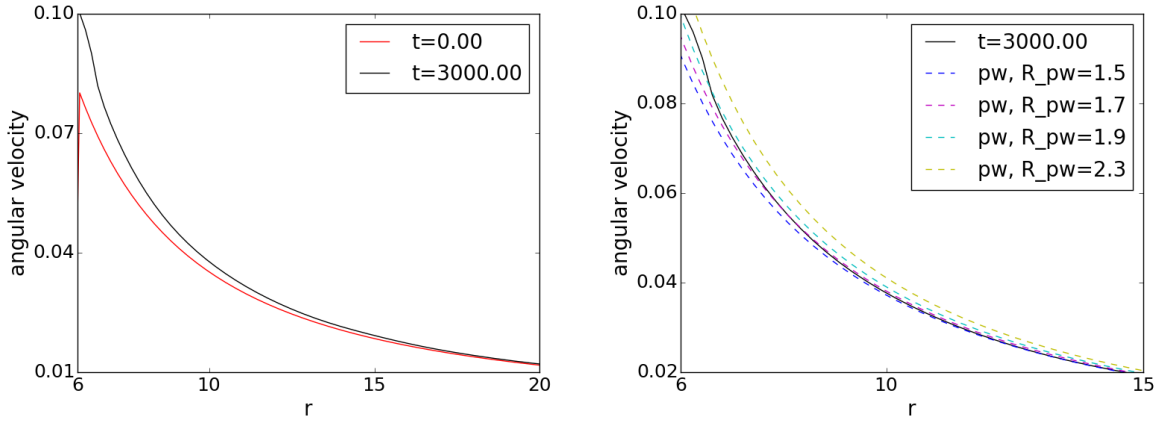


Figure 5.6: *Left*: The disk angular velocity profile for simulation $D0$ at time $t = 0t_g$ and $t = 3000t_g$. The red curve at $t = 0t_g$ also stands for the Paczyński-Witta profile with $R_{pw} = 1.0$. Through this plot, we know that the initial condition given in Equation (5.1) is very close to the angular velocity at $t = 3000t_g$, where the disk has evolved into a steady state. *Right*: A simple fit of R_{pw} in the initial angular velocity. It seems that a pure Paczyński-Witta profile is not able to fit the steady state. Yet, an initial profile with $R_{pw} \sim 1.7$ may reduce the discrepancy to the steady state. Note that the plot starts at $r = 6r_g$ since this is the disk inner radius.

5.3.2 Accretion due to MRI

The accretion rate and ejection rate for simulation $D0$ are plotted in Figure 5.7. It is shown in the time interval from $t = 1000t_g$ to $t = 3000t_g$, where the evolution of the disk is relatively steady. The outer radius for the accretion calibration is at $r = 60r_g$. Among the four plots, the amplitude of the outer accretion rate has, relatively, the largest amplitude and varying signs. This is possibly due to the density perturbation inside the disk caused by the initial condition. Since the period at $r = 60r_g$ is $T \sim 2871t_g$, nothing significant should happen at $t = 3000t_g$.

The disk inner boundary has ~ 195 rotations by $t = 3000t_g$. I thus consider the mass accretion rate at the disk inner boundary as an indicator of the angular momentum transport inside the disk. As shown in the uppermost plot in Figure 5.7, there is a continuous matter accretion which has an average of 1.36×10^{-3} , from $t = 2000t_g$ to $t = 3000t_g$ at this radius. The accretion implies that the angular momentum transport indeed took place in simulation $D0$. Since the magnetic field is weak, field lines that penetrate differentially rotating layers of the accretion disk should not play a role in accelerating and breaking plasma in the large scale. The alternative is then left to be MRI (see Section 2.2), which takes place locally inside the disk. If MRI is present in the disk, we can expect the similar wiggly field line structure as shown in Figure 2.3 (see also Balbus & Hawley 1991). To have an idea about the field structure inside the disk, I plot the radial magnetic field along θ at $r = 12.6r_g$ in Figure 5.8. Note that the rotation period here is $T \sim 258t_g$ and the disk surface extends from $\theta = 75^\circ$ to $\theta = 105^\circ$. The sign change of the radial field in the left plot reflects the curved initial magnetic field lines that penetrate the disk (see Figure 5.3). In the right plot, the frequent sign changes of the radial magnetic field (jagged curve) indicate wiggled

poloidal field lines. Furthermore, the amplitude of the wiggle structure grows during the time evolution as the radial field strength becomes larger. This behavior of the radial magnetic field strongly implies the presence of MRI. Note that the right plot in Figure 5.8 shows a growth of MRI which is symmetric to the disk mid-plane.

5.3.3 Matter collapsing towards the disk mid-plane

The ejection rate for simulation *D0* is shown in the second lowest plot of Figure 5.7. The time averaged ejection from $t = 2000t_g$ to $t = 3000t_g$ is negative. This indicates that in simulation *D0*, the matter at the disk surface collapses towards the disk mid-plane. This behavior is not yet well understood. Nevertheless, the negative ejection rate clearly indicates that there is no disk-driven wind in simulation *D0*. This proves the necessity of a large magnetic field strength in magnetically driven wind production.

5.4 Outflows from accretion disk

Simulation *D0* is the only simulation that has weak magnetic field plasma $\beta = 10$. It is also the only simulation in Table 5.1 that does not show outflows from the disk during the time evolution. The simulations with strong magnetic plasma $\beta = 10$ all show outflows, the evolution of which share many common features. Before the investigation into the properties of the outflows, I will first give a description of the general outflow morphology. Here I take simulation *D6* as the “fiducial model,” because it has the most similarities to all other simulations (see Section 5.1.4), and will focus on its results.

5.4.1 Disk evolution

The density snapshots for simulation *D6* at simulation time $t = 400t_g$, $t = 600t_g$, $t = 1000t_g$, $t = 1600t_g$, $t = 2200t_g$ and $t = 3000t_g$ are shown in Figure 5.9. The time evolution of the accretion disk shows some wave-like structure that moves from the inner disk to the outer disk along the disk mid-plane. This behavior is the disk evolution under the initial condition (see Section 5.3), but in the case of strong magnetic field. The density snapshot at $t = 3000t_g$ (lower right plot in Figure 5.9) itself looks very different compared to that of simulation *D0* (Figure 5.5). However, if we neglect the outflows in simulation *D6*, then common features in the disk shapes can be seen.

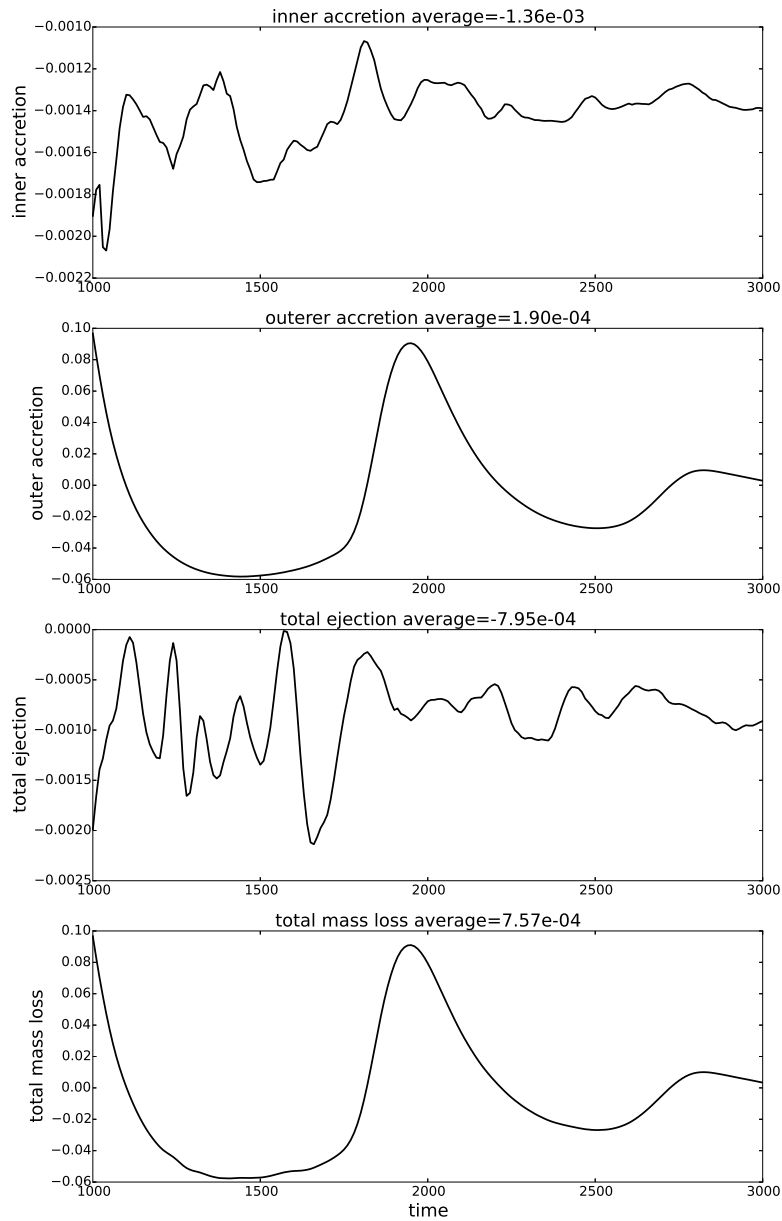


Figure 5.7: Accretion and ejection rates and their average values for simulation *D0* from $t = 1000r_g$ to $t = 3000r_g$. The outer radius for accretion calibration is set at $r = 60r_g$. The most interesting plots are the most upper plot and the second lower plot, which show the accretion and negative ejection (matter moves towards disk plane instead of ejection). The total mass loss in the control volume is dominated the second upper plot, which reflex the radial density perturbation in side the disk (see above).

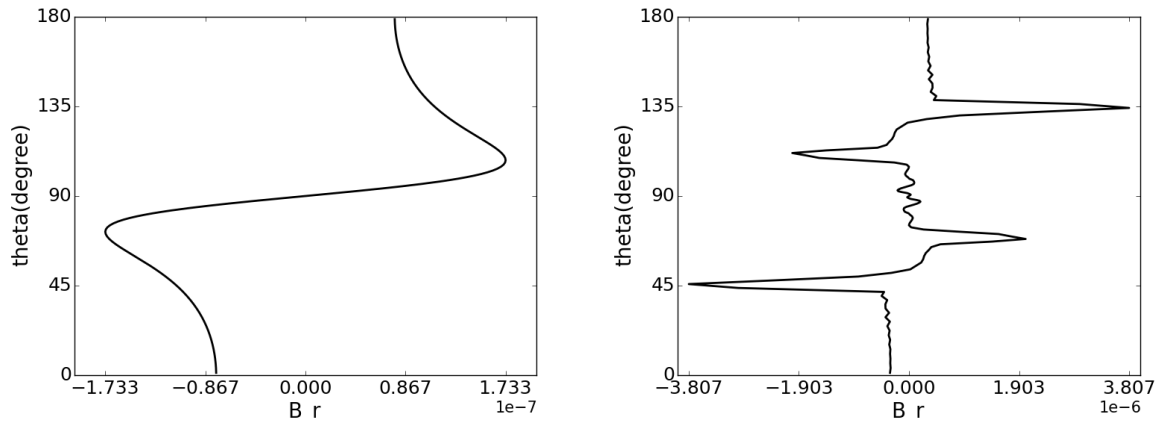


Figure 5.8: Magnetic field in the radial direction measured at $r = 12.6r_g$ at $t = 0t_g$ (left plot) and $t = 1000t_g$ (right plot). The different pointing directions of the radial magnetic field at $t = 0t_g$ is caused by the initial condition (see Figure 5.3), while the center-symmetric jagged curve within the disk range at $t = 1000t_g$ is released by MRI. Note that the curves in both plots are not magnetic field lines.

5.4.2 Disk wind evolution

As is shown Figure 5.9, clear outflows leave the disk surface during the simulation. The outflows originate from the “density bumps” at disk inner boundary caused by the initial condition (see Section 5.3). As these bumps move outwards and carry the growing outflows with them while new produced bumps near the at the inner boundary keep triggering new outflows (see the two top plots in Figure 5.9). The outflows leave further away from the disk mid-plane and show certain degree of collimation towards the axis (the middle left plot), which seems not to be the collimation process of jet (see Section 5.6). As the outflows keep growing, they begin to come out from everywhere on the disk surface, which merges with the former streams (middle right plot). Consequently a steady disk wind is generated (bottom plots). The time averaged ejection rate for simulation *D6* from $t = 2000t_g$ to $t = 3000t_g$ is 7.02×10^{-3} . Note that the only difference between simulation *D6* and *D0* is the initial plasma β (see Table 5.1). Thus the outflows we see here must be related to the strong magnetic field. I will discuss the origin of the outflows later in Section 5.6.

5.4.3 Wind radial velocity

In Figure 5.10, I plot the radial velocity for *D6* at $t = 3000t_g$. Generally, the inward velocity values (of accreting flow) are much smaller than the outward velocity values. Thus, I have applied a two color bar contrast in the left and right plots to show the different regimes. As we can see in the right plot, except for the region inside the disk and some turbulent region above the disk, the radial velocity in the wind are all above zero, insuring an outward flowing wind. We can see in the left plot that the outflow above the disk has a moderate outward radial velocity

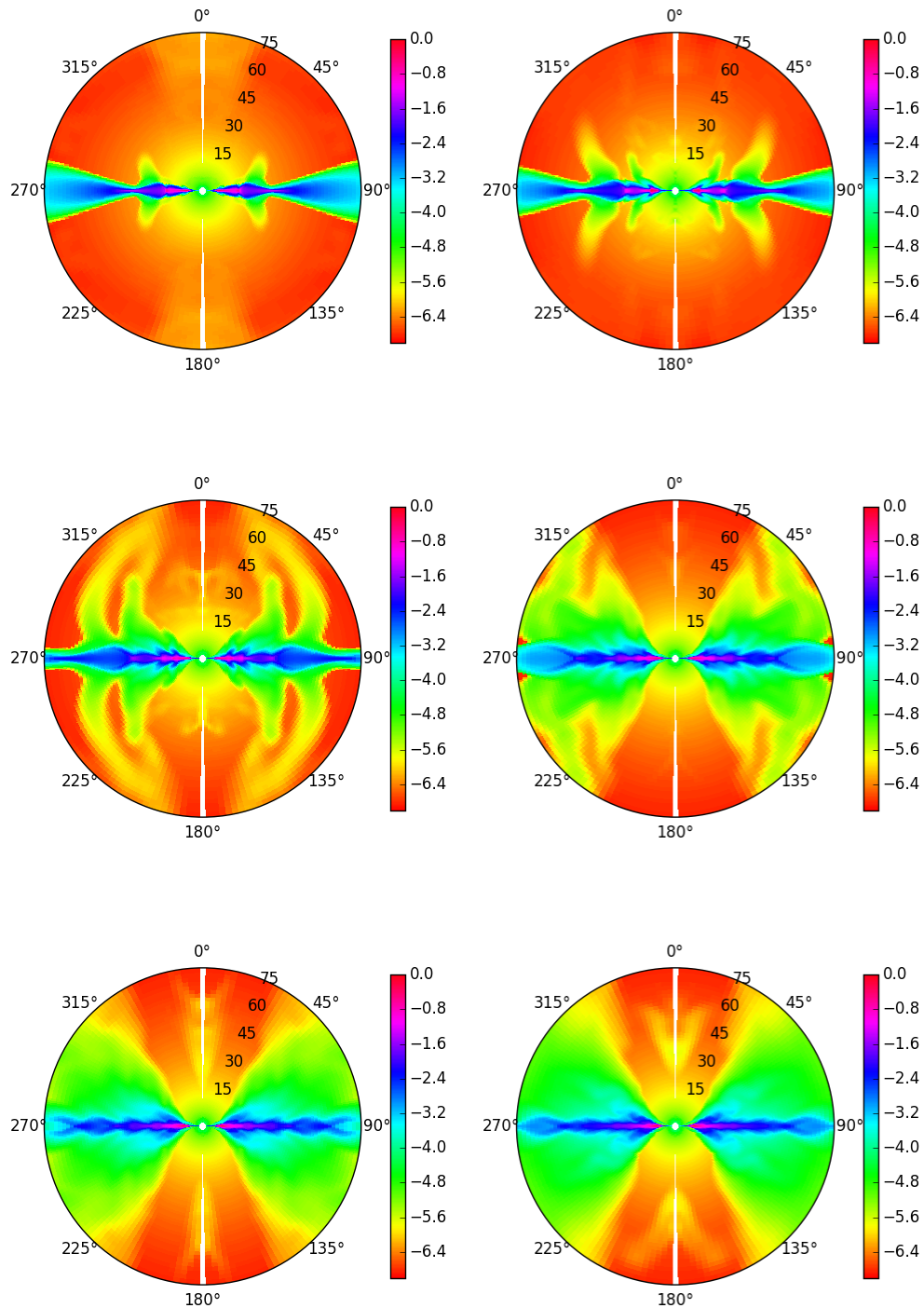


Figure 5.9: Density snapshots in logarithm from simulation *D6* at $t = 400t_g$ (top left), $t = 600t_g$ (top right), $t = 1000t_g$ (middle left), $t = 1600t_g$ (middle right), $t = 2200t_g$ (bottom left) and $t = 3000t_g$ (bottom right). During the time evolution, the process of outflow leaving the disk accretion is clearly observed. The snapshots are presented in Kerr-Schild coordinates.

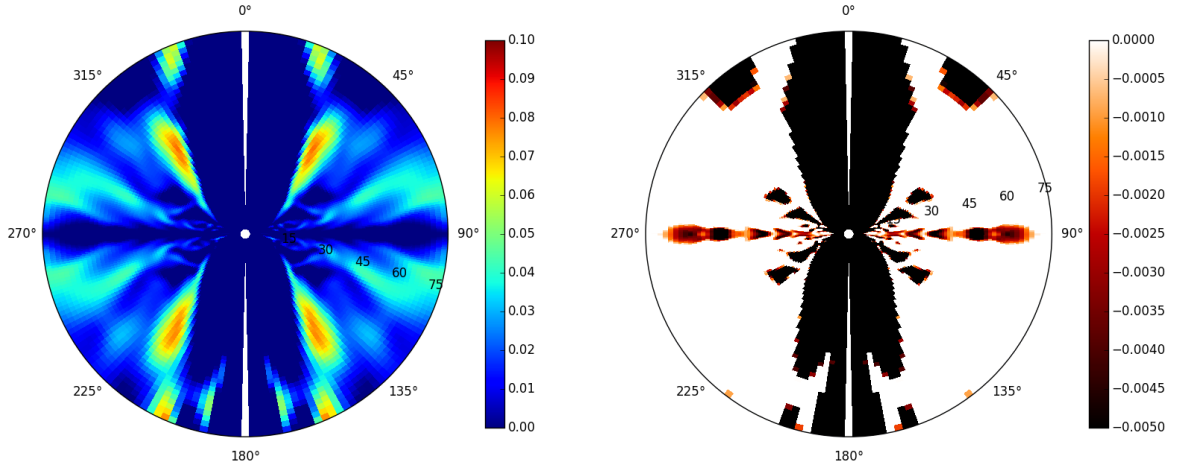


Figure 5.10: Radial velocity profile for simulation *D6* at $t = 3000t_g$ with different contrast. In the left plot, the color bar resolves values from 0 to 0.1. We see that the disk wind has a moderate outward radial velocity $v_r \lesssim 0.1$ (the velocity is normalized by c). Also, to identify the accretion region, the color bar in the right plot resolves values from -0.005 to 0.005 . With the exception of minor turbulent patterns in the wind, negative radial velocities exist only in the accretion. The typical accretion velocity is $v_r \sim 10^{-3}$.

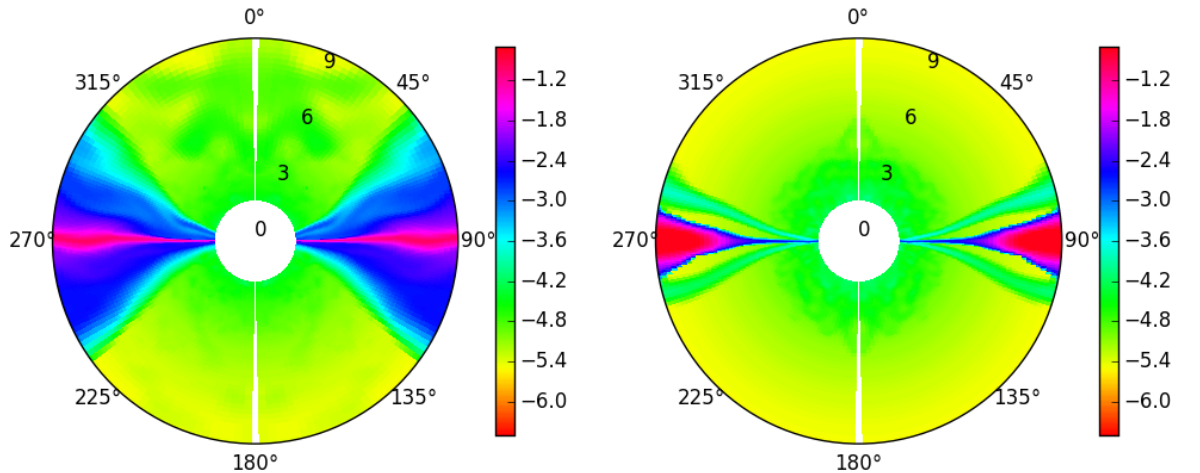


Figure 5.11: ‘Zoomed-in’ density plots in logarithm from simulations *D1* (left plot) and *D6* (right plot) at $t = 3000t_g$. The massive accretion in simulation *D1* connects the disk and the BH while in *D6* the disk inner boundary still keeps its position at the $6r_g$ with a thin flow accreting onto the BH. Note that the circle shapes in both plots come from the initial condition described in Section 5.1. The circle is more obvious in the right plot as the stable inflow stream has not yet destroyed it unlike in the left plot.

$v_r \lesssim 0.1$ (unit of velocity is c). On the other hand, the accretion (negative values) in the right plot mostly appear inside the disk. The averaged value of the radial velocity along the disk mid-plane is 1.03×10^{-3} . Although the outflowing wind is much faster than the accreting flow, the accretion and wind production processes are still in balance, if we take the density into consideration (see Figure 5.9).

5.4.4 Inner boundary of the disk

When changing the magnetic diffusivity level (parameter η_0) in the disk, an interesting behavior of disk inner boundary is observed. As was discussed in Section 1.5.2, by the presence of magnetic diffusivity allows accreting matter to pass through magnetic field lines freely and accrete onto the black hole. However, if the disk is not diffusive (like in simulation *D1*), accreting matter will drag the field lines together towards the black hole, destroying the structure of the initially well ordered field lines. The influence of magnetic diffusivity on the disk morphology can be clearly seen in Figure 5.11. The left plot shows the density snapshot of simulation *D1* at $t = 3000t_g$. Without a diffusivity that allows the matter to pass through the field lines, the massive flow accretes with the field lines and pushes the disk inner boundary towards the black hole. In this case, the accretion disk connects directly to the black hole horizon. As is shown in Figure 5.11 right plot, the magnetic diffusivity, whose value peaks at the disk mid-plane, allows an accreting flow at the disk mid-plane without disturbing the disk inner boundary. The disk inner boundary is then exactly at the initial radius $r_{in} = 6r_g$. Nevertheless, the massive accretion in simulation *D1* implies a stronger angular momentum transport inside the disk. I will discuss this point in Section 5.5.

5.5 Influence of diffusivity on accretion and ejection rates

In Section 5.4, I mentioned that the position of the disk inner boundary is influenced by the presence of magnetic diffusivity. In this context, I also ran a series of simulations *D1*, *D2*, *D3*, *D4*, *D6* and *D17* where diffusivity level (η_0) is the controlled parameter. The evolution of the outflow morphology from these simulations are all similar to simulation *D6* (see Section 5.4). However, their accretion and ejection rates are indeed influenced by different choices of η_0 .

5.5.1 Diffusivity and accretion

Simulations *D1*, *D2*, *D3*, *D4*, *D6* and *D17* have the same initial conditions except for the normalized diffusivity value η_0 , which are, 10^{-12} , 10^{-6} , 10^{-5} , 10^{-4} , 10^{-3} and 10^{-2} , respectively (see Table 5.1). As readers will see, the numerical diffusivity is still predominant in the regime $\eta_0 < 10^{-4}$ according to the simulation results. I will thus focus on the simulations *D1*, *D6* and *D17* in the discussion.

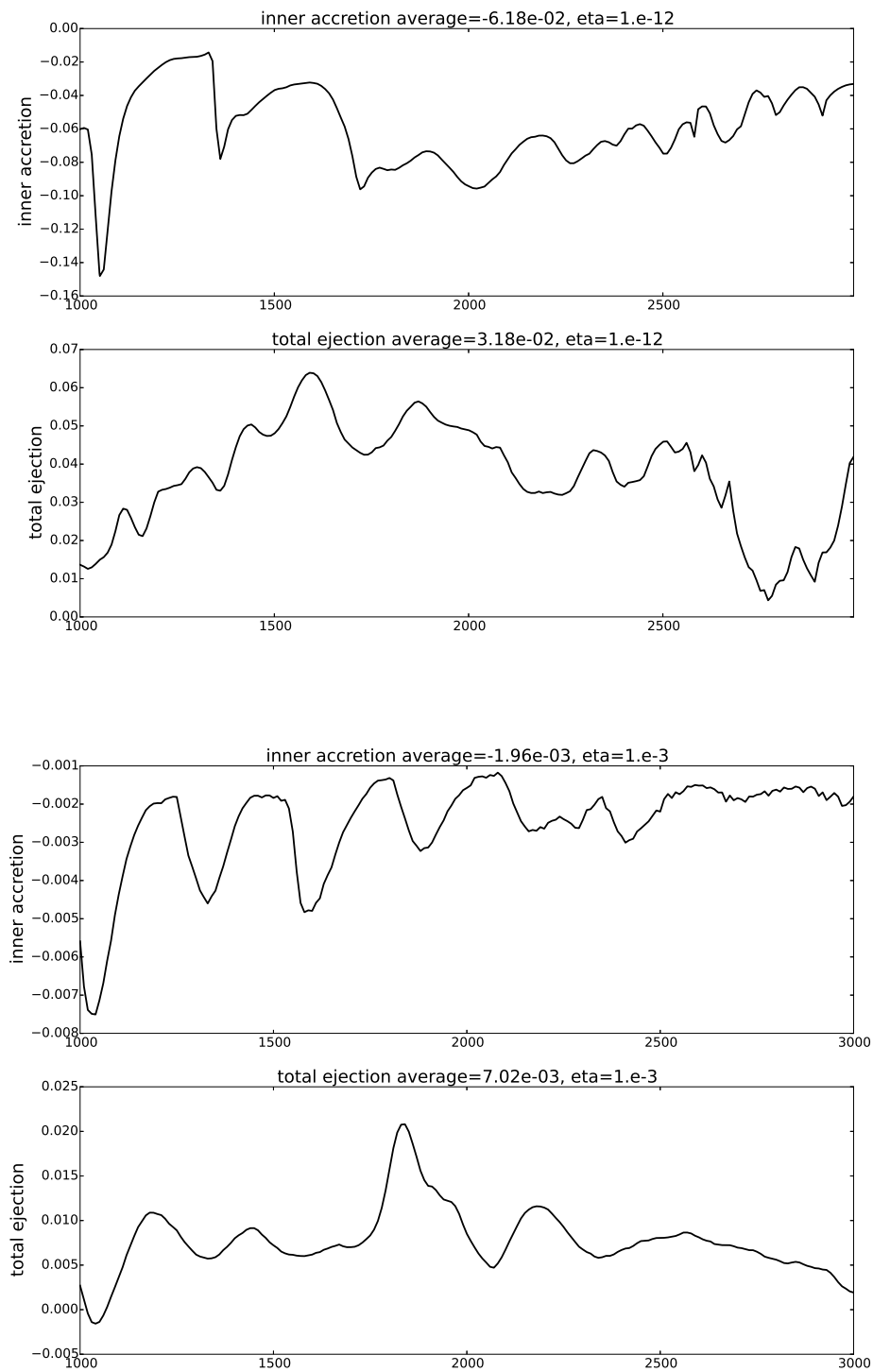


Figure 5.12: The ejection rate and the inner accretion rate for simulations *D1* (upper plots) and *D6* (lower plots) from $t = 1000t_g$ to $t = 3000t_g$. The averages are taken in the time interval from $t = 2000t_g$ to $t = 3000t_g$. The accretion and ejection rates for simulations *D1* are much larger than simulation *D6*. Nevertheless, simulation *D6* has a better efficiency in the outflow production (see text).

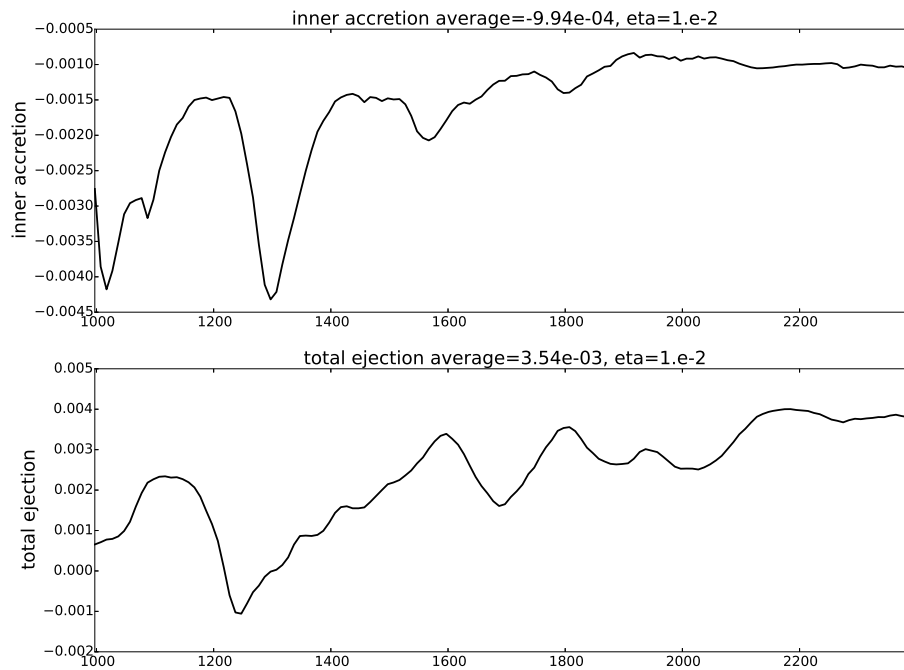


Figure 5.13: The ejection rate and the inner accretion rate for simulation *D17*. Since the simulation has not yet finished, we can only give the data from $t = 1000t_g$ to $t = 2400t_g$. The averages are taken in the time interval from $t = 2000t_g$ to $t = 2400t_g$. Due to the suppressed MRI process by the magnetic diffusivity, the accretion and ejection rates here are weaker than simulation *D6* and much weaker than simulation *D1*.

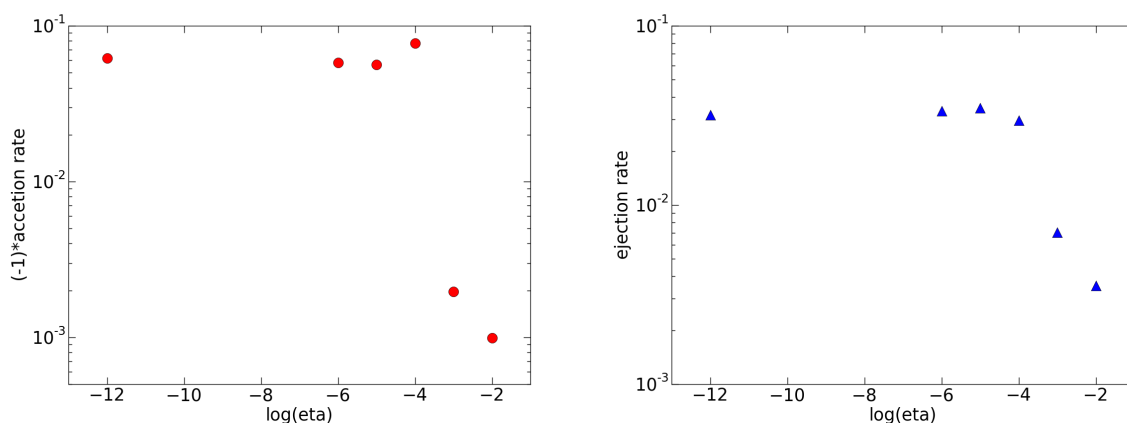


Figure 5.14: The time averaged accretion rate (left plot) and ejection rate (right plot) for simulations *D1*, *D2*, *D3*, *D4*, *D6*, *D17* with normalized diffusivity values $\eta_0 = 10^{-12}$, 10^{-6} , 10^{-5} , 10^{-4} , 10^{-3} and 10^{-2} , respectively. The averages are taken in the time interval from $t = 2000t_g$ to $t = 3000t_g$, except for simulation *D17*, which are taken in the time interval from $t = 2000t_g$ to $t = 2400t_g$ (see text). Note that the accretion rates in the left plot have been multiplied by -1 so that they could be plotted with a logarithm vertical axis.

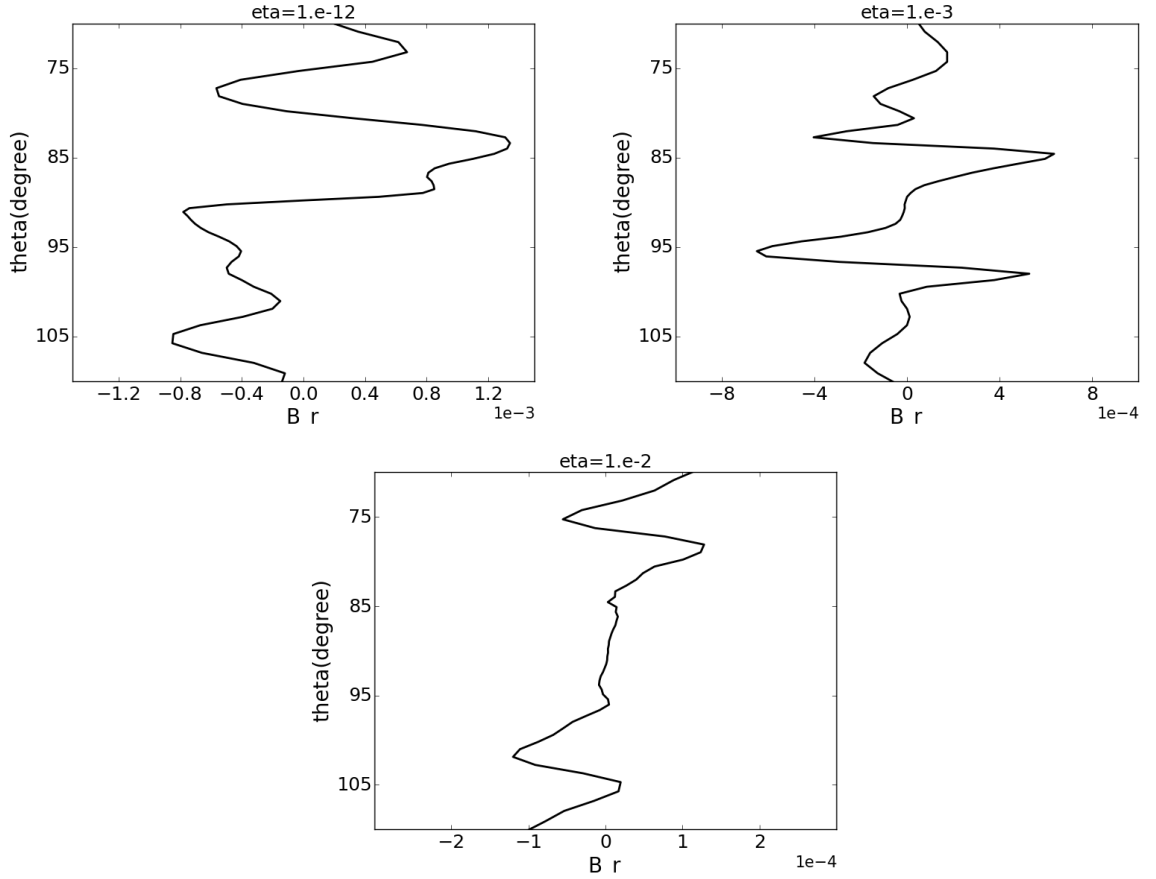


Figure 5.15: The radial component of the magnetic field for simulations *D1* (upper left), *D6* (upper right) and *D17* (lower plot) measured by $r = 12.6r_g$ at $t = 2400t_g$. Note that the disk surfaces in our disk model are at $\theta = 75^\circ$ and $\theta = 105^\circ$ and the Keplerian rotation period at radius $r = 12.6r_g$ is $239.4t_g$. Through these plots, we can see an obvious suppression from the increasing diffusivity level on the MRI inside the disk. The MRI is still growing in simulations *D6* and *D17* (simulation *D17* much weaker than simulation *D6*), while the field in simulation *D1* has already become totally turbulent (see text).

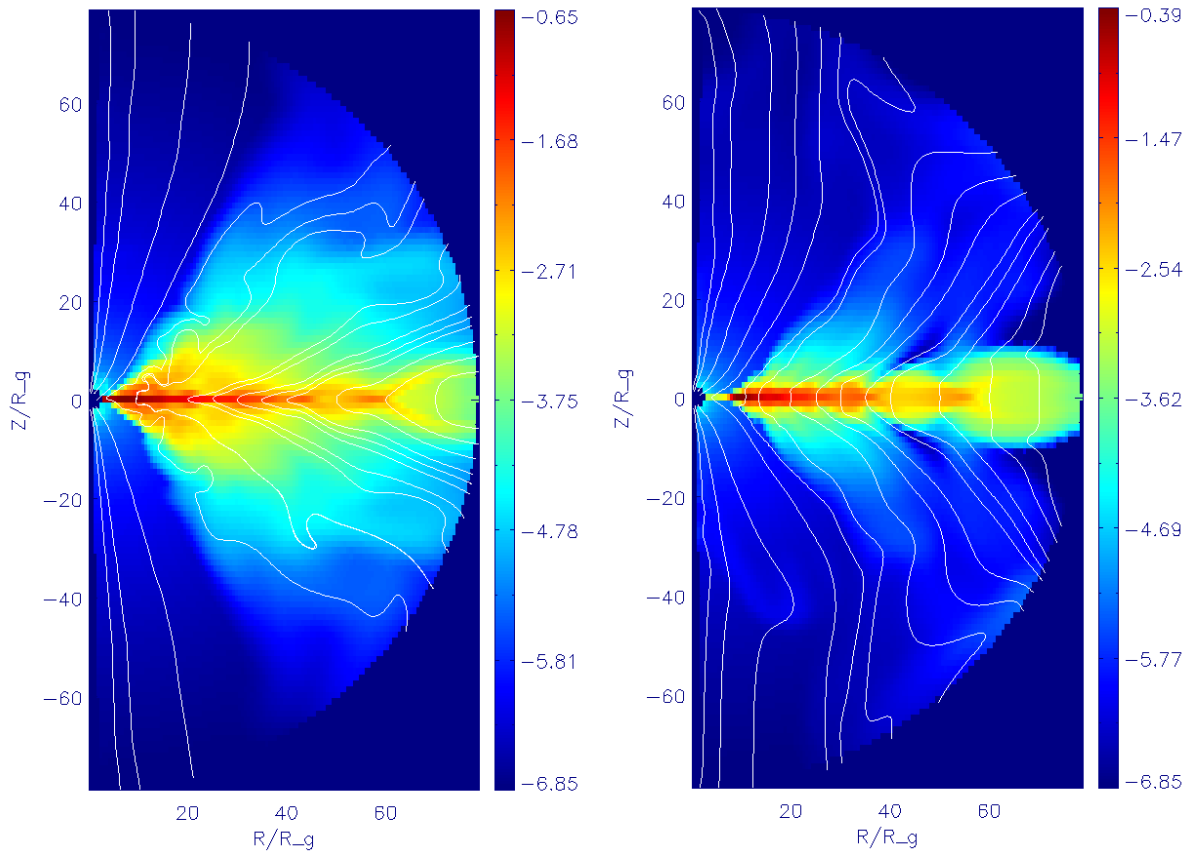


Figure 5.16: Field line structures for simulation *DI* (left plot) and *DI7* (right plot) at $t = 2000t_g$. In simulation *DI*, the field lines inside the accretion disk have become chaotic (especially within $r < 20r_g$) due to the turbulence caused by MRI. However, the field lines in simulation *DI7* still keeps their original structure at $t = 2000t_g$; the reason for this is two-fold. First, the MRI inside the disk is suppressed by the magnetic diffusivity which makes disk less turbulent than in simulation *DI*. Second, with diffusivity, the matter flow is allowed to move across the field lines, which prevent the field lines from being disturbed by the accreting flow and the turbulence inside the disk.

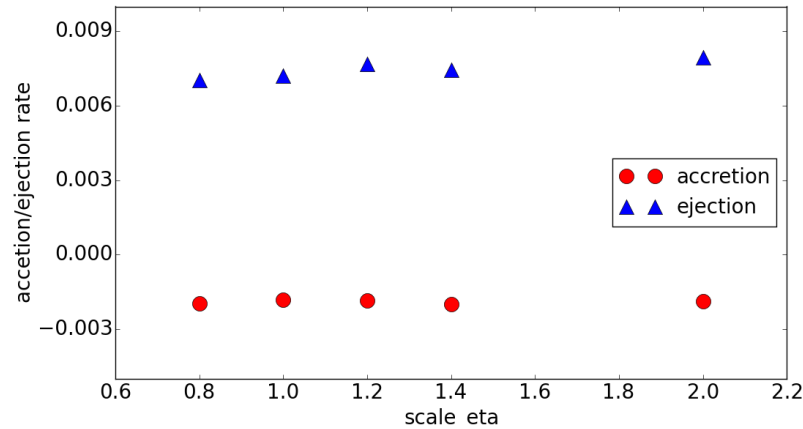


Figure 5.17: The time averaged ejection rate and the inner accretion rate for simulations *D6* ($\chi = 0.8$), *D9* ($\chi = 1.0$), *D12* ($\chi = 1.2$), *D13* ($\chi = 1.4$) and *D14* ($\chi = 2.0$). The averages are taken in the time interval from $t = 2000t_g$ to $t = 3000t_g$. As illustrated in this plot, the accretion and ejection rates do not have significant difference in this set of simulations.

First, I plot the accretion rate at the inner disk boundary and the total ejection rate for simulations *D1* and *D6* in Figure 5.12 from $t = 1000t_g$ to $t = 3000t_g$ and for simulation *D17* in Figure 5.13 from $t = 1000t_g$ to $t = 2400t_g$ (simulation *D17* is still running and $t = 2400t_g$ is the time it reached when this part of the thesis was written). The accretion rate curves in the three plots show a similar period ($\approx 300t_g$) at the time when the local accretion minima take place, e.g. at $t \sim 1000t_g$, $t \sim 1300t_g$, $t \sim 1600t_g$, etc. These local minima can also be also found in the inner accretion rate plot in Figure 5.7. I attribute this feature to the radial velocity fluctuation caused by the initial condition near the inner disk boundary where the initial angular velocity is slower than the “steady state” angular velocity (see Figure 5.6).

I then compare the time averaged accretion rate and ejection rate taken from $t = 2000t_g$ to $t = 3000t_g$ for simulations *D1* and *D6*, and from $t = 2000t_g$ to $t = 2400t_g$ for simulation *D17*. I find that the accretion and ejection rates are clearly suppressed with increasing diffusivity level. In Section 4.4, it was shown that the increasing magnetic diffusivity prevents the MRI from growing in the torus evolution and consequently weakens the accretion rate. Furthermore, I proved the existence of MRI inside the disk in Section 5.3. Thus, I argue that an increase of diffusivity suppresses the MRI, hence the angular momentum transport inside the disk (see Section 2.2), which leads to a less efficient accretion rate.

To prove this argument, I repeat the method used in Section 5.3. We plot the radial component of the magnetic field along θ in Figure 5.15 for simulations *D1* in upper left plot, *D6* in upper right plot and *D17* in the lower plot. The radial magnetic fields are measured by $r = 12.6r_g$ at $t = 2400t_g$. I only show the region $\theta \in [70^\circ, 110^\circ]$ since the disk surfaces in our disk model are at $\theta = 75^\circ$ and $\theta = 105^\circ$. The Keplerian rotation period at radius $r = 12.6r_g$ is $239.4t_g$ and at $t = 2400t_g$, there have been about 10 rotation periods, which is far beyond the linear MRI regime in ideal MHD (see Balbus & Hawley 1991). In the upper left plot, an asymmetric profile of

the radial magnetic field is observed which implies that the field in simulation *D1* has become turbulent at $t = 2400t_g$. On the other hand, in the upper right plot and the lower plot, we can still see the symmetric wave-like structure to the disk mid-plane showing the growing MRI. The amplitudes of the radial magnetic field oscillations largely decreases with the increasing η_0 which strongly supports the argument that the MRI is suppressed by the diffusivity.

In Figure 5.14, the time averaged inner accretion rate (left plot) and the ejection rate (right plot) for the simulations *D1*, *D2*, *D3*, *D4*, *D6* and *D17* are presented. In the regime $\eta_0 < 10^{-4}$, the simulations are dominated by the numerical diffusivities so the increasing η value does not influence the accretion and ejection. However, above $\eta_0 = 10^{-4}$, the increasing diffusivity obviously weakens the accretion rate through the suppression of the MRI inside the disk. In Figure 5.14, a correlation between accretion rate and ejection rate is clearly seen. A larger ejection rate always corresponds to a larger accretion rate. Although, the exact process of how (a part of) accreting matter is turned into outflow is unclear. We can still explain this relation with the following simple logic: a larger accretion rate implies a stronger angular momentum transport inside the disk where more angular momentum is transported outwards, and thus yields a larger ejection rate.

With the current grid resolution (numerical diffusivity), the correlation between accretion and ejection rates can be better investigated by a rHARM survey that searches the parameter space $10^{-4} < \eta_0 < 10^{-2}$.

5.5.2 Efficiency of outflow launching

In Figure 5.14, we notice that the simulations with high diffusivity have higher efficiencies in disk outflow production. Here the outflow efficiency is defined as

$$\xi = \left| \frac{\dot{M}_{eje}}{\dot{M}_{acc}} \right| \times 100\% \quad (5.9)$$

where \dot{M}_{eje} and \dot{M}_{acc} are the total ejection rate and the inner accretion rate defined in Section 5.2. The efficiency for simulation *D1* from $t = 2000t_g$ to $t = 3000t_g$ is 51%, while those for simulations *D6* and *D17* are 358% and 356%. The outflow production efficiencies of a high diffusive disk are much larger than that of a low diffusive disk.

This behavior can be attributed to the field line structure above the disk. According to the Gaussian-like diffusivity profile (see Equation 5.6), the region above the accretion disk can be treated as in ideal MHD. In this case, the disk winds only flow along the field lines. The process of outflow leaving the disk surface is more efficient if the field line that penetrates the disk surface is smoother pointing to the region above the disk (just like the initial field structure in Figure 5.3). In other words, a knotted (chaotic) field line will, to some extent, prevent a smooth outflow launching process (see also Section 5.6 for the discussion over the forces that drive the disk wind).

In Figure 5.16, we show the field line structures for simulation *D1* (left plot) and *D17* (right plot) at $t = 2000t_g$. In the non-diffusive simulation *D1*, the matter flow inside the disk becomes

turbulent due to the MRI, which also disturbs the initial field lines inside the disk. The perturbed field structure inside the disk then also influences the structure above the disk, making it chaotic and consequently jams the outflow efficiency. On the hand, due to the influence of the high diffusivity, the field lines in simulation *D17* keep their initial shape by allowing the matter flow to across the field lines inside the disk. The smooth field structure lets the outflow in simulation *D17* leave the disk more easily in comparison to that in simulation *D1*.

5.5.3 Simulations with different diffusivity profile

As defined in Equation (5.6), the parameter χ controls the width of the diffusivity profile. I thus select simulations *D6*, *D9*, *D12*, *D13* and *D14*, the initial conditions of which only differ in the choices of χ , to investigate the influence of diffusivity profiles with different widths. In this set of simulations, the parameter χ varies from 0.8 (narrower than disk height) to 2.0 (twice the disk height). The time averaged inner accretion rates and the ejection rates from the simulations do not significantly differ from each other as shown in Figure 5.17. This can be explained as a combined effect from a wider diffusive region. On one hand, a wider diffusive region in θ allows more matter to pass the magnetic field lines at certain radii. On the other hand, the diffusivity also suppresses the MRI in this region. The two effects compensate each other, thus the accretion rate does not vary with χ . The ejection rate follows accretion rate (see above), thus also keeps the value. Thus, I conclude that changing the width of the diffusivity profile in this range does not significantly affect the disk evolution much.

5.6 The driving force of outflow

In Section 5.4, I described the morphology of the disk driven outflow in simulation *D6*. It is now important to determine the origin that drives the wind from the disk and whether the Blandford-Payne process is actually observed or not. The best way to do this is to calculate the different force components along the magnetic field lines. Similar analysis have been done in Porth & Fendt (2010) (see also Ouyed & Pudritz 1997; Fendt & Čemeljić 2002). Nevertheless, such analysis requires a steady state where the physical quantities in the simulation region are only position dependent. This condition is well satisfied in Porth & Fendt (2010), where the simulation regions do not include the accretion disk. In such kind of simulation, the outflows come from the (injection) boundary condition which is supposed to be the accretion disk surface.

None of the simulations, all of which include a “real” disk, listed in Table 5.1 have reached such a steady state within the simulation time (see Figure 5.20 of simulation *D6* as an example). For this reason, the displacement current in the simulation results is not zero (see Equation 5.14). Thus the force analysis of diffusive GR-MHD is much more complicated than in Porth & Fendt (2010) and cannot be completely included in this thesis project. I will thus give a preliminary analysis based on the pressures from different force components and conceptually discuss the roles of

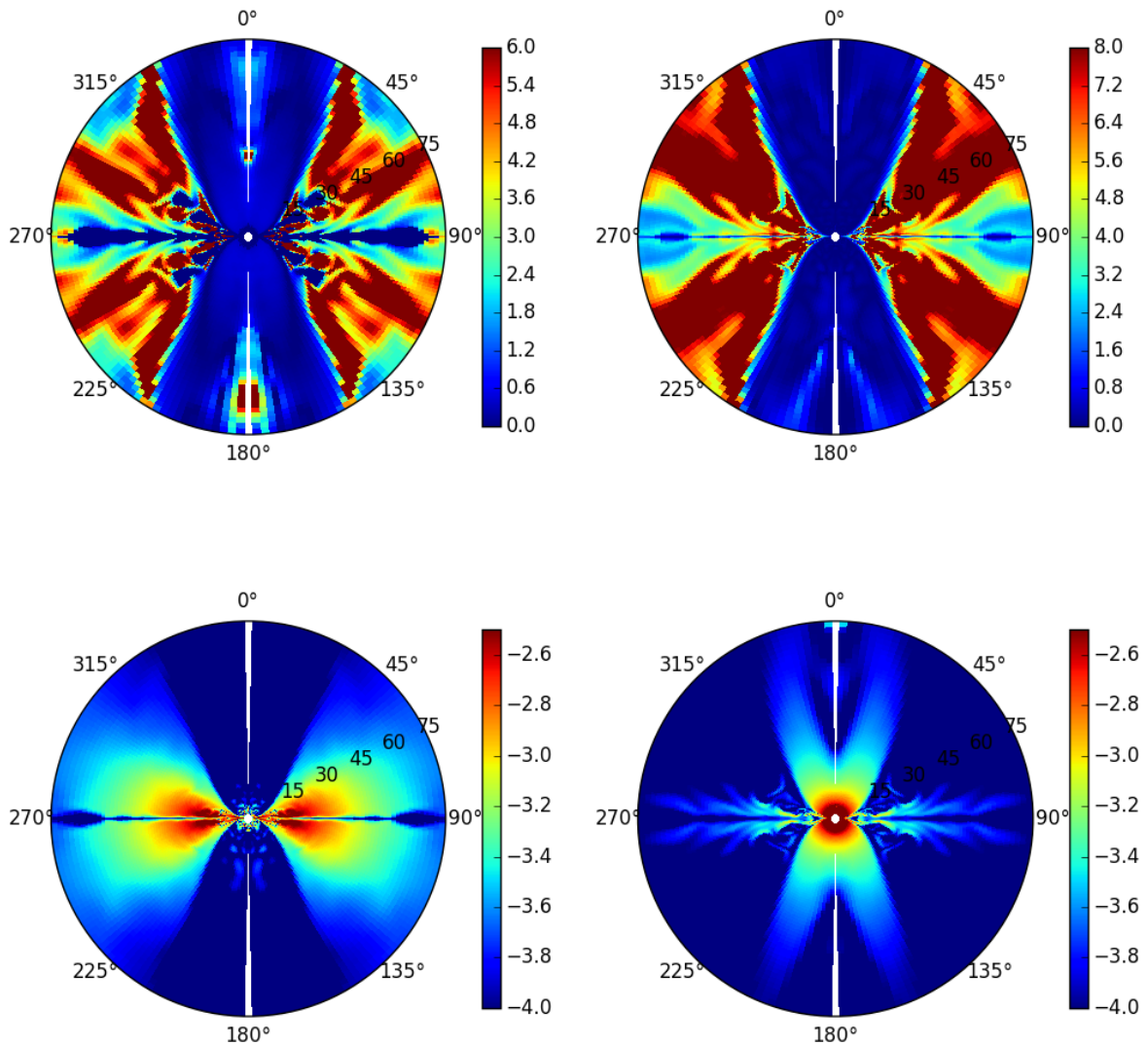


Figure 5.18: The magnetic field characters for simulation $D6$ at $t = 3000t_g$ represented by the Alfvén Mach number (upper left), ratio of poloidal field strength divided by toroidal field strength (upper right), toroidal field strength in logarithm (lower left) and poloidal field strength in logarithm (lower right). According to the plots, the disk outflow becomes almost immediately super-Alfvénic after leaving the disk surface and the strength of the toroidal magnetic field is much larger than that of the poloidal field. To some extent, these facts refute the possibility that the disk wind is driven by centrifugal force, that is, the BP process.

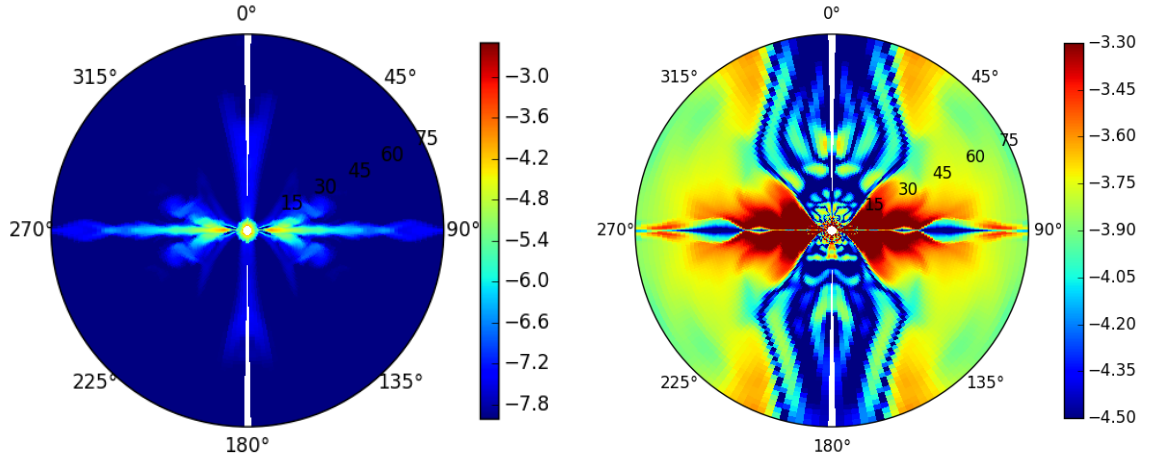


Figure 5.19: *left*: The thermal pressure in logarithm for simulation D6 at $t = 1000t_g$. The thermal pressure shown in this plot is comparable to the magnetic field strength inside the disk, however, it decays exponentially from the disk mid-plane and quickly becomes much smaller than the magnetic field strength. Therefore, the thermal pressure cannot be the dominant factor in the wind production/acceleration. *right*: The toroidal magnetic field strength for simulation D6 at $t = 1000t_g$. According to this plot, the concentration behavior towards the axis in Figure 5.9 is not the “true collimation” caused by Lorentz force.

the centrifugal force, the magnetic force and the thermal pressure force. In the following, I take simulation D6 as the subject of the discussion. Letter “p” in the subscript denotes the poloidal component of a vector where the ϕ component is not considered. The ϕ component is the toroidal component of a vector.

5.6.1 Poloidal Alfvén Mach number

If the disk wind is driven centrifugally (Blandford-Payne effect), we can expect a poloidal magnetic field to dominate the region above the disk surface since the wind should be centrifugally accelerated by the poloidal magnetic field. This can be represented by the poloidal Alfvén Mach number defined by ¹

$$M_{A,p} = \sqrt{\frac{4\pi h u_p^2}{B_p^2}}, \quad (5.10)$$

with the specific plasma enthalpy

$$h = \frac{\gamma}{\gamma - 1} \frac{P}{\rho} + 1. \quad (5.11)$$

¹Note that we set $\mu_0 = 1$ (see Section 1.6), thus the factor 4π in Equation (5.10) is not included in our calculation.

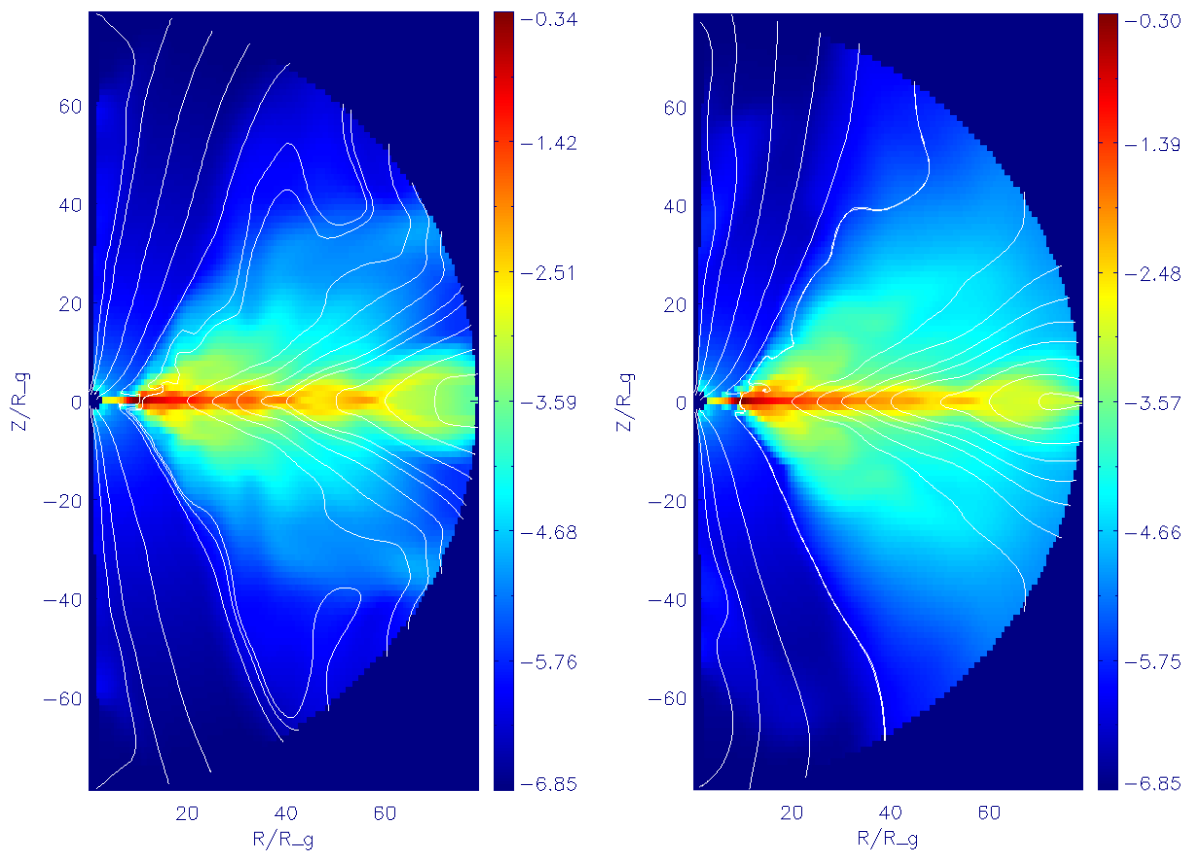


Figure 5.20: Field line structure for simulation *D6* at $t = 2000t_g$ (left plot) and $t = 3000t_g$ (right plot). Although the accretion and outflow become relative steady during this period, the state of the whole system, especially the structure of field lines, still evolves during the time forwarding, making it impossible to do a force analysis along the field lines.

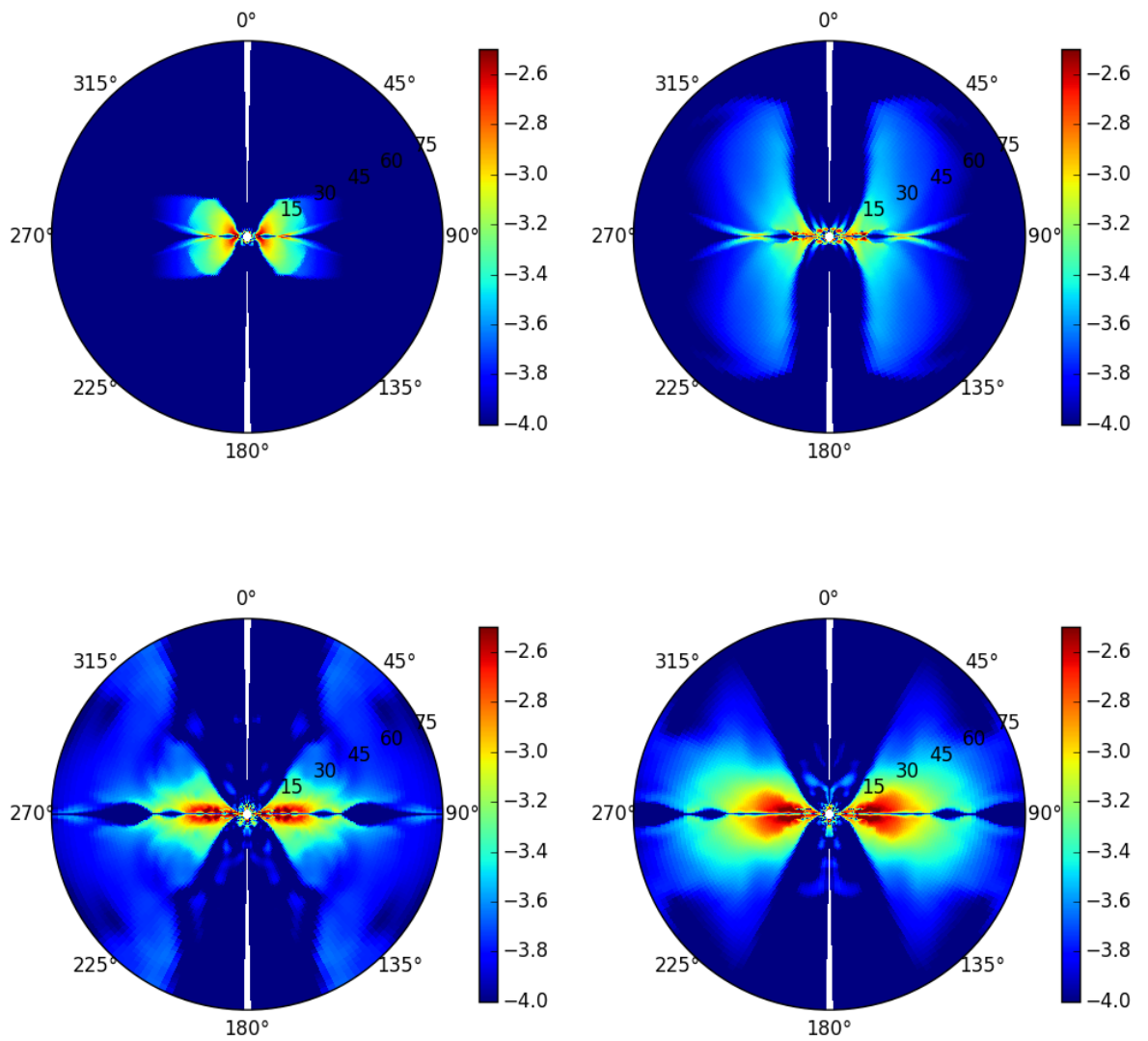


Figure 5.21: Time evolution of the toroidal field strength in logarithm for simulation *D6* at $t = 100t_g$ (upper left), $t = 300t_g$ (upper right); $t = 1100t_g$ (lower left) and $t = 2000t_g$ (lower right), see also the lower left plot in Figure 5.18 for $t = 3000t_g$. It is evident that the propagation of the toroidal field in the direction vertical to the disk plane, which supports the outflow we see in simulation *D6*, is related to tower jets (see corresponding text).

The Alfvén Mach number can be interpreted as the kinetic energy divided by the magnetic pressure. A super-Alfvénic value ($M_{A,p} > 1$) thus implies a weak poloidal magnetic field with a large flow density or velocity. Under such circumstance, a driving outflow by the Blandford-Payne effect is difficult.

The poloidal Alfvén Mach number for simulation *D6* at $t = 3000t_g$ is plotted in Figure 5.18 (upper left plot). We see that despite some minor turbulent regions in the outflow, the disk wind becomes almost immediately super-Alfvénic after leaving the disk surface (defined in Section 5.2). Inside the outflow region, typical values of $M_{A,p}$, at the height of $30r_g$ from the disk mid-plane (5 times the initial disk inner radius) are over 5. On the other hand, the $M_{A,p}$ still keeps being sub-Alfvénic ($M_{A,p} < 1$) over the height of ~ 20 times the disk inner radius in Porth & Fendt (2010). This may arise from the difference between the choice of the accretion disk and injection boundary condition. In rHARM simulations, the fluid element inside the disk has only toroidal rotation initially. By the injection boundary condition in Porth & Fendt (2010), the inflow possesses an initial poloidal velocity that can keep magnetic field lines from bending to toroidal directions due to the ideal MHD assumption explained in Section 1.4.2. The super-Alfvénic Mach numbers starting from the disk surface implies, to some extent, that the outflow is not accelerated magneto-centrifugally (Blandford-Payne effect).

5.6.2 Magnetic field pressure

I then examine at the Lorentz force component in the wind system. The magnetic diffusivity we apply has a Gaussian profile which peaks at disk mid-plane and decays quickly towards the rotating axis (see Equation 5.6 and Figure 5.2). Thus, the ideal MHD condition

$$\mathbf{E} = -\mathbf{v} \times \mathbf{B}, \quad (5.12)$$

can be applied in the region above the disk. For the current density \mathbf{j} , we have ²

$$\mathbf{j} + \frac{\partial \mathbf{E}}{\partial t} = \nabla \times \mathbf{B}. \quad (5.13)$$

Combining Equation (5.12) and (5.13), we get

$$\mathbf{j} - \frac{\partial(\mathbf{v} \times \mathbf{B})}{\partial t} = \nabla \times \mathbf{B}. \quad (5.14)$$

Due to the fact that further analysis with the displacement current would be very complicated and that the poloidal velocity is less than $0.1c$, I neglect the second term on the left side of Equation (5.14) and adopt

$$\mathbf{j} = \nabla \times \mathbf{B}. \quad (5.15)$$

The Lorentz force acting per unit volume on the fluid carrying the current is then

$$\begin{aligned} \mathbf{F}_L &= \mathbf{j} \times \mathbf{B} \\ &= (\nabla \times \mathbf{B}) \times \mathbf{B}. \end{aligned} \quad (5.16)$$

²Again, factors 4π and c do not show up because of the normalization.

With the corresponding vector identity, we can rewrite the above equation as

$$\mathbf{F}_L = -\nabla B^2 + (\mathbf{B} \cdot \nabla)\mathbf{B}. \quad (5.17)$$

Equation (5.17) indicates that the Lorentz force is directly related to the gradient of \mathbf{B} or B^2 . In Figure 5.18, we show the toroidal magnetic field strength $\sqrt{B^\phi B_\phi}$ (lower left plot) and poloidal magnetic field strength $\sqrt{B^p B_p}$ (lower right plot). If we neglect the disk mid-plane where toroidal field cannot be produced by the disk rotation, then we see the toroidal field strength is decreasing along the radius and also from the disk mid-plane to the vertical direction in the outflow region, which builds the gradient outwards. Thus the toroidal magnetic pressure is likely to drive the disk wind outwards.

For the poloidal field, the field strength decreases outwards inside the outflow region as well (see Figure 5.18 lower right plot). However, as also reflected in the Alfvén Mach number profile (Figure 5.18 upper left plot), the poloidal magnetic field does not have much strength compared to the toroidal field above the disk (inside the outflow). If the poloidal field strength itself is small, a large gradient from it cannot be neglected. Although the poloidal field strength in the vicinity around the disk rotational axis shows a large outward gradient, it cannot contribute too much to the wind acceleration too much since the density in these regions is extremely low (see Figure 5.9).

The ratio between the toroidal field and the poloidal field (not in logarithm) is shown in Figure 5.18 upper right plot. It is clear in this plot that the toroidal field strength is much larger than the poloidal field strength in almost the entire outflow region. This also implies that the BP process is not predominant in driving disk wind.

5.6.3 Thermal pressure

Another force that could drive outflow from the disk is the thermal pressure force, which is simply the gradient of thermal pressure. To have an idea of the thermal pressure contribution, I plot the thermal pressure profile in Figure 5.19. A strong gradient at the disk surface is seen. Also, the thermal pressure in the flow region is tiny. This implies that the thermal pressure contributes to the outflow acceleration only near the disk surface. But similar to the poloidal field strength, the pressure drops quickly from the disk mid-plane. Furthermore, the amplitude of the thermal pressure is overall, magnitudes smaller than the toroidal magnetic field strength in the outflow region. Thus, I conclude that the Lorentz force produced by the toroidal field is predominant in driving the disk wind in simulation *D6*.

5.6.4 Tower jet

In Lynden-Bell (1996), it was suggested that the acceleration of the outflow may also come from the pressure gradient of the toroidal magnetic field. An earlier numerical study (Ustyugova et al.

1995) has also reported that in the ideal MHD simulations, where the accretion disk was treated as a boundary condition, the rotation of the disk twisted the initial poloidal magnetic field. This twist then propagates into the corona pushing and collimating matter into jet-like outflows in a cylindrical region. The jets are then interpreted as “growing towers of twisted magnetic field together with the currents that they carry.”

I plot the time evolution of toroidal field strength in logarithm in Figure 5.21. It is clear to see the propagation of the toroidal field in the direction that is vertical to the disk plane (the growing tower) in the time evolution. Through such evolution, the toroidal field strength and its pressure gradient are spreading outwards. Additionally, in Section 5.6.2 and 5.6.3, I have showed that the poloidal magnetic pressure and the thermal pressure are negligible compared to the toroidal magnetic pressure in the outflow region above the disk. The toroidal magnetic field plays the most important role in the wind generation. Thus, the outflow we see in simulation *D6* is very likely a tower jet.

5.6.5 Collimation or not?

In Figure 5.9, the behavior of the outflow density at time $t = 600t_g$ and $t = 1000t_g$ show some degree of collimation towards the rotating axis at the simulation board. In jet production, the forces that contribute to the collimation are gravity and the Lorentz force. Here I focus on the collimation through the electromagnetic effect. Since the poloidal magnetic pressure is negligible compared to the toroidal magnetic pressure at the location where the collimating behavior occurs, I plot the toroidal field strength in Figure 5.19 right plot. In general, the correlation between the magnetic pressure differences and the “collimation places” are not clear. The toroidal field (magnetic pressure) difference at $r \sim 45r_g$ seems to match the “collimation” at $r \sim 45r_g$ in the middle left plot of Figure 5.9. Nevertheless, the magnetic pressure difference that matches the “collimation” at $r \sim 60r_g$ is hardly to be seen in the right plot of Figure 5.19. Furthermore, Figure 5.21 shows that the local minimum and maximum of the toroidal field strength disappear as the time evolves. Thus, these “collimation” behavior we see in Figure 5.9 is more likely to be caused by the turbulence from the early stage of the simulation which disappear when the evolution of the outflow becomes relative steady.

5.6.6 Comparison to non-relativistic simulations

Simulations with a similar setup as discussed above have also been presented in [Sheikhnezami et al. \(2012\)](#), where the common magnetic diffusivity profile and initial magnetic field are shared. In that work, the time evolution of the accretion disk structure had also been self-consistently taken into account. However, the disk density profile in [Sheikhnezami et al. \(2012\)](#) was taken from [Zanni et al. \(2007\)](#) and their simulation code does not include relativity, which differs from my disk simulations in Table 5.1. In their low plasma- β ($\beta = 10$) simulations, the magnetocentrifugal acceleration is the most efficient mechanism in outflow production, while for weak magnetic

fields, it is the toroidal magnetic pressure gradient which drives the outflow (tower jet).

In the disk simulations with rHARM where the plasma β values are also 10, the toroidal magnetic fields are much larger than the poloidal fields during the time evolution (see above), making it very unlikely to have an outflow dominated by magnetocentrifugal force. Nevertheless, since it is impossible to project different forces along the field lines in the analysis of my simulations, I cannot determine if the outflow production is dominated by centrifugal forces or the toroidal magnetic pressure gradient.

5.7 Convergence issue in simulations *D8* and *D16*

As in the torus simulations (see Section 4.2), we also encounter convergence problem in simulations *D8*, *D15* and *D16*. The bad convergences started at the outer calculation boundary near around the rotational axis and spread toward the outflow and the disk, making the simulation results unphysical before they reached time $t = 3000t_g$. Thus, in the discussion below (see Section 5.8 and Chapter 6), I will only use the data in the time range prior to the bad convergences, which contaminated the evolutions of these simulations.

5.8 The initial field structure dependence

In order to investigate the influence of the initial field inclination on the outflow generation, we have run simulations *D5* and *D8*. Together with simulation *D6*, these three simulations have the same setup except for the magnetic field inclination parameter m , where $m = 0.2$ in simulation *D5*, $m = 0.4$ in simulation *D6* and $m = 0.6$ in simulation *D8*. A smaller m value indicates a initial field line structure that is more inclined towards the disk mid-plane. The initial field structures of simulation *D5* and *D8* are shown in Figure 5.22 while that of simulation *D6* is shown in Figure 5.3 (it does not matter here that the plot is made from the initial condition of simulation *D1* since the different diffusivity setup is not drawn on the plot).

We first plot the accretion rate from the inner disk boundary and the ejection rate from $t = 1000t_g$ to $t = 3000t_g$ for simulation *D5*. The shape of the inner accretion rate and the ejection rate curves do not seem to have correlation with the two plots in Figure 5.12. It is possible that the alteration of the initial magnetic field line structure changes the process of the disk evolution. One can see from the plot that the absolute value of the time averaged inner accretion and the total ejection rate from $t = 2000t_g$ to $t = 3000t_g$ for simulation *D5* are both weaker than simulation *D6*.

Since simulation *D8* encountered a convergence issue, we can only use the data from $t < 1200t_g$ when comparing simulations *D5*, *D6* and *D8*. We thus calculated the time averaged inner accretion rate and total ejection rate for the three simulations in the time between $t = 500t_g$ and $t = 1200t_g$ in Figure 5.24. The plot illustrates clear relations between parameter m and accre-

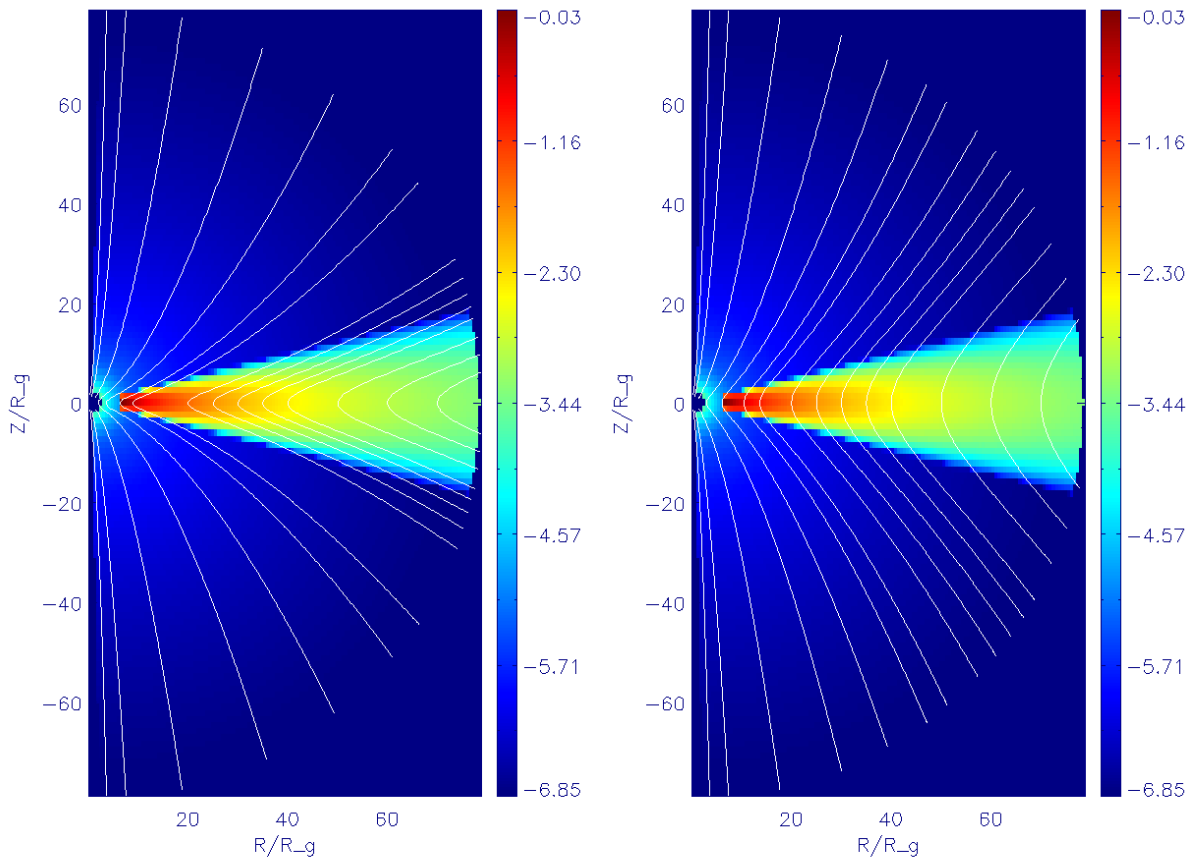


Figure 5.22: Initial field line structure for simulations $D5$ with parameter $m = 0.2$ (left plot) and $D8$ with parameter $m = 0.6$ (right plot). The smaller the parameter m is, the more the field lines are inclined to the disk mid-plane. See also Figure 5.3 for the initial field line structure with parameter $m = 0.4$.

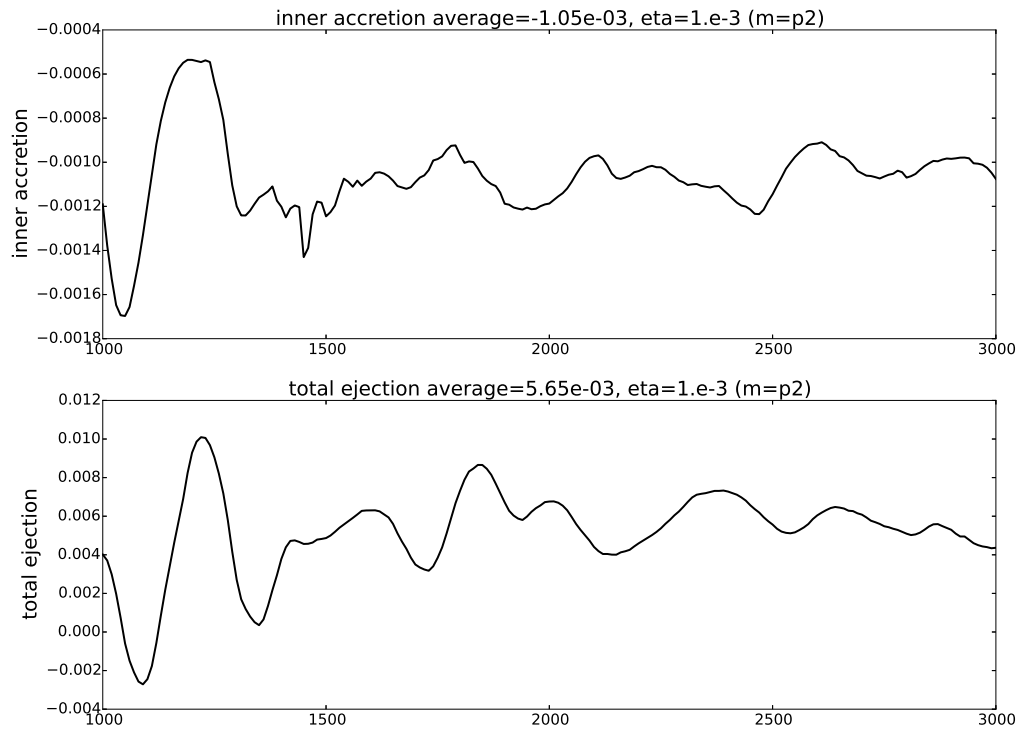


Figure 5.23: The ejection rate and the inner accretion rate for simulation $D5$ from $t = 1000t_g$ to $t = 3000t_g$. The averages are taken in the time interval from $t = 2000t_g$ to $t = 3000t_g$. The accretion and ejection rates for simulations $D5$ are both weaker than simulation $D6$.

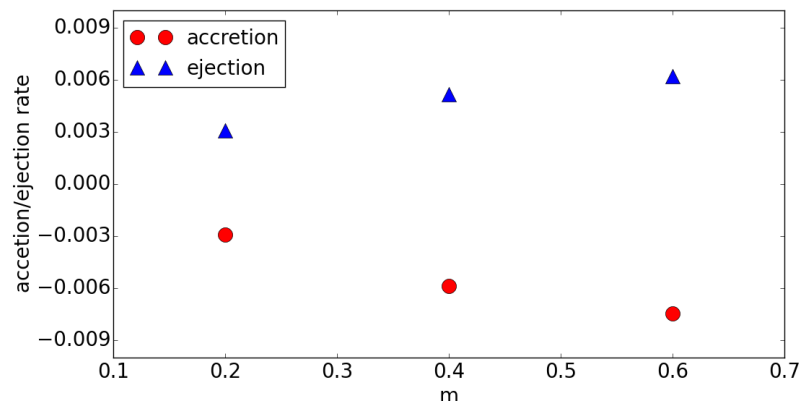


Figure 5.24: The time averaged ejection rate and the inner accretion rate for simulations $D5$, $D6$ and $D8$ (see x axis ticks). The averages are taken in the time interval from $t = 500t_g$ to $t = 1200t_g$ where the outflow states from the simulations are not yet steady. According to this plot, the accretion is enhanced by the increasing parameter m . As well as the corresponding ejection rate. This implies a “more vertical” field is more efficient in the outflow production in our simulations.

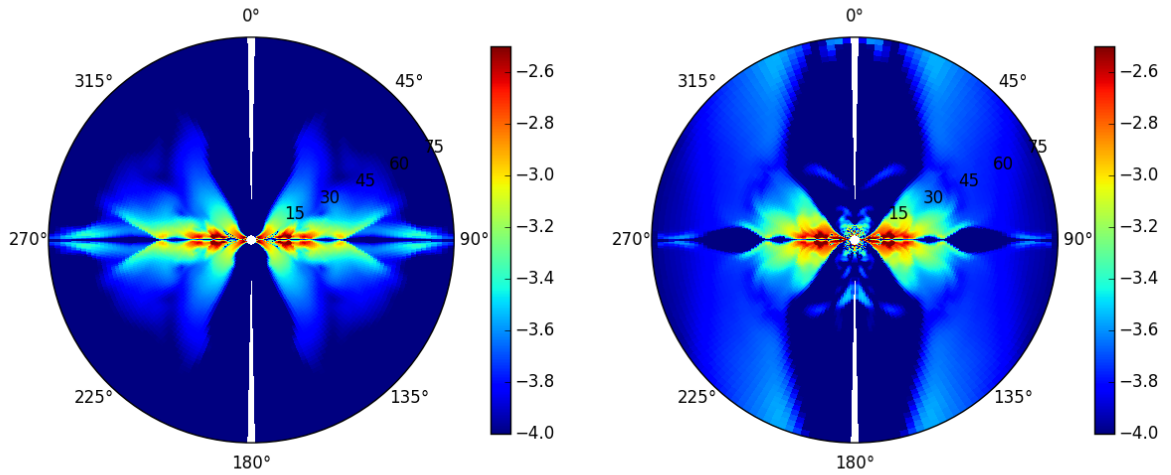


Figure 5.25: The toroidal field strength in logarithm for simulation *D5* (left plot) and *D8* (right plot) at time $t = 1000t_g$. These plots imply that a “more vertical” field structure allows for a faster propagation of the toroidal field in the vertical direction. The wine glass shape in the right plot shows the boundary of the outflow from simulation *D8* at the aforementioned simulation time.

tion/ejection rate. A larger m (“more vertical” field lines) gives a stronger outflow and, as a matter of angular momentum transport, a heavier accretion. From Section 5.6, we know that the largest contribution of the outflow driving comes from the toroidal magnetic field. The two plots in Figure 5.25 show the toroidal magnetic field strength of simulation *D5* (left plot) and simulation *D8* (right plot). Readers can also take the lower left plot in Figure 5.21 as a reference, just note that this plot is made for $t = 1100t_g$. We can then argue that a “more vertical” initial field structure leads to a faster growth of the toroidal field in the vertical direction and, in our simulation setup, stronger accretion and ejection.

Nevertheless, due to the time limitation of my thesis, only three simulations were done for this investigation which could be inadequate. Furthermore, and the plot in Figure 5.24 was made in the time interval where the disk outflows are not yet steady. Thus, more simulation results are needed in order to support the conclusion argued here.

5.9 The resolution dependence of the simulations

As discussed in Section 5.5, I observed a numerical diffusivity $10^{-4} \lesssim \eta_{\text{num}} \lesssim 10^{-3}$ in the survey with simulations *D1*, *D2*, *D3*, *D4*, *D6* and *D17*. Although simulation *D6* with grid resolution 128×128 shows accretion and ejection rates that are clearly influenced by the magnetic diffusivity (see Figure 5.14), it is still unknown how much the numerical diffusivity has influenced the

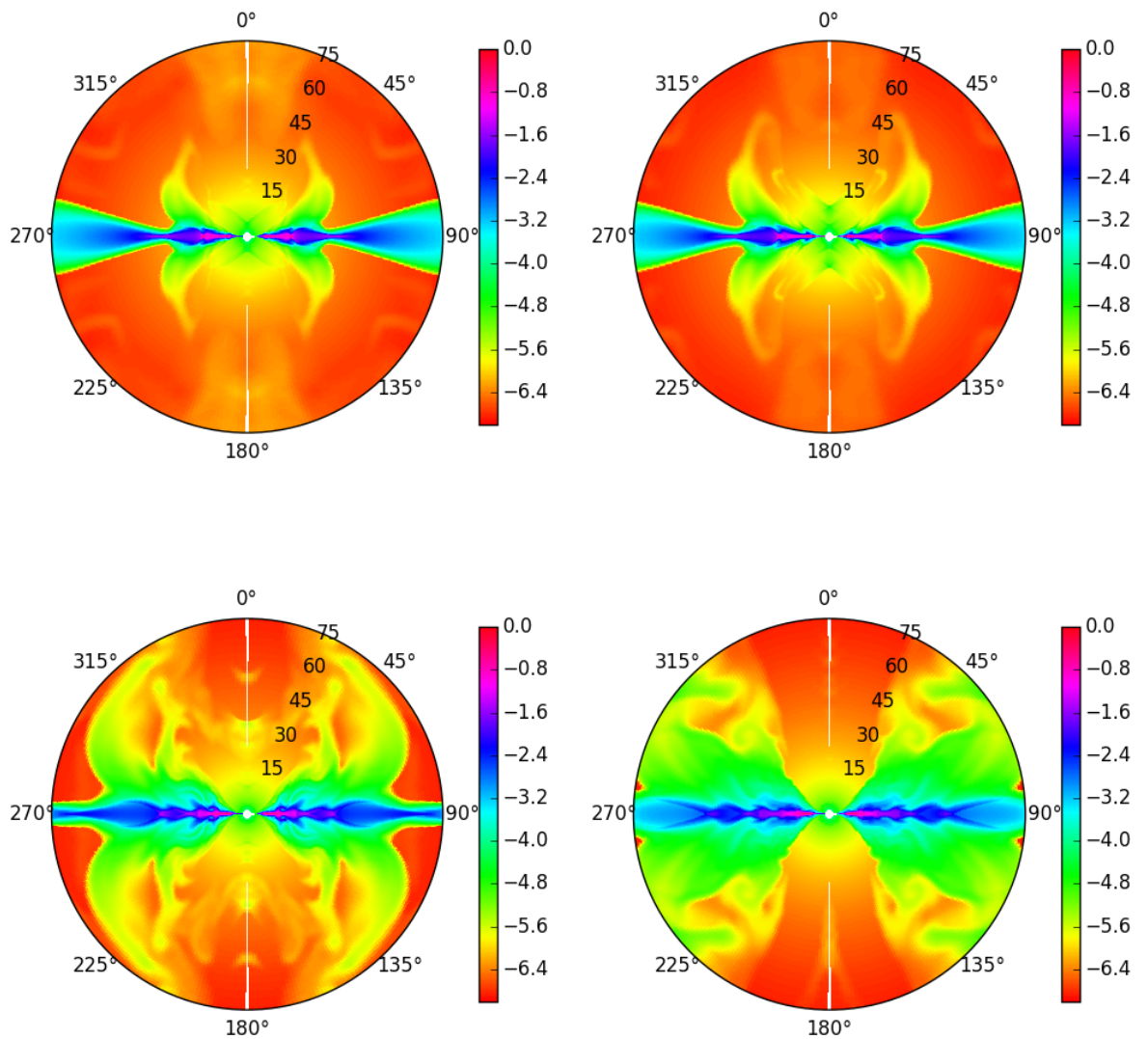


Figure 5.26: Density snapshots in logarithm from simulation *D7* at $t = 400t_g$ (top left), $t = 600t_g$ (top right), $t = 1000t_g$ (lower left) and $t = 1600t_g$ (lower right). The snapshots are presented in Kerr-Schild coordinates. The morphology of the disk wind evolution show differences when compared to simulation *D6* in Figure 5.9, which has the same initial condition but a lower resolution.

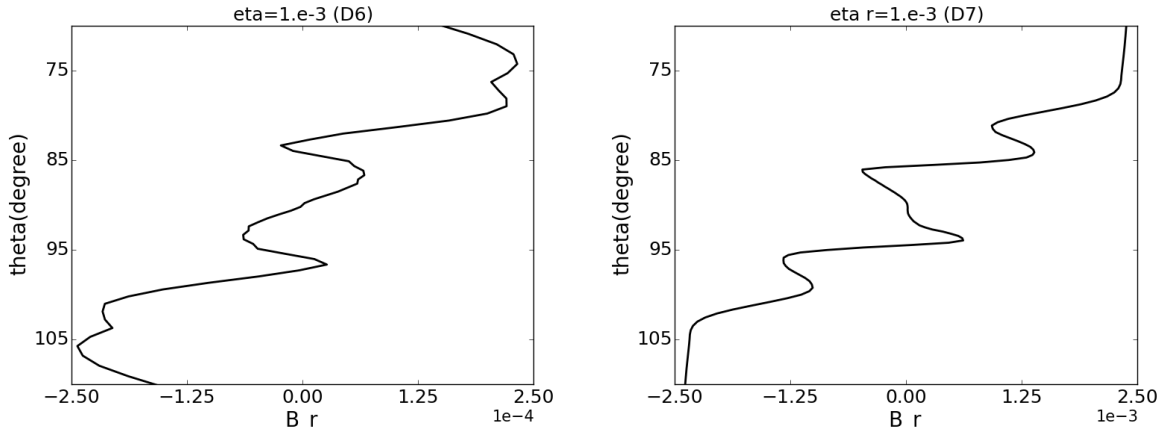


Figure 5.27: The radial component of the magnetic field vector for simulations *D6* (left) and *D7* (right) measured by $r = 12.6r_g$ at $t = 1000t_g$. Note that the disk surfaces in the disk model are at $\theta = 75^\circ$ and $\theta = 105^\circ$, the Keplerian rotation period at radius $r = 12.6r_g$ is $239.4t_g$. The resolution of simulation *D7* doubles that of simulation *D6* in both dimensions that provides the time evolution with less numerical diffusivity.

results of simulation *D6*. Thus, I ran simulation *D7* which has the same initial conditions as in simulation *D6* but double the grid resolutions (256×256) in both dimensions. With this higher resolution, the influence of the numerical diffusivity on simulation *D7* (when still noticeable at all), must be much smaller than on simulation *D6*.

Since the current rHARM code is not in parallel, running an rHARM simulation is time consuming, e.g., the running time of simulation *D6* was about four weeks. For this reason, simulation *D7* which has a higher resolution, is still running at time $t = 1650t_g$ when this part is written. I thus only discussed the data before $t = 1600t_g$ from simulation *D7* here. In Figure 5.26, I present the density snapshot for simulation *D7* at time $t = 400t_g$, $t = 600t_g$, $t = 1000t_g$ and $t = 1600t_g$. Compared to the corresponding plots for simulation *D6* in Figure 5.9, similar processes of outflow leaving disk surfaces can be observed for both simulations. Nevertheless, the disk wind production of the two simulations obviously differ from each other in fine details. These differences can only be attributed to the different grid resolutions, specifically the different levels of numerical diffusivity in both simulations.

I then calculate the time averaged accretion rate for simulations *D6* and *D7*, which are -3.45×10^{-3} and -6.6×10^{-3} , respectively, and the time averaged ejection rate which are 6.41×10^{-3} and 5.66×10^{-3} , respectively. The averages are taken from $t = 1000t_g$ to $t = 1600t_g$. The accretion rate for simulation *D7* almost doubles that for simulation *D6*, while the ejection rate for simulation *D7* is only slightly less than that for simulation *D6*. This is a strong indication for the fact that the numerical diffusivity in simulation *D6* weakens the MRI process inside the disk. The disk in simulation *D6* will then be less turbulent and have a lower level of angular momentum transport, hence weaker accretion rate, than in simulation *D7*. To confirm this, I again plot the radial component of the magnetic field vector inside the disk at $r = 12.6r_g$ for both simulations at $t = 1000t_g$. In Figure 5.27), it is clear to see in these plots, that the growth of MRI

in simulation *D6* is much slower than that in simulation *D7*. Since the MRI growth is slower in simulation *D6*, the magnetic field lines above the disk will be less disturbed in simulation *D6* than in simulation *D7* (see Section 5.5). Thus the ejection efficiency defined by Equation (5.9) is also higher in simulation *D6* (186%) than in simulation *D7* (86%).

According to the discussion above, a resolution higher than 128×128 is recommended to eliminate the influence of numerical diffusivity in my simulation with magnetic diffusivity $\eta_0 = 10^{-3}$. Taking into account that the time forwarding of the code evolution depends on the resolution of the physical length and the value of magnetic diffusivity (see Equation 3.34), higher resolutions mean a huge amount of computing time in running the simulations. With the current version of rHARM, running a simulation with normalized magnetic diffusivity η_0 from 10^{-4} to 10^{-2} , in the same grid resolution as in simulation *D7*, would be unrealistic for a typical usual science project. Thus the parallelization of rHARM is strongly called for!

5.10 Summary and conclusions

In this chapter, I have presented results of MHD launching of disk winds from a thin accretion disk threaded by inclined open poloidal field lines. The results are preliminary since the simulations have not yet reach a quasi-steady state of accretion-ejection that is known from non-relativistic simulations.

I first discussed the results from the simulation with a non-diffusive very weakly magnetized (plasma- $\beta = 10^8$) disk around a zero-spin black hole, in which no outflow was observed and the accretion disk kept its disk-like shape during the evolution. I showed the MRI growth inside the accretion disk which led to the accretion of matter onto the black hole. As far as I know, this is the first time that MRI is directly observed inside the thin accretion disk in a GR-MHD simulation.

In the same simulations with a strong magnetic field (plasma $\beta = 10$), disk wind ejections are clearly detected. I then investigated the relation between accretion and ejection rates and the different levels of diffusivity. In my analysis, I found that (i) the increasing diffusivity level suppresses the MRI process inside the disk and lowers the matter accretion rate onto the black hole. The accretion rate from the simulation with diffusivity normalization factor 10^{-4} is about 10^2 times larger than that from the simulation with diffusivity normalization factor 10^{-2} , (ii) a lower accretion rate is always accompanied by a lower disk wind ejection rate, thus the increasing diffusivity level also weakens the disk wind ejection rate, and (iii) the increasing diffusivity level helps preventing the magnetic field above the disk from turbulent structure. Although the accretion rate is 10^2 times weaker, the ratio of ejection rate to accretion rate from the simulation with diffusivity normalization factor 10^{-2} is almost 8 times larger than that from the simulation with diffusivity 10^{-4} .

From my analysis, I attributed the predominant driving force of the disk wind launching in the

simulations with strong magnetic field to the toroidal magnetic field pressure gradient. I showed that the contributions from the poloidal field pressure gradient and thermal pressure gradient are minor for wind launching. It is not yet clear if the jet is driven centrifugally since the force projection analysis along the steady field lines is not possible here. Additionally, the simulations with the “more vertical” initial magnetic fields (less inclined towards disk mid-plane) show stronger accretion and ejection rates because of the faster propagation of toroidal magnetic fields in the vertical direction.

Finally, I showed that the numerical diffusivity has noticeable influences on the current survey simulations with grid resolution 128×128 . The huge time consumption for a higher resolution survey strongly suggests the parallelization of rHARM.

Table 5.1: Parameter choice in the thin disk simulations that use rHARM. The table shows the value of normalized magnetic diffusivities (defined in Section 5.1), plasma β , the scale of diffusivity profile (defined in Section 5.1), the large scale field line inclination parameter m , the black hole spin parameter a and grid resolutions that are used in the torus simulations. All simulations were done by rHARM. Please see Section 5.1 for other common setups.

	η_0	plasma β	χ	m	a	grid size
<i>D0</i>	10^{-12}	10^8	0.8	0.4	0	128x128
<i>D1</i>	10^{-12}	10	0.8	0.4	0	128x128
<i>D2</i>	10^{-6}	10	0.8	0.4	0	128x128
<i>D3</i>	10^{-5}	10	0.8	0.4	0	128x128
<i>D4</i>	10^{-4}	10	0.8	0.4	0	128x128
<i>D5</i>	10^{-3}	10	0.8	0.2	0	128x128
<i>D6</i>	10^{-3}	10	0.8	0.4	0	128x128
<i>D7</i>	10^{-3}	10	0.8	0.4	0	256x256
<i>D8</i>	10^{-3}	10	0.8	0.6	0	128x128
<i>D9</i>	10^{-3}	10	1.0	0.4	0	128x128
<i>D10</i>	10^{-3}	10	1.0	0.4	0.1	128x128
<i>D11</i>	10^{-3}	10	1.0	0.4	0.2	128x128
<i>D12</i>	10^{-3}	10	1.2	0.4	0	128x128
<i>D13</i>	10^{-3}	10	1.4	0.4	0	128x128
<i>D14</i>	10^{-3}	10	2.0	0.4	0	128x128
<i>D15</i>	10^{-3}	10	1.0	0.4	0.5	128x128
<i>D16</i>	10^{-3}	10	1.0	0.4	0.9375	128x128
<i>D17</i>	10^{-2}	10	0.8	0.4	0	128x128

Chapter 6

Accretion system with rotating black hole

One of the key points in this thesis project is studying the role that a rotating black hole plays in the energy output of the black hole accretion system. In the seminal paper [Blandford & Znajek \(1977\)](#), it was proven that the presence of magnetic field lines around the black hole horizon can extract rotational energy from the central rotating black hole. According to the theory and the existing simulation results (see Section 2.4.2), the power of the energy extraction rises with the increasing black hole spin parameter a . I thus, as a further study of Chapter 5, pick out the series of simulations $D9$, $D10$, $D11$, $D15$ and $D16$ (see Table 5.1) for analysis. Since simulations $D15$ and $D16$ encounter convergence issues (see Section 5.8), I will only discuss the simulation time before $t = 800t_g$ which is the limit of simulation $D16$ where its time evolution is still physical. Due to the time limitation of my PhD project, the discussions in this chapter regarding the disk simulation results are mostly preliminary.

6.1 Influence of the black hole spin on accretion and ejection

The initial conditions are the same in simulations $D9$, $D10$, $D11$, $D15$ and $D16$ except for their black hole spin parameters a , which are 0, 0.1, 0.2, 0.5 and 0.9375, respectively. I first plot the density snapshots for simulations $D9$ and $D16$ at times $t = 200t_g$, $t = 400t_g$, $t = 600t_g$ and $t = 800t_g$ (Figure 6.1 and Figure 6.2). Simulation $D9$ shows the time evolution for a non-rotating black hole. Its only difference compared to simulation $D6$ is the profile of magnetic diffusivity (parameter χ). If we look at the corresponding plots in Figure 5.9, we see that the disk wind evolution in simulation $D9$ is very similar to that in simulation $D6$. Simulation $D16$ has the largest spin parameter $a = 0.9375$. We see that there are outflows leaving the disk surface as well. Nevertheless, the morphology of the outflows is different from that in simulation $D9$. If we compare the two upper plots in Figure 6.1 and Figure 6.2, from the first density “bump” on the disk mid-plane moving outwards, there is a clear outflow production in simulation $D9$ but no outflow production in simulation $D16$. At $t = 800t_g$, there are already two outflow streams leaving the disk surfaces in the 2D snapshot in simulation $D9$, while there is only one in simulation $D16$. Thus, the high black hole spin is indeed influencing the disk wind evolution.

In Figure 6.3, I show the time averaged accretion and ejection rates for simulations $D9$, $D10$, $D11$,

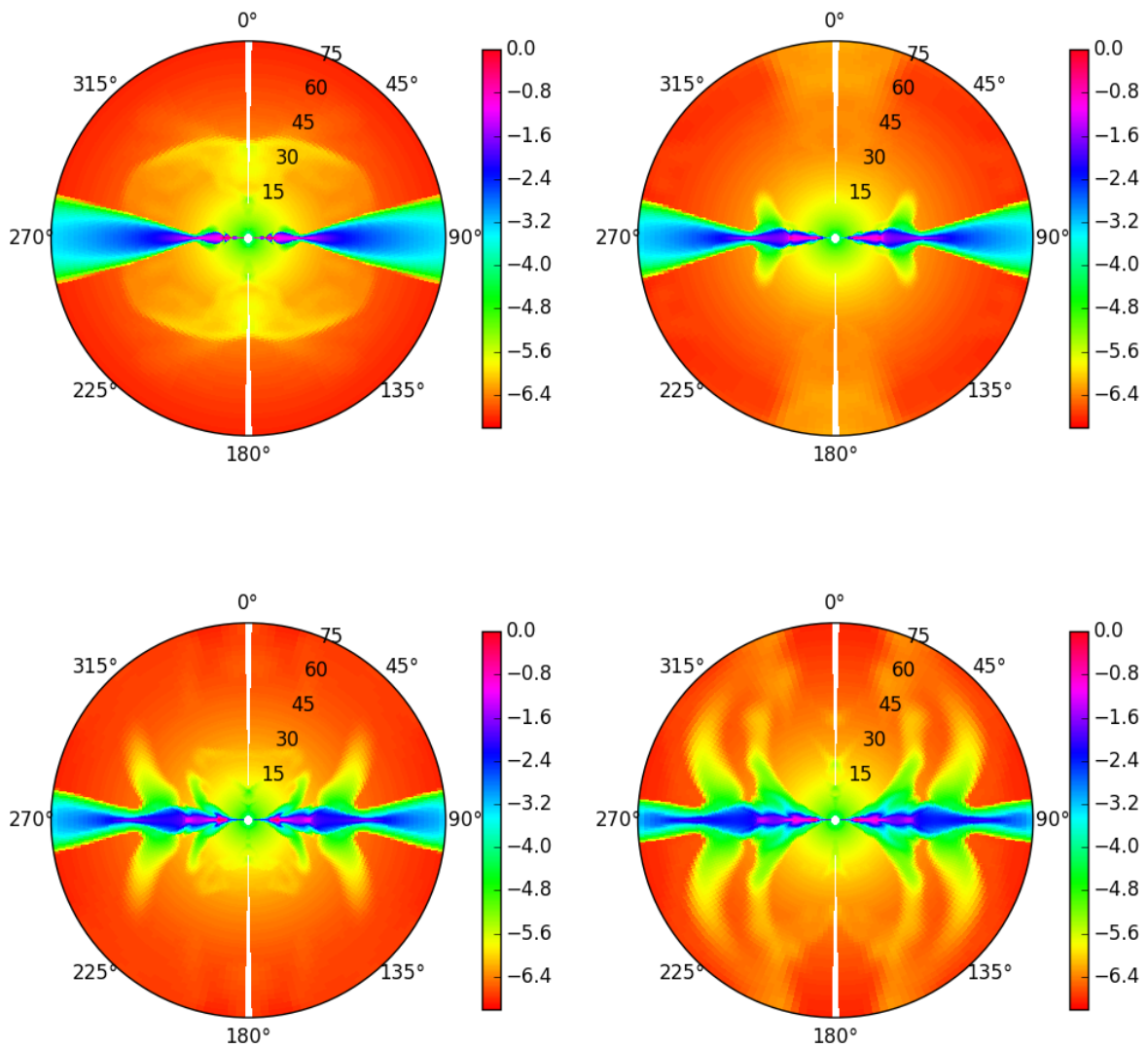


Figure 6.1: Density snapshots in logarithm from simulation *D9* at $t = 200t_g$ (top left), $t = 400t_g$ (top right), $t = 600t_g$ (lower left) and $t = 800t_g$ (lower right). The snapshots are presented in Kerr-Schild coordinates. The morphology of the disk wind evolution is very similar to simulation *D6* in Figure 5.9.

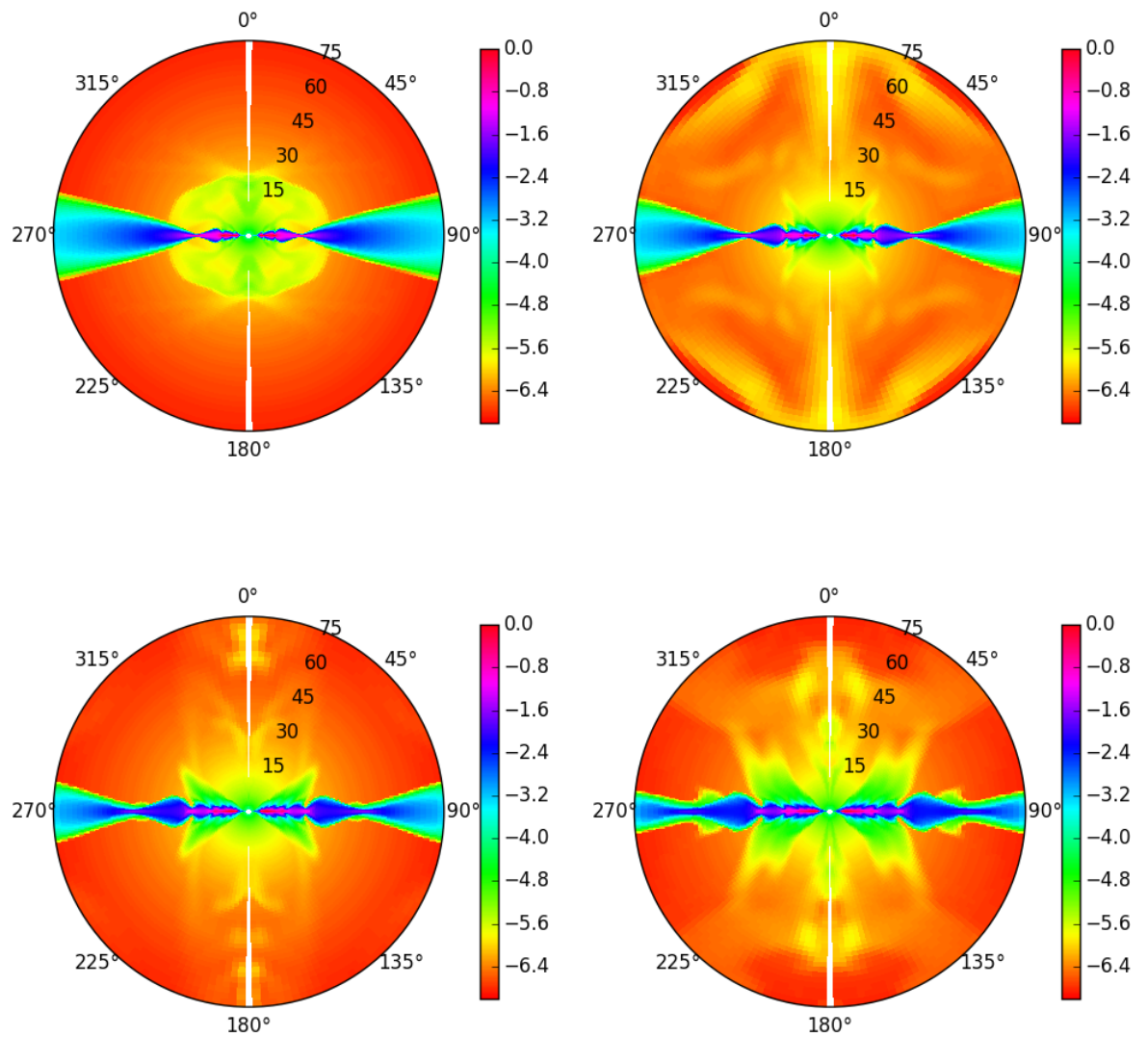


Figure 6.2: Density snapshots in logarithm from simulation *D16* at $t = 200t_g$ (top left), $t = 400t_g$ (top right), $t = 600t_g$ (lower left) and $t = 800t_g$ (lower right). The snapshots are presented in Kerr-Schild coordinates. The morphology of the disk wind evolution show differences being compared to simulation *D9* in Figure 6.1.

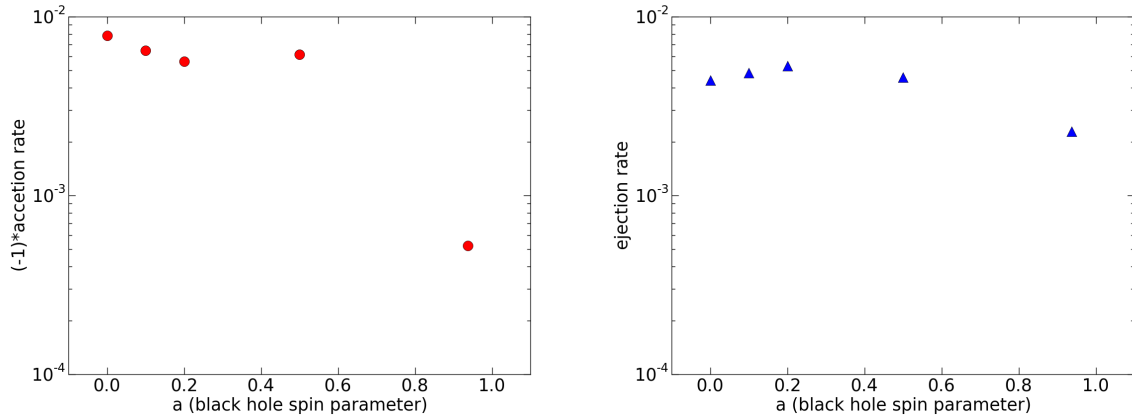


Figure 6.3: The time averaged accretion rate (left plot) and ejection rate (right plot) for simulations $D9$, $D10$, $D11$, $D15$ and $D16$ with the black hole spin parameter $a = 0, 0.1, 0.2, 0.5$ and 0.9375 , respectively. The averages are taken in the time interval from $t = 500t_g$ to $t = 800t_g$. Note that the accretion rates in the left plot have been multiplied by -1 so that they can be plot in a logarithmic vertical axis.

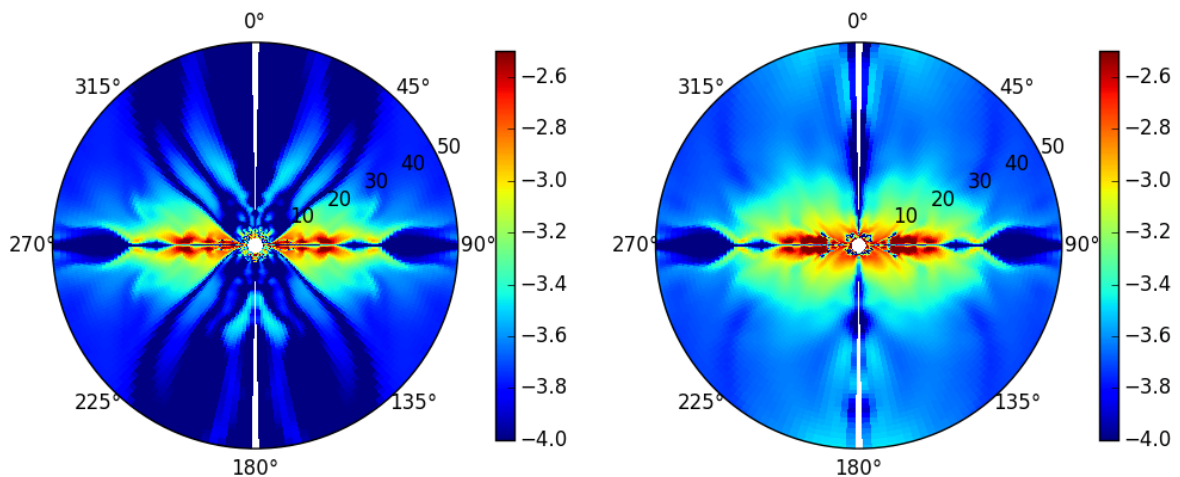


Figure 6.4: The toroidal magnetic field strength in logarithm for simulation $D9$ (left plot) and $D16$ (right plot) at time $t = 800t_g$. In the right plot, the field lines tangled by the black hole rotation create a large amount of toroidal magnetic field around the rotational axis.

D15 and *D16*, with respect to spin parameter a . As we can see in the left plot, the simulations with higher black hole spin parameters return weaker accretion rates. The offsets from simulation *D15* may be caused by the choice of the time interval for averaging; note that the averages are taken from $t = 500t_g$ to $t = 800t_g$ and the accretion system is not yet in steady state at time $t = 800t_g$. The ejection rates presented in Figure 6.3 right plot does not show a clear trend. However, the outflow efficiencies (Equation 5.9) for these simulations, which are $\xi = 56\%$, 75% , 94% , 75% and 434% , respectively, are clearly amplified by the increasing black hole spin.

The influence of the black hole spin on the accretion and ejection rates can be explained by the behavior of the magnetic field lines that penetrate the black hole ergosphere. As illustrated in Section 1.3.2, the rotation of the black hole will create an ergosphere around itself. The magnetic field lines which penetrate the ergosphere will be tangled around the rotation axis, and thus we can expect a larger toroidal field near a rotating black hole than a non-rotating black hole. To confirm this point, I plot the toroidal field strength for simulations *D9* and *D16* (see figure caption) in Figure 6.4. In simulation *D9*, the black hole is not rotating and the toroidal magnetic field is induced by the rotation of the accretion disk. For this reason, the toroidal field can be found mainly in the disk and outflow region. The black hole in simulation *D16* rotates rapidly, thus we see an amplified toroidal field due to the co-rotation of the spacetime with the black hole (see Section 1.3.2). Additionally, simulation *D16* presents strong toroidal magnetic field strength in the vicinity of the black hole horizon whereas no toroidal field is shown in simulation *D9*. This is strong evidence of the black hole frame dragging mentioned above. I believe that the magnetic pressure from the toroidal field near the black hole horizon tends to “push back” the accreting flow, and hence, suppress the accretion rate. This leads to the lower accretion rates for simulations with $a \neq 0$.

6.2 Blandford-Znajek process in the simulation

The power of the Blandford-Znajek process (see Section 2.4) can be calculated by the electromagnetic energy flux that leaves the black hole horizon. Here I follow McKinney & Gammie (2004) and define the total electromagnetic energy flux that goes through a certain radius R as

$$\dot{E}^{(EM)} = 2\pi \int_0^\pi d\theta \sqrt{-g}(r, \theta)|_{r=R} F_E^{(EM)}(r, \theta)|_{r=R}, \quad (6.1)$$

where

$$\begin{aligned} F_E^{(EM)}(r, \theta) &= -T_t^{r(EM)} \\ &= -[(b^2 + e^2)(u^\mu u_\nu + \frac{1}{2}g^\mu_\nu) - b^\mu b_\nu - e^\mu e_\nu \\ &\quad - u_\lambda e_\beta b_\kappa (u^\mu \epsilon_\nu^{\lambda\beta\kappa} + u_\nu \epsilon^{\mu\lambda\beta\kappa})] \end{aligned} \quad (6.2)$$

is the electromagnetic energy flux per solid angle (see Equation 3.24). The time averaged $F_E^{(EM)}$ for simulation *D16* from $t = 500t_g$ to $t = 800t_g$ at radius $r = 2r_g$ is shown in the left plot of

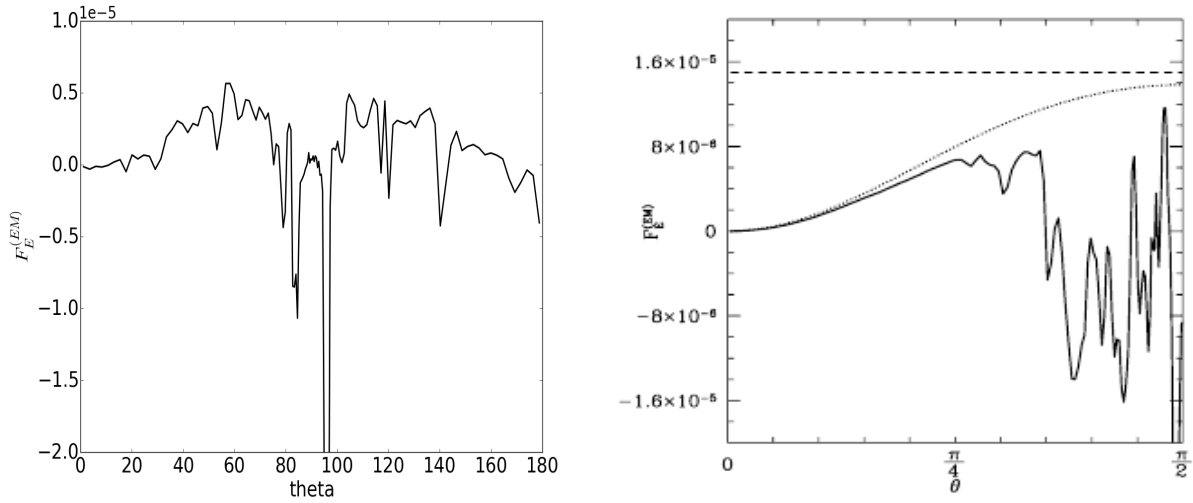


Figure 6.5: *Left*: The time averaged profile of electromagnetic energy flux per solid angle ($F_E^{(EM)}$, defined by Equation 6.2) along θ for simulation *D16*. The values of $F_E^{(EM)}$ are calculated at $r = 2r_g$ and averaged from $t = 500t_g$ to $t = 800t_g$. *Right*: The same profile (but also hemisphere averaged) from an ideal GR-MHD simulation in McKinney & Gammie (2004). The simulation employed a gas torus surrounding a rotating black hole with spin parameter $a = 0.5$. This plot is adopted from McKinney & Gammie (2004).

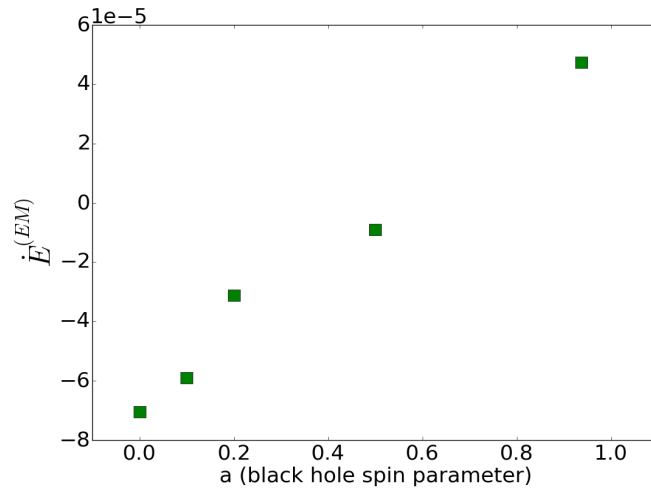


Figure 6.6: The time averaged electromagnetic energy flux defined by Equation (6.1) measured at $r = 2r_g$ for simulations *D9*, *D10*, *D11*, *D15* and *D16*. The averages are taken in the time interval from $t = 500t_g$ to $t = 800t_g$. To eliminate the influence of accreting flow, I only integrate θ from 0° to 75° and 105° to 180° . The energy flux shows a clear enhancement with the increasing black hole spin.

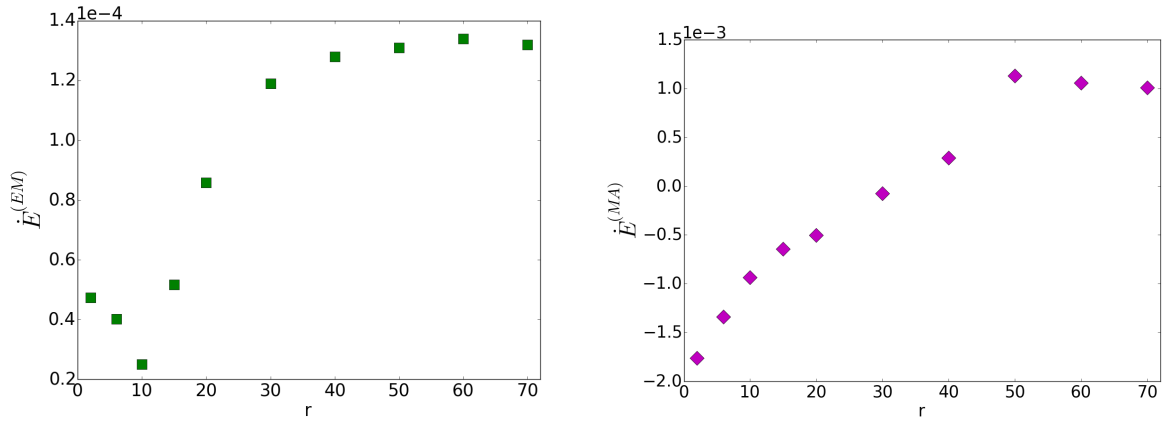


Figure 6.7: The time averaged electromagnetic energy flux (left plot) defined by Equation (6.1) and the time averaged matter energy flux (right plot) defined by Equation (6.3) measured at different radius as indicated in the plots. The averages are taken in the time interval from $t = 500t_g$ to $t = 800t_g$. To eliminate the influence of accreting flow, I only integrate θ from 0° to 75° and 105° to 180° . The energy fluxes increase with the radius which implies that the disk wind has a positive influence on both the electromagnetic and matter energy fluxes.

Figure 6.5. The positive $F_E^{(EM)}$ values in the regions θ from 20° to 70° and from 110° to 160° are specifically the energy output from the black hole through the Blandford-Znajek mechanism. The negative peaks that point down near the disk mid-plane indicate the accreting flow from the disk. The reason why there are several peaks instead of one, is unclear. However, we can compare this plot to the right plot in the same figure, where the same time averaged profile from the ideal GR-MHD simulation in McKinney & Gammie (2004) is presented. Their simulation initially employed a gas torus surrounding a rotating black hole with spin parameter $a = 0.5$. The $F_E^{(EM)}$ values in this plot were also influenced similarly by the disk accretion. Note that McKinney & Gammie (2004) employed a thick torus and ideal GR-MHD, which enhance the influence of the accretion on $F_E^{(EM)}$.

Using the definition in Equation (6.1), I plot the time averaged electromagnetic energy flux measured at $r = 2r_g$ for simulations *D9*, *D10*, *D11*, *D15* and *D16* in Figure 6.6. The simulations with $a \leq 0.5$ still return negative electromagnetic energy flux, even if I do not consider the influence from the accreting flow (see figure caption). I attribute this behavior of the energy flux to the time evolution of the corona density that I set in the spherical region $r < 6r_g$ (see Section 5.1). The black hole horizon cannot provide any support to the corona. Thus the corona will gradually fall into the black hole. The falling corona with a certain density can then cause an amount of Poynting flux that enters the black hole. When the output energy flux from black hole is weaker than that from the corona Poynting flux, the electromagnetic energy flux will then be negative. Taking this into account, the energy output from the black hole clearly increases with the black hole spin parameter.

However, the energy flux of the Blandford-Znajek process does not show an obvious non-linear growth with the increasing a in Figure 6.6 when compared to the results in McKinney & Gammie

(2004); Tchekhovskoy et al. (2010). The reason for this is still unclear to me. Perhaps like I mentioned earlier, in the time interval from $t = 500t_g$ to $t = 800t_g$, the evolution of the system is not yet steady, so the accretion from the disk can influence the magnetic field strength around the black hole horizon and lead to an unexpected Blandford-Znajek power, since the energy output from the black hole also depends on the magnetic field strength (see Section 2.4.1).

6.3 Disk wind v.s. Blandford-Znajek effect

Finally, it is the exciting moment to compare the energy output from the black hole to that from the disk wind. In this analysis, I focus on simulation *D16*, which has the largest spin parameter. Since the energy output from a black hole is indicated by the electromagnetic energy flux in the radial direction, I take here the matter energy flux in the radial direction $\dot{E}^{(MA)}$ as indication of the energy output from the disk wind. Similar to Equation (6.1), $\dot{E}^{(MA)}$ is defined by

$$\dot{E}^{(MA)} = 2\pi \int_0^\pi d\theta \sqrt{-g}(r, \theta)|_{r=R} F_E^{(MA)}(r, \theta)|_{r=R}, \quad (6.3)$$

where

$$\begin{aligned} F_E^{(MA)}(r, \theta) &= -T_t^{r(MA)} \\ &= -[(\rho + u)u^\mu u_\nu + p(u^\mu u_\nu + \frac{1}{2}g^\mu_\nu)] \end{aligned} \quad (6.4)$$

is the matter energy flux per solid angle (see Equation 3.24).

With this definition, I then calculate the time averaged electromagnetic energy flux and matter energy flux for simulation *D16* at different radii in Figure 6.7. In the left plot, the electromagnetic component of the energy flux is presented. The flux values show an obvious growth from $r = r_{10}$ to $r = 40r_g$, which implies that the outflowing disk wind also contributes to the radial component of the electromagnetic energy flux. Note that the outflows originate from the disk surfaces; calibrating the flux at a larger radius means including larger areas of disk surfaces and more outflows, hence larger contribution from the disk wind to electromagnetic energy flux. This growth stops at $r \sim 50r_g$ since the outflow and the launching area have not yet reached that far within $t \leq 800t_g$ (see Figure 6.2). In the right plot of the same figure, the matter component of the energy flux is presented. Similar to the electromagnetic energy flux, the matter energy flux also grows with increasing radius. Within $r \lesssim 30r_g$, the accreting flow is predominant and the matter energy flux is negative, while at $r > 30r_g$, outflow begins to dominate which leads to positive matter energy flux. Above the radius $r = 50r_g$, growth ceases because of the same reason that halted the electromagnetic energy flux growth.

On one hand, according to Figure 6.6, the pure energy output from the black hole in simulation *D16* is $\dot{E}^{(EM)} \sim 10^{-5}$. This value increases to $\sim 10^{-4}$ if we take the Poynting flux from disk wind into account (see Figure 6.7). On the other hand, the energy output from the disk wind is $\dot{E}^{(MA)} \sim 10^{-3}$. Thus, the conclusion in this preliminary study is that the disk wind substantially contributes in the energy production within this specific evolution period of simulation *D16*.

As was once mentioned in Section 2.4.1, (Blandford & Znajek 1977) assumed ideal MHD condition in their derivation of the Blandford-Znajek effect. They argued that “the magnetic flux will be frozen into the accreting material and so the field close to the horizon can become quite large-much larger than the field at infinity.” This condition is, nevertheless, not quite satisfied in the simulations in this section because the disks are magnetically diffusive. On the other hand, the ideal MHD condition above the disk required by disk-driven wind is well satisfied since the diffusivity value drops exponentially in the direction away from the disk mid-plane (see Equation 5.6). This contrast of the diffusivity level may be reflected, to some extent, by the dominance of the energy output from the disk wind.

6.4 Summary and conclusions

For the main purpose of this project, I discussed the simulations that have non-zero spin black holes in this chapter. I found that the accretion rate is suppressed by the increasing black hole spin parameter a , due to the magnetic pressure from tangled toroidal field lines around the horizon induced by the spacetime frame dragging of the rotating black hole. The accretion rate for the simulation with black hole spin $a = 0.9375$ is 10 times smaller than that for the simulation with a non-rotating black hole. Furthermore, the magnetic pressure from the tangled field lines, despite its suppression on accretion, still acts positively on the ejection by increasing the ratio of ejection rate to accretion rate. In the analysis of the simulation with $a = 0.9375$, I observed a spherically integrated radial energy flux from the disk wind that is $\sim 10^2$ times stronger than the electromagnetic energy flux generated by the rotating black hole (Blandford-Znajek effect). Thus, in this preliminary study, the energy production of the accretion system is dominated by disk wind.

Chapter 7

Conclusions and Future Projects

In this thesis, the resistivity, or magnetic diffusivity, has been implemented into an existing GR-MHD code. The new code is named rHARM and its resistivity performance has been tested. The purpose for developing rHARM is to run simulations that can better imitate the physical environment of the black hole accretion system predicted by theories. Thus, several such simulation surveys have been carried out by rHARM after its completion. I now summarize my major conclusions; further results are noted in the corresponding sections of the individual chapters. In this chapter, I will also give an outlook for possible future projects that can extend the content of this thesis work.

Summary of main conclusions

In Chapter 3, I have illustrated the implementation of magnetic diffusivity into the ideal GR-MHD code HARM (Noble et al. 2006) and provided test simulations. The implementation of resistivity requires applying the general form of the stress energy tensor including the electric field to rHARM. The calculation of the electric field follows the equations in Bucciantini & Del Zanna (2013). The inversion scheme in rHARM is based on the 2D inversion scheme in Noble et al. (2006) and uses an extra loop to make the electric field variables converge.

I have verified my implementation of resistivity by comparing the diffusion of an initial magnetic field distribution to the analytic time evolution of the profile as given by the diffusion equation. These simulations were performed in rectangular boxes of weakly magnetized gas, excluding any dynamical effect by Lorentz forces. Boxes at different distances from the black hole were investigated. The magnetic diffusion evolving in rHARM are identical to the known analytic solution for different magnetic diffusivities from $\eta = 10^{-10}$ to $\eta = 10^{-2}$. I have further tested rHARM with a classical shock tube problem and found very good agreement for magnetic diffusivities $\eta < 0.1$. For larger diffusivity, rHARM does not capture the shock front perfectly, but such large diffusivities are anyway beyond the scope of our aims of treating the disk accretion-ejection structure.

Having implemented physical magnetic diffusivity in the code, it is now able to measure the

numerical diffusivity. The magnetic diffusivity clearly depends on the setup and resolution. For a cell size of $\Delta x \simeq 0.01$, the numerical diffusivity is $\eta_{\text{num}} \sim 10^{-5}$.

In Chapter 4, I have applied rHARM to a more astrophysical context, namely, investigated the development of the magneto-rotational instability (MRI) in tori that are magnetically diffusive. Here the simulations follow the initial setup in [Gammie et al. 2003](#); [Noble et al. 2006](#), which is an initially stable gas torus that carries a poloidal magnetic field that follows the density contours. As further verification of the new code rHARM, I have ran a simulation with a very small magnetic diffusivity $\eta = 10^{-12}$ (that is clearly below the numerical diffusivity of the code). This simulation recovers the time evolution of the accretion rate that has been found previously by using the ideal GR-MHD code HARM. In contrast, in the simulation with a high diffusivity $\eta = 10^{-3}$, the mass accretion onto the black hole decreases significantly due to the suppression of MRI. In order to investigate further the influence of magnetic diffusivity on relativistic MRI tori, I have performed a parameter survey ranging from $\eta = 10^{-12}$ to $\eta = 10^{-3}$. I find indication for a critical magnetic diffusivity value of $\eta \gtrsim 5 \times 10^{-4}$ (in this specific simulation model), above which the MRI inside the torus does not grow in the linear regime.

In Chapter 5, I have presented rHARM survey of MHD launching of disk winds from a thin accretion disk threaded by inclined open poloidal field lines. The results are preliminary since the simulations did not yet reach a quasi-steady state of accretion-ejection that is known from non-relativistic simulations.

I first discussed the results from the simulation with a non-diffusive very weak magnetized (plasma- $\beta = 10^8$) disk around a zero-spin black hole. No outflow is observed in this case and the accretion disk keeps its disk-like shape during the evolution. I have shown the MRI growth inside the accretion disk which leads to the accretion of matter onto the black hole (see Section 5.3). As far as I know, this is the first time that MRI is directly observed inside the thin accretion disk in a GR-MHD simulation.

In the same simulations with strong magnetic field (plasma- $\beta = 10$), disk wind ejections are clearly detected. I then investigated the relation between accretion and ejection rates and the different levels of diffusivity. In my analysis, I found that (i) the increasing diffusivity level suppresses the MRI process inside the disk and lowers the matter accretion rate onto the black hole, the accretion rate from the simulation with diffusivity normalization factor 10^{-4} is about 10^2 times larger than that from the simulation with diffusivity 10^{-2} , (ii) a lower accretion rate is always accompanied by a lower disk wind ejection rate, thus the increasing diffusivity level also weakens the disk wind ejection rate, and (iii) the increasing diffusivity level helps to prevent the magnetic field above the disk from turbulent structure. Although the accretion rate is 10^2 times weaker, the ratio of ejection rate to accretion rate from the simulation with diffusivity normalization factor 10^{-2} is almost 8 times larger than that from the simulation with diffusivity 10^{-4} .

From my analysis, I attributed the predominant driving force of the disk wind launching in the simulations with strong magnetic field to the toroidal magnetic field pressure gradient and

showed that the contributions from the poloidal field pressure gradient and thermal pressure gradient are minor for wind launching. It is not yet clear if the jet is driven centrifugally since the force projection analysis along the steady field lines is not possible here. Additionally, the simulations with the “more vertical” initial magnetic fields (less inclined towards disk mid-plane) show stronger accretion and ejection rates because of the faster propagation of toroidal magnetic fields in the vertical direction.

At the end of Chapter 5, I also showed that the numerical diffusivity has noticeable influences on the current survey simulations with grid resolution 128×128 . The huge time consumption for a higher resolution survey strongly suggests the parallelization of rHARM.

Finally, as the main purpose of this project, I discussed the simulations that have non-zero spin black holes in Chapter 6. I found that the accretion rate is suppressed by the increasing black hole spin parameter a due to the magnetic pressure from tangled toroidal field lines around the horizon built by the spacetime frame dragging of the rotating black hole. The accretion rate for the simulation with black hole spin $a = 0.9375$ is 10 times smaller than that for the simulation with a non-rotating black hole. Furthermore, the magnetic pressure build by the tangled field lines, despite its suppression on accretion, still acts positively on the ejection by increasing the ratio of ejection rate to accretion rate. In the analysis of the simulation with $a = 0.9375$, I observed a spherically integrated radial energy flux from the disk wind that is about 10^2 times stronger than the electromagnetic energy flux generated by the rotating black hole (Blandford-Znajek mechanism). Thus, in this preliminary study, the energy production of the accretion system is dominated by disk wind.

Future Projects

Within this thesis, magnetic diffusivity has been implemented into a GR-MHD code and the simulation surveys that are executed by this new code show encouraging results. Nevertheless, there are indeed some elements in this work that deserve improvement. Here, I will write my opinions to and outline how further progress can be achieved.

As one of the two key issues within this work, the huge time consumption of running rHARM simulations has directly lead to the results incompleteness of simulations *D7* and *D17* in Chapter 5. Moreover, I have also pointed out in Section 5.9 that the numerical diffusivity value is comparable to the magnetic diffusivity values that is scientifically interesting in disk wind production, thus requiring rHARM surveys with higher grid resolution. For the future researches with rHARM, it is necessary to speed up the current version of code. From my knowledge of rHARM and HARM (see Gammie et al. 2003; Noble et al. 2006), there is not much space left that can be done to accelerate the current code by changing the routine structures. Nevertheless, a large potential exists in the code parallelization, which would allow for the execution of several processes in rHARM to be carried out simultaneously. If this can be achieved, the results in Chapter 5 will become more accurate and can be discussed over a longer time range.

The other key issue that constrain the performance of rHARM is the robustness of the inversion scheme. Under certain circumstances, the scheme cannot converge the roots properly in converting the primitive variables to conserved variables (see Section 4.2 and 5.8). The convergence issue, which always shows up first at the boundary of the computational domain, will spread out and lead to the unphysical evolution in the whole simulation region. If this issue is solved, interesting simulations, especially those with fast rotating black hole spins can be investigated for a much longer time period than discussed in Section 6. Improving the inversion scheme is a purely numerical problem.

In my opinion, the improvements of the inversion scheme can be done mainly in two aspects, namely improving the solver and improving the structure of the time evolution. The solver is responsible for solving the two implicit equations in Equation (3.45). In rHARM, they are solved by a 2+1 dimensional Newton-Raphson iteration method (see Section 3.2.3 and Appendix A.6), which might not perform well when the shapes of the equations are complicated, e.g., shapes with large slope, local maxima/minima in certain variable, etc. The specific improvement of the solver should be made after diagnosing the exact difficulty in the convergence process.

There are many variations of Newton-Raphson methods that might work better in certain regimes than the standard version applied in the current rHARM. However, I will very roughly discuss the possibility of using a totally different family of methods as another option, i.e., the Markov chain Monte Carlo methods (Berg 2004). The Markov chain Monte Carlo method is usually used for sampling the likelihood of a parameter space. According to Equation (A.6), we can build the parameter space upon (\mathbf{v}^2, W) and define the likelihood as

$$\mathcal{L} = -(\mathcal{A} + \mathcal{B}^2) \quad (7.1)$$

where

$$\begin{aligned} \mathcal{A} &= \tilde{Q}^2 - \mathbf{v}^2 W^2 + (\boldsymbol{\mathcal{E}} \times \boldsymbol{\mathcal{B}})^2 + 2\boldsymbol{\mathcal{E}} \cdot (\tilde{Q} \times \boldsymbol{\mathcal{B}}), \\ \mathcal{B} &= U - W + p(\mathbf{v}^2, W) - \frac{1}{2}(\boldsymbol{\mathcal{E}}^2 + \boldsymbol{\mathcal{B}}^2). \end{aligned} \quad (7.2)$$

The root of (\mathbf{v}^2, W) in Equation (A.6) together with the parameter space near it will return the largest likelihood and be mostly sampled. We can then take the average of the mostly sampled (\mathbf{v}^2, W) samples after the convergence of the Markov chain. In Markov chain Monte Carlo, step length for root searching is independent of the equation, while in the Newton-Raphson method, it depends on the local derivative of the equation to the parameter. Thus applying Markov chain Monte Carlo could avoid problems when the derivative is extremely small. Additionally, an affine-invariant ensemble sampler for Markov chain Monte Carlo is built in Foreman-Mackey et al. 2013, which can handle local maxima/minima in parameter space. Thus the Markov chain Monte Carlo method could be employed in rHARM as a backup solution when the standard solver fails to converge.

Improving the structure of the time evolution may also help the convergence of the inversion scheme in rHARM. The time evolution in current rHARM employs a simple first-second scheme described by Equation (3.48). It is feasible to substitute it with the IMEX schemes introduced in

Palenzuela et al. (2009). As shown in the tests by Bucciantini & Del Zanna (2013), the IMEX schemes return better convergences, especially in the high resistivity regime, than the first-second scheme.

Aside from the improvements that could be made in rHARM, it would also be an interesting future project to extend the current axial-symmetric 2-dimensional code to 3-dimensional. Since rHARM is able to resolve the magnetic reconnection, a fully 3D code would allow one to investigate the energy release of the shock waves that is produced by the reconnection of the toroidal magnetic field (Machida & Matsumoto 2003) and other interesting phenomena.

As the first step of reforming ideal HARM, rHARM only considers the implementation of resistivity (magnetic diffusivity). In Bucciantini & Del Zanna (2013), the evolution equations of both resistivity and mean field dynamo are given. But currently, there are only few existing GR-MHD codes that include mean field dynamo. (Bugli et al. 2014) has studied a kinematic dynamo which assumes the background flow structure as given. Sądowski et al. (2015) has implemented a mean-field model in the general relativistic radiation magnetohydrodynamic code and applied it to thick disk simulations. Based on the derivation in Bucciantini & Del Zanna (2013) and the success of resistivity implementation in this thesis work, it would be very interesting to also develop a resistive GR-MHD code that takes the mean field dynamo self-consistently into account. If this can be achieved, we can run simulations of black hole accretion system where the large scale magnetic field can be evoked by small-scale velocity fluctuations in the accretion disk instead of being given prior.

Everything that was done throughout this thesis and proposed in this final chapter might help to discover the origin of relativistic AGN jets. One day, the “true face” of the unresolved center region in a massive galaxy will be revealed!

Acknowledgments

First and foremost, I would like to express my deepest gratitude to my supervisor Christian Fendt who always answered, with great patience, to my major or minor questions. I thank him for enlightening my understanding of the subject that I was working on. I thank my coauthor Scott Noble who provided the HARM code, which the new code rHARM is based. I appreciate the opportunity to learn directly from him in Tulsa during my PhD study. I am grateful for having an excellent colleague, Matteo Bugli, who helped me substantially in the development of the inversion scheme in rHARM. It has also been a great pleasure to have valuable discussions with Somayeh Sheiknezami and Christos Vourellis. I thank Steffi Yen as the language editor of this thesis.

For being part of my thesis committee and for the follow up of my project, I express my gratitude to Cornelis P. Dullemond and Andrea Macciò. I appreciate my fellowship in the International Max Planck Research School (IMPRS), which was an excellent organization that trained my presentation skills and offered a great communication platform for PhD students. I give my appreciation to the Max-Planck-Institut für Astronomie for the maintenance of the remarkable scientific working environment. I thank my office mates Alexander Hygate, Kalyan Kumar Radhakrishnan Santhakumari, Tobias Schmidt and Kiyun Yun for the cozy company during my PhD.

I am grateful to all the dear singers from Anglistenchor and all the great concerts/activities we performed/did together which greatly enriched my foreign life. I appreciate the encouragement Sherry Föhr gave me and the kindness her family showed to me. I thank Yuechen Guo, Benfang Wang, Bangning Yan and Zezhou Zhang, my outstanding friends, for their understanding and backing me since my Masters study in Heidelberg.

At last I may express my endless gratitude to my dearest parents. You have never stopped believing in me and supporting me. Without you, I never would have had the opportunity and confidence to accomplish what I have achieved so far. To me, you are the greatest parents in the world! (最后, 我要向我的父亲与母亲表达我无尽的感激。你们从未停止过对我的信任与支持。如果没有你们, 我将不可能走到今天这样远。我而言, 你们是世界上最好的父母!)

A.1 Superluminal motion

In astronomical observations, it is possible to see objects whose apparent motion is faster than the speed of light. This phenomenon is called “superluminal motion.” Superluminal motion can be seen in AGN jets, like e.g. some radio galaxies, BL Lac objects, quasars and recently also in some microquasars (Porcas 1983; Biretta et al. 1995). When first observed in the early 1970s, superluminal motion was taken to be a piece of evidence against quasars having cosmological distances. Today, it is believed that apparent velocities greater than the velocity of light are only optical illusions in the frame of special relativity.

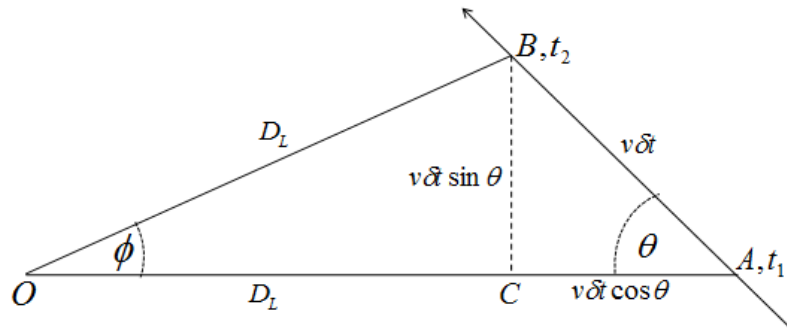


Figure A.1: An illustration for the astronomical superluminal motion. Please see corresponding text for the derivation. Credit: Muhammad, Wikipedia

Superluminal motion can be explained by assuming that jets are travelling very close to the speed of light at a very small angles towards the observer. As shown in Figure A.1, observer O is measures a far away ($\phi \ll 1$, $OB \sim OC = D_L$) event, where an object moves from point A to point B within time $t_2 - t_1 = \delta t$ with velocity $v = |\mathbf{v}|$ ($v < c$) and an angle θ to the line of sight. Because the event is at large distance from O , the observer can only see the event as if the object moves from C to B . On the other hand, the light of the object emitted at point A will be received by the observer at time

$$t_1 = t_1 + \frac{OA}{c} = t_1 + \frac{D_L + v\delta t \cos \theta}{c}, \quad (\text{A.1})$$

while the light of the object emitted at point B will be received at time

$$t_2 = t_2 + \frac{OB}{c} = t_2 + \frac{D_L}{c}. \quad (\text{A.2})$$

Thus, for the observer O , the object moves from point C to B within time $\delta t' = t_2 - t_1 = \delta t - v\delta t \cos \theta/c$. The apparent velocity of this event for O is then

$$v' = \frac{BC}{\delta t'} = \frac{v\delta t \sin \theta}{\delta t - v\delta t \cos \theta/c} = \frac{v \sin \theta}{1 - \beta \cos \theta}, \quad (\text{A.3})$$

where $\beta = v/c$. Equation (A.3) can also be written in the form

$$\beta' = \frac{v'}{c} = \frac{\beta \sin \theta}{1 - \beta \cos \theta}, \quad (\text{A.4})$$

A greater-than-light apparent velocity means that $\beta' > 1$, which implies the condition

$$\beta > \frac{1}{\sqrt{2} \sin(\theta + \pi/4)}. \quad (\text{A.5})$$

The minimum value of β to obtain superluminal effects is then a function of viewing angle θ . The minimum for β appears when the viewing angle is $\theta = \pi/4$. In this case, the original velocity of the object needs to exceed $0.71c$.

A.2 3+1 spacetime

Because of computational reasons, the physical quantities (tensors and vectors) are sometimes projected to the spacetime that is perpendicular to a certain four-vector in the numerical realization of rHARM. In the following, the concepts of spacetime decomposition and “normal observer,” together with the definition of the projection tensor, will be illustrated.

A.2.1 Split spacetime into space and time

In this section, we use (t, x^1, x^2, x^3) to denote the coordinates where t is the time-like component, and (x^1, x^2, x^3) are spatial components. The metric for the spacetime is $g_{\mu\nu}$. Now we “slice” the spacetime in the time coordinate, vectors within each slice Σ_t have vanishing zero-th component. Assuming that the spacetime is curved such that the inner product of a time vector $\tilde{\mathbf{i}} = (1, 0, 0, 0) = \partial_t$ and an arbitrary vector $\mathbf{X} = (0, X^1, X^2, X^3)$ on Σ_t is $g(\tilde{\mathbf{i}}, \mathbf{X}) \neq 0$, the time-like vector $\tilde{\mathbf{i}}$ can then be split into the component on Σ_t and the component normal to Σ_t . We note this decomposition as

$$\tilde{\mathbf{i}} = \alpha \mathbf{n} + \boldsymbol{\beta}, \quad (\text{A.6})$$

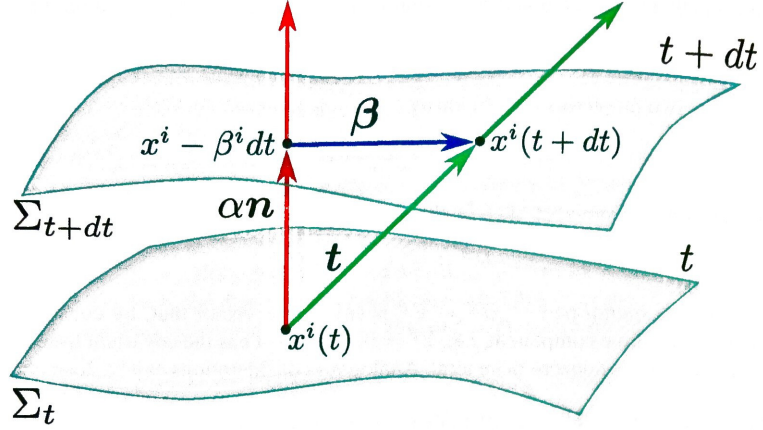


Figure A.2: A schematic explanation of the normal vector in 3+1 spacetime. Between the two slices of pure space, σ_t and σ_{t+dt} (see text), the red vector \mathbf{n} shows the heading of time in local Minkowski space, while the green vector \mathbf{t} shows the direction of coordinate time in curved spacetime, which actually has projections in spacial components. The shift in the space during the coordinate time t and $t + dt$ is given by the blue vector $\boldsymbol{\beta}$. Credit: [Rezzolla & Zanotti \(2013\)](#)

where vector $\boldsymbol{\beta}$ is the spatial decomposition of $\tilde{\mathbf{t}}$ and \mathbf{n} is a vector that is normal to Σ_t ($g(\mathbf{n}, \boldsymbol{\beta}) = 0$). The parameter α is defined by

$$\alpha \equiv -g(\tilde{\mathbf{t}}, \mathbf{n}). \quad (\text{A.7})$$

The task now is to find the expression of the parameter α and the components in α and $\boldsymbol{\beta}$ by known quantities. The restriction of the spacetime metric on Σ_t gives rise to the induced metric

$$\hat{\gamma} = \gamma_{ij} dx^i \otimes dx^j, \quad (\text{A.8})$$

where by definition $\gamma_{ij} \equiv g_{ij}$. According to the definition of dot product,

$$g(\boldsymbol{\beta}, \boldsymbol{\beta}) = \gamma(\boldsymbol{\beta}, \boldsymbol{\beta}) = \boldsymbol{\beta}^2. \quad (\text{A.9})$$

If we write $\boldsymbol{\beta} = (0, \beta^1, \beta^2, \beta^3)$ and with $g(\mathbf{n}, \partial_i) = 0$, we have

$$\begin{aligned} g_{ti} &= g(\partial_t, \partial_i) \\ &= g(\alpha \mathbf{n} + \boldsymbol{\beta}, \partial_i) \\ &= g(\boldsymbol{\beta}, \partial_i) \\ &= g_{ji} \beta^j \equiv \beta_i. \end{aligned} \quad (\text{A.10})$$

Similarly,

$$\begin{aligned} g_{tt} &= g(\partial_t, \partial_t) \\ &= g(\alpha \mathbf{n} + \boldsymbol{\beta}, \alpha \mathbf{n} + \boldsymbol{\beta}) \\ &= -\alpha^2 + 2\alpha g(\mathbf{n}, \boldsymbol{\beta}) + g(\boldsymbol{\beta}, \boldsymbol{\beta}) \\ &= \boldsymbol{\beta}^2 - \alpha^2. \end{aligned} \quad (\text{A.11})$$

Equations (A.10) and (A.11) give the expression of the parameter α and components in β by the components of metric tensor. We can then also write the metric tensor in the following way

$$ds^2 = (\beta^2 - \alpha^2)dt^2 + 2\beta_i dt dx^i + \gamma_{ij} dx^i dx^j. \quad (\text{A.12})$$

According to the definition, the normal vector \mathbf{n} is then

$$\mathbf{n} = \frac{1}{\alpha}(\tilde{\mathbf{t}} - \boldsymbol{\beta}) \equiv \frac{1}{\alpha}(1, -\beta^i). \quad (\text{A.13})$$

A trivial calculation shows that

$$n_\mu = g_{\mu\nu} n^\nu = (-\alpha, 0, 0, 0), \quad (\text{A.14})$$

which is the covariant form of the normal vector n^μ . The observer with a four velocity of \mathbf{n} is then called a “normal observer” or “Eulerian observer.” A schematic explanation of the normal vector is given in Figure A.2.

A.2.2 The projection tensors

Knowing a four vector \mathbf{u} , it is possible to write a projection tensor that can project any vector onto the spacetime that is perpendicular to \mathbf{u} by writing the projection tensor as

$$h^\mu_\nu = g^\mu_\nu + u^\mu u_\nu. \quad (\text{A.15})$$

The correctness of tensor h^μ_ν can be easily proven in the following way. Assume an arbitrary vector \mathbf{v} , its projection is

$$\begin{aligned} \mathbf{v}_\perp &= h^\mu_\nu v^\nu \\ &= g^\mu_\nu v^\nu + u^\mu u_\nu v^\nu \\ &= v^\mu + u^\mu \cdot \langle \mu, \nu \rangle. \end{aligned} \quad (\text{A.16})$$

The inner product of \mathbf{v}_\perp and \mathbf{u} is then

$$\begin{aligned} \langle \mathbf{v}_\perp, \mathbf{u} \rangle &= v^\mu u_\mu + u^\mu \cdot \langle \mu, \nu \rangle u_\mu \\ &= \langle \mu, \nu \rangle - \langle \mu, \nu \rangle \\ &= 0. \end{aligned} \quad (\text{A.17})$$

Thus, \mathbf{v}_\perp is indeed perpendicular to \mathbf{u} . Similarly, we can define a projection tensor j^μ_ν which projects any vector onto the spacetime that is perpendicular to the normal observer \mathbf{n} where

$$j^\mu_\nu = g^\mu_\nu + n^\mu n_\nu. \quad (\text{A.18})$$

The projection tensor j^μ_ν will be used in defining the primitive variables in rHARM (see Chapter 3).

A.3 Orbits shift of Keplerian rotating object

Consider an object with mass m rotating around a massive object with mass M on an orbit r_1 . The mass m is ignorable in comparison with M , as $m \ll M$. The angular momentum L of the object as a function of radius r is

$$L = m\sqrt{GMr}. \quad (\text{A.19})$$

The Keplerian velocity v_1 and the kinetic energy E_1 of the object are

$$\begin{aligned} v_1 &= \sqrt{\frac{GM}{r_1}}, \\ E_1 &= \frac{1}{2}mv_1^2 = \frac{GMm}{2r_1}. \end{aligned} \quad (\text{A.20})$$

Imagine that the object now moves to orbit r_2 , during which only gravity does work so that angular momentum is always preserved. Then, the new kinetic energy E_2 at r_2 can be expressed by

$$E_2 = E_1 + V_2 - V_1 = \frac{GMm}{2r_1} + GM\left(\frac{1}{r_2} - \frac{1}{r_1}\right), \quad (\text{A.21})$$

where V_1 and V_2 denote the gravitational potential at r_1 and r_2 . Using the definition

$$E_2 = \frac{1}{2}mv_2^2, \quad (\text{A.22})$$

we can solve for the final velocity of the object

$$v_2 = \sqrt{GM} \cdot \sqrt{\frac{1}{r_2} + \left(\frac{1}{r_2} - \frac{1}{r_1}\right)}. \quad (\text{A.23})$$

On the other hand, the Keplerian velocity at r_2 is

$$v_2 = \sqrt{GM} \cdot \sqrt{\frac{1}{r_2}}. \quad (\text{A.24})$$

Thus if the object moves inwards, $r_2 < r_1$, hence $v_2' > v_2$, the object will then be accelerated outwards back to r_1 by the centrifugal force. If it moves outwards, $r_2 > r_1$, $v_2' < v_2$ and the centrifugal force is weaker against gravity, then the object is pulled again back to r_1 . As a result, in a differentially rotating medium with a distribution of angular momentum increasing outwards, matter is stable with respect to small shifts preserving the angular momentum.

A.4 Different regimes in the radial direction of the Shakura & Sunyaev disk model

In the Shakura & Sunyaev disk model, the disk structure in the radial direction consists of the combination of three different regimes a), b) and c) (see Section 2.1.2). It is convenient to

introduce the following non-dimensional parameters

$$\begin{aligned}
 m &= \frac{M}{M_\odot}, \\
 \dot{m} &= \frac{\dot{M}}{\dot{M}_{\text{cr}}} = \frac{\dot{M}}{3 \cdot 10^{-8} \frac{M_\odot}{\text{yr}}} \times \left(\frac{M_\odot}{M} \right), \\
 r &= \frac{R}{3r_{\text{H}}} = \frac{1}{6} \frac{Rc^2}{GM} = \frac{M_\odot}{M} \frac{R}{9\text{km}},
 \end{aligned} \tag{A.25}$$

where M_\odot is the solar mass, r_{H} is the horizon of a Schwarzschild black hole and \dot{M}_{cr} is the mass accretion rate at Eddington critical luminosity. In the regime a), radiation pressure and Thomson scattering is dominant, namely $P_r \gg P_g$ and $\sigma_T \gg \sigma_{ff}$. Using Equation (2.8) with Equations (2.15) and the condition of sound speed $v_s^2 = \frac{\varepsilon}{3\rho}$, the disk half thickness in this regime is

$$z_0[\text{cm}] = \frac{3}{8\pi} \frac{\sigma_T}{c} \dot{M} (1 - r^{-1/2}) = 3.2 \cdot 10^6 \dot{m} m (1 - r^{-1/2}). \tag{A.26}$$

Regime a) represents the middle part of the disk, thus $r \gg 1$ and the disk thickness along the radius is almost constant (see Shakura & Sunyaev 1973 for a detailed discussion of the disk structure). Apply the sound speed condition to Equation (2.13), we obtain from Equations (2.13) and (2.15)

$$\begin{aligned}
 u_0 \left[\frac{\text{g}}{\text{cm}^2} \right] &= \frac{64\pi}{9\alpha} \frac{c^2}{\sigma_T^2} \\
 &= 4.6\alpha^{-1} \dot{m}^{-1} r^{3/2} (1 - r^{-1/2})^{-1}, \\
 \varepsilon \left[\frac{\text{erg}}{\text{cm}^3} \right] &= 2 \frac{c}{\sigma_T} \Omega \\
 &= 2.1 \cdot 10^{15} \alpha^{-1} m^{-1} r^{-3/2}, \\
 n \left[\text{cm}^{-3} \right] &= \frac{u_0}{2m_p z_0} \\
 &= 4.3 \cdot 10^{17} \alpha^{-1} \dot{m}^{-2} m^{-1} r^{3/2} (1 - r^{-1/2})^{-2}, \\
 v_r \left[\frac{\text{cm}}{\text{s}} \right] &= \frac{\dot{M}}{2\pi u_0 R} \\
 &= 7.7 \cdot 10^{10} \alpha \dot{m}^2 r^{-5/2} (1 - r^{-1/2}), \\
 H[\text{Gauss}] &\leq \sqrt{\frac{4\pi}{3} \alpha \varepsilon} \\
 &= 10^8 m^{-1/2} r^{-3/4}.
 \end{aligned} \tag{A.27}$$

The effective temperature can be calculated by Equation (2.16):

$$T[\text{K}] = 2.3 \cdot 10^7 (\alpha m)^{-1/4} r^{-3/4}. \tag{A.28}$$

The optical depth, with respect to absorption for a plasma with $\sigma_T \gg \sigma_{ff}$ is determined as:

$\tau^* = \sqrt{\sigma_T \sigma_{ff}} u_0$, namely

$$\tau^* = 8.4 \cdot 10^{-5} \alpha^{-17/16} m^{-1/16} \dot{m}^{-2} \cdot r^{-93/32} (1 - r^{-1/2})^{-2}. \tag{A.29}$$

With the similar derivation for regime a), the physical quantities in regime b) and c) are

b) $P_g \gg P_r$ and $\sigma_T \gg \sigma_{ff}$

$$\begin{aligned}
u_0 &= 1.7 \cdot 10^5 \alpha^{-4/5} \dot{m}^{3/5} m^{1/5} r^{-3/5} (1 - r^{-1/2})^{3/5}, \\
T &= 3.1 \cdot 10^8 \alpha^{-1/5} \dot{m}^{2/5} m^{-1/5} r^{-9/10} (1 - r^{-1/2})^{2/5}, \\
z_0 &= 1.2 \cdot 10^4 \alpha^{-1/10} \dot{m}^{1/5} m^{9/10} r^{21/20} (1 - r^{-1/2})^{1/5}, \\
n &= 4.2 \cdot 10^{24} \alpha^{-7/10} \dot{m}^{2/5} m^{-7/10} r^{-33/20} (1 - r^{-1/2})^{2/5}, \\
\tau^* &= \sqrt{\sigma_{ff} \sigma_T} u_0 = 10^2 \alpha^{-4/5} \dot{m}^{9/10} m^{1/5} r^{3/20} (1 - r^{-1/2})^{9/10}, \\
v_r &= 2 \cdot 10^6 \alpha^{4/5} \dot{m}^{2/5} m^{-1/5} r^{-2/5} (1 - r^{-1/2})^{-3/5}, \\
H &\leq 1.5 \cdot 10^9 \alpha^{1/20} \dot{m}^{2/5} m^{-9/20} r^{-51/40} (1 - r^{-1/2})^{2/5}.
\end{aligned} \tag{A.30}$$

and

c) $P_g \gg P_r$ and $\sigma_{ff} \gg \sigma_T$

$$\begin{aligned}
u_0 &= 6.1 \cdot 10^5 \alpha^{-4/5} \dot{m}^{7/10} m^{1/5} r^{-3/4} (1 - r^{-1/2})^{7/10}, \\
T &= 8.6 \cdot 10^7 \alpha^{-1/5} \dot{m}^{3/10} m^{-1/5} r^{-3/4} (1 - r^{-1/2})^{3/10}, \\
z_0 &= 6.1 \cdot 10^3 \alpha^{-1/10} \dot{m}^{3/20} m^{9/10} r^{9/8} (1 - r^{-1/2})^{3/20}, \\
n &= 3 \cdot 10^{25} \alpha^{-7/10} \dot{m}^{11/20} m^{-7/10} r^{-15/8} (1 - r^{-1/2})^{11/20}, \\
\tau^* &= \sigma_{ff} u_0 = 3.4 \cdot 10^2 \alpha^{-4/5} \dot{m}^{1/5} m^{1/5} r^{3/20} (1 - r^{-1/2})^{1/5}, \\
v_r &= 5.8 \cdot 10^5 \alpha^{4/5} \dot{m}^{3/10} m^{-1/5} r^{-1/4} (1 - r^{-1/2})^{-7/10}, \\
H &\leq 2.1 \cdot 10^9 \alpha^{1/20} \dot{m}^{17/40} m^{-9/20} r^{-21/16} (1 - r^{-1/2})^{17/40}.
\end{aligned} \tag{A.31}$$

A.5 The electromagnetic component in the stress-energy tensor in resistive GR-MHD

The electromagnetic part in the stress-energy tensor is defined by

$$T^{\mu\nu} = F^{\mu\alpha} F^\nu{}_\alpha - \frac{1}{4} g^{\mu\nu} F_{\alpha\beta} F^{\alpha\beta}. \tag{A.32}$$

Note that changing the order of ν and α in expression $F^\nu{}_\alpha$ makes a difference, since

$$F^\nu{}_\alpha = F_{\beta\alpha} g^{\nu\beta} = -F_{\alpha\beta} g^{\beta\nu} = -F_\alpha{}^\nu. \tag{A.33}$$

We can start the calculation of $T^{\mu\nu}$ with the Faraday tensors

$$\begin{aligned}
F^{\mu\nu} &= u^\mu e^\nu - e^\mu u^\nu + \epsilon^{\mu\nu\lambda\kappa} u_\lambda b_\kappa, \\
F_{\mu\nu} &= u_\mu e_\nu - e_\mu u_\nu + \epsilon_{\mu\nu\lambda\kappa} u^\lambda b^\kappa.
\end{aligned} \tag{A.34}$$

The above definition has discrepancies with Equations (9) & Equation (17) in [Bucciantini & Del Zanna \(2013\)](#) due to a different sign choice in the definition of Levi-Civita tensor $\epsilon^{\mu\nu\lambda\kappa}$. The

second part in Equation (A.32) is determined by

$$\begin{aligned}
F_{\mu\nu}F^{\mu\nu} &= (u^\mu e^\nu - e^\mu u^\nu + \epsilon^{\mu\nu\lambda\kappa} u_\lambda b_\kappa) \cdot (u_\mu e_\nu - e_\mu u_\nu + \epsilon_{\mu\nu\lambda\kappa} u^\lambda b^\kappa) \\
&= u^\mu e^\nu u_\mu e_\nu - u^\mu e^\nu e_\mu u_\nu + u^\mu e^\nu \epsilon_{\mu\nu\lambda\kappa} u^\lambda b^\kappa \\
&\quad - e^\mu u^\nu u_\mu e_\nu + e^\mu u^\nu e_\mu u_\nu - e^\mu u^\nu \epsilon_{\mu\nu\lambda\kappa} u^\lambda b^\kappa \\
&\quad + \epsilon^{\mu\nu\lambda\kappa} u_\lambda b_\kappa u_\mu e_\nu - \epsilon^{\mu\nu\lambda\kappa} u_\lambda b_\kappa e_\mu u_\nu + \epsilon^{\mu\nu\lambda\kappa} u_\lambda b_\kappa \epsilon_{\mu\nu\lambda\kappa} u^\lambda b^\kappa.
\end{aligned} \tag{A.35}$$

It is straightforward to find that

$$\begin{aligned}
u^\mu e^\nu u_\mu e_\nu &= e^\mu u^\nu e_\mu u_\nu = -e^2, \\
-u^\mu e^\nu e_\mu u_\nu &= -e^\mu u^\nu u_\mu e_\nu - (e \cdot u)^2 = 0, \\
\epsilon^{\mu\nu\lambda\kappa} b_\lambda u_\kappa \epsilon_{\mu\nu\lambda\kappa} b^\lambda u^\kappa &= 2b^2.
\end{aligned} \tag{A.36}$$

where the last equality comes from ideal GR-MHD. Also, using the identity $\epsilon^{\alpha\beta\gamma\delta} u_\alpha u_\beta = 0$, which makes all terms except those in Equation (A.36) vanish. Thus we have

$$F_{\mu\nu}F^{\mu\nu} = 2b^2 - 2e^2. \tag{A.37}$$

On the other hand, the first part in Equation (A.32) is determined by

$$\begin{aligned}
F^{\mu\alpha}F^\nu{}_\alpha &= (u^\mu e^\alpha - e^\mu u^\alpha + \epsilon^{\mu\alpha\lambda\kappa} u_\lambda b_\kappa) \cdot (u_\beta e_\alpha - e_\beta u_\alpha + \epsilon_{\beta\alpha\theta\varphi} u^\theta b^\varphi) \cdot g^{\nu\beta} \\
&= (u^\mu e^\alpha - e^\mu u^\alpha + \epsilon^{\mu\alpha\lambda\kappa} u_\lambda b_\kappa) \cdot (u_\beta e_\alpha - e_\beta u_\alpha - \epsilon_{\alpha\beta\theta\varphi} u^\theta b^\varphi) \cdot g^{\nu\beta} \\
&= u^\mu e^\alpha u_\beta e_\alpha g^{\nu\beta} - u^\mu e^\alpha e_\beta u_\alpha g^{\nu\beta} - u^\mu e^\alpha \epsilon_{\alpha\beta\theta\varphi} u^\theta b^\varphi g^{\nu\beta} \\
&\quad - e^\mu u^\alpha u_\beta e_\alpha g^{\nu\beta} + e^\mu u^\alpha e_\beta u_\alpha g^{\nu\beta} + e^\mu u^\alpha \epsilon_{\alpha\beta\theta\varphi} u^\theta b^\varphi g^{\nu\beta} \\
&\quad + \epsilon^{\mu\alpha\lambda\kappa} u_\lambda b_\kappa u_\beta e_\alpha g^{\nu\beta} - \epsilon^{\mu\alpha\lambda\kappa} u_\lambda b_\kappa e_\beta u_\alpha g^{\nu\beta} - \epsilon^{\mu\alpha\lambda\kappa} u_\lambda b_\kappa \epsilon_{\alpha\beta\theta\varphi} u^\theta b^\varphi g^{\nu\beta}.
\end{aligned} \tag{A.38}$$

Here we also have the following relations which can help the calibration

$$\begin{aligned}
u^\mu e^\alpha u_\beta e_\alpha g^{\nu\beta} &= e^2 u^\mu u^\nu, \\
-u^\mu e^\alpha e_\beta u_\alpha g^{\nu\beta} &= -e^\mu u^\alpha u_\beta e_\alpha g^{\nu\beta} = 0, \\
e^\mu u^\alpha e_\beta u_\alpha g^{\nu\beta} &= -e^\mu e^\nu, \\
e^\mu u^\alpha \epsilon_{\alpha\beta\theta\varphi} u^\theta b^\varphi g^{\nu\beta} &= -\epsilon^{\mu\alpha\lambda\kappa} u_\lambda b_\kappa e_\beta u_\alpha g^{\nu\beta} = 0, \\
-\epsilon^{\mu\alpha\lambda\kappa} u_\lambda b_\kappa \epsilon_{\alpha\beta\theta\varphi} u^\theta b^\varphi g^{\nu\beta} &= b^2 g^{\mu\nu} + b^2 u^\mu u^\nu - b^\mu b^\nu,
\end{aligned} \tag{A.39}$$

where the last relation can be derived as following

$$\begin{aligned}
-\epsilon^{\mu\alpha\lambda\kappa} u_\lambda b_\kappa \cdot \epsilon_{\alpha\beta\sigma\gamma} u^\sigma b^\gamma g^{\nu\beta} &= \epsilon^{\alpha\mu\lambda\kappa} u_\lambda b_\kappa \cdot \epsilon_{\alpha\beta\sigma\gamma} u^\sigma b^\gamma g^{\nu\beta} \\
&= -\delta_{\beta\sigma\gamma}^{\mu\lambda\kappa} u_\lambda b_\kappa u^\sigma b^\gamma g^{\nu\beta} \\
&= -(\delta_\beta^\mu \delta_\sigma^\lambda \delta_\gamma^\kappa - \delta_\beta^\mu \delta_\gamma^\lambda \delta_\sigma^\kappa - \delta_\sigma^\mu \delta_\beta^\lambda \delta_\gamma^\kappa - \delta_\gamma^\mu \delta_\sigma^\lambda \delta_\beta^\kappa \\
&\quad + \delta_\sigma^\mu \delta_\gamma^\lambda \delta_\beta^\kappa + \delta_\gamma^\mu \delta_\beta^\lambda \delta_\sigma^\kappa) u_\lambda b_\kappa u^\sigma b^\gamma g^{\nu\beta} \\
&= b^2 g^{\mu\nu} + b^2 u^\mu u^\nu - b^\mu b^\nu.
\end{aligned} \tag{A.40}$$

The remaining two terms $-u^\mu e^\alpha \epsilon_{\alpha\beta\theta\varphi} u^\theta b^\varphi g^{\nu\beta}$ and $\epsilon^{\mu\alpha\lambda\kappa} u_\lambda b_\kappa u_\beta e_\alpha g^{\beta\nu}$ can be rearranged using the identity $\epsilon_{\alpha\beta\gamma\delta} = g_{\alpha\zeta} g_{\beta\eta} g_{\gamma\theta} g_{\delta\ell} \epsilon^{\zeta\eta\theta\ell}$, hence

$$\begin{aligned}
-u^\mu e^\alpha \epsilon_{\alpha\beta\theta\varphi} u^\theta b^\varphi g^{\nu\beta} &= -u^\mu e^\alpha (\epsilon^{ABCD} g_{A\alpha} g_{B\beta} g_{C\theta} g_{D\varphi}) u^\theta b^\varphi g^{\nu\beta} \\
&= -u^\mu e^\alpha \epsilon^{ABCD} g_{A\alpha} g_B^\nu u_C b_D \\
&= -u^\mu \epsilon^{A\nu CD} b_D u_C e_A \\
&= -u^\mu \epsilon^{\beta\nu\lambda\kappa} b_\kappa u_\lambda e_\beta \\
&= -u_\lambda e_\beta b_\kappa u^\mu \epsilon^{\nu\lambda\beta\kappa}
\end{aligned} \tag{A.41}$$

and

$$\begin{aligned}
\epsilon^{\mu\alpha\lambda\kappa} u_\lambda b_\kappa u_\beta e_\alpha g^{\beta\nu} &= \epsilon^{\mu\alpha\lambda\kappa} u_\lambda b_\kappa e_\alpha u^\nu \\
&= u_\lambda e_\beta b_\kappa \epsilon^{\mu\beta\lambda\kappa} u^\nu \\
&= -u_\lambda e_\beta b_\kappa u^\nu \epsilon^{\mu\lambda\beta\kappa}.
\end{aligned} \tag{A.42}$$

Thus, Equation (A.38) becomes

$$F^{\mu\alpha} F^\nu{}_\alpha = (b^2 + e^2) u^\mu u^\nu - b^\mu b^\nu - e^\mu e^\nu + b^2 g^{\mu\nu} - u_\lambda e_\beta b_\kappa (u^\mu \epsilon^{\nu\lambda\beta\kappa} + u^\nu \epsilon^{\mu\lambda\beta\kappa}). \tag{A.43}$$

After applying the results in Equations (A.37) and A.43 to Equation (A.32), the electromagnetic component in the stress-energy tensor in resistive GR-MHD can be then expressed by

$$T_{EM}^{\mu\nu} = (b^2 + e^2) (u^\mu u^\nu + \frac{1}{2} g^{\mu\nu}) - b^\mu b^\nu - e^\mu e^\nu - u_\lambda e_\beta b_\kappa (u^\mu \epsilon^{\nu\lambda\beta\kappa} + u^\nu \epsilon^{\mu\lambda\beta\kappa}), \tag{A.44}$$

or with the definition $\epsilon^{\alpha\beta\gamma\delta} u_\delta = \epsilon^{\alpha\beta\gamma}$, by

$$T_{EM}^{\mu\nu} = (b^2 + e^2) (u^\mu u^\nu + \frac{1}{2} g^{\mu\nu}) - b^\mu b^\nu - e^\mu e^\nu - e_\beta b_\kappa (u^\mu \epsilon^{\nu\beta\kappa} + u^\nu \epsilon^{\mu\beta\kappa}). \tag{A.45}$$

A.6 Newton-Raphson Method

(The following paragraph refers to the article on Wikipedia.) Newton's method (also known as the Newton–Raphson method), is a method for finding successively better approximations to the roots (or zeroes) of a real-valued function. Generally, in mathematical language, if $f(x)$ is a non-trivial function of x , the Newton–Raphson method can then be used to approximate the root for

$$f(x) = 0 \tag{A.46}$$

by a series of guesses for x . Starting with the initial guess x_0 , a better approximation x_1 is given by

$$x_1 = x_0 - \frac{f(x_0)}{f'(x_0)}, \tag{A.47}$$

where $f'(x_0)$ is the derivative of $f(x)$ to x at $x = x_0$. Geometrically, $(x_1, 0)$ is the intersection of the x-axis and the tangent of the graph of $f(x)$ at $(x_0, f'(x_0))$. The process is repeated as

$$x_{n+1} = x_n - \frac{f(x_n)}{f'(x_n)}, \quad (\text{A.48})$$

until the solution for x returns an acceptable tolerance.

The Newton-Raphson method can be extend to equation systems with N functions and N variables. In our context, the equation system in Equation (3.45) is two dimensional. If we name the two variables x and y , and the first equation $\mathbf{A}(x, y)$, the second equation $\mathbf{B}(x, y)$, the process of the Newton–Raphson method is then expressed by

$$\begin{aligned} x_{n+1} &= x_n - \frac{\partial \mathbf{A}(x_n, y_n)}{\partial x_n} \Big|_{(x_n, y_n)} - \frac{\partial \mathbf{B}(x_n, y_n)}{\partial x_n} \Big|_{(x_n, y_n)}, \\ y_{n+1} &= y_n - \frac{\partial \mathbf{A}(x_n, y_n)}{\partial y_n} \Big|_{(x_n, y_n)} - \frac{\partial \mathbf{B}(x_n, y_n)}{\partial y_n} \Big|_{(x_n, y_n)}. \end{aligned} \quad (\text{A.49})$$

Bibliography

- Abramowicz, M., Jaroszynski, M., & Sikora, M. 1978, *Astronomy and Astrophysics*, 63, 221
- Antonucci, R. R. J., & Ulvestad, J. S. 1985, *Astrophysical Journal*, 294, 158
- Antonucci, R. 1993, *Annual Review of Astron and Astrophys*, 31, 473 radio-loud AGN unification model
- Antonuccio-Delogu, V., & Silk, J. 2010, *Monthly Notices of the RAS*, 405, 1303
- Bacciotti, F., Ray, T. P., Mundt, R., Eisloffel, J., & Solf, J. 2002, *Astrophysical Journal*, 576, 222
- Balbus, S. A., & Hawley, J. F. 1991, *Astrophysical Journal*, 376, 214
- Baldwin, J. E., & Smith, F. G. 1956, *The Observatory*, 76, 141
- Bally, J. 2007, *Astrophysics and Space Science*, 311, 15
- Barthel, P. D. 1989, *Astrophysical Journal*, 336, 606
- Berg, B. A. 2004, [arXiv:cond-mat/0410490](https://arxiv.org/abs/cond-mat/0410490)
- Biretta, J. A., Zhou, F., & Owen, F. N. 1995, *Astrophysical Journal*, 447, 582
- Biretta, J. A., Sparks, W. B., & Macchetto, F. 1999, *Astrophysical Journal*, 520, 621
- Blandford, R. D., & Königl, A. 1979, *Astrophysical Journal*, 232, 34
- Blandford, R. D., Netzer, H., Woltjer, L., Courvoisier, T. J.-L., & Mayor, M. 1990, *Active Galactic Nuclei*, 97
- Blandford, R. D., & Payne, D. G. 1982, *Monthly Notices of the RAS*, 199, 883

- Blandford, R. D., & Znajek, R. L. 1977, *Monthly Notices of the RAS*, 179, 433
- Bolton, J. G., Gardner, F. F., & Mackey, M. B. 1963, *Nature*, 199, 682
- Bolton, J. G., Clarke, M. E., Sandage, A., & Véron, P. 1965, *Astrophysical Journal*, 142, 1289
- Boyer, R. H., & Lindquist, R. W. 1967, *Journal of Mathematical Physics*, 8, 265
- Boyer, R. H., & Lindquist, R. W. 1982, *Black Holes: Selected Reprints*, 61
- Bucciantini, N., & Del Zanna, L. 2013, *Monthly Notices of the RAS*, 428, 71
- Bugli, M., Del Zanna, L., & Bucciantini, N. 2014, *Monthly Notices of the RAS*, 440, L41
- Burnham, S. W. 1890, *Monthly Notices of the RAS*, 51, 94
- Casse, F., & Keppens, R. 2002, *Astrophysical Journal*, 581, 988
- Coffey, D., Bacciotti, F., Woitas, J., Ray, T. P., & Eislöffel, J. 2004, *Astrophysical Journal*, 604, 758
- Cohen, M. H., Linfield, R. P., Moffet, A. T., et al. 1977, *Nature*, 268, 405
- Croston, J. H., Hardcastle, M. J., Harris, D. E., et al. 2005, *Astrophysical Journal*, 626, 733
- Curiel, S., Ho, P. T. P., Patel, N. A., et al. 2006, *Astrophysical Journal*, 638, 878
- Curtis, H. D. 1918, *Publications of Lick Observatory*, 13, 9
- Dhawan, V., Mirabel, I. F., & Rodríguez, L. F. 2000, *Astrophysical Journal*, 543, 373
- Del Zanna, L., & Bucciantini, N. 2002, *Astronomy and Astrophysics*, 390, 1177
- Del Zanna, L., Bucciantini, N., & Londrillo, P. 2003, *Astronomy and Astrophysics*, 400, 397
- Del Zanna, L., Zanotti, O., Bucciantini, N., & Londrillo, P. 2007, *Astronomy and Astrophysics*, 473, 11
- Del Zanna, L., Papini, E., Landi, S., Bugli, M., & Bucciantini, N. 2016, *Monthly Notices of the RAS*, 460, 3753
- De Villiers, J.-P., & Hawley, J. F. 2002, *Astrophysical Journal*, 577, 866
- De Villiers, J.-P., & Hawley, J. F. 2003, *Astrophysical Journal*, 589, 458
- De Villiers, J.-P., & Hawley, J. F. 2003, *Astrophysical Journal*, 592, 1060
- Dionysopoulou, K., Alic, D., Palenzuela, C., Rezzolla, L., & Giacomazzo, B. 2013, *Physical Review D*, 88, 044020
- Doeleman, S. S., Fish, V. L., Schenck, D. E., et al. 2012, *Science*, 338, 355

- Dumbser, M., & Zanotti, O. 2009, *Journal of Computational Physics*, 228, 6991
- Einstein, A. 1915, *Sitzungsberichte der Königlich Preußischen Akademie der Wissenschaften (Berlin)*, Seite 844-847.,
- Einstein, A. 1916, *Annalen der Physik*, 354, 769
- Einstein, A. 1917, *Sitzungsberichte der Königlich Preußischen Akademie der Wissenschaften (Berlin)*, Seite 142-152.,
- Fanaroff, B. L., & Riley, J. M. 1974, *Monthly Notices of the RAS*, 167, 31P
- Fath, E. A. 1909, *Lick Observatory Bulletin*, 5, 71
- Fender, R. P., Garrington, S. T., McKay, D. J., et al. 1999, *Monthly Notices of the RAS*, 304, 865
- Fendt, C. 2009, *Astrophysical Journal*, 692, 346
- Fendt, C., & Ćemeljić, M. 2002, *Astronomy and Astrophysics*, 395, 1045
- Fendt, C., & Sheikhnezami, S. 2013, *Astrophysical Journal*, 774, 12
- Ferreira, J. 1997, *Astronomy and Astrophysics*, 319, 340
- Fishbone, L. G., & Moncrief, V. 1976, *Astrophysical Journal*, 207, 962
- Fleming, T. P., Stone, J. M., & Hawley, J. F. 2000, *Astrophysical Journal*, 530, 464
- Foreman-Mackey, D., Hogg, D. W., Lang, D., & Goodman, J. 2013, *Publications of the ASP*, 125, 306
- Gaibler, V., Khochfar, S., Krause, M., & Silk, J. 2012, *Monthly Notices of the RAS*, 425, 438
- Gammie, C. F., McKinney, J. C., & Tóth, G. 2003, *Astrophysical Journal*, 589, 444
- Gómez, L., Rodríguez, L. F., Loinard, L., et al. 2005, *Astrophysical Journal*, 635, 1166
- Gorbatskii, V. G. 1965, *Soviet Astronomy*, 8, 680
- Greenstein, J. L., & Schmidt, M. 1964, *Astrophysical Journal*, 140, 1
- Greiner, J., Cuby, J. G., & McCaughrean, M. J. 2001, *Nature*, 414, 522
- Hada, K., Kino, M., Doi, A., et al. 2013, *Astrophysical Journal*, 775, 70
- Hada, K., Kino, M., Doi, A., et al. 2016, *Astrophysical Journal*, 817, 131
- Hartigan, P., Morse, J. A., Reipurth, B., Heathcote, S., & Bally, J. 2001, *Astrophysical Journal, Letters*, 559, L157
- Hawley, J. F., & Balbus, S. A. 1992, *Astrophysical Journal*, 400, 595

- Hawley, J. F., & Balbus, S. A. 2002, *Astrophysical Journal*, 573, 738
- Hawley, J. F., Smarr, L. L., & Wilson, J. R. 1984, *Astrophysical Journal*, 277, 296
- Homan, D. C. 2012, *International Journal of Modern Physics Conference Series*, 8, 163
- Igumenshchev, I. V., Narayan, R., & Abramowicz, M. A. 2003, *Astrophysical Journal*, 592, 1042
- Impey, C. 1987, *Superluminal Radio Sources*, 233
- Jorstad, S. G., Marscher, A. P., Mattox, J. R., et al. 2001, *Astrophysical Journal, Supplement*, 134, 181
- Jorstad, S. G., Marscher, A. P., Lister, M. L., et al. 2005, *Astronomical Journal*, 130, 1418
- Kerr, R. P., & Schild, A. 2009, *General Relativity and Gravitation*, 41, 2485
- Khanna, R., & Camenzind, M. 1996, *Astronomy and Astrophysics*, 307, 665
- Kim, J.-Y., Lu, R.-S., Krichbaum, T. P., et al. 2016, arXiv:1609.07896
- Kippenhahn, R., & Moellenhoff, C. 1975, Mannheim: Bibliographisches Institut, 1975,
- Klein, U. 1999, *The Radio Galaxy Messier 87*, 530, 56
- Koide, S., Shibata, K., & Kudoh, T. 1999, *Astrophysical Journal*, 522, 727
- Komissarov, S. S. 1999, *Monthly Notices of the RAS*, 303, 343
- Komissarov, S. S. 2005, *Monthly Notices of the RAS*, 359, 801
- Komissarov, S. S. 2007, *Monthly Notices of the RAS*, 382, 995
- Lister, M. L., Cohen, M. H., Homan, D. C., et al. 2009, *Astronomical Journal*, 138, 1874-1892
- Longaretti, P.-Y., & Lesur, G. 2010, *Astronomy and Astrophysics*, 516, A51
- Lynden-Bell, D. 1996, *Monthly Notices of the RAS*, 279, 389
- Machida, M., & Matsumoto, R. 2003, *Astrophysical Journal*, 585, 429
- Marscher, A. P. 2006, *Relativistic Jets: The Common Physics of AGN, Microquasars, and Gamma-Ray Bursts*, 856, 1
- Martí, J. M., & Müller, E. 1999, *Living Reviews in Relativity*, 2, 3
- Matthews, T. A., & Sandage, A. 1962, *Publications of the ASP*, 74, 406
- McKinney, J. C. 2006, *Monthly Notices of the RAS*, 367, 1797
- McKinney, J. C. 2006, *Monthly Notices of the RAS*, 368, 1561

- McKinney, J. C., & Gammie, C. F. 2004, *Astrophysical Journal*, 611, 977
- McKinney, J. C., Tchekhovskoy, A., & Blandford, R. D. 2012, *Monthly Notices of the RAS*, 423, 3083
- Mignone, A., Bodo, G., Massaglia, S., et al. 2007, *Astrophysical Journal, Supplement*, 170, 228
- Miller-Jones, J. C. A., Fender, R. P., & Nakar, E. 2006, *Monthly Notices of the RAS*, 367, 1432
- Mirabel, I. F., & Rodríguez, L. F. 1994, *Nature*, 371, 46
- Mirabel, I. F., & Rodríguez, L. F. 1998, *Nature*, 392, 673
- Mirabel, I. F., & Rodríguez, L. F. 1999, *Annual Review of Astron and Astrophys*, 37, 409
- Misner, C. W., Thorne, K. S., & Wheeler, J. A. 1973, San Francisco: W.H. Freeman and Co., 1973,
- Mizuno, Y. 2013, *Astrophysical Journal, Supplement*, 205, 7
- Narayan, R., Igumenshchev, I. V., & Abramowicz, M. A. 2003, *Publications of the ASJ*, 55, L69
- Noble, S. C., Gammie, C. F., McKinney, J. C., & Del Zanna, L. 2006, *Astrophysical Journal*, 641, 626
- Orosz, J. A., Groot, P. J., van der Klis, M., et al. 2002, *Astrophysical Journal*, 568, 845
- Ouyed, R., & Pudritz, R. E. 1997, *Astrophysical Journal*, 482, 712
- Ouyed, R., & Pudritz, R. E. 1997, *Astrophysical Journal*, 484, 794
- Paczynski, B., & Wiita, P. J. 1980, *Astronomy and Astrophysics*, 88, 23
- Palenzuela, C., Lehner, L., Reula, O., & Rezzolla, L. 2009, *Monthly Notices of the RAS*, 394, 1727
- Pelletier, G., & Pudritz, R. E. 1992, *Astrophysical Journal*, 394, 117
- Piran, T. 2004, *Reviews of Modern Physics*, 76, 1143
- Porcas, R. 1983, *Nature*, 302, 753
- Porth, O., & Fendt, C. 2010, *Astrophysical Journal*, 709, 1100
- Porth, O., Fendt, C., Meliani, Z., & Vaidya, B. 2011, *Astrophysical Journal*, 737, 42
- Porth, O. 2013, *Monthly Notices of the RAS*, 429, 2482
- Prendergast, K. H., & Burbidge, G. R. 1968, *Astrophysical Journal, Letters*, 151, L83
- Pringle, J. E., & Rees, M. J. 1972, *Astronomy and Astrophysics*, 21, 1

- Pu, H.-Y., Nakamura, M., Hirovani, K., et al. 2015, *Astrophysical Journal*, 801, 56
- Pudritz, R. E., & Norman, C. A. 1986, *Astrophysical Journal*, 301, 571
- Pudritz, R. E., Ouyed, R., Fendt, C., & Brandenburg, A. 2007, *Protostars and Planets V*, 277
- Qian, Q., Fendt, C., Noble, S., & Bugli, M. 2017, *Astrophysical Journal*, 834, 29
- Ray, T., Dougados, C., Bacciotti, F., Eisloffel, J., & Chrysostomou, A. 2007, *Protostars and Planets V*, 231
- Readhead, A. C. S., Cohen, M. H., Pearson, T. J., & Wilkinson, P. N. 1978, *Nature*, 276, 768
- Readhead, A. C. S., Pearson, T. J., Cohen, M. H., Ewing, M. S., & Moffet, A. T. 1979, *Astrophysical Journal*, 231, 299
- Rees, M. J. 1966, *Nature*, 211, 468
- Reipurth, B., Bally, J., & Devine, D. 1997, *Astronomical Journal*, 114, 2708
- Rezzolla, L., & Zanotti, O. 2013, *Relativistic Hydrodynamics*, by L. Rezzolla and O. Zanotti. Oxford University Press, 2013. ISBN-10: 0198528906; ISBN-13: 978-0198528906,
- Romanova, M. M., Ustyugova, G. V., Koldoba, A. V., & Lovelace, R. V. E. 2012, *Monthly Notices of the RAS*, 421, 63
- Ruderman, M. A., & Sutherland, P. G. 1975, *Astrophysical Journal*, 196, 51
- Ruffini, R., & Wilson, J. R. 1975, *Physical Review D*, 12, 2959
- Sądowski, A., Narayan, R., Tchekhovskoy, A., et al. 2015, *Monthly Notices of the RAS*, 447, 49
- Sari, R., Piran, T., & Halpern, J. P. 1999, *Astrophysical Journal, Letters*, 519, L17
- Schmidt, M. 1963, *Nature*, 197, 1040
- Schutz, B. 2009, *A First Course in General Relativity* by Bernard Schutz. Cambridge University Press, 2009. ISBN: 9780521887052,
- Schwarzschild, K. 1916, *Abh. Konigl. Preuss. Akad. Wissenschaften Jahre 1906,92*, Berlin,1907, 1916,
- Seyfert, C. K. 1943, *Astrophysical Journal*, 97, 28
- Shakura, N. I. 1973, *Soviet Astronomy*, 16, 756
- Shakura, N. I., & Sunyaev, R. A. 1973, *Astronomy and Astrophysics*, 24, 337
- Sheikhnezami, S., Fendt, C., Porth, O., Vaidya, B., & Ghanbari, J. 2012, *Astrophysical Journal*, 757, 65

- Sheikhnezami, S., & Fendt, C. 2015, *Astrophysical Journal*, 814, 113
- Stepanovs, D., & Fendt, C. 2014, *Astrophysical Journal*, 793, 31
- Stepanovs, D., & Fendt, C. 2016, arXiv:1604.07313
- Stone, J. M., & Norman, M. L. 1992, *Astrophysical Journal*, Supplement, 80, 753
- Takamoto, M., & Inoue, T. 2011, *Astrophysical Journal*, 735, 113
- Tchekhovskoy, A., Narayan, R., & McKinney, J. C. 2010, *Astrophysical Journal*, 711, 50
- Titarchuk, L., & Shrader, C. R. 2002, *Astrophysical Journal*, 567, 1057
- Tzeferacos, P., Ferrari, A., Mignone, A., et al. 2009, *Monthly Notices of the RAS*, 400, 820
- Urry, C. M., & Padovani, P. 1995, *Publications of the ASP*, 107, 803
- Ustyugova, G. V., Koldoba, A. V., Romanova, M. M., Chechetkin, V. M., & Lovelace, R. V. E. 1995, *Astrophysical Journal*, Letters, 439, L39
- Vermeulen, R. C., & Cohen, M. H. 1994, *Astrophysical Journal*, 430, 467
- Watanabe, N., & Yokoyama, T. 2006, *Astrophysical Journal*, Letters, 647, L123
- Wills, B. J., & Browne, I. W. A. 1986, *Astrophysical Journal*, 302, 56
- Wilson, J. R. 1977, 1st Marcel Grossmann Meeting on General Relativity, 393
- Woltjer, L. 1959, *Astrophysical Journal*, 130, 38
- Zanni, C., Ferrari, A., Rosner, R., Bodo, G., & Massaglia, S. 2007, *Astronomy and Astrophysics*, 469, 811
- Zhang, S. N., Mirabel, I. F., Harmon, B. A., et al. 1997, *Proceedings of the Fourth Compton Symposium*, 410, 141
- Zinnecker, H., McCaughrean, M. J., & Rayner, J. T. 1998, *Nature*, 394, 862